Downloaded from orbit.dtu.dk on: May 05, 2023

DTU Library

Development of an Electrochemical-Cantilever Hybrid Platform

Fischer, Lee MacKenzie

Publication date:
2011

Document Version
Publisher's PDF, also known as Version of record

Link back to DTU Orbit

Citation (APA):
Fischer, L. M. (2011). *Development of an Electrochemical-Cantilever Hybrid Platform*. Technical University of Denmark.

General rights
Copyright and moral rights for the publications made accessible in the public portal are retained by the authors and/or other copyright owners and it is a condition of accessing publications that users recognise and abide by the legal requirements associated with these rights.

- Users may download and print one copy of any publication from the public portal for the purpose of private study or research.
- You may not further distribute the material or use it for any profit-making activity or commercial gain
- You may freely distribute the URL identifying the publication in the public portal

If you believe that this document breaches copyright please contact us providing details, and we will remove access to the work immediately and investigate your claim.

Development of an Electrochemical-Cantilever Hybrid Platform

Lee MacKenzie Fischer
Ph.D. Thesis

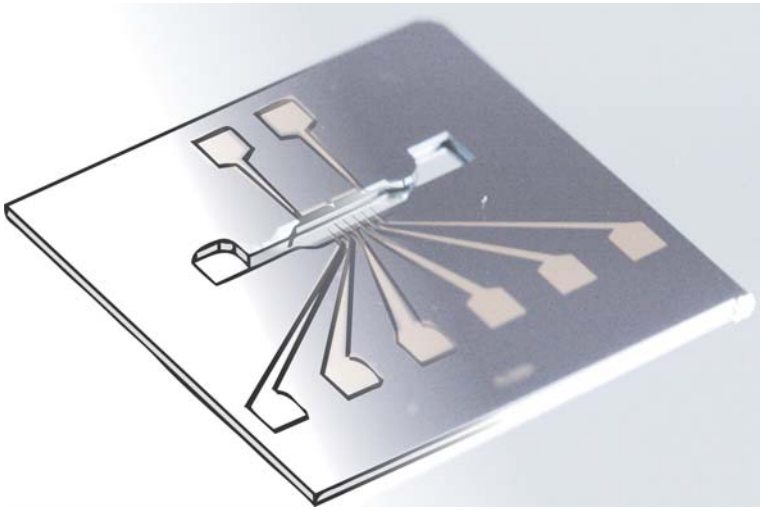

December 17, 2010

DTU Nanotech - Department of Micro and Nanotechnology
Technical University of Denmark
Building 345 East
2800 Kgs. Lyngby
DENMARK

Abstract

This thesis presents the development of a novel electrochemical-cantilever hybrid sensing platform. Microcantilevers are highly sensitive transducers of surface stress, while electrochemical methods allow control and monitoring of the surface charge and potential, which can be used to identify compounds or selectively modify the surface. A device combining these two complementary techniques was designed, produced, and tested with the target application being the detection and speciation of toxic heavy metals.

A new electrochemical-cantilever chip format was designed, incorporating six individually addressable cantilever electrodes and two reference/counter electrodes in a microchannel, all on a single chip. The fabrication process was optimized to consistently achieve nearly 100% chip yield. This chip was combined with a polymer flow cell that could be assembled, used, and disassembled repeatedly without the need for wax or epoxy to seal the cell. The flow cell was optimized to provide reliable electrical and fluidic connections, as well as optical access for control and interrogation of the cantilevers and their environment.

The cantilever arrays were functionalized with the amino acid L-cysteine (Cys) and tetrapeptide Cys-Gly-Gly-His (CGGH) for binding copper (II) ions. This functional layer was removed from one cantilever by selective application of a voltammetric signal to generate a clean reference cantilever for differential measurements. The responses of the monolayers to three different concentrations of copper ions were investigated, and an estimate of the adsorption rate constant was found for the Cu-(Cys) and Cu-(CGGH) binding systems.

Potential steps and sweeps were applied to a cantilever in buffered electrolyte, resulting in surface stress behavior in agreement with theory. A differential stress response due to cyclic voltammetry performed in electrolyte with and without a reversible redox couple was found to agree with a first order approximation of Lippmann's equation, verifying that the source of the motion is stress induced by a charged surface.

This prototype system was successfully tested and demonstrated to be a powerful analytical tool, but still requires a deeper understanding to reach its full potential.

Dansk Resume

I denne afhandling er udviklingen af en nyskabende elektrokemisk-cantilever hybrid sensor platform præsenteret. Mikro cantileverer er meget følsomme over for ændringer i overflade stress, mens elektrokemiske metoder tillader kontrol og udlæsning af overflade ladning og potentiale. Det kan bruges til at identificere kemiske forbindelser eller selektivt modificere overfladen. Et apparat der integrerer de to komplementre teknikker, er blevet designet, produceret og testet med det mål at kunne detektere og type bestemme giftige tungmetaller.

Et nyt elektrokemisk-cantilever chip format indeholdende 6 cantilever elektroder, og to reference elektroder der kan adresseres hver for sig er udviklet. Alle cantileverer sidder i en mikro kanal, og det hele er integreret på en enkelt chip. Fabrikationsprocessen blev optimeret til konsekvent at give et 100% udbytte. Chippen blev kombineret med en polymer flowcelle, der kan samles, blive anvendt og skilt ad gentagne gange uden brug af voks eller epoxy til forsegling. Flowcellen er optimeret til at give pålidelige elektriske og fluide forbindelser, samt optisk adgang til kontrol og aflæsning af cantileverene og det miljø de befinder sig i.

For at binde kobber (II) ioner blev rækker af cantilevere funktionaliseret med aminosyre L-cysteine(Cys) og tetrapeptid Cys-Gly-Gly-His (CGGH). Dette funktionelle lag blev fjernet fra en enkelt cantilever, ved selektivt at anvende et voltammetrisk signal til at generere en ren reference cantilever til brug for differentielle målinger. Reaktionen for 3 forskellige koncentrationer af kobber ioner blev undersøgt, og et estimat af absorption rate konstanten fundet for Cu-(Cys) og Cu-(CGGH) bindings systemer.

Potentiale trin og skanninger blev påtrykt en cantilever i en buffered elektrolyt. Det resulterede i overflade stress ændringer, som passer med teorien. Det differentielle stress respons givet ved cyklisk voltammetri udført i elektrolyt med og uden reversible redox par passer med første ordens tilnærmelsen af Lippmanns ligning. Det bekræfter, at kilden til bevægelse er stress induceret af en ladet overflade.

Dette prototype system blev succesfuldt testet, og har vist sig som et kraftfuldt analytisk vrktøj, der dog stadig kræver en dybere forståelse for at opnå sit fulde potentiale.

Contents

List of Figures

List of Tables

Chapter 1

PROJECT INTRODUCTION

1.1 Project Motivation

Toxic heavy metal contaminants in drinking water are well known to have adverse health effects, both acute and chronic [1–4]. The carcinogenic effects of nickel have been documented [5, 6], while arsenic, in addition to being a carcinogen [7], has been linked to mutagenesis [8]. Heavy metals are also known to bioaccumulate in organisms [9], making the ability to detect them at trace levels necessary to ensure public safety.

A number of methods are available for determining the presence and concentration of toxic metal ions. Atomic absorption spectroscopy and inductively-coupled plasma mass spectrometry are two highly sensitive and well established techniques [10], but typically require sample preparation and are confined to the lab due to the size of the instruments. Electrochemical methods such as anodic stripping voltammetry, however, typically require no sample pretreatment [11] and can be made small enough for measurements in the field [12]. Detection limit and speciation of metal ions has also been recently enhanced through the application of chemically functional layers to electrodes [13–17].

Microcantilevers are highly sensitive transducers of surface events [18–21], and cantilevers modified with appropriate monolayers have even been used for detecting metal ions [22–25]. Electrochemical methods have been combined with cantilever measurements [26–30], and applied to generation of motion [31, 32], as well as detection purposes [33–35].

This aim of this thesis project was to develop a device capable of detecting and speciating toxic heavy metal ions, based on a combined

electrochemical-cantilever sensing platform, to be implanted in residential water pumps by Grundfos A/S, the world's largest manufacturer of these pumps. However, long before any commercial applications could be considered, the basic operating principles of all aspects had to be understood. Electrochemical behavior and surface modification had to be characterized before it could be reliably applied to microcantilevers. Additionally, since no suitable platform for combined electrochemical-cantilever measurements existed at DTU Nanotech, one had to be designed and fabricated from the ground up. Toxic heavy metals such as Ni^{2+} and As^{3+} were the target species originally, but the focus was quickly shifted to Cu^{2+}. While the toxic effects of copper only manifest at relatively high concentrations compared to other metals (2 mg/l), the copper-binding schemes presented herein offered an excellent model system to test this new sensor platform.

1.2 Thesis Outline

Introduction

Part I holds the background for the thesis. The basic concept of cantilever sensing and measurement as it pertains to this work is highlighted in chapter 2, while the electrochemical theory and techniques that apply to the rest of the thesis are discussed in chapter 3. These two chapters provide a brief introduction to two different methods of sensing in an effort to make reading the thesis coherent to a range of different expertise levels.

Chapter 4 reviews the literature available on combined electrochemical-cantilever measurements. It concludes by noting that all of the systems in the literature reviewed are comprised of discrete components, *i.e.* the cantilever, reference and counter electrodes are separate articles, often sealed into a liquid cell by wax or epoxy. This emphasizes how the electrochemical-cantilever hybrid platform at the focus of this thesis is the first of its kind to have all electrodes and multiple cantilevers integrated into a flow microchannel on a single chip.

Electrochemistry Basics

Part II covers the initial work on microfabricating gold electrodes and using them for measurements. Chapters 5 and 6 follow the development of the 2^{nd} gen. (second generation) 1 mm^2 gold electrode and the protocol to reliably obtain a clean surface. The combination of this electrode format and the cleaning protocol served as the basis for a great number of screening trials for investigating various surface chemistries, and has since been used by

a number of Ph.D. students and post-docs for similar applications. The protocol developed using these 2^{nd} gen. electrodes was eventually successfully applied to the electrochemical-cantilever chips, facilitating ion detection.

Chapter 7 describes investigations into the effects of pH on the charge state of carboxyl and amine groups on self-assembled monolayers. This work led to an understanding of the behavior of these functional groups and highlighted the importance of controlling pH levels.

Functional Layers

Part III follows the screening of the two functional layers that were then applied to the cantilevers. Chapter 8 describes the immobilization protocol used to reliably attach the amino acid L-cysteine and the tetrapeptide Cys-Gly-Gly-His to a gold surface. Electrochemical and quartz crystal microbalance methods were used to confirm the attachment of the molecules, as well as their ability to capture Cu^{2+} ions. The chapter concludes with a short investigation into the development of a new peptide for specifically capturing As^{3+} ions. While this effort was unsuccessful, the concept of using crown ethers for specific metal ion detection was presented as a promising alternative.

The ECC Platform

Part IV takes the electrochemical-cantilever (ECC) platform from mere ideas and sketches to a functioning device capable of combined measurements. Chapter 9 describes the rationale behind the design of the ECC chip, the optimized, high-yield fabrication process, and several alternative methods. Additionally, the design, fabrication, and operation of the flow cell is explained in detail. The flow cell and ECC chip were designed to operate together to create a versatile platform which could be quickly and reliably assembled and disassembled without the need for wax or epoxy.

Chapter 10 describes the development of the operating procedure, and the work required to make the ECC chip and flow cell operable and ready for measurements. Issues such as sealing, noise, and electrical connections were addressed to ensure that reliable data could be acquired with this platform.

Characterization & Measurements

Part V concludes this work by describing two applications of the hybrid platform. Chapter 11 presents the differential measurements used to explore the

reactions of the two monolayers selected in chapter 8. The electrochemical capabilities were used to voltammetrically clean a cantilever *in situ*, generating a reference for differential measurements. In this way the signal of the clean cantilever could be subtracted from that of the functional cantilever, thus revealing only the response of the functional monolayer. The cysteine monolayer could be chemically regenerated and reused by applying ethylenediaminetetraacetic acid to remove the copper ions. Evidence was found to support electrochemical regeneration of the cysteine monolayer.

Chapter 12 presents the combined electrochemical and surface stress data acquired using the ECC platform. First, the motion of a cantilever to potential steps and cycling in buffered electrolyte was investigated, and was found to agree with theory. Then, cyclic voltammetry on a cantilever in a reversible redox couple was executed, and a vastly different stress response was observed. Nonetheless, the motion of the cantilever was found to closely follow the accumulation of charge on the electrode surface, fitting very well with the first order approximation of the Lippmann equation, thus confirming the successful operation of the ECC platform.

Appendices

Three appendices are included in this work to allow full recreation of the device and results that have been presented. Appendix A contains the process flow used to produce the 1^{st} gen. and 2^{nd} gen. microelectrodes described in chapters 5 and 6. Appendix B describes the optimized process flow used to create the ECC chips. Last, appendix C contains the engineering drawings for the components of the flow cell.

Part I

Introduction

Chapter 2

Microcantilevers as Sensing Elements

2.1 Cantilever Transducers

Microcantilevers have been used to detect and monitor a variety of chemical and biological reactions [21, 36, 37]. Typical cantilever dimensions used are hundreds of μm in length, tens of μm in width, and 1 μm or less in thickness (with respect to figure 2.1), and can be fabricated from any number of materials [38].

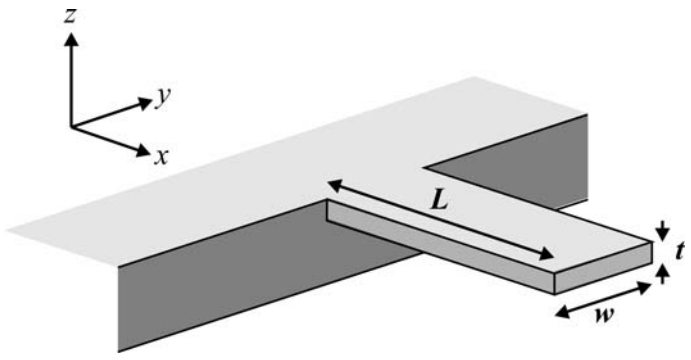

Figure 2.1: An illustration of a microcantilever, labeled with the relevant geometric parameters length, L, width, w, and thickness, t.

The sensitivity of a cantilever, such as the one in figure 2.1, to an applied force (*e.g.* a homogenous loading) can be described by the spring constant k, which is evaluated using equation 2.1

$$k = \frac{2Ewt^3}{3L^3} \tag{2.1}$$

where E is the Young's modulus for the material, w is the cantilever width, t is the thickness, and L is the length [39]. Typical k-values lay in the mN/m range, and the vertical deflection of the tip can be measured with sub-nm precision using any of a several different techniques [40]. This means that the incredibly small forces of molecular interactions occurring on the cantilever surface can be detected. Indeed, events such as self-assembly of alkanethiol monolayers [41–43], protein interactions [44–46], and DNA-hybridization [20, 47, 48] are just a few examples of microcantilever-based sensing.

2.2 Measurement of Surface Stress

These microcantilevers are sensitive to the surface stress created by the interactions of molecules on the surface with each other, the surrounding environment, or the cantilever itself [18]. Since the thickness of these cantilevers is an order of magnitude smaller, or more, than the others dimensions they can be approximated as having only two significant surfaces for stresses to act upon, indicated by figure 2.2.

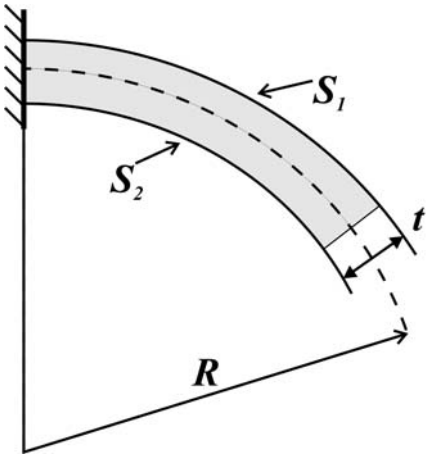

Figure 2.2: A profile illustration of a bending cantilever, indicating the radius of curvature R, the beam thickness t, and the top (S_1) and bottom (S_2) surfaces.

It is difficult to measure the absolute surface stress, σ, on each surface of the cantilever. However, using *Stoney's formula* [49] it is possible to calculate the difference between the stress on the top surface, σ_1, and the bottom surface, σ_2. Stoney's formula relates the differential stress, $\Delta\sigma$, to the radius of curvature of the cantilever, R, via equation 2.2

$$\Delta\sigma = \sigma_1 - \sigma_2 = \frac{Et^2}{6R(1-\nu)} \tag{2.2}$$

with ν being the Poisson's ratio for the material. Since it is the differential stress between the surfaces that is monitored, the molecular interaction of interest must occur on only one of the sides, otherwise there will be no change in R. This is typically accomplished by modifying only one side of the cantilever with a receptor layer [19].

It was previously mentioned that there are a number of different ways to measure displacement of the cantilever. For the purposes of monitoring the quasi-static motion of the cantilevers in this thesis, the optical lever technique was employed [50, 51]. In this method a laser is focused upon the surface of the cantilever where it is reflected onto a position sensitive detector (PSD). The PSD measures the position of the laser spot as the cantilever changes the angle of reflection, due to the applied stress. Then, by applying equation 2.2 to the measured R, one can acquire a measurement of the differential surface stress for the observed cantilever.

Chapter 3

Electrochemistry: Concepts and Methods

In the broadest sense, the field of electrochemistry is the study of the interplay between chemical and electrical effects. Analytical techniques rely upon measuring an electrical characteristic or response of the electrolyte through an arrangement of electrodes. This chapter is meant to introduce and define the electrochemical terms and methods that will be applied within this work. For an in-depth review of principles and techniques please refer to an appropriate electrochemistry text book [52–54].

3.1 Reduction and Oxidation

The core concepts of electrochemistry revolve around controlling and observing electron transfer between species in a medium.

$$A + e^- \rightleftharpoons A^- \tag{3.1}$$

A species is *reduced* when it *gains* or *accepts* electrons (equation 3.1, left to right), while a species is *oxidized* when it *loses* or *donates* electrons (equation 3.1, right to left). Generally speaking, the reduced and oxidized forms of a species can have positive, negative, or zero charge, and does not necessarily have to closely resemble equation 3.1. This equation is an equilibrium which occurs at a specified voltage or *potential*, measured with respect to an accepted *reference* potential (see section 3.3.2). At this potential, the reduction potential E^0, the rates of reduction and oxidation are equal. An example of such a system is the reversible redox couple ferri-ferrocyanide, $[Fe(CN)_6]^{3-/4-}$, the equilibrium of which is described by equation 3.2

$$[Fe(CN)_6]^{3-} + e^- \rightleftharpoons [Fe(CN)_6]^{4-} \qquad E^0 = +0.235 \text{ V (vs. Ag/AgCl)} \tag{3.2}$$

Thus, by applying a potential more negative of E^0 the reduction reaction (left to right) dominates, and a current is measured in this direction. Conversely, by applying a potential more positive of E^0 the oxidation reaction (right to left) dominates. Control of the applied potential and measuring the associated current as a function of it is the basis of the measurements performed within this work.

3.2 The i vs. E Relationship

3.2.1 System Response to a Potential Step

Considering the reaction in equation 3.2, applying a potential $E < E^0$ will supply enough energy for electrons to jump from the electrode to the species, making the reduction reaction dominant in the electrolyte. A reduction current will be measured as electrons flow into the solution, reducing the 3- ion to the 4- state. Initially the current will be high, as all the 3- species near the electrode are reduced. Once this supply is used up, however, the rate of reaction, and thus the reduction current, will depend on how quickly new 3- species can be transported to the electrode surface. This mass transport is dictated by three effects: *migration*, charged species being attracted or repelled by the charge surrounding the electrode, *diffusion*, species moving from a region of high concentration to a region of relatively low concentration, and *convection*, the movement of the electrolyte relative to the electrode which delivers new species for the reaction [52]. Thus, after the initial current spike, the reduction current (or similarly, the oxidation current) will decrease and plateau at a value limited by mass transport, reaching a steady state.

3.2.2 The Electrical Double Layer

Electron-exchange currents, or *Faradic* currents, are only one of two contributions. Assume a solution contains ionic species which do not undergo reduction or oxidation within the active potential range. Upon application of a potential E a *non-Faradic* current (not due to electron transfer) will flow until the charge on the metal electrode surface is q^M and satisfies equation 3.3:

$$\frac{q^M}{E} = C \tag{3.3}$$

where C is the capacitance of the interface. Since the solution contains dissolved ionic species of both negative a positive charge, the concentration profile near the interface will be altered, depicted in figure 3.1. Consequently,

the thin layer of solution surrounding the interface will reorganize to produce a charge q^S, where $q^S = -q^M$. The combination of these charged layers in the metal surface and solution is termed the *electrical double layer*. The solution-side of the double layer is believed to consist of two layers itself. First, nearest the surface is a compact layer, called the *inner Helmholtz plane* or IHP, which contributes a charge of q^i to the solution charge and is made of ions adsorbed to the metal surface. Beyond this is the diffuse layer, also called the *outer Helmholtz plane* or OHP, which consists of hydrated ions in solution, non-specifically adsorbed to the electrode surface, and contributing a charge of q^d to the solution charge [54]. Thus, the composition of double layer charge in this simple model satisfies equation 3.4:

$$q^S = q^i + q^d = -q^M \tag{3.4}$$

and the electrical double layer, taken as a whole (q^M and q^S together), is electrically neutral. While the potential difference across the double layer is typically on the order of 1 V, the electric field in this region can be as high as 10^7 V/cm due to the minuscule layer thickness.

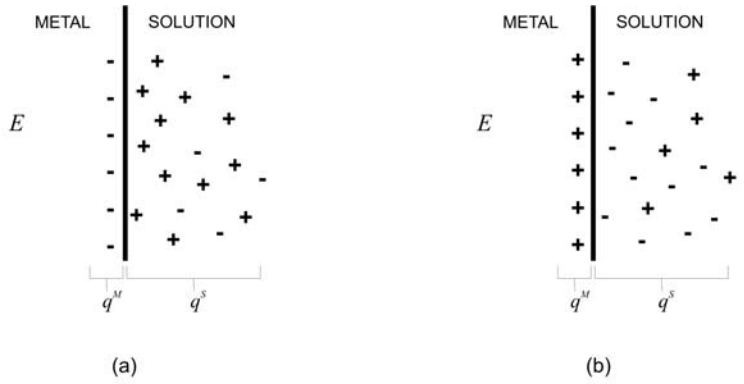

Figure 3.1: Illustrations of the electrode-electrolyte interface in the cases that a (a) negative or (b) positive potential is applied to the electrode. The ions in solution arrange to mirror the charge at the electrode surface.

Naturally the adsorption of ions to the surface and the large electric field across the interface will exert a force on the electrode. Considering this is a consequence of an initially unequally charged solid-liquid interface, one realizes that the electrical double layer forms at all phase boundaries, and is not confined to the special case of an electrified surface in an electrochemical experiment.

3.3 The Three-electrode Setup

The electrochemical measurements conducted in this project are all performed using a *three electrode setup*. A *working electrode* (WE) provides the solid-liquid interface to be investigated, a *reference electrode* (RE) provides a stable voltage against which the potential of the WE is measured, and a *counter electrode* (CE) provides a current path. The three electrodes are fit into an electrochemical cell (figure 3.2(a)) and connected as shown in figure 3.2(b). A *potentiostat* (figure 3.2(c)) is used to control and measure potential, current, charge, and other parameters of the system, and in many cases record the data as well. Further description of each electrode can be found in the following sections.

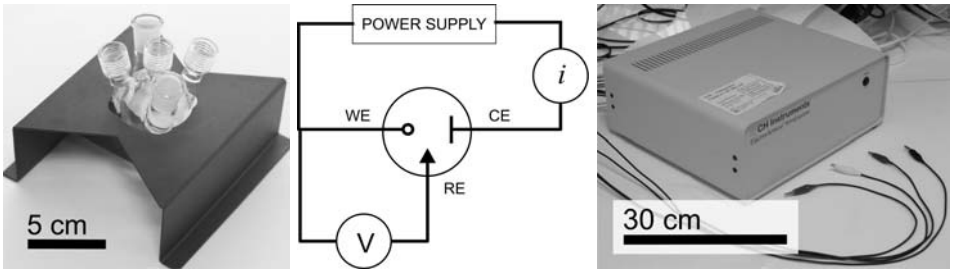

(a) (b) (c)

Figure 3.2: (a) A glass cell to contain electrodes and electrolyte during experiments (Gamry Instruments, USA, "Dr. Bob" small volume cell). (b) Schematic of the three-electrode cell. The voltmeter (V) measures the potential of the WE with respect to the RE, while the ammeter (i) measures the current flowing in the circuit completed by the WE and CE. In modern experimental configurations, the voltmeter, ammeter, and power supply are contained in one unit called a *potentiostat*. (c) A photograph of a CHI 660C potentiostat (CH Instruments, USA).

3.3.1 The Working Electrode - WE

The surface of the WE is the focus of electrochemical measurements. It is the interface at which the events under investigation happen, and where all parameters are monitored. Working electrodes can be purchased (*e.g.* figure 3.3(a)) or constructed (see chapter 5 or 6) in a range of sizes and materials, both of which are dictated by how the electrode will be used. The composition of the WE sets the limits on what potentials can be applied. Specifically, the *potential window* of the electrode (figure 3.3(b)) is the useful range of potentials for which measurements may be made. This is typically limited by the oxidation of the electrode on the positive side and by the evolution of hydrogen at the interface on the negative side.

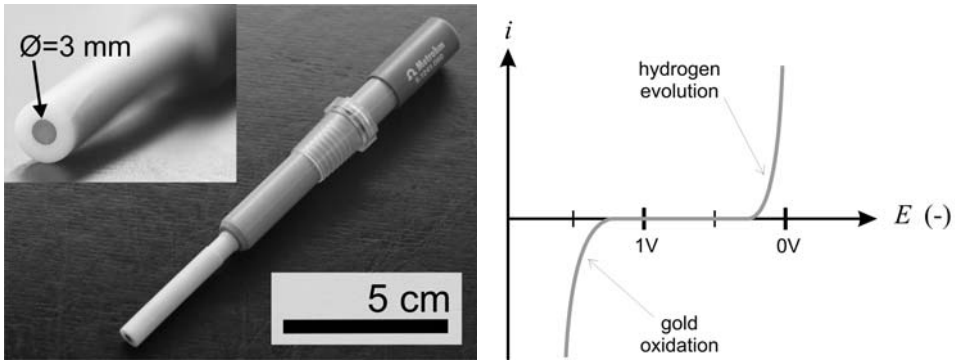

(a) (b)

Figure 3.3: (a) A purchased 3 mm gold disk electrode (Metrohm AG, Switzerland). (b) A sample potential window of a gold disk electrode in 1 M KOH. The useful range of a working electrode is typically limited by its own oxidation (positive side) and the evolution of hydrogen (negative side), both of which are highly pH dependent.

Some common choices for working electrode material include liquid Hg, noble metals (Au and Pt), carbon-based materials (graphite, glassy carbon), or other transition metals (*e.g.* Ni, Cu, Ag) [53]. Again, the choice of material depends on its use which will lay specific requirements upon the potential window, chemical reactivity, and in some cases environmental factors.

In this project we will deal exclusively with microfabricated gold thin film electrodes. Gold has the benefits of a relatively large potential window, ease of chemical modification via thiol groups, relative chemical stability (*e.g.* etch resistance), as well as being simple to fabricate, thus lending itself to be quickly integrated into microsystems.

3.3.2 The Reference Electrode - RE

All applied potentials must be measured with respect to a reference potential, which must be stable during the course of the measurement. The ideal RE will provide a stable reference potential regardless of the current at the working electrode.

Special reference electrodes are available for exactly this application. While a range of REs are available, for the purposes of this thesis only the Ag/AgCl reference electrode will be considered. Commercial electrodes are composed of a sealed glass tube, filled with (in the case of figure 3.4) KCl at a specific concentration. A silver wire covered in a layer of silver-chloride is immersed in the electrolyte in the tube, and connected by wire to the potentiostat. A

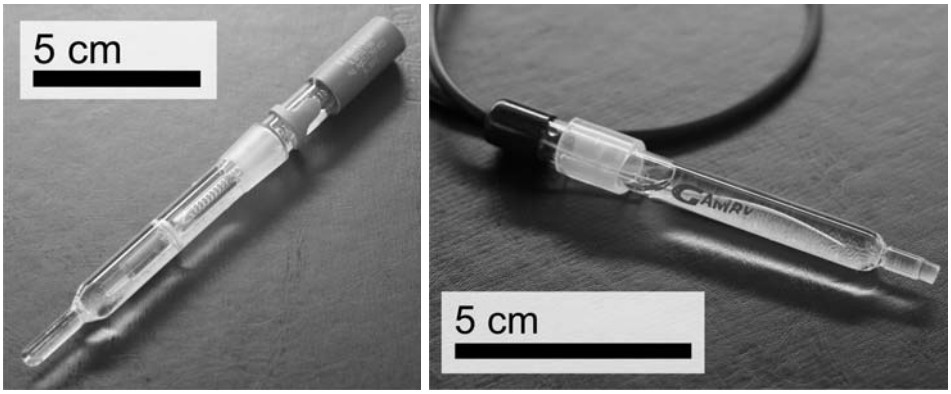

(a) (b)

Figure 3.4: (a) A large Ag/AgCl reference electrode (Metrohm AG, Switzerland), filled with 3 M KCl. (b) A smaller reference electrode (Gamry Instruments, USA) filled with saturated KCl. Both REs are sealed glass vessels with a porous glass frit, which facilitates ion exchange without letting the reference and experimental electrolytes mix.

porous glass frit is embedded at the bottom of the glass tube to isolate the reference electrolyte from the experimental electrolyte while still allowing some ion transfer and the potential drop to be felt.

In the three-electrode configuration (figure 3.2(b)) the path of the reference electrode is designed to have an incredibly high electrical resistance. This is done so the reactants used and products generated within the reference electrode are minimal (lending to its longevity and stability) while still providing a reference voltage against which the WE may be measured. However, measuring current as a function of applied potential is a useful technique, and requires the flow of an appreciable current. Thus a path for the current must be provided that does not pass through the RE.

3.3.3 The Counter Electrode - CE

The counter electrode's sole purpose is to facilitate current flow through the system. Typically made of an inert, electrically conductive material, such as graphite or platinum (figure 3.5), the only two requirements of the CE are that it: (i) has a large enough surface area to not be a bottleneck for current flow in the system, and (ii) not degrade in or contaminate the experimental electrolyte. Solid rods, wires, grids, or other structures of sufficiently large area can be employed as CEs, and in some cases the reference electrode itself might be used to conduct current instead. Whereas the potential is measured/controlled between the working and reference electrodes, so the

same goes for the current between the working and counter electrodes.

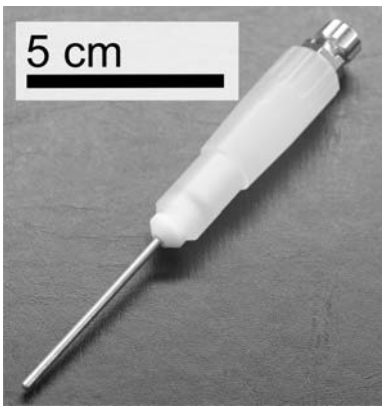

Figure 3.5: A photograph of a platinum rod used as a counter electrode in experiments (Metrohm AG, Switzerland).

3.4 Electrochemical Techniques

3.4.1 Cyclic Voltammetry - CV

Cyclic voltammetry refers to sweeping the potential linearly in time. The applied potential is scanned or swept one way (positive-to-negative) and then swept the other way (negative-to-positive). This cycle continues back and forth between two bounding values of potential, labeled E_1 and E_2 in figure 3.6, for a defined duration. During this cycling the reduction potential passes E^0 and tips the equilibrium, which is read as a current peak, after which the current settles to a steady state value. This is useful for characterizing the redox behavior of a new species, or characterizing the electrode interface given a well defined *redox couple*, which refers to an ionic species exhibiting reversible reduction/oxidation behavior.

The reversible redox couple $[Fe(CN)_6]^{3-/4-}$(equation 3.1) will be the focus couple in this thesis. This system has been studied extensively and is quite well understood. Thus it can be used as an electrochemical *probe* to investigate such parameters as electrode size (chapter 5), interface cleanliness (chapter 6), or various surface modifications and charging effects (chapter 7).

3.4.2 Electrochemical Impedance Spectroscopy - EIS

In this technique the electrical impedance of a cell is measured as the frequency of an applied AC potential is swept through a range of val-

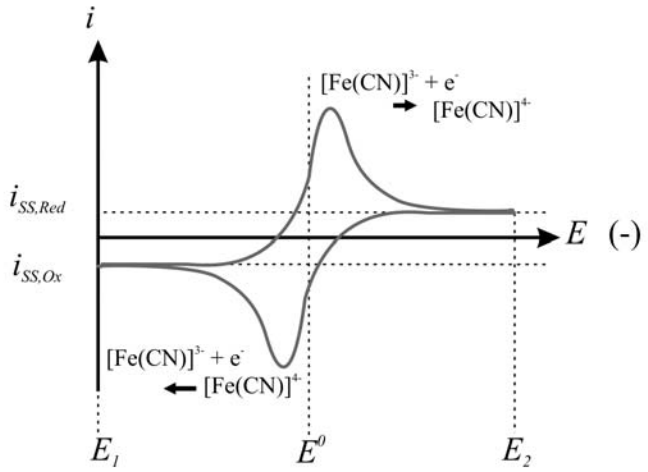

Figure 3.6: A sample cyclic voltammagram. Starting at E_1 and moving towards E_2 a reduction current peak is observed as a large amount of $[Fe(CN)_6]^{3-}$ is reduced to $[Fe(CN)_6]^{4-}$. Following the reduction peak a steady-state reduction current ($i_{SS,Red}$) is established and the potential continues sweeping towards negative values until it reaches E_2 and changes direction. With the potential sweeping in the opposite direction, towards E_1, we observe an oxidation peak as we approach and pass E^0, where the $[Fe(CN)_6]^{4-}$ at the interface is oxidized to $[Fe(CN)_6]^{3-}$. The current peaks (opposite to the reduction peak) and settles at a mass-transfer limited value $i_{SS,Ox}$

ues. As with cyclic voltammetry a well-defined and reversible redox couple ($[Fe(CN)_6]^{3-/4-}$in this project) is required to examine the working electrode-electrolyte interface. Equal concentrations of the reduced and oxidized species must be present in the probing solution to fix the equilibrium potential of the working electrode.

A small AC-potential ($1 - 10$ mV) is applied to the electrochemical cell, superimposed upon a DC-voltage, which is the equilibrium potential E^0. The amplitude and phase of the current response is plotted against the frequency of the applied potential, typically recorded in a Bode plot. However this form is not conducive to comparison of results, thus a Nyquist plot is instead used (figure 3.7(a)).

This plot can then be fit to the Randles equivalent circuit [52] (figure 3.7(b)). The electrochemical cell can be modeled as a collection of circuit elements which are arranged in parallel to account for the separate contributions from the Faradic current i_f (*i.e.* current due to electron exchange) and the non-Faradic (or capacitive) current i_c (*i.e.* the transient electron flow due to the electrical double layer charging). Both Faradic and non-Faradic currents must flow through the solution, thus the resistance of the bulk solution can be modeled as simply a resistor, R_S. The charging of the double

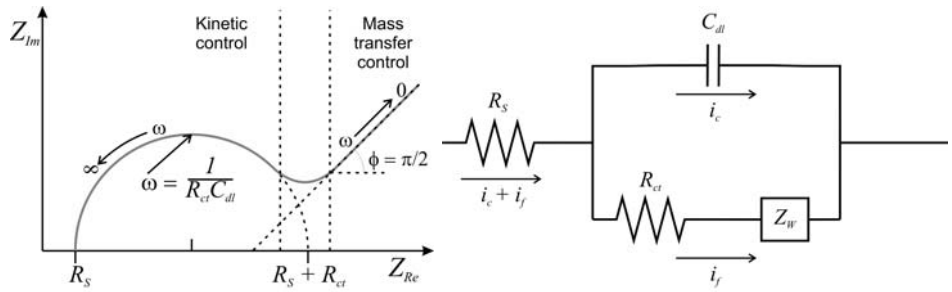

Figure 3.7: (a) A sample Nyquist plot with major system parameters indicated. This plot is then fit to (b) the Randles equivalent circuit, which is accurate for relatively clean electrode-electrolyte interfaces. Circuit elements are defined as follows: R_S - solution resistance, C_{dl} - double layer capacitance, R_{ct} - charge transfer resistance, and Z_W - the Warburg impedance.

layer can be well-approximated by a capacitor, C_{dl}.

There are two separate contributions to the Faradic current. The first contribution is the resistance encountered by the electrons as they cross the electrode-electrolyte interface, which is referred to as the *charge transfer resistance*, R_{ct}. This is an important parameter, as will be demonstrated in part II, which can be used to measure interfacial properties of the electrode. The other contribution to the Faradic current is Z_W, called the Warburg impedance. This is typically represented in the Randles circuit as a constant phase element and is an effective impedance caused by mass transfer limiting the maximum current.

Chapter 4

Electrochemistry & Cantilevers: State of the Art

As the ultimate goal of this thesis is to both build and use an electrochemical-cantilever (ECC) platform, it is relevant to note the current and past literature in the field. This chapter briefly outlines the work done in performing and understanding combined electrochemical-cantilever measurements, as well as the measurement setups employed in the field.

4.1 Early Work and Theory

Electrocapillary curves, or surface stress versus applied potential measurements, were acquired to assist in understanding the structure of the electrical double layer. One possible way of obtaining such data was to use an extensometer [55] where the change in length of a metal strip was measured, which yielded a surface stress value. However, such techniques were prone to inaccuracy or irreproducibility due to interference from thermal effects [56]. The first electrocapillary curve acquired by monitoring the static deflection of a cantilever was taken in 1971, reported by Fredlein *et al.* [57] who used a $13 \times 1.5 \times 0.0085$ cm^3 glass strip coated with gold on one side as an electrode, the deflection of which was measured using the optical lever method, and converted to surface stress using Stoney's formula [49].

Fredlein and Bockris used the Shuttleworth equation [58] to determine the surface excess of solvated ions [59]. The Shuttleworth equation in scalar form

$$\sigma = \gamma + \frac{d\gamma}{d\varepsilon} \tag{4.1}$$

describes the surface stress, σ, in terms of the surface tension, γ, and its

derivative with respect to strain, ε. Equation 4.1 plays a central role in understanding stress-dominated behavior of electrode surfaces [60], and has been the subject of much misunderstanding and debate [61–64]. The second term in equation 4.1 is commonly believed to be so small that it can be ignored [26,34,65,66], although some disagreement on this matter exists [67]. The Lippmann equation,

$$\frac{d\gamma}{dE} = -q - (\gamma - \sigma)\frac{d\varepsilon}{dE} \tag{4.2}$$

relates surface tension to the applied surface potential, E, and surface charge-per-area, q. Again the second term has been deemed too small to be noticeable under other effects [34, 66, 68, 69], with opposing views existing [70, 71].

4.2 Current State

4.2.1 Active Research

With the advent of the atomic force microscope [72] it was only 10 years before similar cantilevers were used to monitor electrochemically-induced surface stress. The mid-1990s saw Raiteri and Butt observe potential-induced changes in surface stress [26], Rayment and Welland monitor the stress in electrodeposited layers of silver [27] and lead [33, 73], while Haiss and Sass investigated the stress in electrodeposited copper [74, 75]. Further studies of stress during electrodeposition of metals have been executed with the goal of understanding under-potential deposition [76], investigating film formation for metallization technologies [77], and developing chemical sensors [35].

Several groups have made efforts towards the development of actuators based on redox-induced physical deformation of chemical layers. Lahav *et al.* electrodeposited a layer of polyaniline on a cantilever [31], while Tabard-Cossa *et al.* chose polypyrrole as their actuating polymer [32]. In the case of polypyrrole, reducing the polymer layer through application of a negative potential to the cantilever caused an uptake of cations and their solvation shell into the polymer. This caused the polypyrrole to swell, build a compressive stress, and caused a downward deflection of the cantilever. Oxidizing the polypyrrole layer returned a positive charge to the polymer, expelling the cations, returning the polymer to its original state. Conversely, oxidation caused repulsion bewteen the polyaniline chains, causing swelling, a compressive stress, and a downward cantilever deflection as well, which was relieved by reducing the polyaniline layer. Further, Tabard-Cossa *et al.* found that the cantilever deflection was qualitatively similar to that of a clean gold cantilever if the redox activity of the polypyrrole was suppressed [32]. Cantilever actuation via ferrocenyl-terminated alkanethiol SAMs has been investigated [78, 79], with physical deformation of the ferrocenyl structure

during reduction the main cause of compressive stress, and not any double layer charging effects.

Other investigations within the domain of electrochemical-cantilevers include observations of interactions between charged surfaces [80], and monitoring the effect of adsorbed alkanethiols on the electrochemically-induced motion of the cantilever [34]. An interesting biological application from Bongrain *et al.* uses resonating cantilevers to measure the change in surface stress due to the potential-induced denaturing of immobilized DNA, confirmed by CV and fluorescence imaging [81].

However, most of the effort in this field is directed towards observing and analyzing the simple motion of metallized cantilevers in ionic solutions. Monitoring cantilever motion during voltammetry in aqueous solutions of ClO_4^- [28, 30, 65, 66, 70, 71], Cl^- [34], SO_4^{2-} [28] [82], or $I^-/Br^-/NO_3^-$ [26] has been done in an effort to understand the true nature of the motion, the origin of the stress formed at a charged surface, and the factors affecting its behavior. Still, with so much effort directed at the same basic goal, large discrepancies exist. Basic shapes of surface stress-potential graphs have been reported as both parabolic [26, 28, 66, 70, 82] and linear [29, 65, 71] due to variations in cantilever preparation protocol.

A final note: Amiot *et al.* have investigated the surface charging of cantilevers using a novel full-field imaging setup [83, 84]. In contrast to the assumptions made in chapter 2 regarding a uniform loading of the cantilever, Amiot *et al.* report the electrical double layer charging to occur at the edge of the cantilever, which will have an impact on the values of surface stress reported. These results are supported qualitatively in other works [85].

4.2.2 Understanding and Issues

The discrepancies in observations mentioned in section 4.2.1, as well as occasional misunderstanding of the equations in section 4.1 have led to much debate [60–64]. Tabard-Cossa *et al.* reported a strong dependence of the surface stress-potential response on the electrode surface morphology, as well as surface cleanliness. In fact, surface contamination was found to be the cause of a parabolically-shaped surface stress-potential curve, like those observed in select literature [26, 28, 70], highlighting the importance of generating a reliably clean surface.

In all works, however, a negative potential is observed to cause a tensile stress (*i.e.* upward deflection) on the cantilever's gold surface [86]. Ibach *et al.* suggest that this surface stress is far larger than could be caused by only

the double layer charging [71], and that the strain derivative of surface tension (second term in equation 4.1) contributes to the stress, as in [67], and should not be ignored, as in [34, 66]. A possible model for this tensile stress under a negative potential is presented by Weigend *et al.* [87]. Essentially, in the electron liquid model for metals, an excess surface charge (*e.g.* an applied potential) causes the electron density function to extend outward from the metal surface. This effectively displaces the electronic center of gravity, transferring electrons into in-plane bonds, resulting in a tensile surface stress. The reverse is believed to be true, where a positive potential causes a compressive stress. This agrees with the DFT simulation performed by Weigend *et al.* [87], as well as with the previously cited literature, and fits with the work of Godin *et al.* [88].

4.3 Electrochemical-Cantilever Systems

Finally, given that a large part of this thesis work is centered around the design of a new electrochemical-cantilever platform, a summary of the systems used in literature seems appropriate. Of the electrochemical-cantilever literature cited here, the majority of groups use the optical lever method to read out beam deflection, while some use an STM to monitor z-displacement [28,71,74,75], or other "visual" methods [86]. Monitoring systems employing the optical lever method fall into two categories; those using a commercial AFM system [26, 29, 34, 66, 67, 81], and those optical setups which are custom [27, 30–33, 35, 65, 73, 77–79]. Most of these optical lever interrogation systems use commercially available silicon or silicon nitride microcantilevers. However, a number of articles describe using larger (mm-sized) glass strips, metallized on one side, as cantilevers. These "macrocantilevers" have been the used from the early work of Fredlein and Bockris [57, 59] up to recently [70, 76, 77, 82], possibly for ease of handling or to avoid effects of the microelectrode regime.

Regardless of cantilever type or measurement method, all electrochemical activities must be conducted in a liquid environment, which takes the form of a liquid cell. Most of these cells are sealed units, made of inert polymers (commonly PTFE), and are incapable of flow, with a few exceptions [26,34,77]. These cells typically have volumes of several ml, built large enough to house the reference and counter electrodes, which are separate articles from the cantilevers, inserted into the liquid cell. A recurring issue in the description of these systems is the combined need to electrically connect the cantilever electrode while simultaneously insulating the contact point. One reliable method for electrical contact is a metal spring clip [29,30,32,34,35,57,59,65,66,78], where the contact point is insulated by

wax [30, 32, 35, 65, 66, 78], silicone [26], or even fingernail polish [29], which also defines the electrode surface area. Conductive epoxy is also noted to make reliable electrical contact [27, 31, 33, 73], with additional insulating epoxy applied over the contact area. It should be noted that none of the previously cited literature describe a cantilever chip in which all electrodes are integrated into a channel, all on a single chip. This is presumably due to the high degree of difficulty associated with successfully creating such an apparatus.

Part II

Electrochemistry Basics

Chapter 5

Microfabricated Electrodes: Development & Characterization

This chapter describes the initial development of the microfabricated thin film gold electrodes that would become the benchmark platform for testing immobilization chemistry and electrochemical methods.

5.1 Background: The Microelectrode Regime

As with many other sensing structures, the behavior of the working electrode changes upon miniaturization [89]. The small size of microelectrodes means a higher flux density of reactants is transported to the electrode surface by diffusion [52]. This naturally leads to a higher reaction rate at the surface and, therefore, an increased current density [90], but at the price of a significant reduction in current [91, 92]. While small currents can be difficult to measure due to noise, in many cases this side effect can be overcome by using arrays of microelectrodes [89, 93–99], thus increasing the overall current, as well as the signal to noise ratio [94].

The diffusion profile acts to concentrate species in the electrolyte around the microelectrode, leading to the aforementioned increase in current density, meaning successful measurements can be made in solutions where the concentration of electrolyte or analyte is too low to be measured by electrodes of normal size. This higher current density also allows accumulation times of seconds instead of minutes [95] in techniques were the pre-concentration of the analyte upon the electrode is of importance (*e.g.* stripping voltammetry). Another advantage is the low sensitivity of microelectrodes to dissolved

oxygen in the electrolyte [89, 93] due to low non-faradic currents[1] [100].

Fletcher *et al.* considered arrangements of microelectrodes, and how spacing affects performance [94]. Effects of interacting electrical double layers and sharing of solution resistance were examined for possible limitations on current. However, it was found that current limiting due to diffusion dominated the proximity effects of microelectrode arrays. The minimum electrode spacing d in an array of electrodes with radius r to avoid limiting the current due to diffusion was estimated by equation 5.1.

$$\frac{d}{r} \geq 20 \tag{5.1}$$

5.2 Microelectrode Development

Two chip designs were created during this phase of the thesis project. A first generation (1^{st} *gen.*) mask was produced to test the effect of different electrode sizes and develop a successful fabrication process. From the observations of the 1^{st} gen. design a second generation (2^{nd} *gen.*) mask was created which would form the foundation of all electrochemical measurements for the rest of the project, described in chapter 6. The development of such a chip, however simple it may be, was paramount to the success of the entire project. Solidifying a reliable testing platform means that, in the worst case of experimental failure, the methods and protocol could be rolled back to a well-defined starting point and debugged in an efficient manner.

5.2.1 Electrode Design & Fabrication - 1^{st} gen.

The first chip was created to illuminate the possible differences between macro- and microelectrodes, as well as microfabricated and bulk metal gold electrode surfaces. With a high value placed on simplicity, to construct microelectrode arrays a 1 mm^2 gold square was used as a base (see figure 5.1(a)). Then this surface was masked with silicon nitride to the desired electrode array sizes and spacings. The 1 mm^2 gold pad was connected to a 3 $\times$ 3 mm^2 contact pad via a 200-nm-wide gold wire. A 10 nm layer of Ti was used as an adhesion layer for 300 nm gold to form the electrode. Plasma-enhanced chemical vapor deposition (PECVD) was used to deposit silicon nitride, which was patterned using photolithography and then reactive ion etched (RIE) to open the array holes. A detailed process flow can be found in Appendix A. Table 5.1 lists the different hole sizes (square-side length a) and spacings (center-to-center distance b), and figure 5.1(b) defines the

[1] Recall that these are due to the charging of the electrical double layer and involve no actual electron transfer.

parameters a and b.

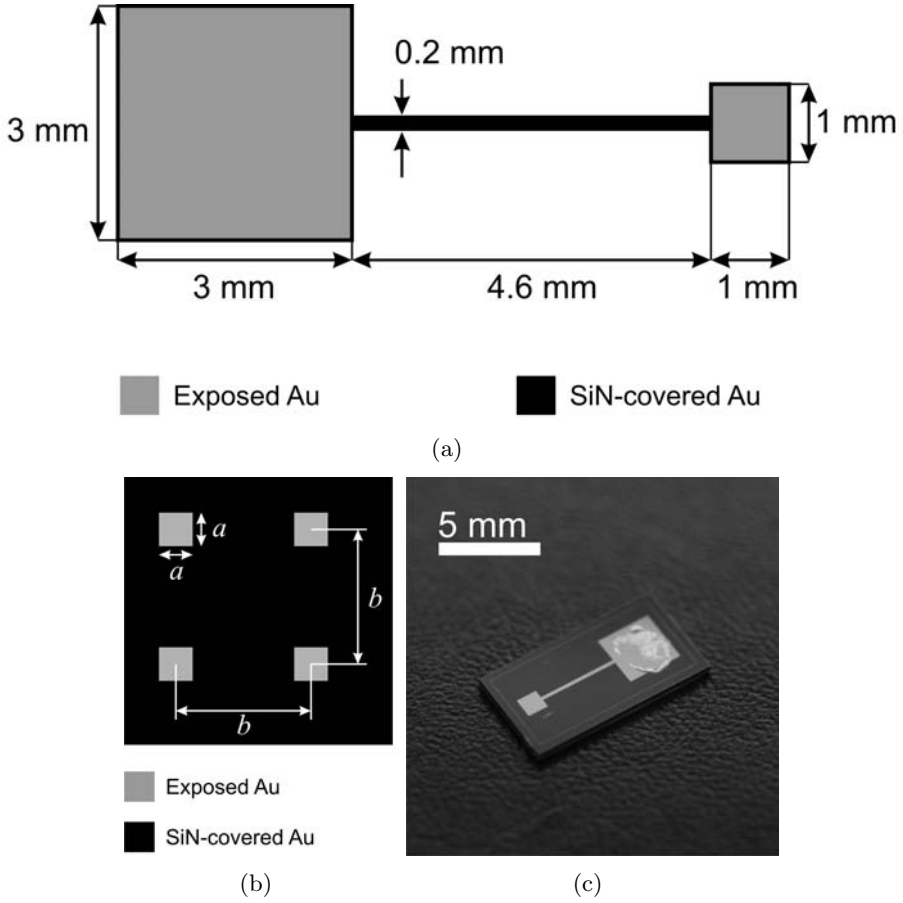

Figure 5.1: (a) Schematic of the 1^{st} gen. microfabricated gold film electrodes. The metal layer consists of 10 nm Ti (for adhesion) and 300 nm Au. Initially 500 nm of PECVD SiN was used to insulate the 200 nm wide wire and define the electrode array on the electrode pad. Due to flaking and peeling of this layer, 1 μm of SiN was used instead. A 1 mm $\times$ 1 mm square is open in this illustration, but holes of sizes and separation specified in table 5.1 were opened in a similar fashion. (b) A close-up drawing of the electrode array design with the holes in the SiN defining the individual electrodes, a being the side length of a square, and b being the center-to-center spacing between the electrodes. (c) A photograph of the 1^{st} gen. chip.

Regarding table 5.1 it should be noted that the 3000-μm-diameter Au disk, pictured in figure 3.3(a), is a purchased electrode and consists of a 99.99% pure Au wire wrapped in a polyetheretherketone (PEEK) insulation (Metrohm AG, Switzerland). This was included in the trials as the bulk gold disk electrode to compare properties with the microfabricated thin film electrodes. Since the gold in the 3-mm-disk is forged it is of a higher purity,

Table 5.1: Electrode array hole size and nearest-neighbor (NN) separation.

Square Size a (μm)	Area (μm^2)	NN Distance b (μm)	Number of Squares	Total Area (μm^2)
5	25	100	121	3025
10	100	100	121	12100
25	625	250	25	15625
50	2500	500	9	22500
100	10000	1000	4	40000
1000	1000000	-	1	1000000
3000*	7068577.5	-	1	7068577.5

*This is the purchased 3-mm-diameter disk Au electrode.

unlike the thin film gold which can accumulate impurities during deposition (more in chapter 6).

5.2.2 Electrode Preparation & Methods

Under the advice of chemists the microfabricated electrodes for these trials were cleaned in concentrated nitric acid (65%) for 1 minute, to remove possible organic contaminants, and then rinsed thoroughly in Milli-Q water. The 3-mm-diameter gold disk electrode was prepared by first polishing the surface using a polishing cloth and a slurry consisting of 0.3 μm alumina beads and water (both included with the purchased electrode), rinsed thoroughly with Milli-Q water, and the given the same nitric acid treatment as the microfabricated electrode.

These individual electrodes needed to be connected to a wire and lowered into the testing solution somehow. In the case of the purchased 3-mm-diameter Au disk a holder was provided that fit into the small volume cell and into which a cable could be plugged and connected to the CHI 660C Electrochemical Workstation (CH Instruments, USA) potentiostat (figure 3.2(c)). The microfabricated electrodes were not so simple to operate. An insulated copper wire was threaded through a 5-mm-diameter glass Pasteur pipette. The stripped copper wire protruding from the end of the pipette was pasted to the 3×3 mm^2 contact pad on the chip using a conductive liquid (Conductive Pen CW220STP, Chemtronics, USA) which dried to create the electrical connection. However, this dried paste did not provide enough strength for the bond between the chip and wire to sustain repeated han-

dling, thus a coating of SU-8 (2002) was applied with a needle and baked on a hotplate (50 °C) overnight to cure (figure 5.2(a)). While this provided sufficient electrical connection to the chip it proved too time consuming to practice this method on 20-30 chips over the course of this experiment. Additionally, it was anticipated that future experiments would require the use of hundreds of chips, thus a quicker way of connecting chips was required, as well as a way to keep the chip connector reusable.

Thus the connection device in figure 5.2(b) was constructed. It consists of the same style pipette and wire, except a paper clip, bent into the correct shape to act as a spring clip contact, is soldered onto the exposed copper wire protruding from the bottom of the pipette. A digital multi-meter was used to test the resistance of the entire electrode, from the wire to the 1 mm square. The resistance of the entire assembly was the same as the chip alone (7-9 Ω) thus the holder contributes a negligible resistance to the working electrode.

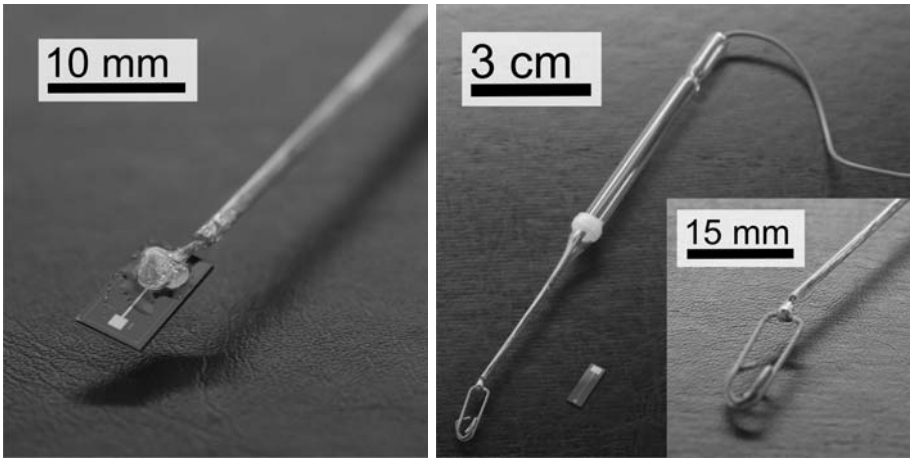

(a) (b)

Figure 5.2: (a) A photograph of the first attempt to make electrical contact. The conductive paste, with SU-8 for passivation and structural stability, performed sufficiently well, but proved far too time consuming. (b) A photograph of the chip holder, constructed from a glass Pasteur pipette, insulated copper wire, and a bent paper clip. *Inset:* A close-up photograph of the paper clip soldered to the wire.

Measurement procedure consisted of connecting one working electrode chip to the holder, placing it in a 10 mM $[Fe(CN)_6]^{3-/4-}$solution with 50 mM phosphate buffer (pH 7). A Ag/AgCl (3 M) reference electrode (figure 3.4(a), Metrohm AG, Switzerland), and a Pt-rod counter electrode (figure 3.5, Metrohm AG, Switzerland) were inserted into the solution as well and

connected appropriately to the potentiostat. Cyclic voltammetry was performed from -0.4 V to +0.8 V, at a scan rate of 0.1 V/s. Three chips of each array configuration were tested, and on each chip 5 cycles between the aforementioned potentials were scanned.

5.3 Voltammetry Results

The resulting cyclic voltammagrams are shown in figure 5.3. The voltammagrams are plotted in terms of current density (A/cm^2) so they can be compared more accurately. Before examining these plots, one should note that none of the electrodes match the independence criteria. All other microelectrode arrays have a spacing one-quarter that required for theoretical diffusive independence (equation 5.1).

The first observation we can make is that regarding which electrode delivers the greatest current density. One would expect it to come from the smallest electrode array, but since the concentration of the redox couple is relatively high (10 mM), electrode size does not play as important a role as one would expect. The 5 μm square array does display a higher current density than the 10 μm square array, since the 5 μm array comes closer to satisfying the equation for diffusive independence, and thus is more of a microelectrode array. Between the rest of the electrode chips current density appears to be dependent on electrode surface size, with the highest current density being observed in the 1 mm square electrode chip. Oddly enough, the 3-mm-diameter disk electrode does not have the highest peak current density, as the trend would indicate. The 3-mm-diameter disk *does* display the highest absolute current, but the higher current density in the 1 mm square electrode may be due to the electrode shape (square instead of circular).

The second observation is the peak position of the reduction (positive current) and oxidation (negative current) peaks, highlighted in figure 5.4. All visible peaks for the microfabricated gold film electrodes reside at a range of potentials, resulting in a range of peak separation values of $\Delta E_p = 103$ mV to 200 mV. In contrast, the 3-mm-diameter gold disk always a has peak separation value of $\Delta E_p \leq 90$ mV. For comparison, the theoretical minimum peak separation for a single electron transfer reaction, such as we have with the the $[Fe(CN)_6]^{3-/4-}$redox couple, is $\Delta E_p = 59$ mV [52]. This difference can be accounted for by the purity of the gold. Microfabricated gold, even below the surface, is known to be less pure than metallurgically produced gold structures (*i.e.* wires, rods, smelted items), because the contaminants within the vacuum chamber (mainly oxygen, nitrogen, and carbon) become trapped in the film bulk, leading to a gold purity of only 90%, and less on

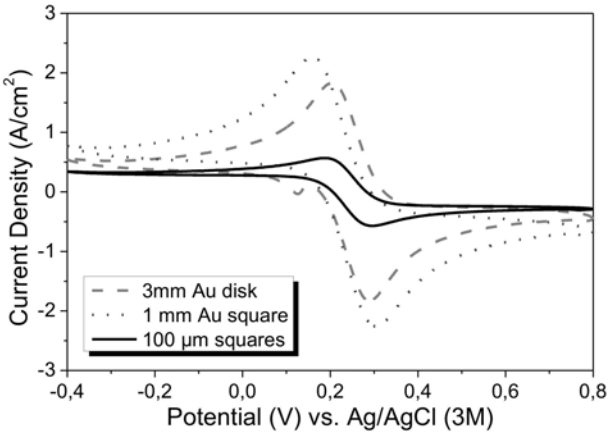

(a) CVs for the 3-mm-disk, and 1 mm and 100 μm squares.

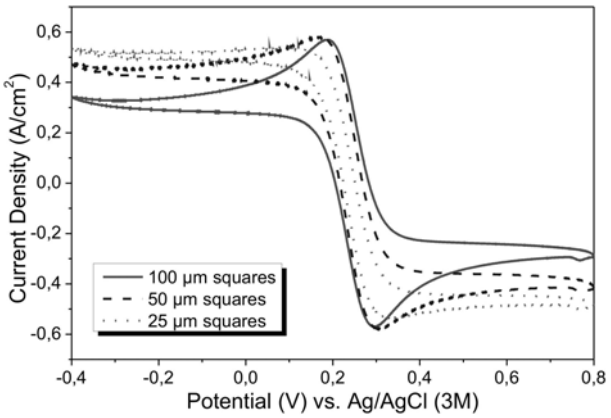

(b) CVs for the 100 μm, 50 μm, and 25 μm squares.

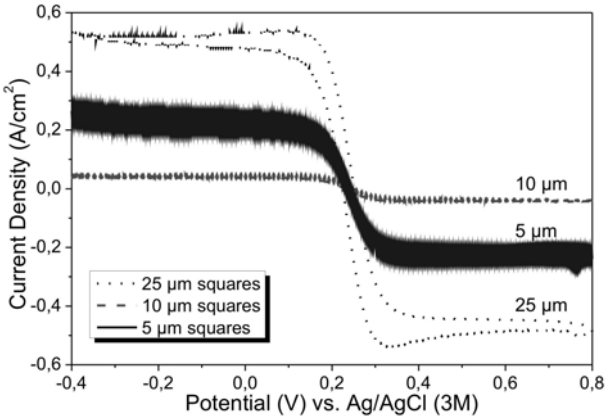

(c) CVs for the 25 μm, 10 μm, and 5 μm squares

Figure 5.3: The cyclic voltammagrams corresponding to microelectrode arrays of different sizes.

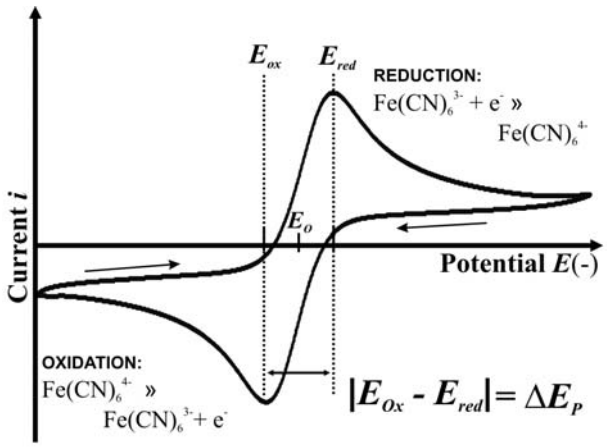

Figure 5.4: A sample cyclic voltammagram with the peak potential separation ΔE_p defined as the absolute difference between the reduction and oxidation peaks.

the surface [101]. Gold surface purity will be discussed further in chapter 6.

The final observation is the progression of the voltammagram shape from diffusion-limited currents (as described in figure 3.6) to currents not limited by mass transport (figure 5.3(c)). The CVs cease to exhibit the typical reduction and oxidation peaks of maximum and minimum current, respectively, with electrode square sizes of 25 μm or less. Current peaks are still observed for square sizes of 50 μm or larger (figures 5.3(a) and 5.3(b)), but square sizes of 25 μm and below show the typical CV behavior of the microelectrode regime [52, 100].

Considering these observations, as well as the fact that these electrodes will be used for screening binding chemistry and surface functionalization which will not require readings in dilute situations, electrodes in the microelectrode regime would not be used as the base platform throughout the rest of the project. Furthermore, given typical dimensions, cantilevers do not qualify as true microelectrodes, and will most likely exhibit the typical current-limited voltammagram behavior. Thus, the format of the working electrode chip to be used from this point in the project forward is that of a 1 mm gold square.

5.4 Conclusion

This chapter represents the first attempts at electrochemistry in this project. A theoretical understanding of microelectrode behavior aided in designing electrode arrays and interpreting the results. The purity of the gold used was

found to play a vital role, prompting further investigation and development of a reliable gold cleaning protocol, which will be the topic of chapter 6. The design for the 2^{nd} gen. chip was decided to be a 1 mm gold square for the sake of simplicity and the fact that even on cantilevers we will not be operating in the ultramicroelectrode regime. Nonetheless, a practical understanding of electrode characterization and size dependance on measurements was gained, which assisted in understanding other phenomena observed.

Chapter 6

Gold Cleaning Methods for Electrochemical Applications

The surface of a working electrode is the observed interface in all electrochemical methods; all that happens in the solution is seen through this surface. In chapter 5 it was found that the purity of the gold made a difference in the electron transfer characteristics, and a more pure metal electrode will exhibit electron transfer characteristics closer to the theoretical predictions. However, for the eventual purpose of creating electrodes on microcantilevers in this project, we are forced to use microfabricated gold deposited by electron beam evaporation. For the purposes of reliable and repeatable chemical functionalization, and to allow fair comparison between measurements taken on different electrodes, it was decided to make a significant effort to develop a protocol for cleaning the gold surface. While convenient to use in the MEMS field, microfabricated gold is quickly contaminated after deposition [102] and cannot be cleaned by typical bulk electrode cleaning processes (*e.g.* polishing).

The work in this chapter focused on obtaining a reliably clean gold thin film surface. Nine different treatments were explored and characterized using cyclic voltammetry, electrochemical impedance spectroscopy, and x-ray photoelectron spectroscopy. The electrochemical activity of the gold surface was characterized using the same methods that will later be applied to the screening of surface modifications, and the atomic composition was determined and compared relative to the bulk film. This work can be found in published form in reference [101].

6.1 Materials & Methods

6.1.1 Electrode Design & Fabrication - 2^{nd} gen.

A second generation, 2^{nd} gen., electrode chip design was created, building on the knowledge obtained in chapter 5. Figure 6.1 depicts the electrode design that will not only be used in this experiment, but in all screening experiments to follow, as well as by other researchers[1]. Notable changes to the design are the slightly smaller contact pad, reduced to 2×3 mm^2, and the positions of the contact pad and working electrode square moved closer towards their respective ends of the chip. This has been done to accommodate the extension of the 200-μm-wire to a length of 10.9 mm, ensuring the working electrode surface is sufficiently immersed in the solution while the contact pad and chip holder (seen in figure 5.2(b)) do not touch the solution.

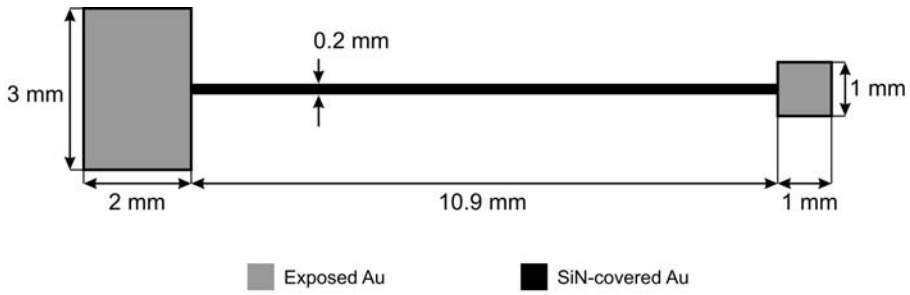

Figure 6.1: Schematic of the 2^{nd} gen. microfabricated gold film electrodes. The metal layer consists of 10 nm Ti (for adhesion) and 300 nm Au, and wire and electrode edges (Ti/Au interface) are insulated by 1 μm of PECVD SiN, as in the 1^{st} gen. design. Also note that the 200-μm-wide wire connecting the contact pad to the 1 mm $\times$ 1 mm electrode is now 10.9 mm long, to ensure only the working electrode is immersed in the solution and no current reaches the contact pad.

The electrode chips were fabricated in the manner described in section 5.2.1 and described in detail in appendix A. A 100 mm (100) silicon wafer was wet oxidized at 1050 °C for 1.5 hours to form ~500 nm of SiO_2 for electrical insulation. Standard UV lithography and lift-off processes were used to pattern the 10 nm Ti / 300 nm Au electrode layer. A ~1 μm PECVD silicon nitride layer was deposited using an STS PECVD reactor. A second UV photolithography step, followed by a reactive ion etch defined the working electrode and contact pad areas. Acetone and a 10 minutes plasma ashing removed the residual resist, and the wafers were removed from the cleanroom for dicing. Chips were then left in plastic containers in a typical chemistry laboratory atmosphere for 2 weeks, a normal time between fabrication and

[1] As of this writing, Ph.D. students Xueling Quan and Shoko Yamada have used this chip design for materials investigations and nanoparticle toxicity screening, respectively

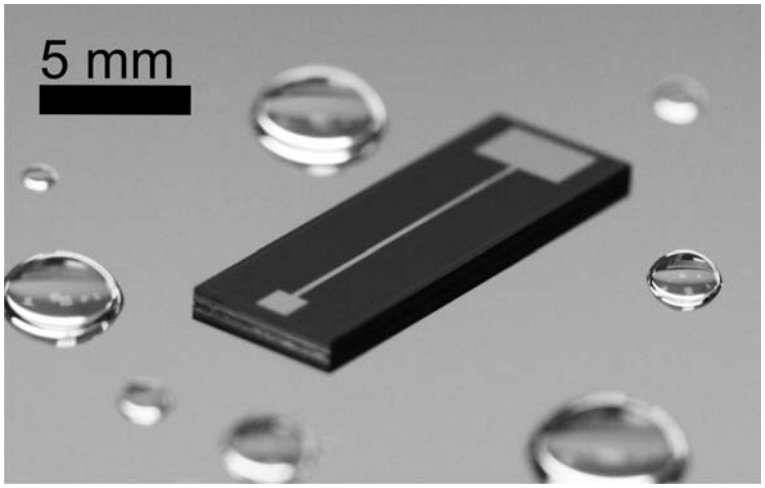

Figure 6.2: A photograph of the 2^{nd} gen. electrode chip.

use. This functioned as the standard contamination for this experiment. A photograph of the finished 2^{nd} gen. electrode chip is presented in figure 6.2.

6.1.2 Cleaning Methods

Two gold etches and a variety of common gold cleaning methods were investigated. All compounds mentioned are diluted with Milli-Q water. Each cleaning method was applied to four gold samples for statistical relevance. The applied treatments are described below, including solution concentrations and voltammetry parameters. Cleaning times are explicitly stated for non-voltammetric techniques, while all voltammetric techniques were accomplished in under 2 minutes.

Ultraviolet Ozone Cleaning

Gold samples spent 40 minutes in a Merck Eurolab PR-100 UV ozone photoreactor. This treatment is commonly used when working with biological samples as a way to restore or regenerate the gold surface after experiments [103, 104]. Abbreviated "UV" in the results.

Potassium Hydroxide and Hydrogen Peroxide

This method has been used by Heiskanen *et al.* as an intermediate step in a gold cleaning protocol [105]. Samples spent 10 minutes in a solution of

50 mM KOH and 25% H_2O_2 before rinsing with Milli-Q water. Abbreviated "KOH+H_2O_2" in the results.

Potassium Hydroxide Potential Sweep

This the the second part of the cleaning protocol used by Heiskanen *et al.* [105]. After the treatment described above the samples were placed in 50 mM KOH and connected to a potentiostat. the electrode potential was swept from -0.2 V to -1.2 V (vs. Ag/AgCl) once, at a 50 mV/s scan rate, and then rinsed in Milli-Q water. Abbreviated "KOH sweep" in the results.

Sulfuric Acid and Hydrogen Peroxide

A very mild version of a piranha clean, commonly used to remove organic contaminants from silicon wafers, is formed from 50 mM H_2SO_4 and 25% hydrogen peroxide [106]. Gold samples spent 10 minutes in this treatment before being rinsed with Milli-Q water. Abbreviated "H_2SO_4+H_2O_2" in the results.

Sulfuric Acid Potential Cycling

Cycling the electrode potential in a weak sulfuric acid solution until a stable CV scan is achieved is a very common electrochemical cleaning technique [107, 108]. Sample potential was cycled from -0.4 V to 1.4 V (vs. Ag/AgCl, 3 M) at a rate of 0.1 V/s in 50 mM sulfuric acid until the CV becomes stable (approximately 12 cycles). Abbreviated "H_2SO_4 CV" in the results.

Hydrochloric Acid Potential Cycling

Gold is known to form a stable compound with chlorine [109, 110], thus this cleaning method is actually more of an electrochemical etch. Samples are subjected to only three potential cycles from -0.5 V to 1.5 V (vs. Ag/AgCl, 3 M) at 0.1 V/s scan rate in 50 mM HCl. The number of cycles was kept low since it was observed to take only 10 cycles to remove the gold layer, and we would like a substantial amount of gold left as our working electrode surface. Abbreviated "HCl CV" in the results.

Reducing Agent Solutions

This technique is based on the principle of trying to electrolessly reduce[2] the gold oxide on the electrode surface to form metallic gold. This solution contains the reducing and electron-supplying agents from an electroless deposition recipe for gold [111]: 0.8 M KOH, 0.75 M Na_2CO_3, and 50 mM dimethylamine borane (DMAB). One set of samples spent 10 minutes in this solution at room temperature, abbreviated "DMAB@25C", and another set at 65°C, abbreviated "DMAB@65C".

Aqua Regia

A dilute version of the extremely powerful Aqua Regia noble metal etchant was formed from 1 M NHO_3 and 3 M HCl [110]. Samples only spent 2 minutes in this solution as the gold was visibly etched after 8 minutes. Abbreviated "Aqua Regia" in the results.

6.1.3 Characterization Methods

Electrochemical Characterization

A CH Instruments 660C Electrochemical Workstation was used to perform all CV and EIS. The probe solution consisted of 10 mM $[Fe(CN)_6]^{3-/4-}$redox couple and 0.2 M KCl (reference/counter-electrolyte) in Milli-Q water. A chlorinated silver wire, produced beforehand by potential cycling in saturated KCl between -1.2 V and +1.2 V at 25 mV/s for 12 hours, formed the Ag/AgCl pseudo-reference electrode, pictured in figure 6.3. All electrochemical measurements were conducted in a "Dr. Bob's" glass cell (Gamry Instruments, USA, figure 3.2(a)) with 6 ml of probe solution without stirring. Fresh probe solution was used for every different cleaning method sample set.

Before and after cleaning, each electrode was subjected to CV of five cycles sweeping potential from -0.3 V to +0.7 V at a rate of 0.1 V/s. Additionally, EIS was performed by applying a 10 mV AC voltage on a DC bias of 280 mV (the E^0 value of the $[Fe(CN)_6]^{3-/4-}$couple) at frequencies from 0.1 Hz to 100 kHz and measuring the frequency response. Each cleaning technique and accompanying measurements were performed on four separate samples to generate statistically significant results.

[2]Similar to electrolytic deposition of metal from solution, electroless deposition techniques, while still requiring electron transfer, do not require an applied current. Instead, the agents needed to provide the driving energy (reducing agent) and the electrons are contained within the solution itself, which is usually activated by the application of elevated temperatures.

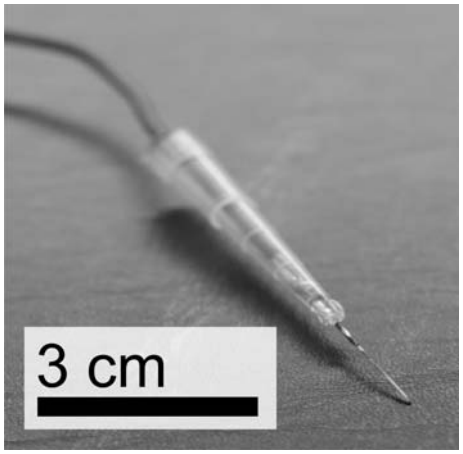

Figure 6.3: A photograph of a hand-made pseudo-reference electrode, the reference electrolyte is contained in the probe solution: 200 mM KCl.

X-ray Photoelectron Spectroscopy

A Kα X-ray photoelectron spectrometer from Thermo Scientific was used to conduct XPS to obtain an atomic percent (at.%) composition readout of the electrode surface following each of the cleaning methods, as well as the uncleaned electrode. A final sample was sputter-cleaned with Ar ions and scanned until a stable composition was observed, indicating the bulk gold had been reached.

6.2 Results & Discussion

6.2.1 Electrochemical Results

Following the fabrication and dicing, all samples spent 2 weeks on a shelf in the lab. It is known that, in ambient storage conditions, the gold surface is quickly contaminated [112], thus we used this as standard "contamination" for our tests.

The potential-difference between the peak reduction and oxidation currents, ΔE_p, previously seen in figure 5.4, is used as a measure of electrochemical cleanliness of the electrode surface, where a smaller ΔE_p indicates a cleaner surface. Theoretically, for a single electron transfer reaction such as in the $[Fe(CN)_6]^{3-/4-}$couple on a perfect gold surface, the potential difference should be $\Delta E_p = 58$ mV [52], and we interpret any increase in this value to be caused by surface imperfections and contaminations.

The frequency response from the EIS measurements were fit to the Randles equivalent circuit (seen in figure 3.7(b)), from which the charge transfer resistance, R_{ct}, was extracted. Since R_{ct} is a measure of the resistance encountered by the electron as it travels between the redox species and the electrode surface, a lower R_{ct} indicates a cleaner and more electrochemically active surface.

Table 6.1: Potential difference and charge transfer resistance for each gold cleaning method. A negative sign indicates a percentage decrease from uncleaned values.

Cleaning Methods	ΔE_p		R_{ct}	
	%Δ	σ_E	%Δ	σ_R
UV	-7.1	12.0	-40	31
KOH+H_2O_2	-20.3	3.1	-63	9
KOH sweep	-28.4	3.3	-71	6
H_2SO_4+H_2O_2	-9.3	3.5	-38	9
H_2SO_4 CV	-9.8	3.1	-6	17
HCl CV	-17.2	5.8	-52	10
DMAB@25C	-8.1	1	-27	4
DMAB@65C	-18.7	2.2	-69	6
Aqua Regia	-8.8	6.2	-58	18

Table 6.1 shows the change in ΔE_p and R_{ct} as a percent difference (%Δ) from their original, uncleaned sample values, while the standard deviation (σ) is given as a percentage of the original uncleaned ΔE_p or R_{ct} values. All samples exhibited values of $\Delta E_p = 99.2 \pm 3.6$ mV and $R_{ct} = 259 \pm 41\ \Omega$ before cleaning. Considering this, and the theoretical minimum value $\Delta E_p = 58$ mV, a "perfectly clean" version of this gold surface would have a percentage decrease in ΔE_p of $\%\Delta = -41.5$.

The large standard deviation in the UV cleaned samples indicates possible contamination of the photoreactor. The KOH+H_2O_2 and KOH sweep methods appear to deliver the cleanest gold, while the very common H_2SO_4 CV method delivers a surface less clean than expected. The HCl, Aqua Regia, DMAB@25C and DMAB@65C methods appear to have similar effects on the electrode surface.

6.2.2 XPS Results

Automated peak-fitting analysis in the Kα spectrometer provided elemental composition information. The at.% composition is plotted in figure 6.4, ignoring trace signals. We expect observing a larger percentage of elemental gold to indicate a cleaner surface, while carbon and nitrogen signals are indicative of contamination. The oxygen 1s peak is shifted from 534.2 eV to 531.5 eV, indicating that the majority of oxygen found on the surface was in the form of metal oxide. Chlorine signals are only observed in the samples cleaned in acidic chlorine environments, and in the UV cleaned sample, possibly due to contamination of the photoreactor. Again, the KOH sweep sample is believed to be the cleanest as it has the highest at.% of elemental gold on the surface. The H_2SO_4 CV sample has the second highest gold percentage, which is unexpected after the electrochemical results. One would expect the etching methods to reveal a fresh surface and have a high at.% of gold, close to that of bulk gold, but the HCl CV and Aqua Regia cleaning methods actually make the surface *less* pure by introducing chlorine contamination. The KOH+H_2O_2 method attains a cleanliness nearly that of the H_2SO_4 CV, but clearly benefits from the addition of a voltage sweep. The DMAB@25C and DMAB@65C methods behave similarly to the etches and do not reduce the gold oxide, although they do remove the nitrogen-containing contaminants, while the mild piranha clean, H_2SO_4+H_2O_2, severely oxidizes the gold surface.

The H_2SO_4 CV and HCl CV results appear contradictory between the electrochemical and XPS measurements. One possible explanation of this is that potential cycling in acidic solution affects the surface charge of the gold. Since the redox couple being used is negatively charged it may affect electrochemical measurements. An uncharged redox couple, hydroquinone/benzoquinone (H2Q/PBQ), which is a 2-electron transfer reaction, was briefly explored to address this issue with using a charged redox couple [113, 114]. It was found, how ever, that H2Q/PBQ is far less stable and much more pH sensitive than $[Fe(CN)_6]^{3-/4-}$, as well as far more toxic. Thus, the $[Fe(CN)_6]^{3-/4-}$couple remained as the workhorse redox couple for the rest of the project.

6.2.3 AFM Results

Preliminary contact-mode AFM was performed on two samples[3]. One sample was from the batch of microfabricated electrodes used in this paper, stored for 2 weeks in the lab, then scanned before and after the KOH+H_2O_2 cleaning method. The second was a 2-year-old gold sample from the same de-

[3]Contact-mode AFM was performed by bachelor student Noriyuki Masuda.

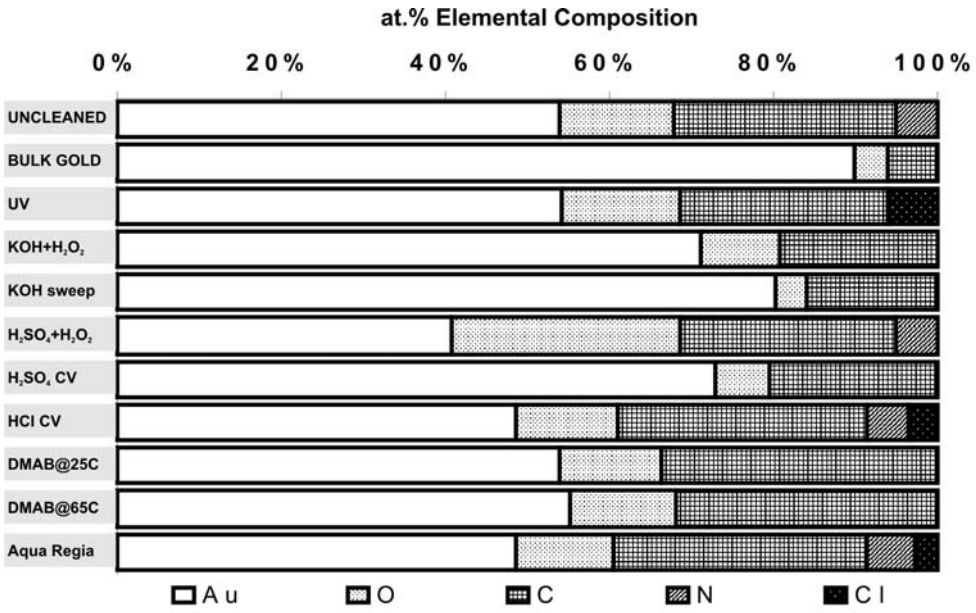

Figure 6.4: Elemental surface composition (at.%) of gold samples following each cleaning technique.

position machine, scanned before and after treatment with the KOH sweep method. Table 6.2 describes the results where samples are characterized by RMS roughness, width of the gold islands, and pitch of the islands, giving an indication of the surface structure. Uncleaned sample scans, especially the 2-year-old sample, appear noisier with less visible islands, while after cleaning the islands appear clear and smooth. Also note that both samples exhibit nearly identical roughness, width, and pitch after cleaning, despite their prior differences.

Table 6.2: Description of features in the AFM images.

Sample description	RMS Roughness (nm)	Island Width (nm)	Island Pitch (nm)
2 weeks old - uncleaned	1.10	40	100
2 years old - uncleaned	0.30	100	200
2 weeks old - cleaned	0.70	40	80
2 years old - cleaned	0.65	40	80

6.3 Conclusion

After investigating these cleaning methods we can conclude the KOH sweep method is the best, while the H_2SO_4 CV appears to be acceptable when investigated using XPS. The H_2SO_4+H_2O_2 method severely oxidizes the gold, while the HCl CV and Aqua Regia etches do not appear to produce a significantly cleaner surface. Finally, the attempt to reduce the surface gold oxide using the electroless-style solution in DMAB@25C and DMAB@65C is ineffective and merely behaves as an etch. Preliminary AFM supports the effectiveness of these cleaning techniques.

Given these results, the cleaning method chosen for future experiments is the KOH+H_2O_2 technique. The voltammetric sweep method is not practically feasible to perform in large batches of chips, thus this step was omitted. Instead, the cleaning protocol was modified to end with a 2 minute bath in 95% ethanol. Reports in literature suggest that ethanol is capable of reducing gold oxide to metallic gold [115], thus replacing the voltammetry step.

Chapter 7

Chemically Modified Electrodes

Self-assembled monolayers (SAMs) have proven useful in adding chemical functionality to sensor surfaces [116, 117], allowing specific detection to be performed [37, 118, 119]. The monitoring of hybridization by immobilizing single-strand DNA (ssDNA) and observing a signal only when the functionalized surface encounters the corresponding complementary strand [20, 120–124] has become a prototypical example of specific sensing obtained through surface modification. Specific detection of metal ions by SAM-modified surfaces has been demonstrated using quartz crystal microbalance (QCM) [125], cantilevers [126–128], and an assortment of electrochemical techniques [14, 129–134]. Specific sensing of metals has also been demonstrated using functional polymers [135–137] or pastes [108, 138], but fabrication of such materials proves much more involved than SAM immobilization [139]. Thus, for the remainder of the project SAMs would be pursued as the functional layer for metal ion detection.

This chapter describes the testing of surface modification protocol, the reaction of various SAMs to pH change as probed by the $[Fe(CN)_6]^{3-/4-}$redox couple, and initial screening of metal-specific molecules. The understanding gained in this work formed the basis for screening procedure in future experiments.

7.1 Background

7.1.1 Dissociation Considerations

Since functional monolayers are to be used, a practical understanding of them was required. Chemical groups such as -COOH, -NH_2, -OH, and -SH

are known ligands for binding metal ions [126, 140]. However, due to the mobility of the proton, the charge state of these ligands is pH dependent. Tables cataloging the pK_a of these groups [141], a measure of the dissociation constant with special reference to the pH between protonation (addition of a proton, H^+) and deprotonation (loss of a H^+), are available for a variety of molecules. While values for numerous substances in solution have been recorded, there is no such definitive table for surface bound ligands. The pH required for protonation or deprotonation is strongly affected by what other structures the ligand in question is attached to, thus it follows that immobilizing such ligands via a carbon chain to a gold surface make it difficult to predict pK_a values. It comes as no surprise then that the investigation of ligand-containing monolayers is an active field of research [142–145]. Nonetheless, for the specific purposes of this project a first-hand investigation was required.

7.1.2 Interpretation of Charge Transfer Resistance

Electrochemical impedance spectroscopy is incredibly well-suited for such an investigation. As previously described in section 3.4.2, EIS can characterize the electrode surface in a number of ways using an appropriate redox probe. Of specific importance is the charge transfer resistance, which is a measure of the impedance felt by an electron crossing the electrode-electrolyte interface. It then follows that the addition of an insulating or blocking layer to the surface would raise the R_{ct} observed. Impedance spectroscopy has been used to characterize the completeness of simple alkanethiol layers [146], in which case the electrons reach the surface by tunneling through the monolayer[1].

Given an insulating barrier, electrons will have a finite probability of tunneling through to the other side. An insulating self-assembled monolayer behaves in much the same manner, thus it follows that we can write an expression for the tunneling current i_t [146, 147]:

$$i_t = i_0 \exp(-\beta x) \tag{7.1}$$

where i_0 is the current measured at a clean gold electrode, x is the distance across which the tunneling occurs (such as the thickness of a SAM, one CH_2 segment is approximately 1.27 Å long), and β is the electron tunneling coefficient, defined as [52]:

[1] It's interesting to note in the cases where the SAM molecule consists of a series of benzene-like rings the inclusion of π-orbital electrons creates a conduction band in the monolayer, of normal incidence to the electrode surface, thus drastically reducing the observed charge transfer resistance [143].

$$\beta \approx \frac{4\pi\sqrt{2m\Phi}}{x} \approx [1.02\frac{\mathrm{eV}^{\frac{1}{2}}}{\text{Å}}]\sqrt{\Phi} \tag{7.2}$$

with m being the electron mass, and Φ being the work function of the metal, typically given in eV. The work function of gold in vacuum is typically stated as $\Phi = 5.1$ eV, thus, for a gold surface modified by a short-chain thiol-SAM the electron tunneling coefficient is estimated to be $\beta = 1.05$ Å^{-1}, in agreement with [113, 147, 148]. Equation 7.1 can also be described in terms of electron-transfer rate constant k^0:

$$k^0(x) = k_S^0 exp(-\beta x) \tag{7.3}$$

where $k_S^0 = k^0(x = 0)$. The rate constant can then be related to the charge transfer resistance R_{ct}, our solution parameter obtained from fitting the Randles circuit (section 3.4.2) to EIS data, by the following equation [146, 149]:

$$k_{app}^0 = \frac{RT}{n^2F^2}\frac{1}{R_{ct}c} \tag{7.4}$$

where R is the gas constant, T is the absolute temperature, n is the number of electrons exchanged in the reaction per ion, F is Faraday's constant, and c is the concentration of the redox probe species; if the concentration of the reduced (c_{red}) and oxidized (c_{ox}) species are equal, then $c_{red} = c_{ox} = c$.

Using this interpretation of electron transfer across an insulating self-assembled monolayer a number of groups have attempted to determine monolayer coverage [146, 150, 151] and thickness [143, 147, 152], as well as investigate the protonation state of immobilized functional groups [142, 144, 145].

7.2 Materials & Methods

7.2.1 Electrode Preparation

The 2^{nd} gen. electrodes, previously described in section 6.1.1, were used as the substrate for these investigations. Following dicing, each electrode was subjected to cleaning in a solution of 50 mM KOH and 25% H_2O_2 for 8 minutes, followed by thorough rinsing in Milli-Q water, following the conclusions reached in chapter 6. Electrodes were blown dry with filtered (0.3 μm) compressed air and immediately set in their respective functionalization solutions.

7.2.2 Surface Modification

A number of short-chain thiol-terminated molecules were selected based on what typical metal-binding molecules contained [15, 140]. In certain cases, chain lengths of 3-carbon and 6-carbon atoms were also used. All solutions were prepared at a concentration of 10 mM in 95% ethanol. Immobilization was accomplished by letting the electrodes incubate in the ethanol solution overnight (16-20 hours), before being rinsed with fresh ethanol 3 times, rinsed in Milli-Q water once (to remove the ethanol), blown dry with filtered compressed air, and measured. All chemicals were purchased from Sigma and used as provided without further purification.

Carboxyl-Terminated Monolayers: 3-Mercaptopropionic acid (**MPA**), $HS(CH_2)_2COOH$, and 6-mercaptohexanoic acid (**MHA**), $HS(CH_2)_5COOH$, were chosen to create a carboxyl-terminated surface with 3- and 6- methyl-groups distance from the surface, respectively.

Amine-Terminated Monolayers: Cysteamine (**CA**), $HS(CH_2)_2NH_2$, and 6-aminohexanethiol (**AHT**), $HS(CH_2)_5NH_2$, were chosen to create an amine-terminated surface with 3- and 6- methyl-groups distance from the surface, respectively.

Sulfur-Terminated Surface: 1, 6-Hexanedithiol (**HDT**), $HS(CH_2)_6SH$, was used to create the sulfur terminated surface. This surface-modification was not included in the EIS measurements since any pH extreme enough to change the protonation state of the free thiol group would likely damage the gold-thiol bond, biasing results. This surface was included in the XPS measurements, however.

Methyl-Terminated Surface: 1-Hexanethiol (**HT**), $HS(CH_2)_6$, was used to create the methyl-terminated surface, considered to be the passivating and non-reactive monolayer in the experiment.

7.2.3 Characterization Techniques

Impedance measurements were performed in an aqueous solution of 5 mM $[Fe(CN)_6]^{3-/4-}$, buffered by 50 mM hydrogen phosphate with 200 mM potassium nitrate to ensure a high solution conductivity. Solutions were created with pH values of 1.89, 3.94, 6.08, 8.09, and 10.0. The $[Fe(CN)_6]^{3-/4-}$solution was found to be negatively affected by low pH values, hence each solution was made and used within hours to ensure the highest activity of the couple. Impedance spectroscopy applied a 5 mV AC signal at frequencies from 0.1 Hz to 100 kHz on a DC setpoint of 238 mV, the experimentally determined half-way point between the reduction and oxidation peak of

the $[Fe(CN)_6]^{3-/4-}$couple in this experiment. Data was analyzed by fitting to a Randles equivalent circuit model (figure 3.7(b)) using the CHI 600C software (CH Instruments, USA). Measurements were conducted using the same CHI 600C potentiostat as in chapters 6 and 5, using the same three-electrode setup. Three samples each of clean gold, methyl-terminated, amine-terminated, and carboxyl terminated surface were measured in this way.

X-ray photoelectron spectroscopy was conducted using a Kα Thermo Scientific spectrometer. Survey scans were taken, as well as high energy scans of the Au 4f, C 1s, O 1s, N 1s, and S 2p peaks. Data was analyzed using Thermo Avantage software. Two samples of each modification were measured by XPS.

7.3 Results

7.3.1 EIS Results

Figures 7.1, 7.2, and 7.3 plot the charge transfer resistances (R_{ct}) versus pH values for a clean Au surface, HT (-CH_3), MPA (-COOH, 3C), MHA (-COOH, 6C), CA (-NH_2, 3C), and AHT (-NH_2, 6C). Before examining these plots closely , first consider a rough estimate of the charge transfer resistance expected, $R_{ct,theory}$, in the same manner as Shervedani *et al.* [113]:

$$R_{ct,theory} = R_0 \exp(\beta d) \tag{7.5}$$

where d is the number of carbon atoms in the alkyl chain. Thus, using an average value of the charge transfer resistance we have experimentally obtained for R_0 (the clean gold surface), we should expect a theoretical charge transfer resistance of $R_{ct,theory} = 4.4 \times 10^4\ \Omega$ for a 3-carbon chain (MPA, CA), and $R_{ct,theory} = 2.4 \times 10^6\ \Omega$ for the 6-carbon chains (HT, MHA, AHT). Figure 7.1 plots the measured R_{ct} for the clean gold surface and the HT-modified surface, and immediately we can see that the resistances observed for the HT surface are nearly an order of magnitude less than expected. Keep in mind, however, that the above theory assumes a perfectly formed monolayer blocking the electron transfer, while in reality the surface morphology can hinder monolayer formation (*e.g.* polycrystalline vs. thin film vs. Au (111) crystal). Additionally, in the cases where a "perfect" Au (111) surface has been used the surface coverage measured by EIS is still below the theoretical value [143], due to pinholes and grain boundaries in the monolayer providing a low resistance path for electron transfer, thus lowering the observed R_{ct}. Furthermore, the R_{ct} of the HT layer appears to change with

pH, even though no deprotonation should be occuring.

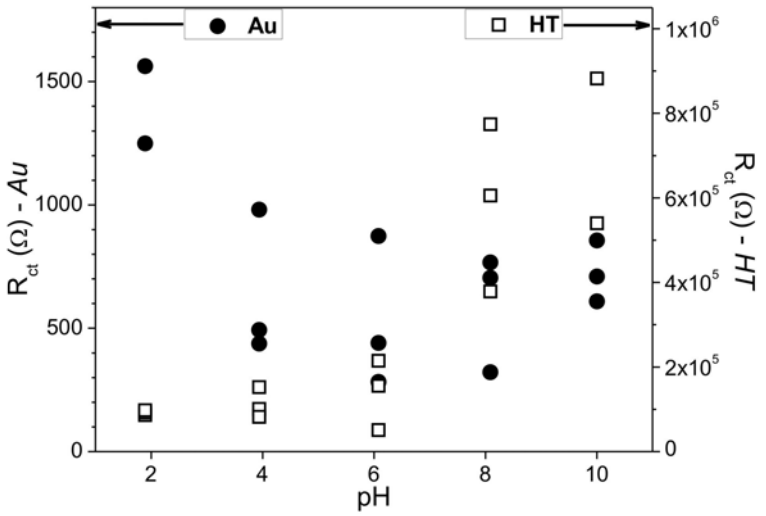

Figure 7.1: Charge transfer resistance R_{ct} vs. pH for bare gold and a methyl-terminated monolayer, 6C carbon chain length.

Figure 7.2 plots the R_{ct} of the carboxyl-terminated monolayers versus pH. Here we see a well defined step in the resistance between pH 4 and pH 6, a 5× increase in R_{ct} for both MPA and MHA layers. Since we are using a charged redox couple, $[Fe(CN)_6]^{3-/4-}$, the R_{ct} measured will be affected by the charge state of the monolayer surface. A negatively charged surface will repel the probe species, increasing the energy required for an electron transfer event, which will manifest itself as a higher apparent charge transfer resistance, while a positively charged monolayer will have the opposite effect. Carboxyl-groups are known to deprotonate at a wide range of pH values, from 2 to 7 [141], in aqueous solution depending on the molecule to which they are joined. Previous studies have experimentally determined the pK_a of carboxyl groups immobilized at the end of alkyl chains to be in the range of 5.5-6.5 [142, 144, 145], examined with both positively charged ($[Ru(NH_2)_6]^{2+/3+}$) and negatively charged ($[Fe(CN)_6]^{3-/4-}$) redox couples. Although further experiments would be required to determine the actual pH value of deprotonation, it is clear enough that the R_{ct} step occurs between pH 4 and 6, in agreement with literature, and is independent of alkyl chain length. Also, we again observe that the measured R_{ct} far below the expected value. In addition to the layer not being perfectly formed, as in the case with HT, the ionized end group can lead to charging effects in the double layer or surface, or structure or charge of the functional groups may cause enlarged pinholes [113].

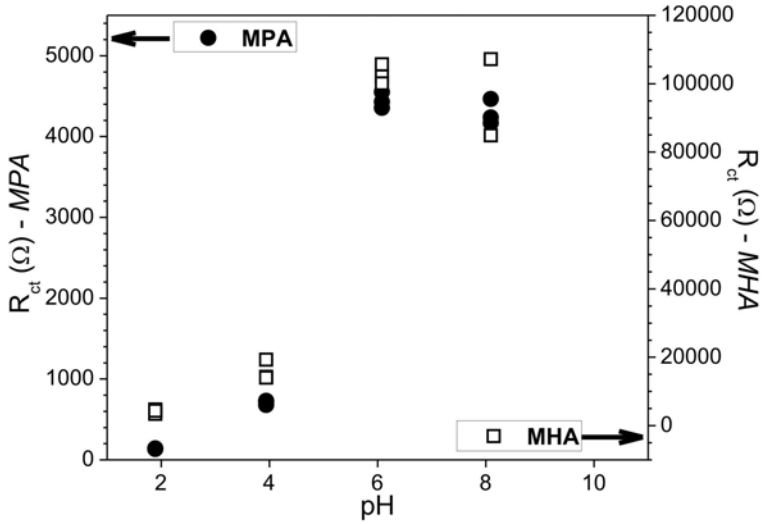

Figure 7.2: Charge transfer resistance R_{ct} vs. pH for carboxyl-terminated monolayers, 3C and 6C chain lengths.

In figure 7.3 the R_{ct} of the amine-terminated monolayers is plotted versus pH. First notice that, unlike the carboxyl-terminated layers, there is no step in the charge transfer resistance measured for CA and AHT. This is most likely due to the fact that the pK_a for amine groups is generally 9 or higher [67,141], thus it is probable that the protonation state, and therefore the charge, of the CA and AHT monolayers will not change within this experiment. Second, the R_{ct} of both amine-terminated monolayers is far below not only the theoretically expected value, but also the charge transfer resistance of of a clean gold surface. Again, this can most likely be attributed to the charge state of the amine-terminus, which remains in a NH_3^+ protonated form at the pH values examined in this experiment [141]. In such a case, opposite to the negatively charged layer in the MPA and MHA monolayers, the positively charged end group would attract the negatively charged $[Fe(CN)_6]^{3-/4-}$redox couple, thus lowering the energy required for an electron transfer event which would manifest itself in the measurements as a decrease in the charge transfer resistance. In the two data points in figure 7.3 that appear higher than the rest (at pH 8), this is probably the result of a damaged monolayer or extra large pinholes, leading to portions of the gold surface that, while now exposed to the solution, are no longer surrounded by a positive charge and thus contribute to a R_{ct} closer to that of a clean gold surface (figure 7.1).

The hexanedithiol HDT SAM was not present in the impedance measurements for two reasons: First, the pK_a of the thiol group is known to be fairly

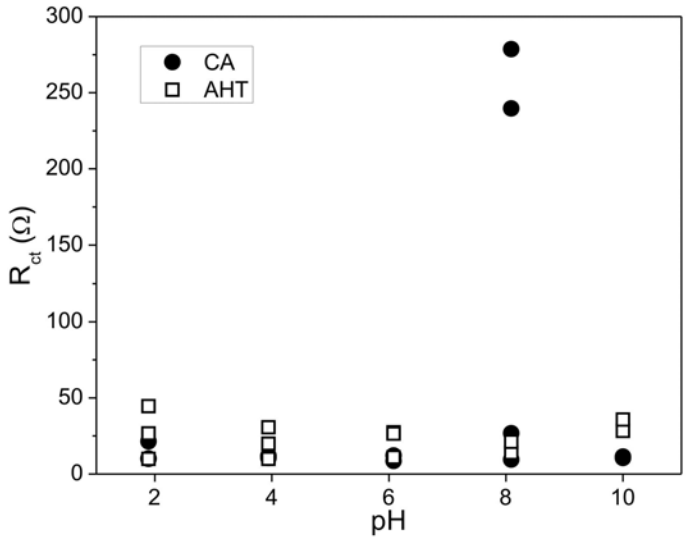

Figure 7.3: Charge transfer resistance R_{ct} vs. pH for amine-terminated monolayers, 3C and 6C chain lengths.

high, comparable with the amine group, and thus we would not expect to see any change at the pH levels examined in this experiment. Second, and more importantly, a pH high enough to cause a deprotonation to the thiol group at the free end of the HDT molecule would also likely affect the bound thiol, causing a decrease in coverage of the monolayer. In this case we would not be measuring the effect of pH on the charged state of the thiol group, but rather the effect of the monolayer being removed.

Figure 7.4 plots the effective carbon chain lengths of each monolayer versus pH using their measured R_{ct} values, and the charge transfer resistance value of the clean Au surface as the resistance for a chain length of zero, calculated using equations 7.3 and 7.4. Here a value greater than zero corresponds to a monolayer which is impeding electron transfer, while a value less than zero indicates that transfer events on that surface occurred easier than on clean gold. In all cases the measured apparent chain length is less than the nominal chain length of the actual molecules, *i.e.* 3 for MPA and CA, 6 for HT, MHA, and AHT. The simple methyl-terminated HT monolayer comes closest to its expected chain length of 6, with defects in the monolayer, due to incomplete formation and SAM and Au grain boundary effects, the probable cause of this value falling short of theory, as previously described. The apparent chain length of the MPA and MHA layers increases with pH and plateaus at pH 6, nearly matching the apparent chain length of HT at pH 6. A slight positive charge on the monolayer in its protonated state is a plausible cause of the low values for apparent chain length, negative in the

case of MPA, at low pH values. The amine terminated values, believed to remain protonated at all pH values in this experiment, maintain apparent chain length values of -3 or less, due to the effect of the positive charge on the $[Fe(CN)_6]^{3-/4-}$redox couple.

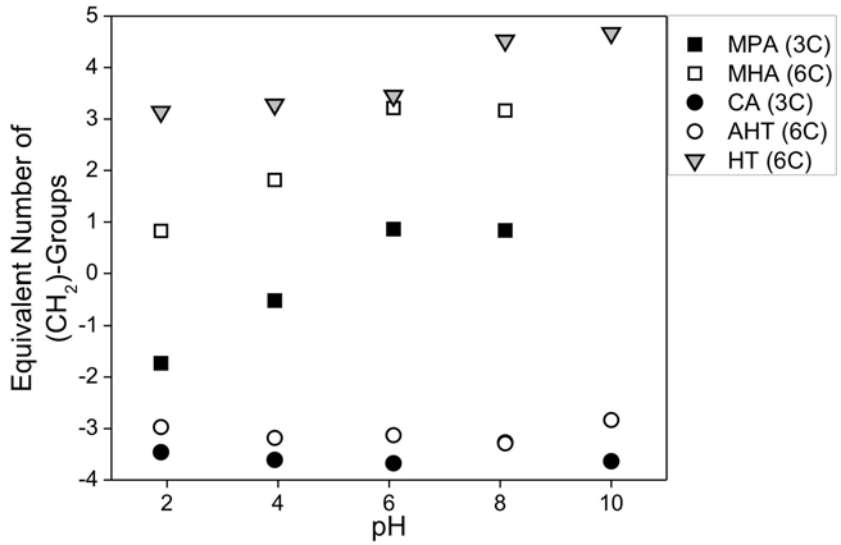

Figure 7.4: Effective carbon chain length (in number of methyl-groups) for each self-assembled monolayer from figures 7.1, 7.2, and 7.3, calculated according to equations 7.3 and 7.4, using the measured R_{ct} for clean Au as the zero-chain-length value. While physically impossible, an apparent chain length in the negative values indicates electron transfer occurs across this monolayer easier than the clean Au surface.

Lastly, notice how both the chain length value (figure 7.4) and R_{ct} value (figure 7.1) for the HT monolayer steadily increase with increasing pH. While no protonation of the methyl groups is expected, the increase in OH^- ions in the solution surrounding the electrode surface may impede the electron transfer of the negatively charged redox couple. Additionally, in figure 7.1 an initially high R_{ct} for the clean Au surface could be attributed to the increase in H^+ ions in the solution generating a slightly negative screening charge in the Au surface (*i.e.* inducing a weak electrical double layer) which would cause a minor increase in resistance, as observed.

7.3.2 XPS Results

X-ray photoelectron spectroscopy was used to ensure that monolayers had immobilized as expected. Table 7.1 presents the binding energy values that were used to identify each monolayer. Only the surfaces terminated with a carboxyl group exhibited the C1s peak at 289.4 eV, indicating a double-

bonded carbon and oxygen, while an amine bond was confirmed by the presence of a nitrogen-hydrogen bond peak at 400.2 eV. The thiol terminated surface of the HDT was identified by the presence of a free thiol binding energy at 163.4 eV, while the methyl-terminated monolayer exhibited an S2p peak only at 162.0 eV, meaning a S-Au bond was present, but all other functional groups were absent. The pure gold surface exhibited none of these peaks. From these results it can be concluded that the monolayers had been immobilized and expressed the correct functional groups.

Table 7.1: The identifying signals from the XPS performed on the monolayers investigated.

Surface Modification	Identifying Group	Identifying Signal
MPA/MHA	-COOH	C1s: 289.4 eV, C=O bond
CA/AHT	$-NH_2$	N1s: 400.2 eV, N-H bond
HT	$-CH_3$	S2p: 162.0 eV, S-Au bond
HDT	-SH	S2p: 163.4 eV, S-H bond

7.4 Conclusion

The charge state of the investigated functional groups is affected by pH as expected. Additionally, in certain samples the SAM was observed to degrade at high pH values. Further, the effect of pH-induced surface charge is to be kept in mind when performing measurements using charged redox probes, such as $[Fe(CN)_6]^{3-/4-}$, or in detecting charged species. A charge in the monolayer could potentially cause an increase or decrease in the reaction rate constant, and thus must be taken into account, and control of the solution pH is deemed necessary. Finally, the immobilization protocol and screening procedure developed will be used in future experiments to determine binding events.

7.5 Binding Metal Ions: A First Look

7.5.1 Metal Binding Molecules

More complex molecules than those described above were investigated in an effort to find a suitable monolayer for binding metals to an electrode on

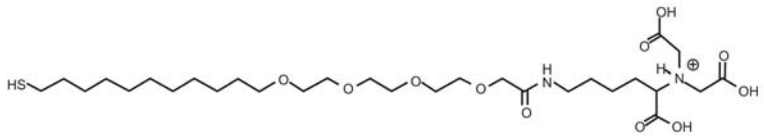

Figure 7.5: A schematic of the NTA-terminated thiol molecule immobilized on the gold electrode surface to capture Ni^{2+} ions, chemical formula HS-$(CH_2)_{11}$-EG3-NTA (Prochimia, Poland).

a cantilever. As an initial endeavor the well known nickel-binding molecule nitrilotriacetic acid (NTA) was selected [153–156]. The specific molecule, chemical formula HS-$(CH_2)_{11}$-EG3-NTA (from Prochimia, Poland) and pictured in figure 7.5, was dissolved in 50 mM phosphate buffered saline (pH 7) to a concentration of 1 mM, then incubated overnight on gold electrodes that had been cleaned. Cyclic voltammetry (-0.4 V to 0.8 V vs. Ag/AgCl, 0.1 V/s) and EIS (0.1 Hz to 100 kHz, 10 mV amplitude, 250 mV DC bias) were performed on clean Au electrodes (Au), electrodes modified with the NTA-moleclue (Au-NTA), modified electrodes with Ni^{2+} ions (Au-NTA-Ni), as well as the Au-NTA-Ni after CV cycles until a stable voltammagram is achieved (Au-NTA-Ni cycled).

7.5.2 Screening Results

Cyclic voltammetry of the different surfaces (figure 7.6) revealed the suppression of electron transfer events in the Au-NTA and Au-NTA-Ni samples, as expected, while table 7.2 shows the corresponding charge transfer resistances (R_{ct}). Upon cycling the Au-NTA-Ni-modified electrode 20 or 30 times, the CV was observed to steadily evolve from the blocked voltammagram (see in figure 7.6, the "Au-NTA-Ni" signal) towards that of the clean Au surface. The CV stabilized at the signal plotted in the figure labeled "Au-NTA-Ni cycled", however, and ceased to change with further cycling. We believe this to be the result of thiol removal from the surface via reductive desorption [84, 157–159] at certain sites where the SAM is flawed (*e.g.* grain boundaries). Desorption is typically observed at potentials closer to 1 V (vs. Ag/AgCl), but weakly adsorbed molecules may desorb at slightly lower potentials. In any case, this is a demonstration that, in a probing solution, the SAM-modified surface could be altered via potential sweeps, thus a surface could be simultaneously cleaned and monitored for cleanliness at the same time.

Assuming the same packing as simple alkanethiol chain and using the back-calculation methods previously described we interpret the charge transfer resistance as the addition of a SAM 8-methyl groups long. Clearly this is far shorter than the molecule that was actually used. In addition to the

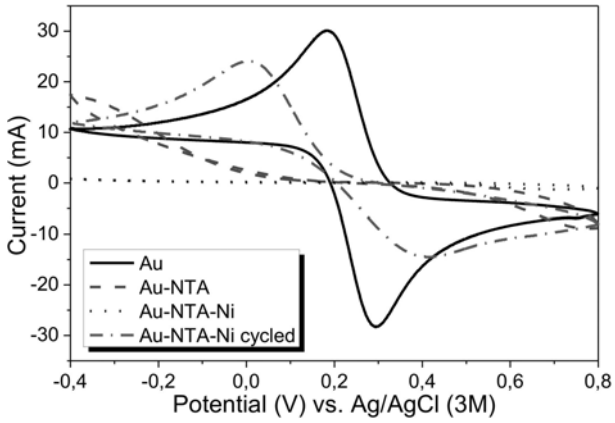

Figure 7.6: Cyclic voltammagrams of the Au, Au-NTA, and Au-NTA-Ni surfaces, as well as the Au-NTA-Ni surface after excessive cycling, plotting the stable CV obtained. The long thiolated-NTA molecule almost completely blocks the electron transfer, while the addition of Ni^{2+} ions further suppresses the transfer. Excessive cycling (20-30 cycles) was found to alter the monolayer such that the redox peaks of the $[Fe(CN)_6]^{3-/4-}$couple reappeared but did not return to their positions in the clean gold surface, indicating partial removal from the electrode surface. Probing solution: 10 mM $[Fe(CN)_6]^{3-/4-}$in 50 mM hydrogen phosphate (pH 7).

Table 7.2: Average charge transfer resistance values measured with EIS for the 4 types of surfaces investigated in figure 7.6.

Surface	R_{ct} (Ω)
Au	3×10^2
Au-NTA	5×10^6
Au-NTA-Ni	1×10^7
Au-NTA-Ni cycled	6×10^4

reasons already mentioned for an apparent chain length less than expected, the NTA-terminal on this molecule could also be responsible for steric effects in the sense that these bulky end groups do not allow the same level of packing found in the simple alkanethiol SAMs, which would leave space for the $[Fe(CN)_6]^{3-/4-}$redox couple to encounter the electrode surface, manifesting as a lower charge transfer resistance.

7.5.3 Summary

This screening method was effective in sensing the difference between a clean electrode surface, a functionalized surface, and a functionalized surface

in which something had been bound. Additionally, the effect of monolayer erosion due to potential cycling was encountered, which must be considered both for its positive and negative implications. It was decided to proceed with metal detection using specifically functional SAMs, but the NTA-molecule would not be used. Simpler prototypical systems that are also well understood would later be selected, screened, and applied to cantilever-based sensing in this project.

Part III

Functional Layers

Chapter 8

Functional Layers for Copper Ion Detection

Both cantilever and electrochemical detection methods will require a functional layer to capture metal ions. Cantilevers require this functional layer to transduce specific molecular interactions into mechanical stress to cause a deflection [20, 21, 37, 41, 45, 48, 121, 160–163]. While electrochemical methods are capable of speciation through interpretation of the current-voltage relationship, a functional chemical layer can increase the measurement sensitivity to a particular analyte. Speciation and sensitivity in voltammetric methods has been enhanced through the use of functional polymers [135–137,139], pastes [108,138,164], and self-assembled monolayers [13,15,16,165–167]. This chapter describes the screening procedures to find a functional chemistry for detecting copper (II) ions, the model metal ion system for the ECC platform.

8.1 Biomolecules For Metal Ion Detection

8.1.1 Amino Acids

The design of functional layers for metal ions is based on their affinities to specific chemical groups or ligands [2]. Beyond merely having an affinity for a single chemical group, metal ions can be strongly bound by these groups if they form a specific coordinating structure, which is the basis for *chelation* [141]. This is precisely the case in systems such as Ni^{2+}/dimethylglioxime (DMG), where both the chemical groups and coordinating structure create a very high affinity between Ni^{2+} and DMG, and a very low affinity between DMG and most other metals [138]. This is also the basis for heavy metal toxicity in living organisms, where an incorrect metal ion can interact with proteins to either block essential metal ions or change the folding of the protein, causing adverse effects [2].

It then makes sense to detect the toxic metal ions in the same manner in which they cause damage, *i.e.* by using simple biological molecules immobilized on transducers. Work has been done on the use of amino acids to capture metal ions, which is the simplest implementation of this methodology. The Cu^{2+}/L-cysteine system in particular has been investigated for its use in sensing copper ions [126,130,168–170]. The cysteine amino acid binds so well with the Cu^{2+} ion that the only interfering ion, Ni^{2+}, must be present in 5000-fold excess to Cu^{2+} to interfere with detection [169]. This makes the Cu^{2+}/L-cysteine pair a great prototype system to test an electrochemical-cantilever platform since it's binding configuration [170], seen in figure 8.1, has also been shown to generate a stress response [126].

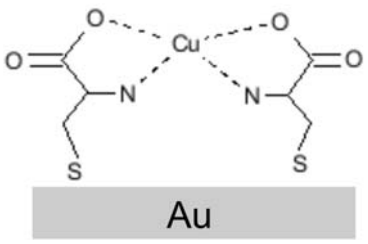

Figure 8.1: A schematic of the binding configuration of the amino acid L-cysteine to a Cu^{2+} ion.

8.1.2 Peptides

While cysteine can be easily immobilized and has a strong affinity for copper ions, we can only accomplish so much with a simple, single amino acid. The routes for specific metal toxicity in organisms include the infiltration of certain amino acid sequences in proteins and disrupting cellular functions [2]. Thus, using peptides based on these sequences can increase the selectivity of target metals, and also make devices more sensitive to the metals that actually cause harm [6,171–174]. A specific example is the short-chain peptide Glycine-Glycine-Histidine (GGH), a sequence designed to mimic the copper transport site on human albumin, which has been shown to have a high affinity and to actively compete with proteins for Cu^{2+} ions [175,176]. Researchers in J. J. Gooding's group have investigated the use of GGH to selectively bind Cu^{2+} ions to be detected voltammetrically [15,140,177–179]. Using a novel layer-by-layer approach they are able to bind arbitrary amino acid sequences to a mercaptopropionic acid (MPA) surface via a peptide bond to detect copper ions, as well as other metals [180].

Of additional interest to the cantilever community is the folding action that occurs during binding with a metal ion. Proteins immobilized on a surface are known to change shape or folding upon binding a metal ion, thus creating a stress in the protein layer [46]. While short-chain peptides (such as GGH) are much smaller than the proteins typically investigated, they too fold upon binding with a metal ion [177, 181] and cause a change in surface stress [25].

8.1.3 Custom Peptide: CGGH

The layer-by-layer technique used by Chow *et al.* [15, 178, 180] to graft arbitrary amino acid chains to a carboxyl-terminated surface via a peptide bond, while extremely versatile, could not be accomplished in this project. Although significant efforts were made by experts in organic chemistry[1], a surface-immobilized peptide bond could not be achieved reliably.

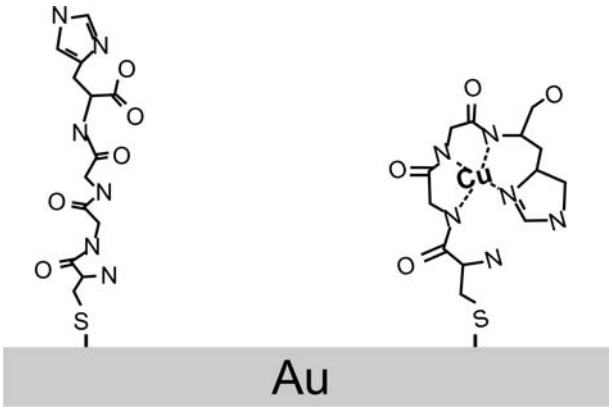

Figure 8.2: A schematic of the tetrapeptide Cysteine-Glycine-Glycine-Histidine (CGGH) bound to a gold surface in both its free (*left*) and Cu^{2+} ion-coordinated (*right*) configurations.

An alternative and simplified functionalization scheme was proposed in the interest of reducing time spent modifying chips and maximizing the anticipated reproducibility of results. All peptide attachment would be performed on gold surfaces. The chosen proof-of-concept metal ion was the Cu^{2+}, and cysteine was picked to be functional layer. The tripeptide GGH, as previously mentioned, is designed to selectively bind copper ions [175, 176, 181] and is capable of doing so when immobilized onto surfaces via MPA [15, 140, 177–179]. Thus the obvious simplification of this process was

[1] Under the guidance of associate professor Mogens Havsteen Jakobsen and with the practical assistance of assistant professor Gabriela Blagoi (DTU Nanotech).

to simply attach a cysteine residue to the GGH sequence. This created the tetrapeptide CGGH[2], which could be immobilized in a single step onto a clean gold surface and still provide the functionality of the GGH peptide. Figure 8.2 depicts the immobilized CGGH molecule, as well as the expected coordination structure around a Cu^{2+} ion, as described in the literature [176, 178, 179].

8.2 Screening of Functional Layers

Cysteine (Cys) and the tetrapeptide CGGH have been chosen for the different ways in which they bind the proof-of-concept target ion: Cu^{2+}. Two Cys molecules bind a single Cu^{2+} ion (figure 8.1) and there is no significant change in the physical structure of the immobilized molecules. In contrast, a single CGGH molecule is believed to coordinate around one Cu^{2+} ion, and the peptide undergoes quite a significant folding event (figure 8.2).

Cantilever behavior is affected by a great number of factors, meaning the reaction of the functional layer to Cu^{2+} might be only one of many factors affecting the change in surface stress. Thus a screening process was applied to prove beyond a reasonable doubt that: (a) the protocol used to immobilize the molecules is effective, and (b) the immobilized molecules are binding the Cu^{2+} ions. The remainder of this chapter describes the screening techniques applied to this end. Impedance spectroscopy and cyclic voltammetry are performed on Cysteine-modified surfaces and compared with literature results to confirm functionality of the layer. As well for the CGGH monolayers, EIS and quartz crystal microbalance (QCM) are used to confirm the presence of the monolayer, and that there is a reaction to copper ions. Ethylenediaminetetraacetic acid (EDTA) is applied to the CGGH monolayer during QCM measurements to demonstrate the regenerability and reusability of the layer.

8.2.1 Experimental Methods

Materials

The custom peptide CGGH (sequence Ac-Cys-Gly-Gly-His-OH, molecular weight 413.44 g/mol) was made to specifications by TAG Copenhagen (Denmark). The CGGH purity was measured by high-performance liquid chromatography (HPLC) to be 98.92% (confirmed by mass spectrometry) and

[2]This peptide sequence, and the associated immobilization protocol have since been used by Ph.D. student Alberto Cagliani to capture copper ions on silicon bulk disk resonators.

was used without further purification. All other chemicals were obtained from Sigma-Aldrich (Denmark) in analytical grade purity and used as received. All dilutions were made with Milli-Q water (18.2 MΩcm) from an in-house dispenser (Millipore Direct-Q UV).

Immobilization Protocol

All electrochemical measurements were performed on the 2^{nd} gen. working electrode chips (section 6.1.1, figures 6.1 and 6.2), while QCM measurements were performed on AT-cut quartz substrates with 100 nm of Au (Q-Sense, Sweden). Both types of substrates were cleaned using the protocol developed in chapter 6, and as applied in section 7.2.1. Following rinsing each electrode was set in 5 ml of a 5 mM solution of either Cys or CGGH, buffered to pH 6 by 0.1 M hydrogen phosphate. Substrates remained in this solution for 16-20 hours (overnight incubation) and were then rinsed in two 10 ml baths of clean 0.1 M phosphate buffer for 1 hour each.

Electrochemical Methods

All electrochemical measurements were performed using a CHI 660C electrochemical workstation (figure 3.2(c)), a Ag/AgCl (KCl saturated) reference electrode (Gamry Instruments, USA, figure 3.4(b)), and a Pt rod counter electrode (figure 3.5). Cyclic voltammetry and EIS were performed in 5 mM $[Fe(CN)_6]^{3-/4-}$with 0.2 M potassium nitrate, 0.1 M phosphate buffer (pH 6), on both clean gold and electrodes modified with Cys and CGGH to determine if the immobilization protocol worked. Voltammetry sweeps were performed at 0.1 V/s between the potentials indicated in the figures for 5 cycles. In the case of the Cys-modified surfaces, an additional CV (0.1 V/s) was performed in 0.2 M potassium nitrate, 0.1 M phosphate buffer (pH 6) before and after accumulating copper for 20 minutes in a 100 μM $CuSO_4$ solution. After copper accumulation the substrates were rinsed with Milli-Q and phosphate buffer extensively, to ensure the only copper present was that which was specifically bound by the Cys.

Impedance measurements were performed on clean gold surfaces, and those modified with Cysteine and CGGH. Additionally, EIS measurements were taken on Cys and CGGH substrates that had Cu^{2+} ions bound, as well as CGGH substrates that had been exposed to 5 mM EDTA to remove bound copper. Frequencies from 0.1 Hz to 100 kHz were applied at a 5 mV amplitude on a 240 mV setpoint bias. Four samples of each functionalization were measured to obtain statistically significant results.

Quartz Crystal Microbalance - QCM

A Q-Sense E1 quartz crystal microbalance flow system with dissipation monitoring (QCM-D) (Q-Sense, Sweden) was used to monitor the effect of copper binding and removal on immobilized CGGH molecules[3]. This instrument is capable of not only measuring the frequency shift due to the change in mass on the resonator surface, but can also measure the rate at which resonator energy is dissipated due to the change in viscoelasticity of the absorbed layer [182–184]. The CGGH-modified QCM chips were mounted and a 40 μl/min Milli-Q water flow was initiated and carried on for approximately 2 hours, the typical time required to reach a drift-free baseline. Then a 100 μM $CuSO_4$ solution was flowed over the surface for 10 minutes, after which the Milli-Q water flow was re-initiated. A 5 mM solution of EDTA was then introduced to remove the copper ions from the system, after which Milli-Q water was once again introduced. This cycle was carried out repeatedly to investigate if the monolayer could be reused.

8.2.2 Results

Cyclic Voltammetry

As mentioned in chapters 6 and 7, the CV of a working electrode in a known redox couple ($[Fe(CN)_6]^{3-/4-}$in this case) can be used to interpret the degree of electron transfer blocking compared to a clean, unmodified gold surface. In this experiment, since all solutions and surface treatments are known, and electrode cleaning has been verified (in chapter 6 and in reference [101]), then the degree of blocking on the surface measured by CV is an indication of whether the immobilization protocol has worked. Figures 8.3 and 8.4 plot the CVs taken before and after the deposition of the two aforementioned monolayers. The peak-to-peak separation, ΔE, for the L-Cysteine modified electrode (figure 8.3) is 13 mV less than that of the clean gold electrode. While one might expect a clean, unmodified gold surface to host the most efficient electron transfer, we know from previous experience (chapter 7) that the charge state of the surface can greatly affect the behavior of electrochemical measurements when using a charged redox probe, such as $[Fe(CN)_6]^{3-/4-}$.

Thus, figure 8.3 implies that the gold surface has gained a net positive charge, as experienced in section 7.3.1. There an amine-terminated surface was seen to have a positive charge at all pH values between 2 and 10, due to the amine group remaining protonated in this pH range (figure 7.3), while a carboxyl-terminated surface underwent a change in charge state (most likely

[3]QCM measurements were performed using the equipment and facilities at the Danish Technological Institute (DTI), with assistance from post-doctoral researcher Yihua Yu.

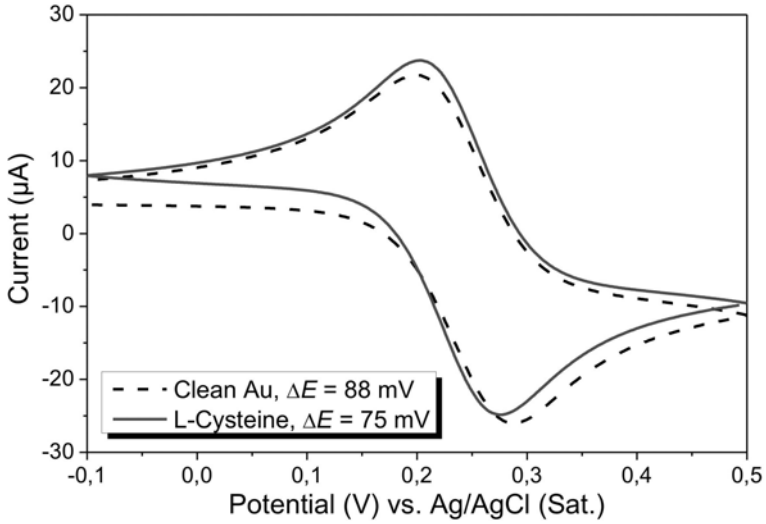

Figure 8.3: Cyclic voltammagrams of the gold electrode surface before and after modification with the amino acid L-cysteine. The peak separation ΔE is slightly less after modification due to the positively charged surface attracting the negatively charged redox couple, causing an apparent increase in electron transfer kinetics. Probing solution: 5 mM $[Fe(CN)_6]^{3-/4-}$, 0.2 M KNO_3, and 0.1 M H_2PO_4 (pH 6).

COOH to COO^-) between pH 4 and 6 (figure 7.2). Further qualification of the surface state is difficult when considering only the CV presented. Further evidence is provided by impedance spectroscopy.

Figure 8.4 plots the CVs obtained before and after the gold surface was modified with the tetrapeptide CGGH. Here the surface is blocked to a large degree, preventing any reduction of the redox couple, and allowing what appears to be only a faint oxidation peak to be observed. This molecule is far longer than the simple Cysteine molecule previously mentioned, and thus should provide a much greater resistance to electron tunneling, hindering the transfer kinetics, resulting in a suppression of the $[Fe(CN)_6]^{3-/4-}$couple redox behavior. Figure 8.4 is the first evidence indicating that the functionalization protocol is adequate.

A Cysteine modified electrode was placed in a $CuSO_4$ solution to accumulate copper ions. Since performing a CV on a copper-charged electrode in the $[Fe(CN)_6]^{3-/4-}$redox couple would result in both $[Fe(CN)_6]^{3-/4-}$and Cu^{2+} reduction and oxidation peaks appearing, making interpretation of the plot difficult, a different approach was taken. Cyclic voltammagrams were conducted in phosphate-buffered electrolyte before and after copper accumulation, with the results plotted in figure 8.5. Prior to copper accumulation the CV in the buffered electrolyte appears flat, with this absence of peaks

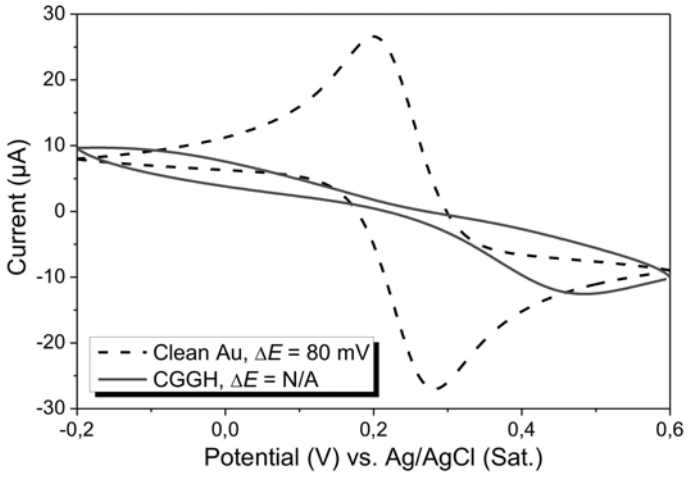

Figure 8.4: Cyclic voltammagrams of the gold electrode surface before and after modification with the custom tetrapeptide CGGH. The electron transfer at the surface is effectively blocked by the relatively long chain molecule, since no reduction peaks are observable. Probing solution: 5 mM $[Fe(CN)_6]^{3-/4-}$, 0.2 M KNO_3, and 0.1 M H_2PO_4 (pH 6).

indicating no redox activity on the surface. After copper accumulation, however, two peaks are observed, $E_{red} = 46$ mV and $E_{ox} = 252$ mV. These peaks agree very well with Yang *et al.* [170], where these voltammetry values correspond to Cu^{2+} being reduced to Cu^{+} at E_{red}, and Cu^{+} being oxidized to Cu^{2+} at E_{ox}. This is further confirmation that the cysteine monolayer is binding copper as expected.

Impedance Measurements

Impedance spectroscopy was employed to further explore the blocking behavior of the surface modification. Table 8.1 lists the average values of the charge transfer resistance, $\bar{R_{ct}}$, and the standard deviation in these values, σ_{Rct}. Additionally, the equivalent length of a carbon chain that would modify the clean gold R_{ct} as it appears in the table is calculated in the same manner as it was in section 7.3.1. This was done in the interest of easy comparison between this work and that of section 7.3.1. While a carbon chain with a negative value length has no physical meaning, the basic idea to be obtained from these results is: (1) the cysteine layer, due to being positively charged, increases electron transfer kinetics at the surface, and (2) the binding of copper to the cysteine surface does not change the apparent charge of the surface, at least not in any significant way.

Table 8.2 lists the values of charge transfer resistance and equivalent carbon chain length for CGGH-modified electrodes. The table shows data for

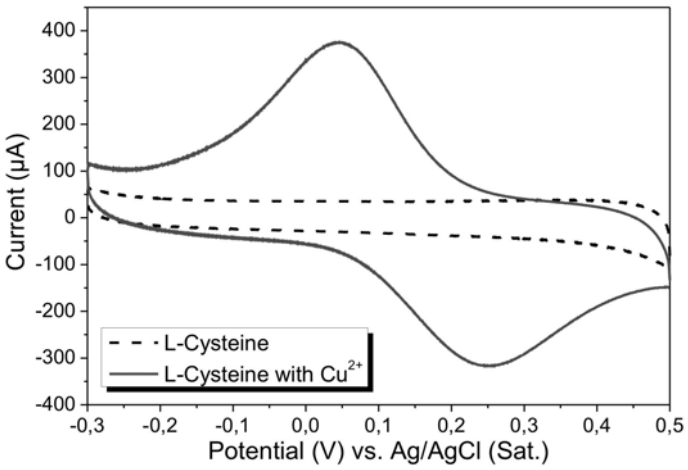

Figure 8.5: Cyclic voltammagrams of the L-Cysteine modified surface in buffered electrolyte before and after a 20-minute copper ion accumulation. Very clear copper oxidation and reduction peaks appear after the Cu^{2+} ions are bound to the surface. Electrolyte: 0.2 M KNO_3 and 0.1 M H_2PO_4 (pH 6).

Table 8.1: Impedance spectroscopy results for L-cysteine modified electrodes.

Surface	$\bar{R_{ct}}$ Ω	σ_{Rct} Ω	Calculated Carbon Chain Length	Actual Carbon Chain Length
Au	314	-	$n = 0$	$n = 0$
Au+Cys	36	8	$n = -2.1$	$n = 3$
Au+Cys+Cu	35	5	$n = -2.1$	$n = 3$

two different rounds of EIS measurements. These were performed on two different batches of electrodes, and the difference in R_{ct} values for the same surfaces is attributed to variations in microfabrication.

There is a very large increase in R_{ct}, again indicating a severe hindrance to electron transfer, implying CGGH was successfully immobilized on the electrode surface. Unlike the Cysteine layer, however, we see a change in the R_{ct} with the addition of Cu^{2+} ions to the CGGH layer. If we interpret this as electron tunneling through a simple alkanethiol monolayer, as we did in chapter 7, the results seem to contradict our understanding. If the immobilized CGGH molecule coordinates to the Cu^{2+} ion as expected from literature [15,25,140,175–179,181,185], depicted in figure 8.2, then the folding should cause a decrease in monolayer height. This would decrease the

tunneling distance between the solution and the electrode surface, which should in turn decrease the measured charge transfer resistance. This is entirely contrary to what is observed.

Table 8.2: Impedance spectroscopy results for CGGH modified electrodes.

Surface	$\bar{R_{ct}}$ Ω	σ_{Rct} Ω	Calculated Carbon Chain Length	Actual Carbon Chain Length
Au[1]	1.5×10^2	-	$n = 0$	$n = 0$
Au+CGGH[1]	3.1×10^4	2×10^3	$n = 5.1$	$n = 13$
Au+CGGH[1]	8.4×10^4	6×10^3	$n = 6.0$	$n = 8$
Au[2]	6.8×10^2	-	$n = 0$	$n = 0$
Au+CGGH[2]	1.5×10^5	4×10^4	$n = 5.1$	$n = 13$
Au+CGGH+Cu[2]	2.2×10^5	5×10^4	$n = 5.5$	$n = 8$
Au+CGGH+Cu, after EDTA[2]	1.0×10^5	4×10^4	$n = 4.8$	$n = 13$

[1]The first round of CGGH and Cu^{2+} measurements.

[2]A second round of measurements were made to test regeneration by EDTA.

There are two effects to consider here. First, recall the effect of positively charged groups decreasing the charge transfer resistance, as in table 8.1 and figure 7.3. The sequence for the CGGH molecule, Ac-Cys-Gly-Gly-His-OH, indicates that the N-terminal on the Cys residue is neutralized by an acetyl group, and leaving the active carboxyl group at the C-terminal on the His residue free. There are also amine and carboxyl groups along the peptide backbone, the charges of which could contribute to a large decrease in R_{ct}. However, based on what was seen in chapter 7, even a single protonated amine group can cause a massive decrease in charge transfer resistance, and at pH 6 we don't expect the carboxyl groups to decrease R_{ct} significantly either.

A more likely interpretation of the results comes from considering a second effect. The CGGH molecule is not a slim, straight alkanethiol chain-like

molecule. It is a peptide, with functional groups hanging off the side, and thus will not form a dense, well packed monolayer. Instead there are likely to be large holes in the monolayer, or at least very common defects where the solution is either in direct contact with the electrode surface, or the tunneling distance is far less than the estimated 13 carbon bonds from the surface, which would account for the apparent carbon chain length of $n = 5.1$, similar to the work of Diao *et al.* [146]. Then, upon coordinating to the copper ions, the peptide folds, decreasing in height, but also filling in defects and becoming more dense, which would increase the tunneling resistance felt by the electrons, manifesting itself in an observed increase in charge transfer resistance as observed. For comparison, this can be interpreted as a carbon-chain-length value ($n = 6.0$ and 5.5) closer to the expected for a folded CGGH molecule ($n = 8$). The same concept of a folding peptide altering the access of a redox probe to the electrode surface (thus changing electron transfer characteristics) has been observed by Chow and Gooding [140].

Finally, during the second round of impedance measurements, EDTA was introduced to remove the Cu^{2+} ions from the CGGH molecules. Being an incredibly strong chelator, EDTA is capable of pulling metal ions from other coordination schemes, even ones with a high affinity such as the Cu-GGH system [130, 185]. The EDTA reduces the charge transfer resistance to a value below that of the freshly formed CGGH monolayer. This indicates that, while the monolayer still appears to be mostly present (the order of magnitude R_{ct} remains the same) it has been altered somehow. Further tests are required to investigate if the CGGH monolayer has maintained its functionality and is still capable of generating a reaction to bound copper.

QCM Measurements

Quartz crystal microbalance measurements were conducted to observe the reaction of the peptide to copper ions in real-time. The electrochemistry setup used so far was incapable of introducing any type of fluid flow, thus real-time monitoring of charge transfer resistance was not possible. The Q-Sense E1 QCM-D system was thusly employed to monitor binding events. Figure 8.6 plots the reaction of the frequency (seventh overtone, $f_7 = 34.710905$ MHz) of the functionalized crystal to 100 μM $CuSO_4$. We observed a large drift in the frequency, initially a negative drift, which evolved to a relatively stable positive drift ($f/t = 1.5$ Hz/h) over the course of approximately 2 hours[4]. As indicated in the figure, a baseline was acquired

[4]It should be noted that while this drift appeared stable it continued to evolve to towards a drift of $f/t = 0$ Hz/h. However this was estimated to take an additional 4 hours beyond the 2 hour baseline already performed, and, due to logistics and other issues of practicality, such long baselines required to achieve zero drift were simply not feasible.

under a 40 μl flow of Milli-Q water. Then, at $t \approx 33$ minutes, the injected copper ion solution meets the functionalized surface causing a sudden decrease in frequency, ~ 0.4 Hz drop in ~ 18 s, corresponding to an added mass of ~ 1 ng, before settling into a stable negative drift of $f/t \approx -2.4$ Hz/h (occurring for as long as the copper solution was flowing), with a transition time of roughly 200 s between these two stages.

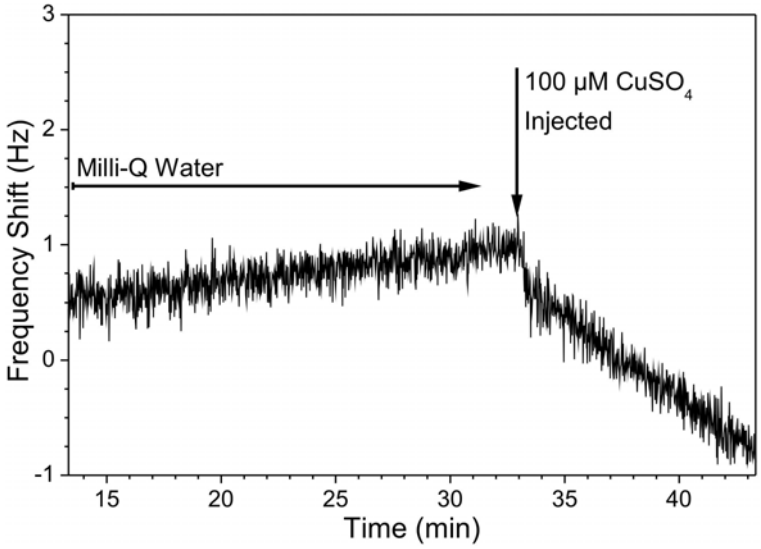

Figure 8.6: The frequency shift of a CGGH-modified QCM sensor upon exposure to 100 μM $CuSO_4$. Note the two different stages in the binding reaction. The first stage is a very fast ($\tau \approx 18$ s) frequency drop of ~ 0.4 Hz, followed by a stable change in frequency of -2.4 Hz/hour. There appears to be a short transition between these two stages of approximately 200 s.

This long term stable drift that occurs with flow of the copper solution appeared to continue without end, as long as the flow was sustained. Similar experiments were conducted with the copper solution flowing overnight (8 hours) and the drift remained constant during the entire duration. At such a high concentration, and in a complex with such a high affinity constant, we would expect the binding to be very fast, on the order of seconds or minutes [25]. We believe the initial sudden drop in frequency is the ion-peptide coordination event. Additionally, since the QCM crystal surface is finite and, subsequently, so is the number of CGGH molecules, the signal due to Cu-CGGH binding should saturate at some point. Thus, this constant drift occurring with copper solution flow should not be indicative of ions coordinating to the peptide, and must be the result of some other accumulation. The noise in the frequency signal is on the order of ~ 0.4 Hz. While this makes these results not very quantitatively reliable we are still

able to make qualitative observations and gain the confirmation of peptide functionality that we sought at the outset of this experiment.

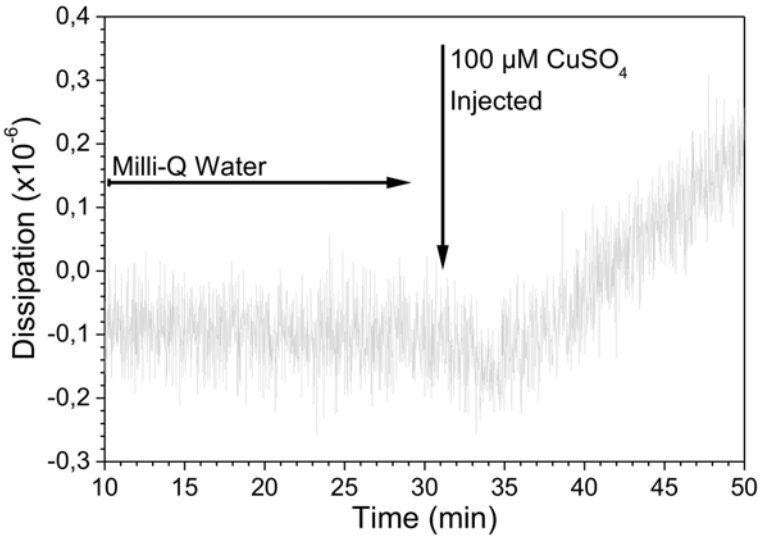

Figure 8.7: The change in the dissipation of resonator energy due to the copper-peptide binding event. Notice the brief, slight decrease in dissipation, on the same time scale as the sharp drop in frequency from figure 8.6, immediately following the injection of copper. Again, similar to the frequency response, there is then a steady drift increasing dissipation following the initial response. This drift continues as long as copper solution flows.

Figure 8.7 plots the dissipation of energy of the crystal corresponding to the frequency plot in figure 8.6. A decrease in dissipation value means that less energy is dissipated per cycle, which is a result of the adsorbed layer becoming more rigid and thus more strongly coupled to the surface. This increase in rigidity, or density, due to the peptide coordinating to copper is consistent with what we observed in the impedance measurements, where the R_{ct} increased after the peptide folded around the copper ion, thus becoming more dense. The positive drift, as with the frequency, must correspond to some molecular deposition other than the peptide-ion binding events, since it decreases surface rigidity.

The goal behind using QCM was to observe the real-time binding of ions, but also to investigate if the surface could be regenerated by applying a chelating solution, namely a solution of 5 mM EDTA. Figure 8.8 plots the frequency shift (black) and energy dissipation (gray) responses to a sequence of solutions. As seen in figures 8.6 and 8.7, there is a small instant decrease in both frequency and dissipation signals, followed by the drift due to the flow of the 100 μM copper solution induces the stable drift. Around $t = 60$ minutes a flow of Milli-Q replaced the flow of copper ions. A drift similar to, but

slightly steeper than that observed during the Milli-Q baseline is seen with this second Milli-Q flow. At $t = 85$ minutes a flow of 5 mM EDTA is introduced, which causes both signals to spike in the direction of the copper-free signal, almost reaching the same value, before the EDTA takes its own effect on the frequency and dissipation response. The high concentration of EDTA is felt as a change in the viscoelasticity of the fluid, manifesting itself in the altered but relatively stable values (compared to the drift occurring under a copper flow) in both signals. This is supported by observing the signals when a Milli-Q water flow is re-introduced, which returns the values to that of the copper-free signals, taking into consideration the drift and how it has evolved over the course of the experiment.

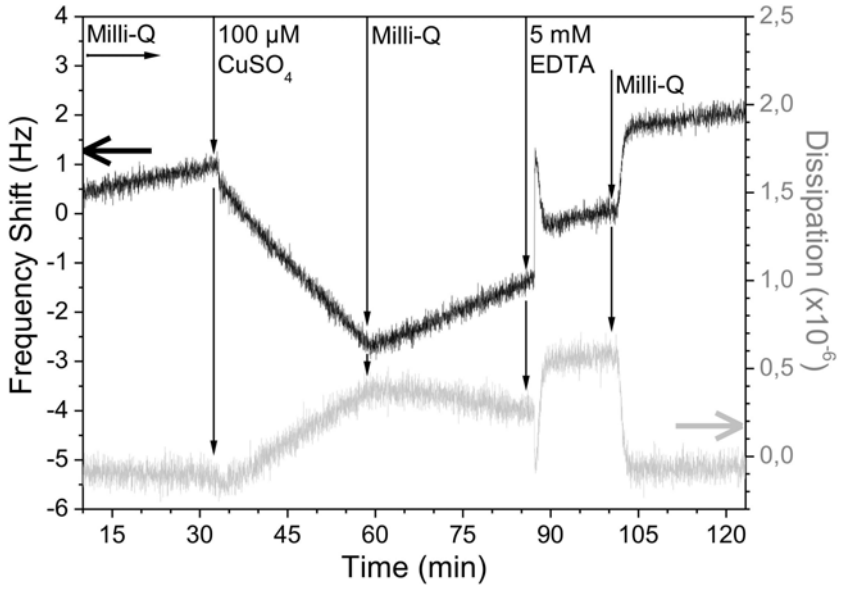

Figure 8.8: The frequency (black) and dissipation (gray) responses of a CGGH-functionalized QCM crystal surface.

Although the CGGH surface appears to have been restored to its copper-free state, observing the frequency and dissipation signals return to their pre-copper value does not necessarily indicate that the surface has been regenerated. For evidence to support this we subjected the same CGGH-modified crystal to another flow of 100 μM $CuSO_4$. In figure 8.9 the frequency (black) and dissipation (gray) responses of the CGGH-functionalized QCM crystal to copper and EDTA solutions, as plotted in figure 8.8, but with a second round of exposure to copper and EDTA. The second copper exposure (figure 8.9, region 6) is 35% longer than the first copper exposure (region 2), resulting in a larger frequency drop caused by the constant drift. It should then be noted that, despite this larger frequency shift, the second

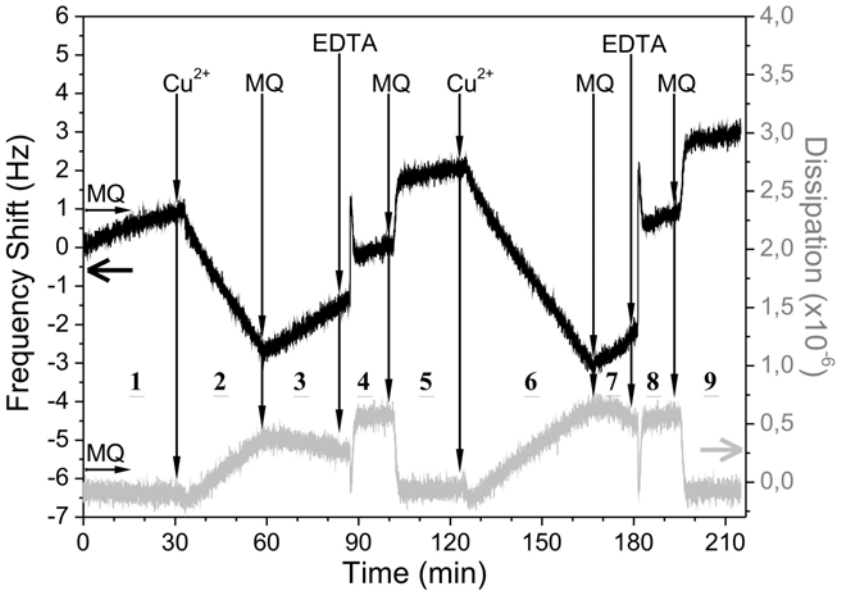

Figure 8.9: The frequency (black) and dissipation (gray) signals of the same QCM crystal from figure 8.8, now showing the two exposures to copper ions, follow by a two exposures to EDTA. The underlined numbers label regions of resonator behavior.

EDTA exposure (figure 8.9, region 8) behaves in the same manner as the first EDTA exposure (region 4), both how the initial spike almost reaches the copper-free frequency value, and that the EDTA-dominated frequency is the same in both regions 4 and 8, taking the evolving drift into consideration. The dissipation signal also shows congruence between the two rounds of exposure. The magnitude of dissipation due to EDTA (regions 4 and 8) are the same, and the initial spike following EDTA introduction almost reaches the copper-free value both times, as in the frequency signal. Finally, as with the frequency signal, the copper-free surface under the Milli-Q flow shows the same value for dissipation when the surface is fresh (region 1), regenerated once (region 5), and regenerated twice (region 9).

For comparison between rounds of exposure, the values for the slopes in each region for both the frequency shift (black) and energy dissipation (gray) are estimated as a straight line (within the region) and tabulated in table 8.3.

8.2.3 Conclusion

The objective of the work in this chapter was to identify two different molecules to capture a metal ions, Cu^{2+}, for eventual use in the cantilever system. The amino acid L-Cysteine was chosen since it is a prototypical

Table 8.3: Summary of the slopes of the frequency and dissipation signals in each region, from figure 8.9.

		Slope	
Region Number	Flow Solution	Frequency Hz/h	Dissipation $\times 10^{-6}$/h
1	Milli-Q water	1.5	-0.1
2	100 μM $CuSO_4$	-2.4	1.3
3	Milli-Q water	1.0	-0.3
4	5 mM EDTA	0.6	0.2
5	Milli-Q water	1.1	0.1
6	100 μM $CuSO_4$	-2.2	1.2
7	Milli-Q water	1.1	-0.7
8	5 mM EDTA	0.5	0.3
9	Milli-Q water	0.9	0.0

SAM for metal sensing, as found in literature. The custom peptide Cys-Gly-Gly-His was fabricated to behave as our folding capture molecule, chosen since the Gly-Gly-His peptide is well known to capture copper (II) ions in the same way, and with the same strength as the copper transport proteins in human serum albumin. A functionalization protocol was developed and investigated to ensure that the monolayers had been formed, and that they were binding copper as expected. The attachment of the cysteine monolayer was confirmed by CV and EIS, and the capture of copper was confirmed by a CV in clean phosphate buffer after a short accumulation time in a copper ion solution.

The immobilization of the CGGH monolayer and its binding of copper was confirmed by CV and EIS as well. Quartz crystal microbalance experiments were used to observe the binding of copper in real-time, and to confirm that the CGGH monolayer could be regenerated and used again after the bound copper ions were removed by EDTA. The CGGH monolayer appeared to retain its functionality after regeneration. These two layers will be applied to the cantilevers which will be fabricated in future chapters.

8.3 Further Development of Chelating Peptides

Although chosen as our proof-of-concept target ion, copper is a relatively benign metal, having very minor effects at only very high concentrations ($\sim$ 2 mg/l). Arsenic contamination of drinking water poses a much greater threat, both in the number of affected areas worldwide and the severity of side effects, which include dermal lesions and various cancers [1]. As mentioned in section 8.1.2, different metals have different binding affinities for not only chemical groups, but the arrangement or coordination of those chemical groups as well. Since arsenic toxicity occurs in a similar manner to other metals (substitution in proteins, disruption of function) we can use this to design a chelator to selectively bind the As^{3+} ion. This final section describes the first steps taken to produce such a peptide, as well as considerations for further development of selective molecules.

8.3.1 Peptide Design

Arsenic Binding in Biology

Studies on the metal-binding sites of certain proteins have been conducted in order to better understand the routes and effects of metal toxicity [6, 171,186]. This knowledge has then been leveraged in the design of synthetic molecules to bind metal ions [172–174, 187]. Similarly, arsenic toxicity has been investigated by observing its binding sites in human [7,8,188–191], and animal [192] proteins. The trivalent ion As^{3+} is found to be the more toxic than the pentavalent form [7,190], and As^{3+}-binding sites on proteins share the feature of having two or three thiol (-SH) groups very closely spaced to facilitate coordination [8,188,189,191].

Custom Peptide: CCCC

Based on literature describing arsenic coordinating to thiol groups in proteins, as well as the advice of a consulting collaborator[5] from the University of Copenhagen's Faculty of Life Sciences (KU Life), it was decided to use a short chain molecule with three free thiol groups. This suggestion was modified to fit with our peptide-based chelator methodology, resulting in the peptide sequence Cysteine-Cysteine-Cysteine-Cysteine (CCCC). This sequence was meant to be immobilized on the gold surface via a terminal Cys-residue, and provide three free thiol groups to selectively capture As^{3+}. However, this posed an immediate problem. In CGGH the free thiol was bound to the gold,

[5]Professor Lars Bo Stegeager Hemmingsen, Department of Basic Sciences and Environment/Bioinorganic Chemistry, KU Life

and the rest of the peptide remained free for binding copper, since the nitrogen groups have very low affinity for the gold surface. In the case of CCCC, the As^{3+}-binding site (*i.e.* the thiol groups) also have a very high affinity for the gold surface. Use of the immobilization protocol used for CGGH would result in all four Cys-residues in the CCCC-tetrapeptide being bound to the gold surface, making the peptide unable to bind arsenic ions at all.

A solution was provided by a collaboration with a group in DTU Chemistry[6]. They presented the scheme illustrated in figure 8.10. The CCCC peptide has three of its four thiol groups protected with triphenylmethane (trityl, Trt) groups, leaving only one thiol group free on a terminal Cys residue to be bound to a gold surface. Once the protected peptide is immobilized on the gold the trityl groups can then be removed using trifluoroacetic acid (TFA). This would then leave us with an immobilized peptide with three free, closely-spaced sulfur groups to bind As^{3+} ions.

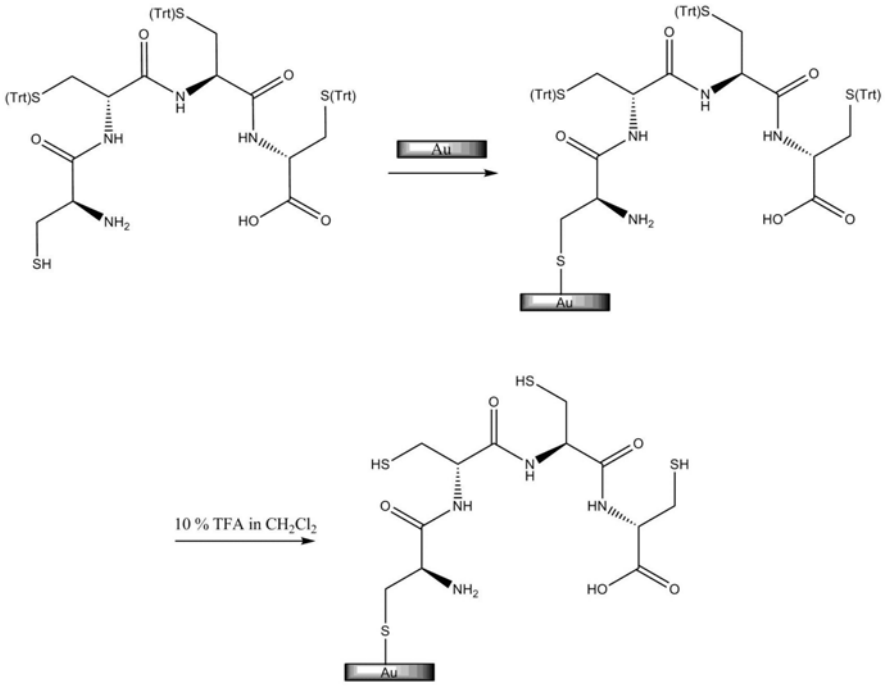

Figure 8.10: The Cys-Cys-Cys-Cys peptide. The scheme presented by Associate Professor Thomas Eiland Nielsen and Dr. Katrine Qvortrup involved protecting the thiol groups that were to be the As^{3+} binding site (*top left*). Once the remaining free terminal thiol was anchored to the gold (*top right*), the protective trityl groups could be removed (*bottom*), leaving a surface bound peptide with three free thiol groups for binding As^{3+} ions.

[6]Associate Professor Thomas Eiland Nielsen, Organic Chemistry and Chemical Biology, and Postdoctoral Fellow Katrine Qvortrup

8.3.2 Discussion

The CCCC peptide was produced by Katrine Qvortrup at DTU Chemistry and immobilized onto electrodes as advised. A solution of 95% TFA was used to removed the trityl groups as is common practice in organic chemistry. Following the same screening methodology as for the L-Cysteine and CGGH monolayers, the CCCC peptide was subjected to EIS before and after removal of the trityl groups and the addition of As^{3+} ions. The charge transfer resistance (R_{ct}) of the electrode surface dropped significantly after the application of TFA to remove the trityl groups. It was confirmed, by using CGGH as a control, that the TFA solution was not simply removing the peptide from the surface. Thus, the large decrease in charge transfer resistance must be due to the removal of the large trityl groups, which would make the monolayer less dense and increase electron transfer kinetics.

Arsenic (III) ions were applied to the de-protected monolayers, but this resulted in no change in charge transfer resistance. X-ray photoelectron spectroscopy revealed that all sulfur atoms in the monolayer were bound to gold after trityl-group removal, *i.e.* there were no free thiols for As^{3+} ions to bind. Upon removal of the trityl groups the SH ligands must have become attached to the gold surface where they remained thereafter. These results led us to the conclusion that, while suitable in the case of CGGH, this simplified, all-in-one peptide technique may not be amenable to all metal ions.

8.3.3 Outlook: Surface-Bound Chelation

Clearly constructing a new and highly-selective capture molecule for As^{3+} is not as simple as stitching together four amino acids. The main fault with applying the methodology above was the fact that both the immobilization surface and the target ion have high affinities for thiols. There are two solutions to this problem. One possibility is the use of a different electrode material that does not have an affinity for thiols, such as graphite. The second solution involves separating the thiol-rich As^{3+} binding site from the gold surface [193]. While this will most likely result in a more complex two-stage functionalization protocol (compared to the CGGH peptide) it will remove the problem of the receptor binding to the substrate before it can bind the analyte.

While peptides offer flexibility and modularity in design, they may not provide the desired selectivity in certain cases. Crown ethers are cyclic molecules which can be tailored in size, as well as type and number of functional groups, thereby making them highly-selective receptors for metal ions [129,194]. By controlling not only what chemical groups are present but

also where they are placed, one could design a molecule that could discriminate ions with similar chemical affinities by size, *i.e.* the metal ion would have to match with the ligands present, the coordinating structure, and the atomic radius to correctly bind with the crown ether. Further development of ion-selective monolayers would greatly benefit from exploring crown ethers, especially if performed in collaboration with an expert in the field[7].

[7]Lars Bo Stegeager Hemmingsen from KU Life, who also suggested crown ethers for such a purpose during one meeting, is one such expert.

Part IV

The ECC Platform

Chapter 9

Design & Fabrication

With an ability to reliably clean gold and having identified functional layers for capturing metal ions we turn to the development of the platform itself. As mentioned in chapter 4 several groups have built cantilever setups for conducting electrochemical cantilever measurements, but such a system did not exist at DTU Nanotech. The electrochemical-cantilever systems reported in literature are typically composed of large, discrete components, and sealed into a liquid cell using wax or epoxy, and many have electrical connection to only one cantilever. The difficulty associated with having to make electrical connection to a cantilever inside a sealed cell is obviously quite difficult, especially when coupled with the need for optical access and a fluid flow.

This chapter describes the design and fabrication of an electrochemical-cantilever (ECC) chip and the encapsulating flow cell. The chip was designed to provide individual electrical access to multiple cantilevers in a sealed liquid environment and all working, reference, and counter electrodes were to be integrated into a microchannel on a single chip. Further, since the Nanoprobes lab contained several systems capable of optically measuring static deflection, the flow cell was designed to be compatible with these. Ease of assembly and part replacement were also considered in the design, and it was decided that no glue, epoxy, wax, or other sealing agent would be used. The fabrication process visualized initially was optimized to produce a robust and reproducible chip in a streamlined process[1].

[1]Bachelor students Karl Elkjær and Christoffer Pedersen performed the bulk of the process optimization and were responsible for fabricating several iterations of the flow cell, as well as initial leak and electrical testing. Their contributions to this project were invaluable.

9.1 Design Considerations

9.1.1 The Chip

Several aspects of operation and assembly must be considered which, when taken together, will dictate the form of the final chip design[2]. While these aspects may overlap or be interdependent, their considerations have been divided into the three primary features of the chip: cantilever parameters, chip material, and fluid handling. Several alternative designs and processes were investigated along the way. For clarity only the design and fabrication of the final chip is presented in the main body of this chapter. Notable alternatives investigated are contained in section 9.3.

Cantilever Parameters

The dimensions of the cantilevers will affect the ultimate sensitivity of the device via the spring constant. This is primarily dictated by the thickness and length of the cantilever (see equation 2.1). However, if the cantilever is too sensitive it will be less likely to survive wet processing (*i.e.* wet etching, chemical modification). Typical lengths for silicon [19, 24, 40, 45, 195, 196] and polymer [197, 198] cantilevers used in literature are 300 μm to 500 μm. Since the effects of the fabrication process on yield and the levels of stress to be measured were largely unknown at this point, this range of cantilever lengths was a reasonable starting point.

A second concern regarding cantilever structure is the pitch, or offset between each cantilever in an array. Again, from literature [19, 24, 40, 45, 195–198] the typical pitch is 250 μm. The laser spot size in the systems for which these cantilevers are intended (roughly 50 μm to 100 μm in diameter) will have a bearing on the cantilever pitch as well. Sufficient space must exist between cantilevers to ensure the reflection from only one cantilever is contributing to the signal measured. A pitch of 250 μm was selected since it leaves a space twice as wide as the laser spot between the cantilevers.

Electrode Parameters

Metal electrodes will be fabricated on the top surface of the cantilevers so each one may function as a working electrode. Additionally, so that each cantilever may function as a working electrode (either simultaneously or sequentially) two large area electrodes (200×1000 μm^2 each) were included

[2] As of writing this chip design is being used as a basis for the experiments conducted by Ph.D. student Xueling Quan and Assistant Professor Maria Tenje.

in close proximity to the cantilevers to act as reference and counter electrodes. These were designed to be made of the same material as the working electrodes, with the intention that further design and fabrication iterations would see a Ag/AgCl pseudo-reference electrode integrated[3].

Electrical contact was required from the cantilever electrodes to the potentiostat. From the work in section 5.2.1 simple mechanical contact was known to be a reliable and reproducible way to create a connection, and made switching chips quick and easy. Conductive pastes and epoxies, while capable of forming excellent contact, take significant time to prepare and make the chips difficult to reuse. With simple mechanical contact the chips remain undamaged and free from contaminants, and can then be functionalized again or reused in other ways. Spring-loaded, gold-plated connectors, or "pogo pins" (Mill Max part nr. 0900-0-00-00-00-00-11-0), seen in figure 9.1 were ordered for this purpose. The contact pads for the cantilevers will then be located sufficiently far from the cantilevers ($\sim$ 5 mm) to avoid interfering with the optical-lever interrogation method. Contact pads were chosen to be 1.2×1.2 mm^2 and spaced at a pitch of 2.5 mm, to allow easy access and avoid unwanted contact between adjacent pogo pins. This led to fit a maximum of six cantilever electrodes per chip (see reasons for chip size in the considerations for materials).

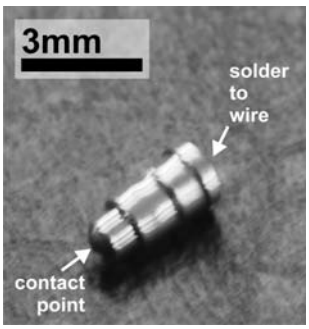

Figure 9.1: A photograph of the spring-loaded, gold-plated connectors, or "pogo pins", used to make electrical connections with the contact pads on the ECC chips. Insulated copper wiring was soldered to one end, to be connected to a potentiostat, while the other end was pressed to the on-chip contact pads. The contact point is spring loaded with $\sim$ 1 mm of travel, which ensures that the gold-plated pin is always making a connection.

[3]Integration of a Ag/AgCl reference electrode was never accomplished in this project for two reasons: (1) the gold reference/counter electrode functioned well enough for the experiments that were performed (*i.e.* no analytical electrochemistry), and (2) using only one type of metal for all electrodes on the chip made the process very simple, and it was decided to not spend further time modifying the process until it was deemed necessary.

Chip Material

First, carrying on from the considerations for cantilever parameters, the material of the cantilever will have a significant effect on its spring constant (see equation 2.1). Second, since these cantilevers will also need to somehow support an applied potential and carry a current the materials electrical conductivity is an issue, as well as the ability to electrically isolate each cantilever from the other. Third, the chemical reactivity of the materials comprising the entire chip must be considered. For example, polymer cantilevers are prone to swelling and drifting in liquid environments [197, 198], and are more susceptible to being dissolved or damaged by solvents, and thus would not be a good choice for our application.

A novel and interesting solution is all-metal cantilever structures [199–203]. To achieve the highest sensitivity one could remove the silicon cantilever and work exclusively with the metal layer, which would still provide electrical conductivity. This avenue was investigated in collaboration with the University of Alberta and the National Institute for Nanotechnology, Canada[4], and results are summarized in section 9.3.1.

Silicon nitride is chemically inert against solvents and many acids [110], and is a standard cantilever material choice. Its high etch resistance means it can also be used as a masking layer, and can thus be used to define the structure of the body chip. Through low-pressure chemical vapor deposition (LPCVD) very uniform layers of silicon nitride can be formed over a wide range of thicknesses ($\sim$nm to $\sim \mu$m), allowing sensitivity to be tuned. Silicon nitride is an electrical insulator, meaning patterned metal electrodes (Au on Cr) will remain electrically isolated from each other. Thus low-stress, silicon-rich silicon nitride was chosen as our cantilever and masking material.

The obvious choice for body chip material is single-crystal silicon. Wafers are readily available, easily machined, and silicon is chemically inert in the anticipated environments. The minimum size for the chips was limited by the need to keep the contact pads far ($\sim$ 5 mm) from the flow channel, and that six cantilevers (with accompanying contact pads and spacing) must be included as well. Wafer size and number of chips per wafer limited the maximum chip size to 15×15 mm^2, arrived at through several iterations of wafer organization. A single wafer could fit 16 of these chips, 5 of each cantilever length, plus one experimental design.

[4]Contacts for this collaboration were Professor David Mitlin (Chemical and Materials Engineering) and Ph.D. student Erik Luber.

Fluid Handling

Due to issues of sealing around the electrical contacts, fluid flow was directed through the chip itself instead of placing the entire chip into the flow, as done by Lang *et al.* [19]. The channel was kept linear for the sake of simplicity, and to reduce corner complications when using a KOH etch [204]. The inlet and outlet were kept far from the cantilevers to reduce chances of turbulence caused by entering or exiting fluid. The size of the chip was basically determined through a combination of cantilever parameters and chip-per-wafer yield, so this size was kept and the inlet and outlet holes were placed accordingly. Cantilevers were placed on one side of the channel and the counter/reference electrodes on the other. The channel in the chip was designed to be completely etched through the wafer to minimize the possibility that any cantilevers would succumb to capillary forces and stick to the bottom of the channel. Encapsulation of the channel is discussed further in section 9.1.2.

The Final Design

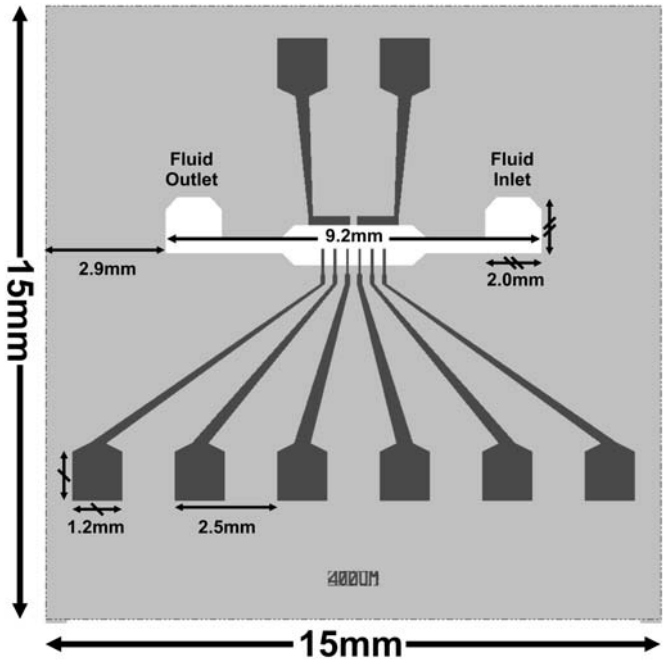

Figure 9.2: A schematic of the final chip design, ECCv2.1n. The chip incorporates six cantilevers and two reference/counter electrodes. Note that while the fluid inlet and outlet are labeled in this illustration, both holes in the chip may act as either inlet or outlet. (Color scheme: light gray = silicon nitride, dark gray = metal)

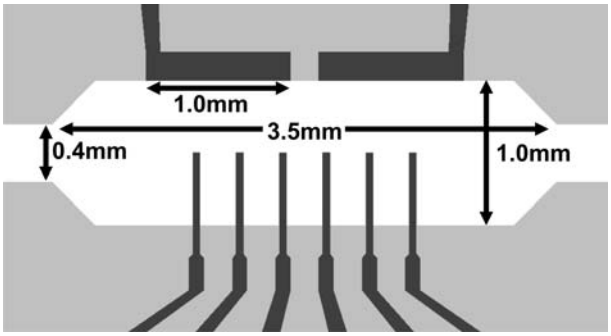

Figure 9.3: A schematic of the cantilevers in the channel region, a close-up from figure 9.2. The channel is 1-mm-wide, 3.5-mm-long, and houses the six cantilevers and two reference/counter electrodes. (Color scheme: light gray = silicon nitride, dark gray = metal)

All of the above considerations have been combined to create the final electrochemical-cantilever chip design, seen in figure 9.2, dubbed ECCv2.1n (version 2.1, using silicon nitride cantilevers). Each chip is 15×15 mm^2, with the six 1.2×1.2 mm^2 cantilever electrode contact pads spread across the width of the chip to allow easy contact without interfering with each other. Two more contact pads above the channel provide a connection to the reference/counter electrodes. The six cantilevers are housed in the 1-mm-wide, 3.5-mm-long section of the channel, seen in figure 9.3. Each chip contains six identical cantilevers, and five chips per wafer contain cantilever lengths of 300, 400, and 500 μm which, if built from 500-nm-thick silicon-rich silicon nitride, were predicted to have spring constants of 18, 8, and 4 mN/m. Each cantilever is 50 μm-wide with a pitch of 250 μm.

9.1.2 The Flow Cell

The flow cell was designed to encapsulate the ECC chip and complete the microfluidic channel by sealing it with a top and bottom. The layout of the chip dictated the dimensions of the internal features of the flow cell, while its outer form was governed by the optical readout systems into which it was to fit. Here we consider two aspects of the flow cell: the general operating principle, and the materials from which it is to be machined.

Cell Configuration

The stacked layer design for the cell was inspired by similar setups created by Dr. Nadine Noeth [205], and Marco Grünefled [206] during their thesis projects. Through stacking, a series of planar geometries were used to create a three-dimensional flow path leading into the cell (via tubing), to the fluid

inlet on the chip, through the channel past the cantilevers, to the fluid outlet on the chip, visualized in figure 9.4. The fluid enters and exits the chip from the back side, *i.e.* the bottom of the cell. This configuration allowed all fluid handling to be done on the back side of the chip, leaving the front unobstructed for cantilever interrogation by the optical lever method.

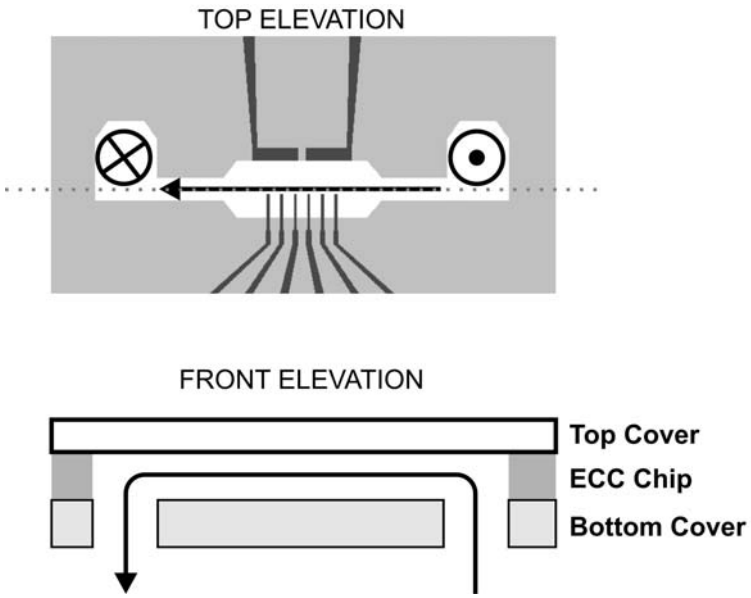

Figure 9.4: A diagram illustrating the path of fluid flow in the ECC chip and flow cell. It was decided to clamp the chip between several layers for sealing. Fluid flows up from under the chip into the inlet, then across the cantilevers to the outlet, where it flows down and out of the cell. The "front elevation" is a cross-sectional view taken at the gray dotted line in the "top elevation".

While the previously cited flow cells were held together by nuts and bolts, the flow cell in this work was held together by metal spring clips. These could be set to a certain optimized pressure and left at this setting. This allowed less time to be spent fastening and unfastening nuts to mount and dismount chips, and less time spent fastening nuts to the correct pressure for proper sealing.

Materials

In a similar fashion to the previous flow cells constructed at DTU Nanotech [205, 206] the materials of choice were poly(methyl methacrylate) (PMMA) and poly(dimethylsiloxane) (PDMS). Both materials are chemically inert enough for the solutions that will be passed through the cell, and

both can be easily machined via an in-house laser cutting system. Sealing between the PMMA and ECC chip was accomplished by PDMS gaskets, which are soft enough to deform under the applied pressure and create an airtight seal [207, 208]. Further, sealing the system with PDMS gaskets and pressure applied by spring clips meant that no epoxy at all was used in the system. Finally, it was predicted that, due to a propensity to scratching and scuffing, PMMA would be a poor choice of optical window. Thus, the section of PMMA over the cantilevers was replaced with a pyrex window.

9.2 Fabrication

9.2.1 ECC Chip Fabrication

A detailed process flow with parameters is available in appendix B. The fabrication started with a clean 100 mm (100) single crystal silicon wafer, 375 μm thick (doping was unimportant). A low-pressure chemical vapor deposition (LPCVD) furnace (Tempress LPCVD nitride furnace) was used to create a 515-nm-thick (verified by a Filmtek elipsometer) silicon-rich silicon nitride thin film on both sides of the substrate. Using standard photolithography techniques (Karl Süss aligner, AZ5214E dual-tone resist, 2.2-μm-thick) the first mask (figure 9.5(a)) was used to define the cantilevers and the body chip on the top side of the wafer. This pattern is then reactive ion etched (RIE, STS Cluster system) through the entire depth of the silicon nitride to reach the substrate (figure 9.5(b)). A similar mask (minus cantilevers) is used to pattern the channel and body chip on the wafer back side (figure 9.6(a)) using the same photolithography, while the same etch is used to remove the desired nitride from the back side (figure 9.6(b)).

A third photolithography step was used to create the pattern for the metal electrodes (figure 9.7(a)). The pattern was created as holes on top of the nitride, into which the metal layer was electron-beam evaporated (Wordentec QCL 800). A 20 nm Au layer was deposited on top of a 2 nm Cr adhesion layer, followed by a 20 minutes in acetone with sonication to remove the resist, leaving behind the patterned electrode layer (figure 9.7(b)).

The final step in the fabrication process is the removal of the silicon substrate to release the cantilevers and create the channel. The wafer was placed in heated potassium hydroxide (KOH, 500 g/l, 80 °C) for 3 hours to etch completely through the wafer from both sides (figure 9.8(b)). Since the channel is opened by an anisotropic KOH etch [209, 210] the edges of the channel must be properly aligned not only to each other on the front and back sides, but to the crystal lattice as well. The chip bodies were released as well during the KOH processing, but were held in place by 500×500 μm^2 pieces

of silicon at both bottom corners, which can be easily broken to pull single chips out of a wafer.

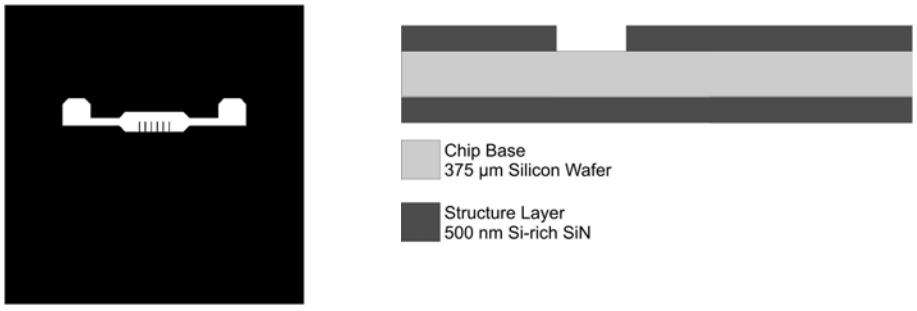

(a) (b)

Figure 9.5: After LPCVD deposition of the silicon-rich silicon nitride, the cantilevers and channel are defined by a mask (a) and reactive ion etched (b).

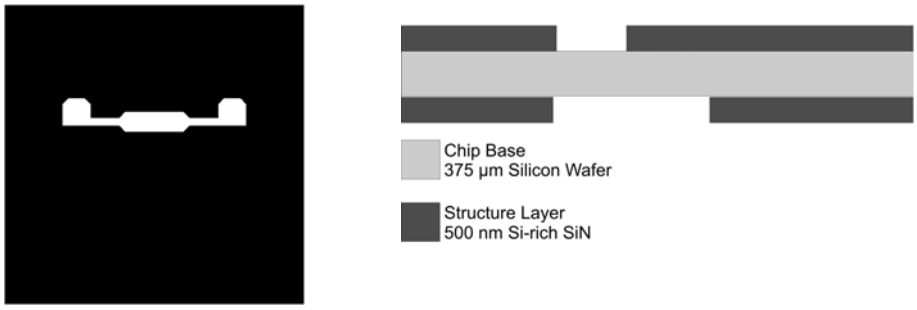

(a) (b)

Figure 9.6: The channel must also be defined on the back side of the wafer by a mask (a) and etched (b) in the same way as figure 9.5.

Following the KOH etch the wafers were rinsed in still, fresh deionized water (four baths, 5 minutes each). The wafers were then placed in 95% ethanol briefly ($<$ 1 minute) and set in a 120 °C oven to quickly evaporate the solvent. The fabricated cantilevers, with the dimensions and material parameters as described above in this section, emerged from this fabrication process with nearly 100% yield, *i.e.* all cantilevers on all chips are free, released, and standing.

The finished chip is shown in figure 9.9. The contact pads to the six cantilever electrodes and two contact pads are clearly visible at the bottom and top of the photograph (figure 9.9(a)), respectively. Wires lead from the

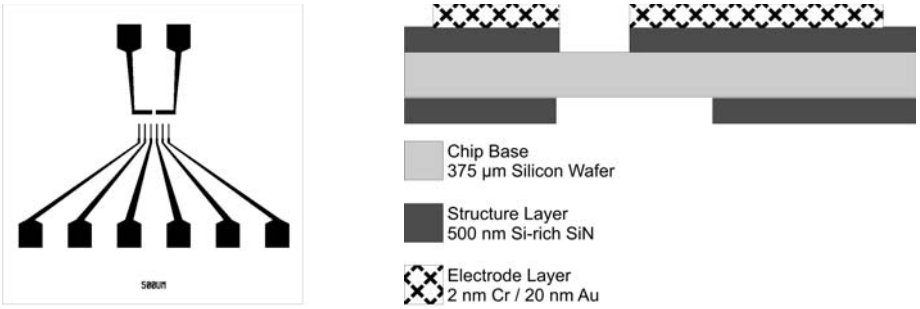

(a) (b)

Figure 9.7: The electrodes and contact pads (a) are patterned in resist, with an electron beam evaporation being performed to deposit the metal layer (b).

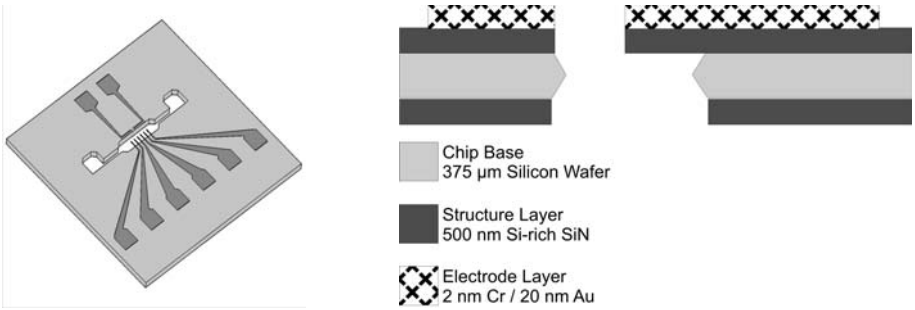

(a) (b)

Figure 9.8: The silicon substrate is removed from beneath the cantilevers using an anisotropic KOH wet etch to form the finished ECC chip ((a) illustration, and (b) process flow view).

contact pads along the chip surface to the electrodes at the channel edge, which can been seen more clearly in the SEM image in figure 9.9(b).

Cantilever Thickness Optimization

The thickness of silicon nitride for the final chips was decided to be 515 nm after a brief optimization. A number of different thicknesses of nitride were tested for yield. Chips will be used rapidly, and time to return to the cleanroom and fabricate new batches must be taken from time in the lab running tests. Thus, the nitride thickness that would deliver the highest yield was sought out.

Silicon-rich LPCVD silicon nitride was deposited on one wafer each at thicknesses of 120 nm, 247 nm, and 515 nm, while 59 nm stoichiometric sili-

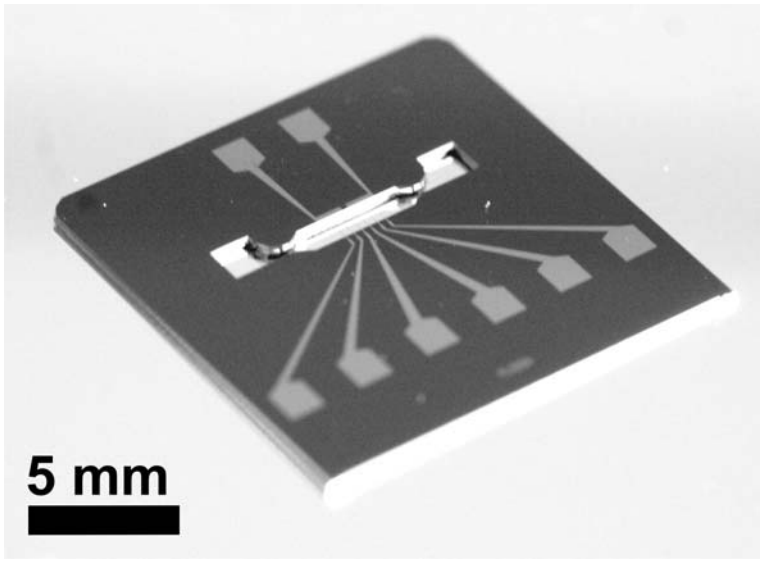

(a)

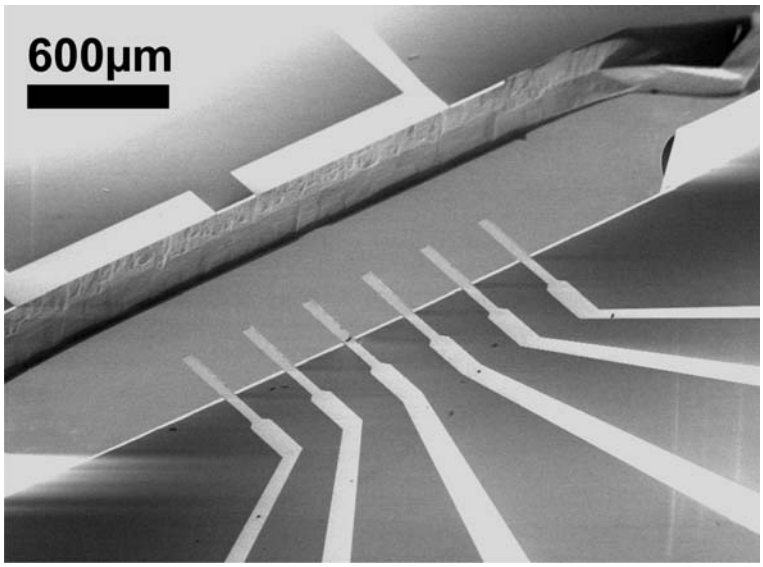

(b)

Figure 9.9: The finished electrochemical-cantilever chip. (a) In this photograph the contact pads for the six cantilever electrodes (*bottom*) and two reference/counter electrodes (*top*) are clearly visible, with wires leading to their respective electrodes on the channel edge. (b) A close-up SEM image of the channel region showing the metalized cantilevers (*bottom*) and reference/counter electrodes (*top*).

con nitride was deposited on yet another wafer. Cantilevers were fabricated using the previously described process in section 9.2, with the one exception of skipping the electrode patterning or deposition steps. The plain silicon nitride cantilevers were released and dried in the same manner as described, then inspected under an optical microscope. Each wafer had 5 chips of each cantilever length (300, 400, or 500 μm) and each chip had 6 cantilevers, totaling 30 cantilevers per length per wafer. The results of this experiment are interpreted in table 9.1.

Table 9.1: Values of cantilever spring constants (calculated from cantilever length and nitride thickness) used in the release yield experiment. Values are given in units of mN/m.

Cantilever	Nitride Thickness		
Length	102 nm	247 nm	515 nm
300 μm	0.14	**2.02**	**18.3**
400 μm	0.06	**0.85**	**7.74**
500 μm	0.03	0.44	**3.96**

Gray values: yield of 10% or less.

Bold values: yield of 90% or greater.

Table 9.1 presents not the yields, but rather the values of the spring constants of each type of cantilever tested, then identifies the approximate yield observed for a given type. First, it should be noted that none of the cantilevers fabricated from 59-nm-thick stoichiometric silicon nitride could be released. In this table of spring constants, gray values indicate cantilever types that showed a release yield of 10% or less, while bold values indicate cantilevers that had a yield of 90% or more. An important rule-of-thumb can be generated from this table: cantilevers with a spring constant of $k \geq 0.85$ mN/m can be easily and reliably released using this process and are very likely to survive repeated wet processing afterwards (*e.g.* wet chemical functionalization). Since a number of wafers with 515-nm-thick nitride had already been produced and were known to release well, this thickness was kept for the duration of the project.

9.2.2 Flow Cell Fabrication

Figure 9.10 presents a profile schematic of the flow cell assembly. Two PMMA plates clamp PDMS sealing gaskets and a pyrex window to form the flow cell. Openings beneath the cantilevers provide and inlet and outlet

for fluid flow, while the optical lever method can be applied through the pyrex window above the cantilevers to monitor deflection. Additional openings in the top PMMA plate (to the left of the pyrex window) provide access for the pogo pins to make electrical connections. Appendix C contains the engineering drawings with dimensions for all parts of the flow cell.

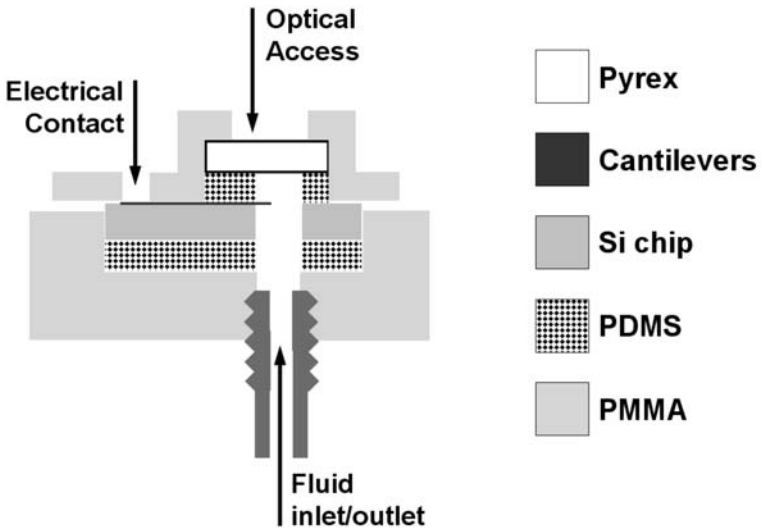

Figure 9.10: A profile schematic of the flow cell assembly. The flow cell is comprised of two PMMA plates clamped together around the ECC chip, with PDMS sealing gaskets between and a pyrex window for passage of the interrogating laser. Access points for fluid flow and electrical access are labeled.

Both the top and bottom PMMA plates were laser machined using a computer controlled CO_2 laser marking system (48-5S Duo Lase carbon dioxide laser, SYNRAD Inc., USA, with a FH/Fenix 200 mm writing head). The PMMA top plate (figure 9.11) is made from a piece of 1.5-mm-thick PMMA, laser cut to 36×39 mm^2. The central hole and recess are created by ablating the area in successive passes of the laser. It was found that allowing a cooling time of 20 to 30 seconds between each ablation pass resulted in a more uniform etch depth and prevented PMMA melting and deformation due to heat build-up. All circular holes were marked using the laser system, and then cut to dimension using the appropriate mechanical drill bit. The rectangular recesses on either side of the center hole were created for alignment purposes. When the flow cell was assembled each recess would fit over the corresponding mesa structure on the bottom plate to (figure 9.12) lock both PMMA components together.

The bottom plate (figure 9.12) was created in a similar fashion from an 8-mm-thick piece of PMMA, 36×50 mm^2. Both the large step and the

center recess were created by the same laser ablation technique as the top plate, while the holes were marked and drilled accordingly. The center recess, 16×16 mm^2, aligns the ECC chip to the fluid inlet and outlet, as well as to the top plate. The mesa structures on either side of the central recess match with the rectangular recesses on the top plate to lock the two components together. The two holes in the central recess act as fluid inlet and outlets and are drilled and threaded to accept fluidic coupling screws (MINSTAC Fitting, The Lee Company, USA) connected to fluidic tubing (FEP NAT 1520) [205].

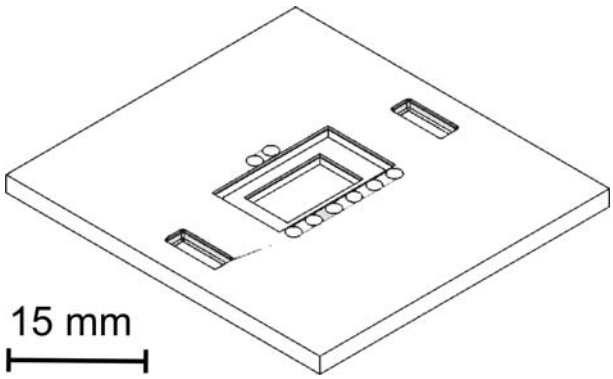

Figure 9.11: A sketch of the PMMA top plate, shown upside-down from its appearance in figure 9.10. The recess in the center holds the pyrex window in place, through which the laser passes to reach the cantilevers. Holes in the plate above and below the pyrex recess allow the pogo pins to reach the electrode contact pads. The small recesses to the right and left of the central hole fit over the protruding mesas on the PMMA bottom plate (in figure 9.12)for precise alignment.

The optical window (figure 9.13, left) was cut to dimension from a 400-μm-thick pyrex wafer (Disco Dicing Saw), while 300-μm-thick spin-coated PDMS layer was laser cut into the top (figure 9.13, top) and bottom (figure 9.13, right) gaskets. The PDMS top gasket seals the pyrex window to the ECC chip (figure 9.13, bottom), while the bottom gasket forms the seal between the chip and the PMMA bottom plate.

Figure 9.14 presents the final assembled flow cell. Figure 9.14(a) shows the assembly order of the components described previously, while figure 9.14(b) presents a top and side photograph of the final assembled cell as it was used. The spring clips applying sealing pressure to the system can be seen in the top photograph, while the fluidic tubing entering the PMMA bottom plate is visible in the bottom photograph. Testing of this system is presented in chapter 10.

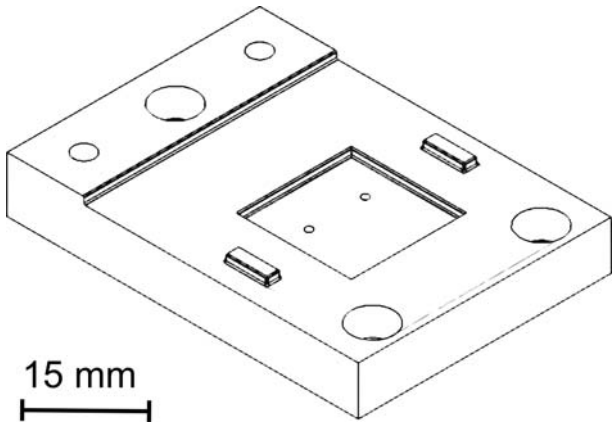

Figure 9.12: A sketch of the PMMA bottom plate. The recess in the center is meant to hold the ECC chip, with a PDMS gasket in between, to assist in aligning to the fluid inlet and outlet (the two holes in the central recess). The two mesas on either side of the central recess fit into the similarly shaped pits on the PMMA top plate for precise alignment of the two pieces. The two smaller holes at the top of the plate host the spring clips to hold the system together, while the three larger holes anchor the bottom plate to an additional mounting plate, which attaches to the measurement stages.

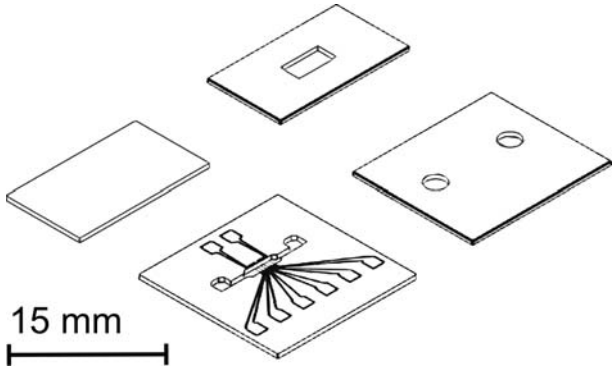

Figure 9.13: Sketches of the PDMS top gasket (*top*), the PDMS bottom gasket (*right*), the pyrex window (*left*), and the ECC chip (*bottom*), shown together for size comparison.

9.3 Alternative Designs

A number design alternatives were investigated during the course of this phase of the project. Two of the more interesting investigations are highlighted below.

9.3.1 Full-Metal Cantilevers

Theoretically, the highest sensitivity for stress sensing would be achieved with the thinnest possible cantilever. To maximize sensitivity an all-metal

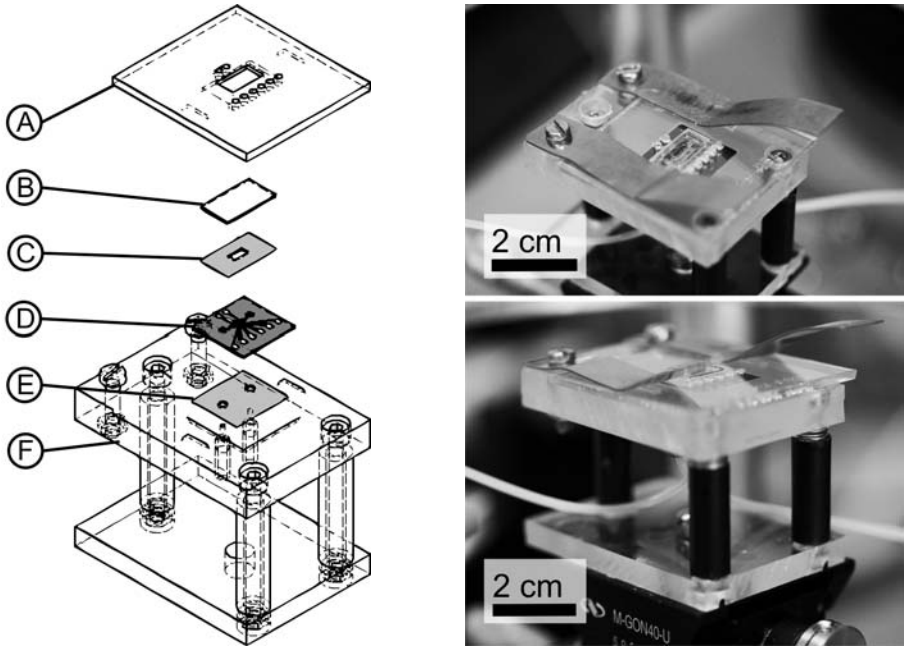

(a) (b)

Figure 9.14: (a) An exploded schematic of the assembly order for the flow cell: A - PMMA top plate, B - pyrex window, C - PDMS top gasket, D - ECC chip, E - PDMS bottom gasket, F - PMMA bottom plate. (b) Photos of the finished and assembled flow cell from the top and side. Notice the fluidic tubing entering the flow cell in the bottom photograph.

cantilever was considered. Through the use of co-sputtered alloys, the properties of the metal could be tuned [199] to achieve an optimized material for this application. The composition of the alloy across the thickness of the cantilever could be adjusted so only the top surface could be chemically functionalized (*e.g.* using thiol chemistry) which would still allow a stress differential to form, causing bending.

Surface Modification

Through our collaboration with colleagues at the University of Alberta the alloy Au-Hf was investigated as a cantilever material. Table 9.2 shows the results of a test of chemical functionalizability. Previous work from our collaborators indicated that, while the bulk of the film possessed a composition comparable to the nominal, the surface was prone to reorganization and migration of atoms. This resulted in a different surface composition, and thus would change how thiols would bind. Eight samples, two of each compo-

sition, were cleaned (using protocol from section 7.2.1) and modified by incubation in 5 mM 1,6-hexanedithiol (95% ethanol solvent) for 16 hours. X-ray photoelectron spectroscopy was used to measure the atomic percent (a.t.%) concentration of surface elements. Samples 1 and 2 are pure gold, and served as the baseline for the test. The a.t.% of sulfur on the surface was used to determine if the thiol molecules had been bound or not. As table 9.2 shows, samples 3 and 4 (90%Au-10%Hf) appeared to host thiol chemistry as well as the pure gold, while samples 5 through 8 were deemed devoid of thiol groups. This indicated that the cantilever should be designed such that the top surface was 90% to 100% Au, with the bottom surface 50% or more Hf to ensure only the top is functionalized to create a stress differential.

Table 9.2: Atomic composition of the Au-Hf alloy surface, and the amount of thiols bound to the surface, determined by XPS.

	Nominal Composition		Measured a.t.% Composition				
Sample	% Au	% Hf	Au	Hf	S	C	O
1	100	0	43.5	0	7.1	47.4	2.0
2	100	0	45.1	0	7.2	45.6	2.1
3	90	10	38.9	2.0	7.4	48.7	3.0
4	90	10	37.7	1.9	7.0	50.0	3.4
5	50	50	6.0	20.0	0	34.1	39.9
6	50	50	0*	22.2	0	36.4	41.4
7	0	100	0	22.8	0	34.9	42.3
8	0	100	0	22.4	0	36.3	41.3

*Indicates values of low confidence.

Fabrication Issues

The back side mask of the ECC process (figure 9.6(a)) was applied to both sides of a nitride wafer, resulting in the channel being defined on the wafer front and back, without cantilevers. A suitable Au-Hf alloy, chosen by our University of Alberta collaborators, was patterned using the electrode mask (figure 9.7(a)) to create a wafer of 200-nm-thick pure metal cantilevers. The cantilevers were then released using the same etching and drying process as the silicon nitride cantilevers from section 9.2.1, the result of which is shown in figure 9.15. While we were assured that there was no net stress gradient

in the metal film, these binary metallic alloys are known to be meta-stable and to be affected by heat. Unfortunately the 3 hours in the KOH bath to release plus the 2-minute oven drying step proved to be too much for the alloy, causing a stress gradient. These alloys could not be used without radical changes being made to the fabrication process, thus they were abandoned.

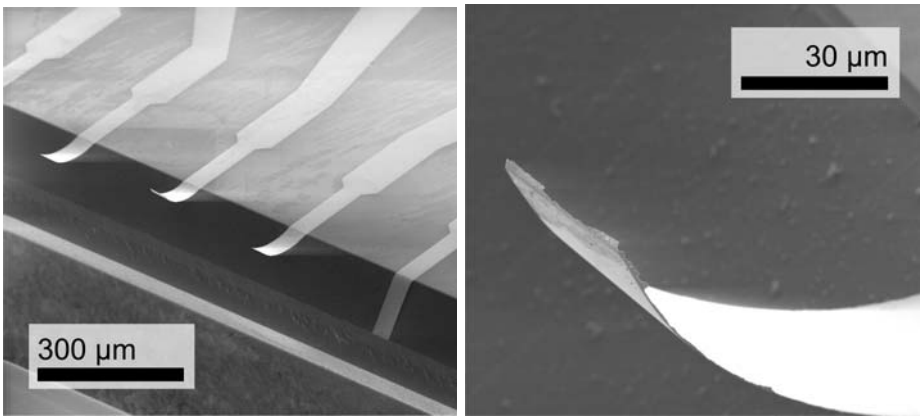

(a) (b)

Figure 9.15: SEM images of pure Au-Hf cantilevers, 200-nm-thick. (a) After the drying process all cantilevers exhibited a severe stress gradient, causing an upwards bending. (b) The sidewalls of the resist pattern became covered with the alloy due to lack of anisotropy in the sputtering process, causing the edges seen in this image.

A second attempt was made at using all-metal cantilevers. Using the same process described above for the Au-Hf alloy cantilevers, 300-nm-thick Au cantilevers were patterned onto the wafer. As shown in figure 9.16 the cantilevers initially seem to have been successfully released. On closer inspection we observe a downward bending across the width of the cantilever due to a strong stress gradient within the gold film. This curvature changes the bending moment of the cantilever, making it more resistant to bending along its length. These cantilevers are unusable for our purposes.

There is one interesting observation to be made from figure 9.16(a). Potassium hydroxide is known to etch along the (111) plane, vertically downward into the (100) plane [210]. When the channel is etched from both front and back sides, the two etch fronts will meet at the center of the wafer. Apparently, after this meeting the KOH etch proceeds to flatten out this point by etching towards the channel edges. This means that, if timed correctly, a channel with vertical sidewalls could be achieved using this etch.

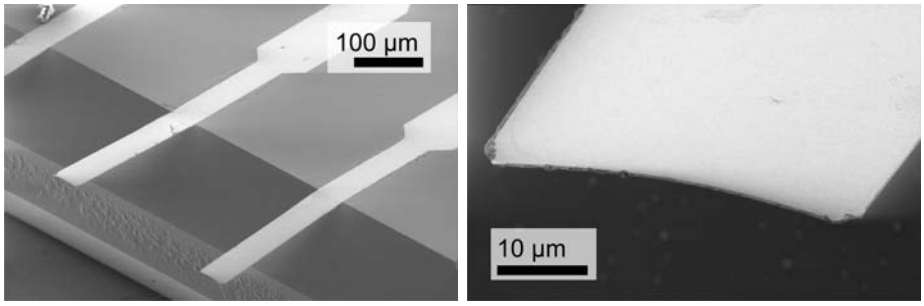

(a) (b)

Figure 9.16: SEM images of pure Au cantilevers, 300-nm-thick. (a) Initial observation shows the cantilevers to be free standing and not curled. (b) However, upon closer inspection we notice a stress gradient in the film causing a downward bending in the cantilevers. The gradient is in fact causing a bending across the width of the cantilever which is aiding in keeping the cantilever straight along its length.

9.3.2 Porous Silicon Etch Processing

The original fabrication process for the ECC chip had incorporated a porous silicon (PS) etch technique [211] to define the channel region. A very thin gold layer was deposited such that it formed dots or small islands rather than a continuous film on a silicon (100) wafer surface. The substrate was then placed in a solution of hydrofluoric acid (40%), hydrogen peroxide (30%), and ethanol (95%) in a 1:1:1 ratio for several hours. The result was the creation of a porous region everywhere the gold dots were in contact with the silicon surface, with the pores leading vertically downward into the silicon, as seen in figure 9.17. Once the PS had been formed it could be removed within minutes in a KOH etch, instead of the hours needed to etch silicon normally. Further, the pores are oriented vertically with respect to the wafer surface, meaning removal of the PS will leave a channel with vertical sidewalls.

Trials of etching time, wafer orientation, and gold dot density led to several conclusions. While the PS can be removed in 5 to 10 minutes in heated KOH, the time taken to create such a porous volume (6 to 8 hours) is far longer than that required to etch through solid Si with KOH ($\sim$ 3 hours). Also, due to the porosity, and the fact that the pores are not exclusively oriented vertically meant that the side walls of the channel after KOH etching were not smooth. Seen in figure 9.17(b) the sidewalls of the channel in which a cantilever has been fabricated are neither vertical nor smooth. This is a stark contrast to the KOH sidewalls seen in figures 9.9(b) and 9.16(a). A variety of other factors, including an inability to find a suitable front side protection layer, PS etch dust formation (a brown grit left on the wafer af-

ter the PS process), and the overall aggressiveness of the solution led to this process being abandoned.

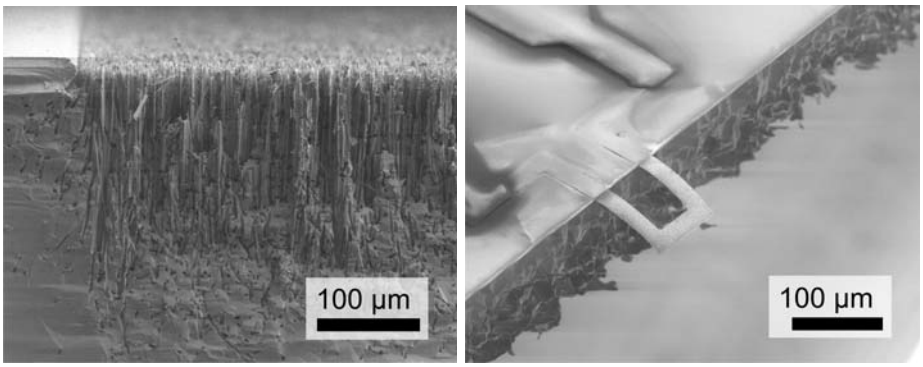

(a) (b)

Figure 9.17: (a) A profile SEM image of a PS etch. The gold dots have catalyzed an etch, creating pores leading vertically downward into the silicon wafer. (b) Pure-Au cantilevers were produced using the PS etch process. Among a number of problems, the channel wall, seen below the cantilever, is not vertical and is quite rough. We concluded that this process would not produce satisfactory devices.

Chapter 10

System Commissioning

The ECC platform, developed in chapter 9, had to be tested before any experiments could be attempted. Protocols were established for sealing and filling the flow cell, and forming reliable electrical connections. The issue of obtaining reliable optical alignment and performance was addressed. These investigations were divided into three aspects: fluid handling, electrical contact, and optical response. This chapter describes the observations made during the commissioning of the platform, and the development of protocols to which they led[1].

10.1 Fluid Handling

Issues of flow cell sealing and filling were addressed as fluid handling aspects. Testing various methods during assembly led to protocols of PDMS treatment, which greatly reduced the occurrence of sealing failure and system leakage.

10.1.1 Sealing Treatment

Following laser cutting the PDMS gaskets were washed briefly in 95% ethanol and then rinsed liberally with Milli-Q water to remove accumulated particulate from the ablation process. Initial trials with the completed system were conducted by simply putting the PDMS gaskets and pyrex components into the flow cell and attempting to pump Milli-Q water through. However, this resulted in the system leaking immediately and severely from the chip/PDMS interfaces. Treatment in a UV Ozone reactor and a corona

[1]Bachelor student Allan Nielsen contributed greatly to the development of the sealing and filling protocol, as well as identified several of the major issues with alignment.

atmospheric plasma discharge was suggested [205, 212], and through repetition and observation of sealing performance a protocol was determined. Further improvements to sealing and reduced drift were obtained by storing the PDMS components in water between uses [205].

All components of the flow cell (ECC chip, PDMS, pyrex) were assembled dry, despite being stored in Milli-Q water. The following protocol was developed iteratively and provides the best sealing of the flow cell.

Sealing Protocol

1. New PDMS and pyrex components were placed in a UV Ozone reactor for 20 minutes per side, then placed into Milli-Q water in a storage container and let to sit for 16 to 20 hours.

2. The PDMS and pyrex components were placed in a corona atmospheric plasma for 60 seconds per side, after drying. Following this treatment the components were ready to be assembled.

3. Upon completion of an experiment the flow cell was disassembled and the PDMS and pyrex components were placed in Milli-Q water when not in use.

4. Subsequent assembly and use of the flow cell was accomplished by repeating steps **2** and **3**.

10.1.2 Flow Cell Operation

The filling procedure of the flow cell had to be done in a specific way to introduce the fewest bubbles into the system. The flow cell was found to seal more completely if all components (ECC chip, PDMS gaskets, PMMA plates, and pyrex window) were assembled dry. Of particular note in the filling protocol is the *in situ* soaking of the PDMS gaskets before actual filling started. The system was connected to a syringe pump (PHD 2000 Infuse/Withdraw syringe pump, Harvard Apparatus, USA) and used exclusively in pulling or "withdraw" mode, where the syringe in the pump holds the waste fluid of the experiment. Having the seals under a negative pressure (having water pulled from the channel rather than forced into it) was found to preserve the seal. Again, this soaking of the PDMS gaskets before fluid pulling was initiated resulted in a drastic reduction of spontaneous sealing failure, observed as air bubbles suddenly originating from inside the channel. The following protocol was adhered to for the majority of the experiments in this thesis.

Filling Protocol

1. The fluidic tubes attached to the PMMA bottom plates were filled up to the floor of the central recess in the bottom plate.
2. The cell components were then assembled.
3. The syringe attached to the fluid outlet was pressed to introduce a small amount of Milli-Q water into the chip channel. This was left for approximately 10 mintues, allowing the PDMS in contact with the fluid to take up water and swell.
4. The outlet syringe was placed in the pump (PHD 2000 Infuse/Withdraw syringe pump, Harvard Apparatus, USA) and set to 50 μl/min.

Of course there were far more issues related to sealing that had to be fine tuned, but these were more a result of incomplete, improperly sized, or damaged components rather than flawed protocol.

10.2 Electrical Connections

10.2.1 Mechanical Contact

The initial configuration for the electrical connections had all eight spring-loaded contact pins (6 for the cantilevers, 2 for the reference/counter electrodes) held in place by heat-cured epoxy, seen in figure 10.1. Contact pins had wires soldered to their back side, and were then pressed through the holes in the PMMA top plate. A heat-curable epoxy was applied to the outside of the top plate, which both held the pins in place and electrically insulated the solder joint, preventing contact between neighboring pins. Though robust, this configuration proved incompatible with flow cell operation. Each spring-loaded pin exhibited a small force on its own, which was insignificant compared to the clamping force for the entire cell. However, placing 6 contact pins in close proximity was able to create enough force to separate the chip from the PDMS, breaking the seal. While it did not occur every time, this PMMA top plate caused system leakage through the PDMS on the cantilever-side of the channel with unacceptable frequency.

Thus, to ensure sealing, the connection method pictured in figure 10.2 was developed. This configuration incorporated two major changes from the previous one. First, the contact pins were no longer held to the PMMA top plate by epoxy. This meant that the force was no longer applied between the PMMA top plate and the chip, which was responsible for having relieved the pressure on the PDMS top gasket, breaking the seal. Second, only the necessary contact pins were to be used at any given time, as opposed to all

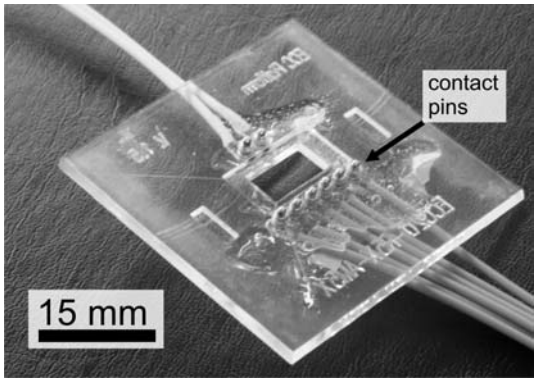

Figure 10.1: The original design for the PMMA top plate included using epoxy to hold in all eight spring-loaded contact pins (6 cantilever, 2 RE/CE). Through testing it was found that the spring force was causing incomplete sealing, leading to leaks. This configuration was abandoned in favor of the one shown in figure 10.2.

eight pins being used. This reduced the force pushing the chip down into the PDMS bottom gasket. As seen in figure 10.2 the pins were still soldered to wires, but then had pressure applied by a modified paper clip. While it may appear crude, this contact method proved highly reliable.

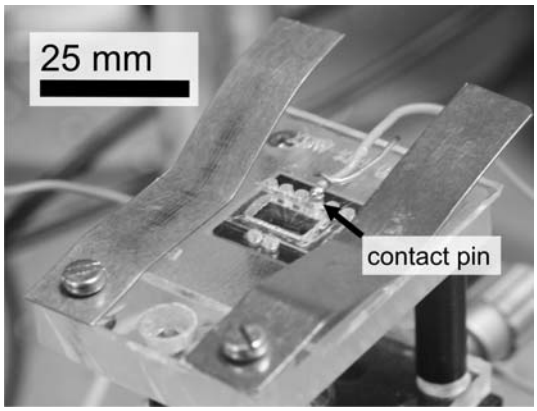

Figure 10.2: A close-up photograph of the spring-loaded contact pins making the electrical connection through the PMMA top plate to the chip. Only those cantilevers being used have a contact pin connected, to prevent wire clutter on the cell surface.

10.2.2 Positive/Negative Connection

Cyclic voltammagrams were run to confirm that the spring-loaded contact pins were making contact. The cell was filled with 10 mM KNO_3 and cycled between the potentials indicated in the figures. One cantilever was connected

as a working electrode while a large area electrode (opposite side of the channel from the cantilevers) was connected as a counter/reference electrode. In the case that one or both of the contact pins was not touching the contact pads we would observe a CV similar to that pictured in figure 10.3(a). Incomplete contact was usually the result of the pins not being sufficiently pressed into the PMMA top plate, or the PMMA top plate or the chip being incorrectly aligned. When aligned correctly, the clipping method seen in figure 10.2 was always effective at making positive contact with the contact pads.

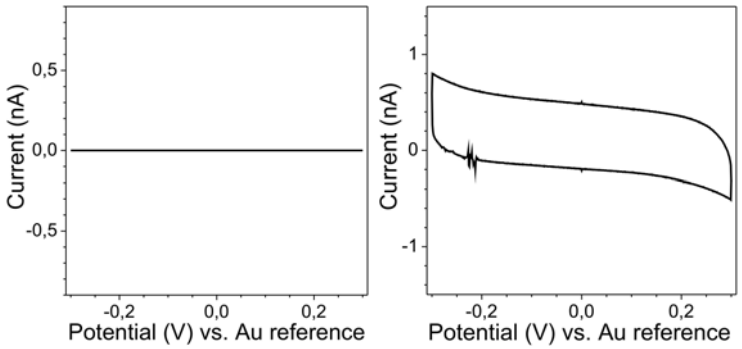

Figure 10.3: Cyclic voltammagrams were used to confirm the electrical connections made to the cantilevers. (a) If the contact pins were not connected properly, or the cantilevers were not in contact with the solution, a zero signal was observed. (b) When performed in a 10 mM KNO_3 solution we observed a signal indicative of a connection, similar to those seen in previous chapters.

10.2.3 Voltammetry Testing

The safe range of potentials had to be determined before these cantilevers could be used for voltammetry. Structural integrity of the metal layer was going to be an issue at high enough potentials since the Cr layer was exposed (even if it was only 2 nm). One cantilever was connected as a working electrode while another acted as a counter/reference electrode. Cyclic voltammetry was conducted with an increasing range, ± 0.5 V and increasing by ± 0.1 V every 10 cycles, in 10 mM KNO_3. At lower potential ranges the cantilevers appearance was normal (figure 10.4(a)) and the CV took on the shape typical of an ionic solution with no redox activity (figure 10.5(a)). However, after repeated cycling at potential ranges above ± 1.6 V the gold surface of the cantilever changed (figure 10.4(b)), and unexpected redox peaks appeared in the CV (figure 10.5(a)). Increasing the range further for more cycles resulted in gas evolution from metal surfaces (seen as bubbles in figure 10.4(c)).

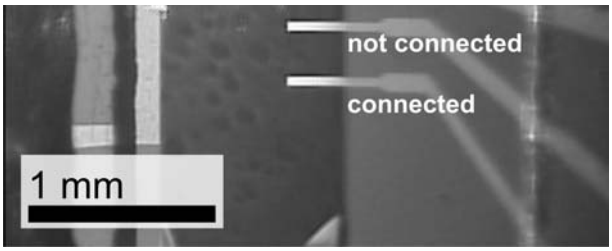

(a)

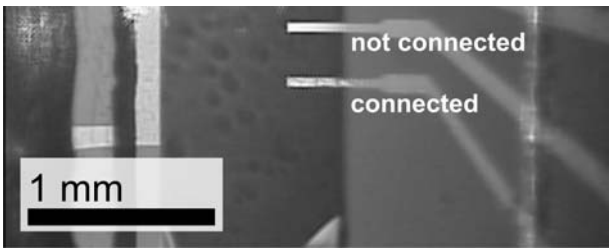

(b)

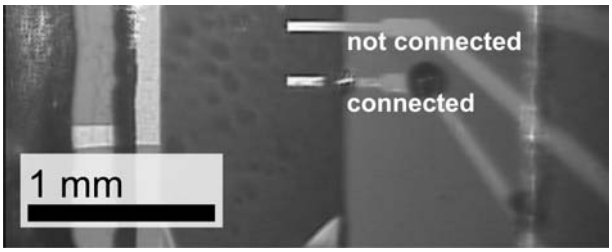

(c)

Figure 10.4: Microscope images of the cantilevers taken during CVs as the potential range was increased to damaging levels. The lower cantilever is connected as a working electrode and has the potential sweeps applied to it, while the upper cantilever is not electrically connected during this test. (a) At lower potential ranges the cantilevers appear normal. (b) At potential ranges in excess of ± 1.6 V irregularities appear on the gold film. (c) Further potential sweeping and increasing the range leads to evolution of gas on the metal surface, seen as dark spots on the lower electrode.

Inspection of the excessively cycled cantilevers in a scanning electron microscope revealed that the electrodes had been severely damaged. Figure 10.6(a) shows a cantilever array in which the first and third cantilevers from the left had been cycled more than 20 times. These cantilevers were still in good operating condition and indistinguishable from those found on a freshly produced chip. However, the cantilevers pictured in figure 10.6(b), subjected to the excessive cycling described above, have had their Cr adhesion layer eroded. The gold layer, which appears unaffected, is no longer attached to

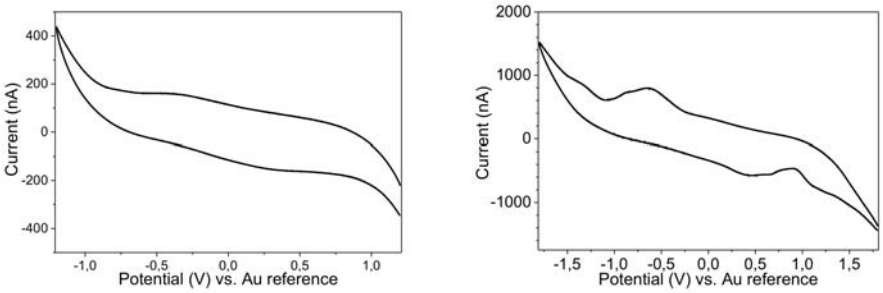

(a) (b)

Figure 10.5: Cyclic voltammagrams conducted in 10 mM KNO_3 to assess the safe range of potentials. (a) At lower potentials the CV appears similar to others taken in ionic electrolytes, with no visible redox activity. (b) At higher potentials, however, repeated cycling causes irregular peaks to emerge, indicating damaging electrochemical activity at the electrodes.

the cantilever and is free to move independently. This is obviously an extremely negative effect on cantilever measurements, thus voltages applied to the cantilever electrodes were kept to ranges of ±1.2 V.

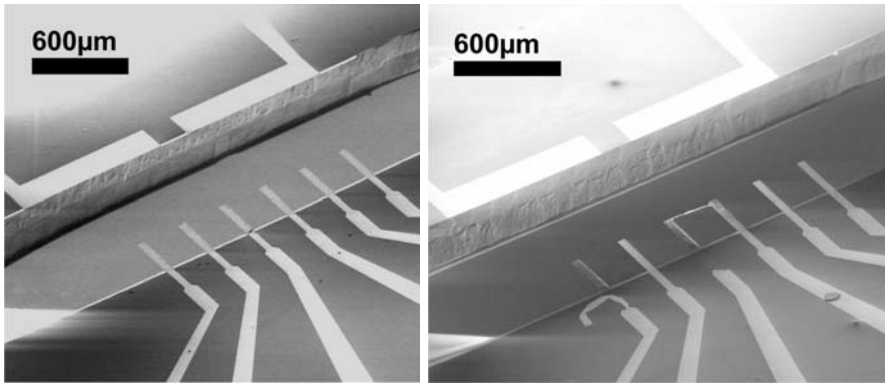

(a) (b)

Figure 10.6: Scanning electron micrographs of cantilever arrays after cyclic voltammetry. (a) Cycling at a potential range of ±1.2 V, even for 20 or 30 cycles, leaves the cantilever electrodes undamaged and virtually indistinguishable from freshly fabricated chips. (b) Cycling at potential ranges in excess of ±1.6 V was shown to completely erode the Cr adhesion layer, delaminating the Au from the cantilever.

10.2.4 Affect of Flow on Voltammetry

The cyclic voltammagram of cantilever electrodes under a flow was briefly observed. Figure 10.7 plots the voltammagrams taken at zero flow (solid line) and 50 μl/min (dotted line). The main feature of note is the diffusion-limited current magnitudes, *i.e.* the plateau regions on either side of the redox peaks. Notice that the CV taken under a flow exhibits a much higher current, similar to that of the microelectrodes of figure 5.3. This is due to a constant supply of fresh reactant and oxidant delivered by the flow and not by diffusion to and from the depletion region near the surface.

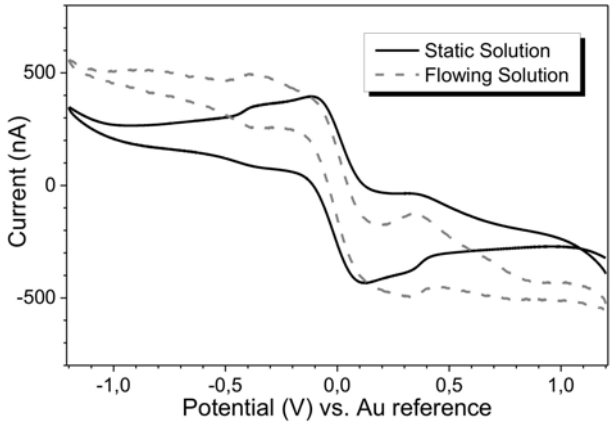

Figure 10.7: Cyclic voltammagrams taken using cantilever electrodes in 5 mM $[Fe(CN)_6]^{3-/4-}$ at zero flow (solid line), and 50 μl/min flow (dotted line). Disregarding other artifacts, the current observed in a flowing solution is larger at the extremities and is less diffusion limited. This is because the flow is constantly delivering fresh species for reduction or oxidation.

10.3 Optical Measurements

10.3.1 Alignment Issues

The NanoNose system seen in figure 10.8, built by Assistant Professor Søren Dohn, was used to acquire all deflection data presented in this thesis[2]. The NanoNose is a dual-laser optical-lever deflection system capable of operating in both static and dynamic mode (only static mode is used in this work). A

[2]The ECC platform was built to be compatible with a number of deflection measurement systems in the Nanoprobes lab. Initially a Polytec MSA-500 doppler vibrometer was considered for use. However, after significant effort, it was found that the system was incapable of measuring static deflection in real-time.

ray-tracing calculation[3] revealed that vertical z deflection of the cantilever (at the laser spot) was approximately $z = (0.109)l$ nm, where l is the position of the laser spot relative to the cantilever base in μm.

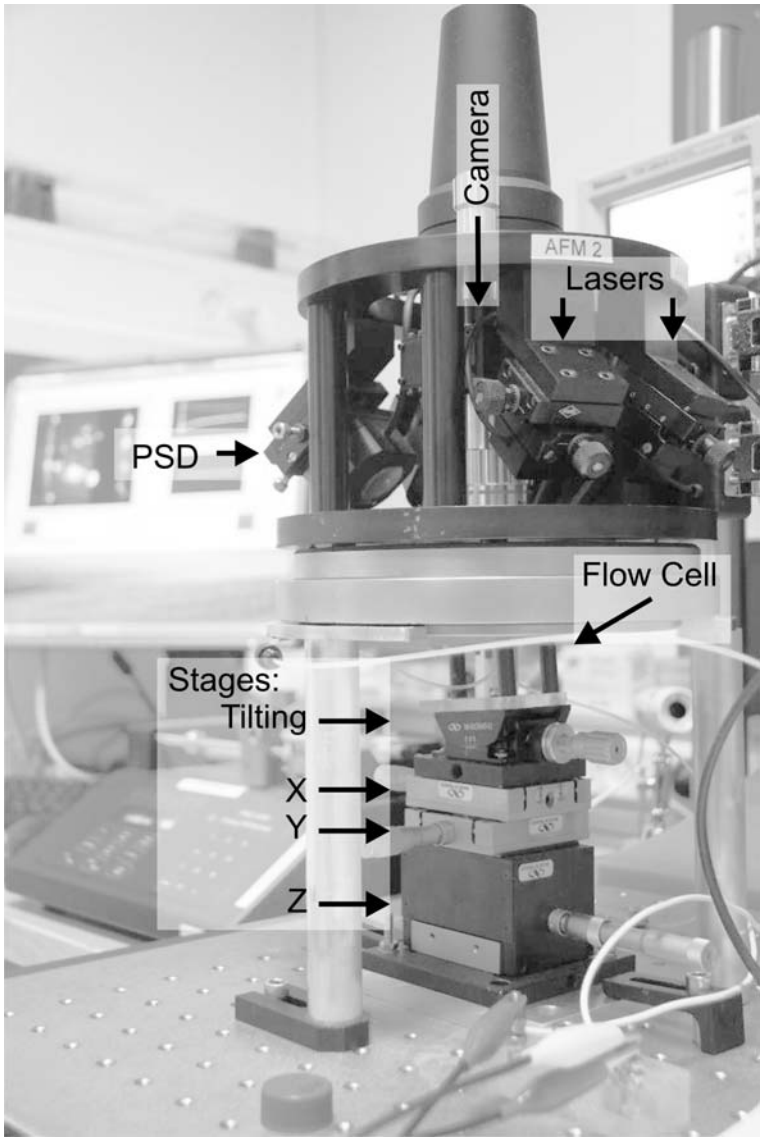

Figure 10.8: A labeled photograph of the NanoNose dual-laser cantilever deflection measurement setup, designed by Søren Dohn. All real-time deflection measurements made in the flow cell were taken with this system.

[3]Performed by bachelor student Allan S. Nielsen, taking into account the refraction of the pyrex and solution [213].

While the NanoNose took all cantilever data presented in this work, it was not originally intended to measure deflection in a liquid environment. The multiple layers of which the flow cell was composed created multiple spots when a laser was introduced. Since observation of the laser spot through a camera was the only method of aligning it to the cantilever, the location of the correct laser spot needed to be determined. By assembling and observing the flow cell in stages (first the chip, then with the PDMS, then glass, then PMMA) we determined the origin of these spots. With respect to figure 10.9, the laser enters from image right directed downwards and into the image (into the z-plane). It passes through the pyrex window (towards image left, and into the image) and creating a diffuse spot (figure 10.9(a)) as it goes. The laser beam reflects off the cantilever's gold surface creating the brightest spot (figure 10.9(b)) in the image. The beam continues upwards (out of the image) and toward image left, exiting the flow cell through the pyrex window and creating a second diffuse spot (figure 10.9(c)), and continues towards the position sensitive detector (PSD) labeled in figure 10.8.

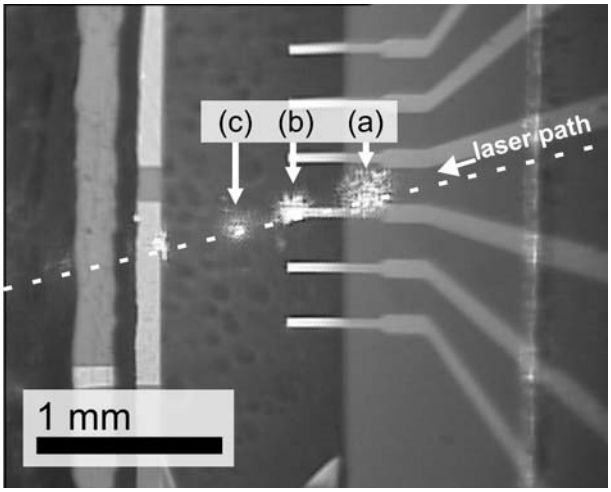

Figure 10.9: A microscope image of the cantilever array with the laser properly aligned to cantilever 3 (the third cantilever from the bottom). The visible laser spots are caused by (a) the laser passing through pyrex, into the fluid, (b) reflecting off the cantilever, and (c) passing through pyrex, out of the fluid.

To rule out the spots that were not cantilever reflections, suspect spots were aligned to the tip of the cantilever. Then the stage holding the flow cell was moved so the cantilever moved out from under the spot. If the laser signal on the PSD dropped significantly it meant the spot was most likely a reflection off the cantilever. Lastly, the PDMS top gasket was found to interfere with the incoming laser path, and thus had to be cut back to expose metal as far back as 1 mm from the channel edge. While this obviously affected the electrode area and the current observed, it was the only solution

in the present configuration that could yield a clear deflection signal.

10.3.2 Bypassing Glass Reflection

The planes of all components in the cell were designed to be parallel. However, as shown in figure 10.10(a) and as experimentally observed, this meant that the reflections from the cantilever and pyrex could occupy the same space on the PSD. Since the signal received from the PSD was a summation of the light on its surface the interpreted cantilever motion was highly dependent on the intensity, size, and position of the pyrex reflection. The solution was to tilt the pyrex window relative to the ECC chip. This was accomplished by placing small PDMS spacers as shown in figure 10.10(b). This was found to apply enough of a tilt relative to the ECC chip to separate the two spots on the detector such that the pyrex reflection could be easily masked, thus removing its contribution to the signal.

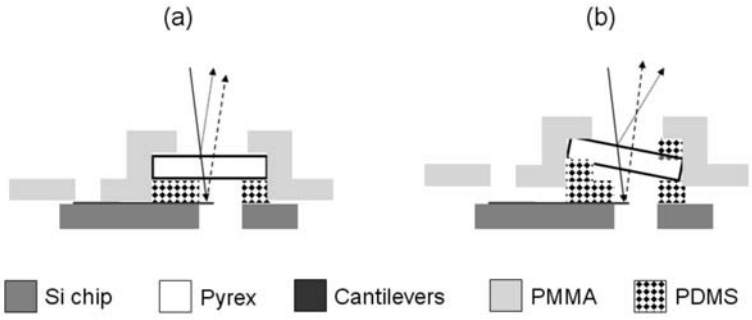

Figure 10.10: A schematic of the pyrex window tilted relative to the cantilevers, done to ensure the laser spots from the cantilever and the front side pyrex reflection were not incident upon the same spot on the PSD. (a) The original assembly of the PDMS top gasket and pyrex window. (b) Two pieces of PDMS were placed accordingly to tilt the pyrex relative to the ECC chip surface. This addition did not affect sealing and separated the pyrex and cantilever reflections enough such that the pyrex reflection could be easily masked.

10.3.3 Noise Level

Once we had the laser aligned and were confident in the signals we could measure, the noise level of the system needed to be addressed. Further, since measurements were to be conducted in a flow, the effects of flow on cantilever deflection also required investigation. A clean ECC chip was mounted in the flow cell and Milli-Q water was pumped in. The system was left under a flow of 30 μl/min for 30 minutes, after which the drift due to PDMS hydration

has ceased[4]. The flow to be measured was set on the syringe pump and a 5 minute section of stable flow was recorded, the results of which are presented in figure 10.11. The noise in the signal remained relatively constant ($\sim$ 0.07 V peak-to-peak) as the flow speed was increased from a standstill (0 μl/min, signal (a) in figure 10.11) to 50 μl/min (signal (d) in figure 10.11). The signal noise became noticeably larger ($\sim$ 0.12 V peak-to-peak) at speeds higher than 75 μl/min (signal (e) in figure 10.11). Additionally, as the flow speed was increased further larger, lower frequency instabilities were noticed (100 μl/min, signal (f) in figure 10.11). Thus, a maximum speed of 50 μl/min was chosen for all cantilever measurements conducted under a flow, as this is the highest speed that could be used before observing an increase in noise.

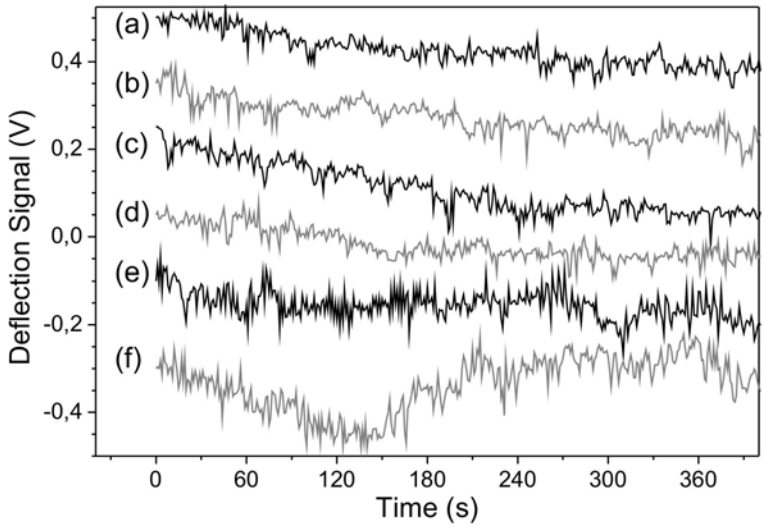

Figure 10.11: Measured deflection of a cantilever (500 μm long) in a flow of Milli-Q for different pump speeds: (a) 0 μl/min, (b) 10 μl/min, (c) 25 μl/min, (d) 50 μl/min, (e) 75 μl/min, (f) 100 μl/min. The syringe pump was used in liquid-pulling or "refill" mode. The noise seen by the NanoNose system is relatively constant from 0 to 50 μl/min, but becomes noticeably worse at speeds of 75 μl/min or higher.

The low-speed noise observed at flows of less than 50 μl/min was believed to be inherent in the system. That is, the noise is due to everything else *except* the cantilevers and flow, *e.g.* acoustic noise in the room or electrical noise in the PSD or other electrical components in the signal acquisition path. Electrical noise is the most likely explanation since the noise was not observed to vary as the level of human activity in the room changed. Finally, the noise in the signal measured on the substrate, or a solid silicon

[4]This stabilization time was only 30 minutes if the PDMS was kept in water overnight. If PDMS was stored dry the stabilization time was 1 to 2 hours, sometimes longer. This is why the PDMS was stored in Milli-Q water when not in use.

wafer (*i.e.* no free hanging cantilevers) was indistinguishable from the signal obtained in figure 10.11(a) at a flow of 0 μl/min.

10.4 Summary

Following platform fabrication several aspects of the device operation had to be investigated before any experiments could be conducted and any useful data could be collected. A protocol for sealing and filling the device was developed, with PDMS treatment as the focus. Successful electrical connection was made by simplifying the contact pin mounting and eliminating epoxy. Electrical contact was confirmed by acquiring voltammagrams in potassium nitrate and $[Fe(CN)_6]^{3-/4-}$solutions. Cycling the cantilever potential above values of $\pm$1.6 V resulted in oxidation of the Cr adhesion layer on the cantilevers and delamination of the gold, hence maximum potential values were set to $\pm$1.2 V for the rest of the project. Issues of optical alignment were addressed and the noise level in the system was observed. A flow of 50 μl/min was decided to be the maximum speed that could be used before the flow started to contribute to the noise. Together, these investigations and observations constituted the commissioning of the ECC platform, and it was deemed ready to start the chemical sensing and electrochemistry experiments.

Part V

Characterization & Measurements

Chapter 11

Differential Sensing of Copper Ions Using Functionalized Cantilevers

This chapter presents the application of the copper-sensitive molecules investigated in Part III to the electrochemical-cantilever platform developed in Part IV. Chip functionalization protocol from chapter 8 is adapted for use with the ECC chip. A clean reference cantilever is generated using the electrochemical capabilities of the platform so that differential measurements can be acquired. The responses of both cysteine and CGGH monolayers are observed in Milli-Q water and buffered electrolyte, and compared. Results of the QCM experiments conducted on CGGH are qualitatively compared with those acquired using cantilevers. The responses of the functional layers to different concentrations of Cu^{2+} ions are used to estimate the adsorption rate constants for Cu-(Cys) and Cu-(CGGH) complexes.

11.1 Experimental Methods

11.1.1 Functionalization Protocol

The ECC chips were functionalized with either cysteine or CGGH in the same manner as the electrodes in chapter 8. Individual ECC chips were cleaned in a solution of 30% hydrogen peroxide and 50 mM potassium hydroxide for 8 minutes, followed by rinsing in 4 separate baths of clean Milli-Q water (18 MΩcm) for 5 minutes each. The chips were then placed in 95% ethanol for 3 minutes to reduce gold oxide that may have formed during the cleaning [115], rinsed once more in Milli-Q water, and placed in 5 ml of 5 mM cysteine or CGGH and 50 mM phosphate buffer (pH 6.2) to incubate overnight (16-20 hours). The chips were rinsed twice in clean phosphate

buffer (1 hour each), then once in Milli-Q water to remove the phosphate, and finally in 95% ethanol to substitute the water. The ECC chips were blown dry with filtered air (0.3 μm filter) to evaporate the ethanol quickly, and then loaded into the flow cell in the method described in chapter 10.

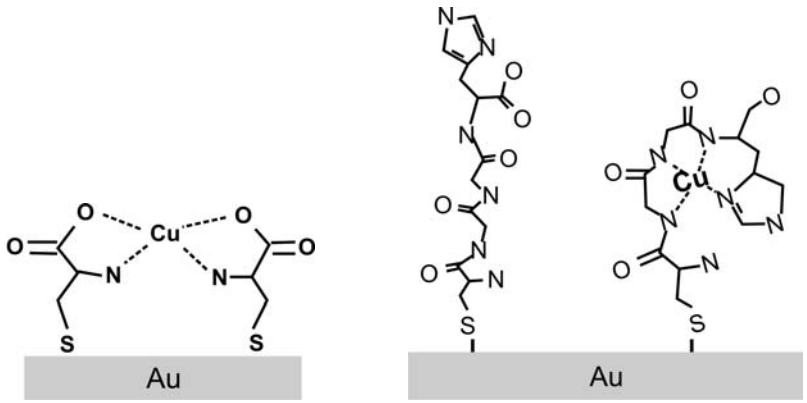

(a) (b)

Figure 11.1: The Cu^{2+}-ion binding configurations of (a) L-cysteine and (b) CGGH, the molecules investigated in chapter 8.

11.1.2 Differential Measurements

Differential measurements, by definition, require cantilevers whose surfaces differ chemically. This allows the signal from one cantilever to be subtracted from another, thereby returning the response of a very specific reaction, minus parasitic effects [20, 21, 24, 41, 214]. In the simplest case two cantilevers are simultaneously monitored as an analyte is introduced. The surface of one cantilever (the *functional* cantilever) hosts a receptor, while the surface of the other cantilever (the *reference* cantilever) is clean and hosts no specifically-functional molecules. Figure 11.2 depicts such a configuration applied to the ECC platform. The application of this methodology is not quite so simple in practice, a result of the fact that cantilevers with inhomogeneous chemical properties will react slightly differently to parasitic effects (*e.g.* changes in temperature, ionic concentration, mechanical vibrations, fluid turbulence). Nonetheless, this method is an improvement over measurements conducted using a single cantilever.

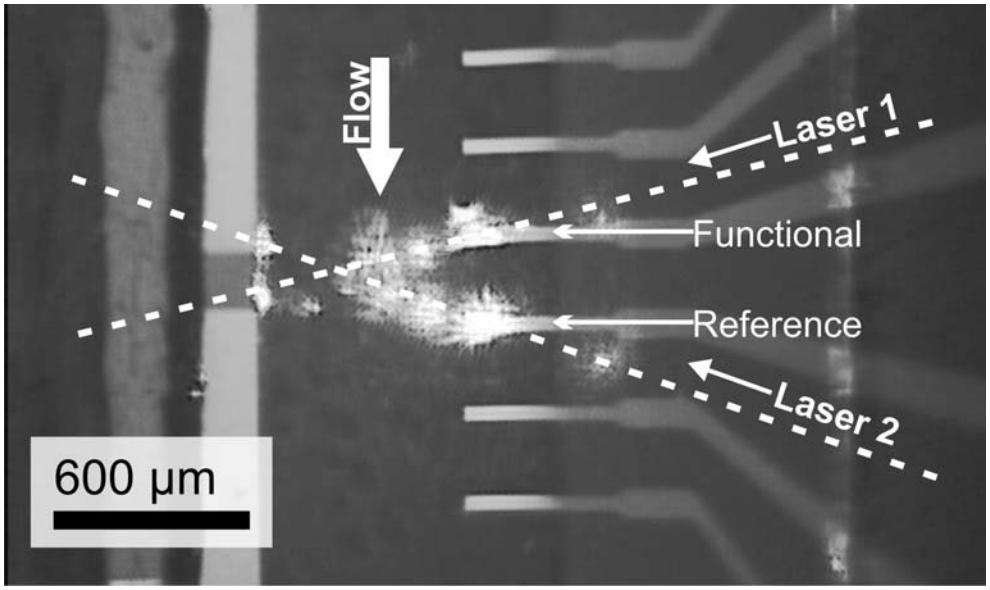

Figure 11.2: A labeled microscope image of differentially functionalized cantilevers being monitored in the NanoNose system. The functional cantilever is coated with a monolayer of cysteine or CGGH, while the reference cantilever has a clean gold surface. The configuration presented here is typical of most measurements taken in this system.

Differential Functionalization

Differentially functionalizing individual cantilevers in an array is challenging due to their small size and close spacing, and several techniques have been developed to accomplish this. Immersing cantilevers in micro-sized containers [41] or capillaries [48] have been used to simultaneously differentially functionalize arrays, while micro-pipetting [215], spray-coating [216], and ink-jet printing [196] have provided a sequential approach. All of these techniques require rather precise alignment of the microcantilevers to the chemical source, and modification is performed before the array is loaded into the measurement setup.

Selective Cantilever Cleaning

The design of the ECC chips was not conducive to being functionalized using microcapillaries [48] since the cantilevers could not be accessed from their tips (due to the channel), and the equipment required for other functionalization techniques was not available. An alternative method of obtaining different surface modifications was needed.

Only the simplest form of differential measurement was to be performed

here, *i.e.* simultaneously measuring one functional cantilever and one clean reference cantilever. This could be accomplished by either selectively functionalizing or selectively cleaning one cantilever of the array. Given the observations of section 7.5.2 and reports from literature [84, 157–159, 217] it was decided to voltammetrically remove the functional layer from one cantilever, thus making it the reference.

Following loading into the flow cell, two cantilevers were electrically connected to a potentiostat, one as a working electrode, the other as a reference/counter, creating a two-electrode configuration. The flow cell was filled with Milli-Q water following the protocol from section 10.1.2, then filled with 1 mM $[Fe(CN)_6]^{3-/4-}$in 50 mM phosphate buffer (pH 6.2) using the syringe pump to pull fluid through the flow cell as depicted in figure 11.3. The potential applied to the working electrode was cycled between +1.2 V and −1.2 V at a rate of 0.1 V/s. This was done until the signal observed ceased to change with time and closely resembled that of the clean cyclic voltammagram in $[Fe(CN)_6]^{3-/4-}$redox couple (typically 15-20 cycles), which indicated that that the functional layer had been removed[1]. Voltammetric cleaning was performed in $[Fe(CN)_6]^{3-/4-}$redox couple to allow simultaneous monitoring of the surface by observing the voltammagram.

Measurement Procedure

Copper detection was performed with Cu^{2+} ions in both clean Milli-Q water and buffered electrolyte (30 mM ammonium acetate, 30 mM potassium hydroxide, pH 6.8). As mentioned in chapter 2, cantilevers react to everything in the solution. It was decided to keep the contents of the solution to a minimum at first, meaning only Milli-Q water with either $Cu(NO_3)_2$ or ethylenediaminetetraacetic acid (EDTA). The EDTA solutions, used to remove Cu^{2+} ions from the cell, were made in both Milli-Q water and buffered electrolyte to a concentration of 2 mM. Stock $Cu(NO_3)_2$ solutions were made to 100 μM and diluted by a factor of 10 three times, to achieve additional concentrations of 10 μM, 1 μM, and 100 nM. All solutions were made fresh on the day of the experiment. In the case of the buffered electrolyte, the 30 mM KNO_3 provided a constant high concentration of nitrate in the solution such that the additional nitrate ions provided by the $Cu(NO_3)_2$ would have a minimal effect on the ionic concentration. Thus, the only major change in the composition of the solution would be the copper (II) ions. This is in contrast to the Milli-Q solutions, where the appearance of copper ions was accompanied by nitrate ions, thus changing two components of the solution simultaneously.

[1]Note that cyclic voltammetry has been previously used to reliably determine the degree of blocking on the surface (chapters 7 and 8) and to determine electrode cleanliness (chapter 6).

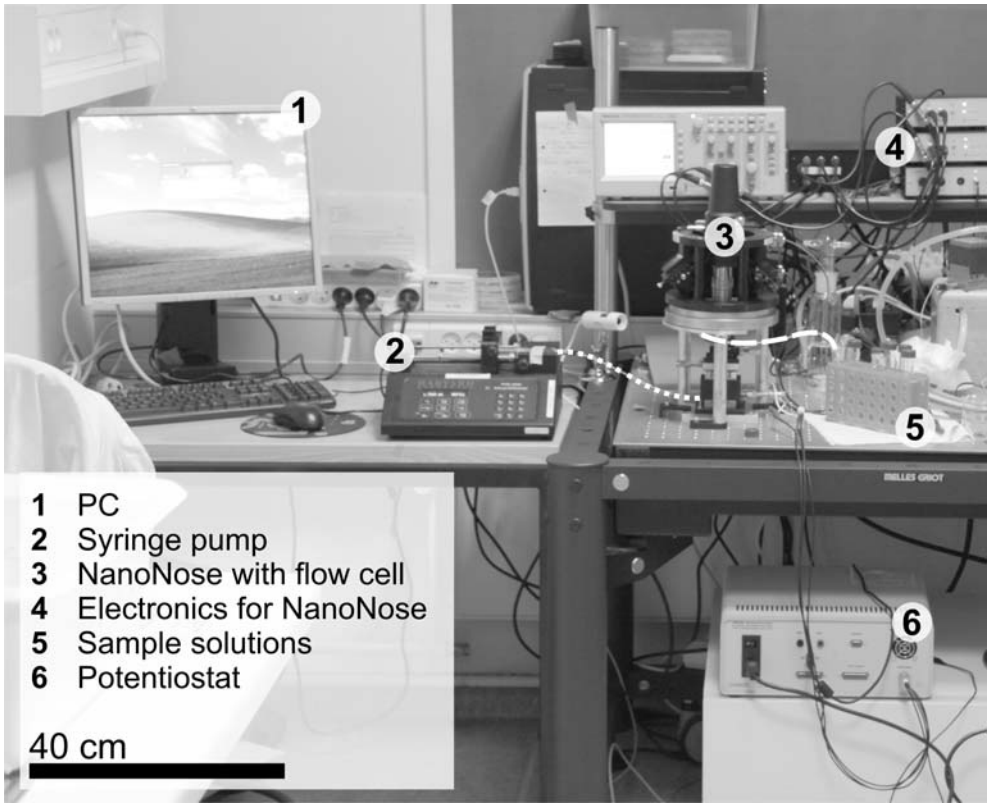

Figure 11.3: A photograph of the entire workstation. The PC (**1**) was used to collect data from the NanoNose (**3**) and to control the potentiostat (**6**). The syringe pump (**2**) was used to pull the sample solutions (**5**) through the flow cell (located under **3**). The fluidic tubing used to connect the syringe pump and flow cell is labeled by the dotted line, while the tubing connecting the flow cell and sample solutions is labeled by the dashed line.

Following the cleaning previously described, lasers were aligned to the cantilevers as indicated in figure 11.2. A 50 μl/min flow of either Milli-Q water or buffered electrolyte (the base solution) was initiated, and the deflection of both cantilevers was monitored for 40 to 60 minutes, until the drift in the cantilever signal was small ($\leq$ 0.1 V/h), stable, and approximately equal for both cantilevers. The introduction of Cu^{2+} ions always caused a continuous drift which would drive the signals out of the range of the photodetectors, similar to that seen in the QCM measurements from section 8.2.2. Instead of waiting for the signals to stop drifting, the signals were monitored under a copper ion flow until the drifts of the functional and reference cantilever were roughly equal, at which point a flow of the base solution was continued. After the signals stabilized in the base solution a flow of 2 mM EDTA was

introduced to removed the copper ions from the cantilevers, as well as the rest of the chamber. This EDTA flow typically lasted 5 minutes or less, after which a flow of the base solution was introduced a final time.

The cantilever tip z-displacement was acquired via the optical lever method and converted into a surface stress using Stoney's formula [49] (equation 2.2. To ensure fair comparison between runs and cantilever sizes, the location of the laser spot on each cantilever (functional and reference) was measured from an image captured before the run. The laser spot location was used as the cantilever length to calculate the surface stress [218, 219]. It was then the length-independent surface stresses that were subtracted to produce the differential signal.

11.1.3 Regeneration

Chemical Regeneration - EDTA

A cysteine-modified cantilever and a clean reference cantilever were exposed to a 50 μl/min flow of 10 μM Cu^{2+} in a solution of the previously described buffered electrolyte (pH 6.8) for 10 minutes. Buffered electrolyte was then introduced into the chamber for another 10 minutes to remove the copper solution and non-specifically bound copper. Then 2 mM EDTA (in buffered electrolyte) was injected for $\sim$ 200 s to purge the system, followed by more buffered electrolyte. This cycle was repeated 3 times to demonstrate the regenerability and reusability of the cysteine-modified cantilevers, in a similar way to the CGGH-modified QCM chips from chapter 8.

Voltammetric Regeneration

One of the main reasons for using an electrochemical-cantilever system for metal ion detection is the possibility of regenerating the monolayer by electrochemical methods, instead of applying a strong chelating chemical (*e.g.* EDTA). Following stabilization in a 50 μl/min flow of 50 mM KNO_3 (the base solution for this experiment), 1 mM $Cu(NO_3)_2$ was injected for 20 minutes. A flow of potassium nitrate was reintroduced to flush the copper ions. The measured cantilever was connected as the working electrode, and an adjacent cantilever acted as counter and reference (2-electrode setup). The potential of the working electrode was swept from 0.5 V to -0.4 V (vs. Au reference) for 2 cycles. The cantilever is allowed to stabilize, after which 1 mM Cu^{2+} ions are injected to test if the cantilever can be reused. All electrochemical methods are conducted at zero flow.

11.2 Results

11.2.1 Voltammetric Cleaning

The cyclic voltammagrams generated during cleaning are shown in figure 11.4. In both cases of cysteine (figure 11.4(a)) and CGGH (figure 11.4(b)) monolayers the CV was run until it ceased to change, *i.e.* until the electron transfer no longer improved with cycling. This indicated that no further layer removal was happening, and that the cantilevers were clean. Recall from previous chapters how a flat looking CV with suppressed peaks indicates a blocked surface, while the presence of redox peaks close together is indicative of a clean surface. The thiol bond is known to be reduced at sufficiently high negative potentials, typically $E = -0.6$ to -1.0 V [84, 157–159, 217]. It should be noted that, in the two electrode setup, potentials of $E = -1.2$ V are not achieved. Rather, the potential difference between the two electrodes is what is read on the axis, relative to the reference/counter electrode. Still, we can see a similar evolution in the CVs as we saw in section 7.5, when using a three electrode setup. Thus, even though we can't measure the potential against a stable reference, we can still monitor the shape of the CV and conclude that the electrode is clean enough to be used as a reference cantilever.

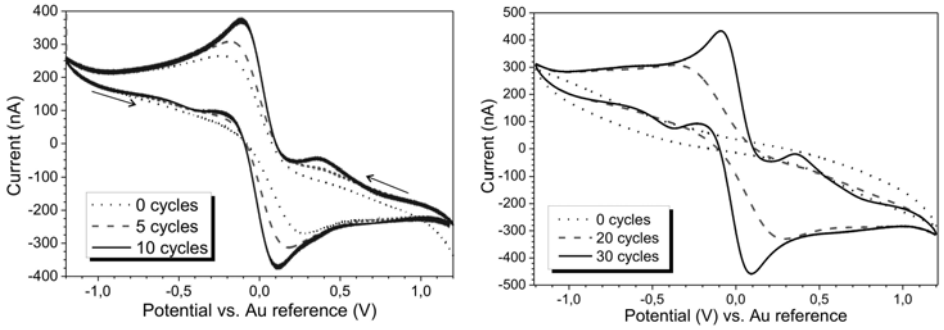

(a) (b)

Figure 11.4: Cyclic voltammagrams acquired at different stages in the cleaning of cantilever electrodes coated with (a) cysteine and (b) CGGH monolayers. Voltammagrams are shown from the beginning (0 cycles), middle, and endpoints of the cleaning. In each plot the CV ceased to change after the last cycle shown, indicating no further layer removal. Electrolyte used: 1 mM $[Fe(CN)_6]^{3-/4-}$ in 50 mM phosphate buffer (pH 6.2).

11.2.2 Cysteine-Modified Cantilever

Cys-Cu^{2+} Binding in Milli-Q Water

Cantilevers functionalized with cysteine were subjected to the flow sequence described in figure 11.5. Clean Milli-Q water flows through the cell initially producing the baseline stress signal. Upon injection of the Cu^{2+} ions the cantilever experiences a compressive stress (negative stress, downward bending) very briefly ($t \approx 4$ min) before developing a large tensile stress, peaking at $\Delta\sigma = 55$ mN/m relative to the reference cantilever. Upon reintroduction of the Milli-Q flow the tensile stress is relieved slightly, but does not return to zero. The binding affinity between cysteine and copper ions is quite large [126,130,168–170], thus we expect very little desorption of bound ions. The introduction of 2 mM EDTA removes all Cu^{2+} ions from the cysteine layer, as well as the rest of the flow cell, and relieves the tensile stress in the layer, briefly reducing it to zero. However, as was seen in the QCM results of section 8.2.2, the EDTA quickly introduces its own drift on the system. This is the first observed effect of not having a "true reference" cantilever. A differential drift has already been removed from figure 11.5, but still introducing something as chemically active as EDTA will cause a further drift of the functional cantilever relative to the reference.

Still, for our purposes here, a clean reference is sufficient. Figure 11.6 shows the differential stress response of cysteine-modified cantilevers to two different concentrations of copper ions. The same response is seen in the 100 nM but it occurs more slowly than in the 10 μM solution. The slight compressive stress before the tensile response, and a relaxation from the maximum stress once Milli-Q is reintroduced is seen again in the 100 nM solution.

The shape of the two curves is quite similar to those obtained by Marie *et al.* [124] during the adsorption of thiol modified DNA-oligos. A similar "super-saturation" was observed by Marie where the surface stress would remain at an elevated level as long as the DNA-oligo solution was flowing, and a higher super-saturation level was seen for higher concentrations. Indeed not only the results, but the conditions of the experiment share similarities to those presented here. Both the DNA-oligo adsorption and cysteine-Cu^{2+} binding events occur on surfaces that have a fixed number of binding sites, the cantilevers are in a flow of solution delivering the detected species, and the binding efficiency is high enough such that the rate of desorption expected is very low. Thus we can analyze this system further by applying the Langmuir adsorption model isotherm [43, 124, 220], described by equation 11.1,

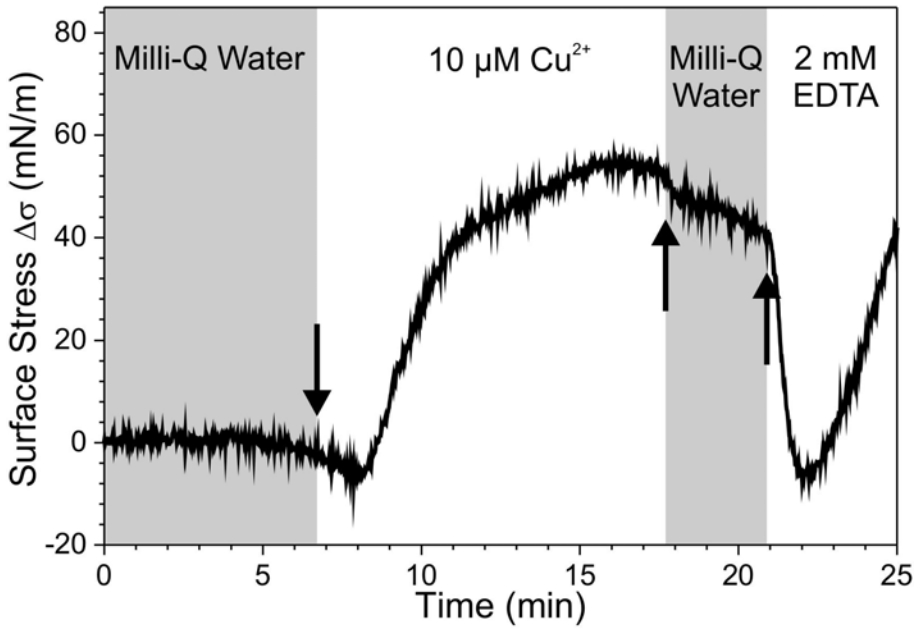

Figure 11.5: The calculated differential surface stress response of a Cysteine-modified cantilever to 10 μM Cu^{2+} ions. The shaded and labeled regions indicate what fluid was flowing through the cell (flow rate 50 μl/min) and when it was changed. The Cu^{2+} ions appear to cause a tensile stress in the cysteine layer, and the EDTA removes the metal ions, briefly reducing the stress to the pre-copper level, before a differential drift takes over.

$$\theta \propto 1 - \exp\{-k_{obs}t\} \tag{11.1}$$

where θ is the fractional occupation of available sites, k_{obs} is the observed reaction rate, and t is the time. One can assume that the number of available copper ion binding sites per cantilever is fixed and is approximately the same, from cantilever to cantilever. Thus the stress at site saturation should be the same from cantilever to cantilever, once the super-saturation effect has been removed, which is a valid assumption from what is observed in figure 11.6. This surface stress at saturation was estimated to be $\sigma_{sat} \approx 38$ mN/m, and the model described by equation 11.1 was fit to the observed stress responses, seen in figure 11.7. The observed rate constants for the 10 μM and 100 nM concentration curves was $k_{obs} = 0.014$ s^{-1} and 0.002 s^{-1}, respectively. Taking the observed rate constant versus copper concentration to be linear[2] the adsorption constant was calculated to be 1.2×10^3 M^{-1} s^{-1}.

[2]Yes, this is a crude assumption, but one that must be made as there are only 2 reliable data points. A 1 μM copper concentration was measured several times, but usable data could not be obtained.

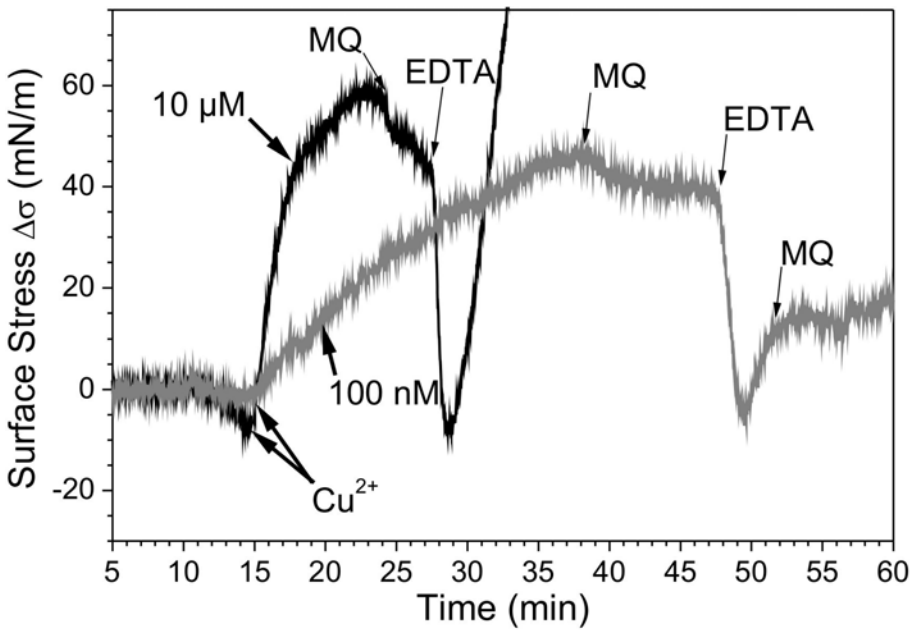

Figure 11.6: The differential surface stress of a cysteine-coated cantilever in response to 10 μM and 100 nM Cu^{2+} ions in Milli-Q water. Note how the 100 nM concentration reaction is similar in shape to the 10 μM curve, but the response is reduced in magnitude and the cysteine layer takes over 5 times longer to saturate. Re-introducing Milli-Q water causes the tensile stress to relax to a stable value (the layer saturation stress) of roughly $\sigma = 38$ mN/m. Removing the copper ions with EDTA has the same effect on stress in the cysteine layer, as is again similar to the QCM response seen in a previous chapter.

This simple proof-of-concept has displayed two main features of the ECC platform. First, the cantilevers in the system are sensitive enough to, pending proper calibration, sense nM concentrations of copper ions. Second, having observed these two surface stress plots with the same shape and characteristics, the voltammetric cleaning has been shown to perform well enough to deliver differential measurements of consistent quality. However, this simple case of a one component solution is unrealistic. After starting simply, more advanced solutions must be investigated in pursuit of using this platform for environmental monitoring.

Further, the initial compression upon injection of copper ions remains a mystery. A similar concentration of nitrate accompanies the copper solution, thus this compression could be a result of either component. The solution must be adjusted such that the only significant difference between the base solution and the analyte solution is the appearance of copper (II) ions.

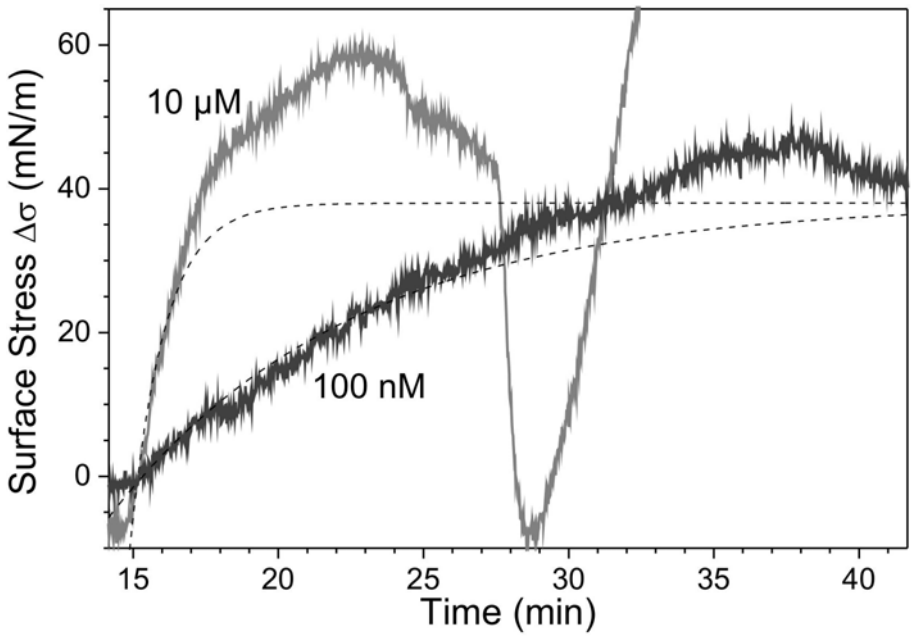

Figure 11.7: The same surface stress responses from figure 11.5 with Langmuir adsorption isotherms fit to the curves (dashed lines). The observed rate constant is $k_{obs} = 0.014$ s^{-1} for the 10 μM concentration curve, and $k_{obs} = 0.002$ s^{-1} for the 100 nM response.

Cys-Cu^{2+} Binding in Buffered Electrolyte

While the pH of degassed Milli-Q water has been measured to be approximately 8, and the process of binding copper ions is not expected to change the solution pH, an unbuffered solution can put the activity of the ligands into question. Ammonium acetate (NH_4Ac) provided a pH of 6.8, while the KNO_3 provides a high concentration (30 mM) of nitrate, making the slight contribution of nitrate from the $Cu(NO_3)_2$ ($\sim \mu$M) negligible. Thus, the only noticeable change in the solution should be the appearance of the copper (II) ions.

Figure 11.8 plots the differential surface stress of cysteine-modified cantilevers due to 10 μM, 1 μM, and 100 nM concentrations of copper (II) ions. Initially these stress plots seem vastly different from those performed in Milli-Q water. The magnitude of the surface stress in the initial increase just after copper injection is less than half that of what was observed in Milli-Q. The 100 nM concentration barely causes a response, unlike that seen in Milli-Q. The tensile stress increase for the 10 μM solution occurs in the same time span as that in Milli-Q ($t \approx 4$ minutes), but only has a magnitude of $\Delta\sigma = 29$ mN/m (measured from the minimum value of the initial compressive response).

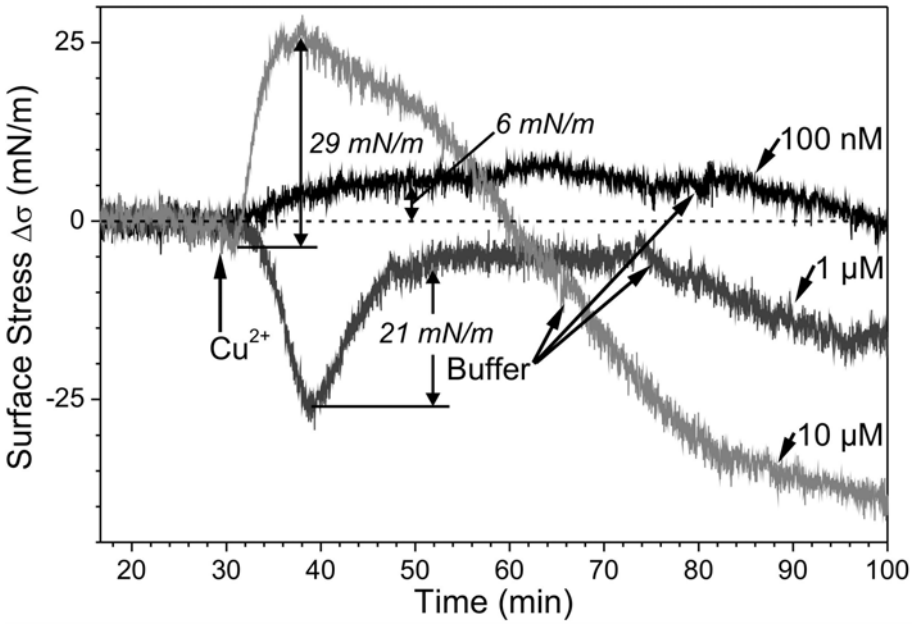

Figure 11.8: Differential surface stress of cysteine-modified cantilevers. The buffered solution consists of 30 mM NH_4Ac and 30 mM KNO_3 (pH 6.8), with 10 μM, 1 μM, or 100 nM concentrations of $Cu(NO_3)_2$. Note the similar shapes on the increasing tensile stress side of the plots, and how the increase becomes less steep as the concentration decreases.

However, there are many similarities between the cysteine monolayer responses observed in Milli-Q and buffered electrolyte. First, and as just mentioned, is the response time. The 10 μM concentration develops its fast tensile response in buffered electrolyte in the same time as in Milli-Q ($t \approx 4$ minutes), while the 1 μM response takes $t \approx 9$ minutes, and achieves a tensile increase of $\Delta\sigma = 21$ mN/m (measured from the minimum value of the initial compressive response). Also, the presence of this initial compressive response persists in the buffered electrolyte. This indicates that it is an artifact of the copper ions. Since all copper solutions are made from the stock buffered electrolyte, the only significant change in composition that occurs when solutions are changed is the appearance of the copper ions[3]. This initial compression could be the result of repulsion caused by the copper ions and their solvation shell accumulating on top of the cysteine layer before binding to the ligands. At lower concentrations the copper ions would accumulate slower, giving each one more time to be broken from its solvation shell and bound to the monolayer. Thus the repulsion between the solvated copper

[3]We assume that a μM change in a nitrate concentration of 30 mM would cause a negligible cantilever response.

ions cannot accumulate fast enough to produce an appreciable compressive response in the lower concentrations, *e.g.* the 100 nM copper concentration.

On cantilevers with a clean gold surface (*i.e.* no functional layer) an injection of 10 μM Cu^{2+} has been observed to generate a strong compressive stress, as seen in figure 11.9. This can be attributed to repulsion between adjacent solvated ions, or a relaxation of the intrinsic tensile stress in the gold surface caused by physisorbed species [88, 221]. Since the surfaces of the two cantilevers are different they will exhibit this adsorbate stress at different magnitudes, in the case of figure 11.9 the functional cantilever experiences a slightly larger compressive stress at first.

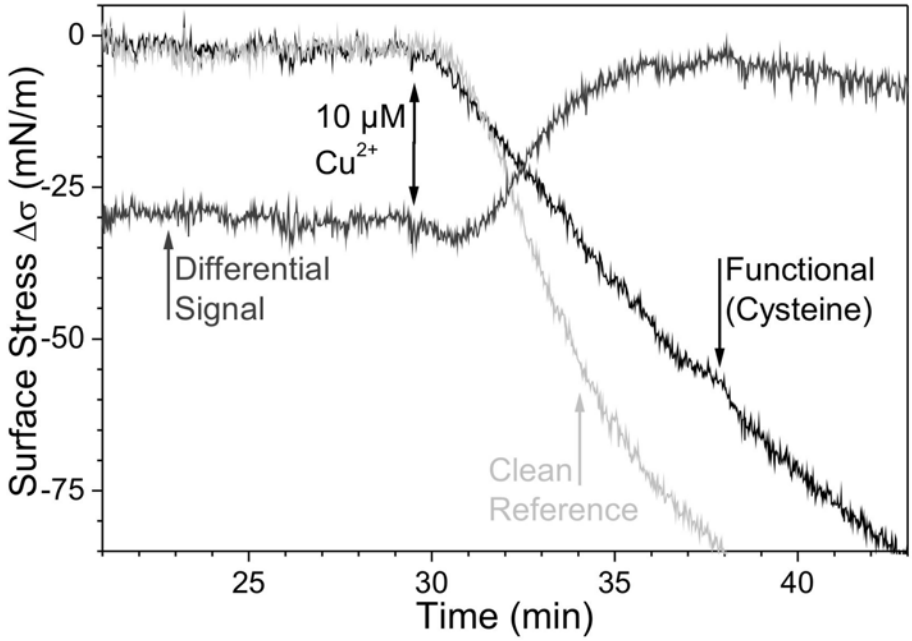

Figure 11.9: Cantilever signals for the functional and reference cantilevers responding to 10 μM Cu^{2+}, in 30 mM KNO_3 and 30 mM NH_4Ac (pH 6.8). The differential signal ([functional]-[reference]) is plotted at an offset for improved visibility.

However, when the Cu^{2+} ions coordinate to the immobilized cysteine molecules the functional cantilever experiences a tensile stress, with respect to the clean reference cantilever. This is the result of two possible effects. The positively charged Cu^{2+} ion coordinates with the cysteine molecules, which are expected to be negatively charged at pH 6.8 [141], and neutralize this charge. Evidence for this has been presented in section 7.3.1 where carboxyl groups were observed to repel a negatively charged redox probe. Pedrosa *et al.* [151] have observed a cysteine layer to become negatively charged at

pH values approaching 7, as is the case here. Neutralizing the charge of the molecules on the surface would reduce electrostatic repulsion between them, as seen in figure 11.10(a), reducing overall compressive stress, which would be observed as a tensile stress through cantilever motion.

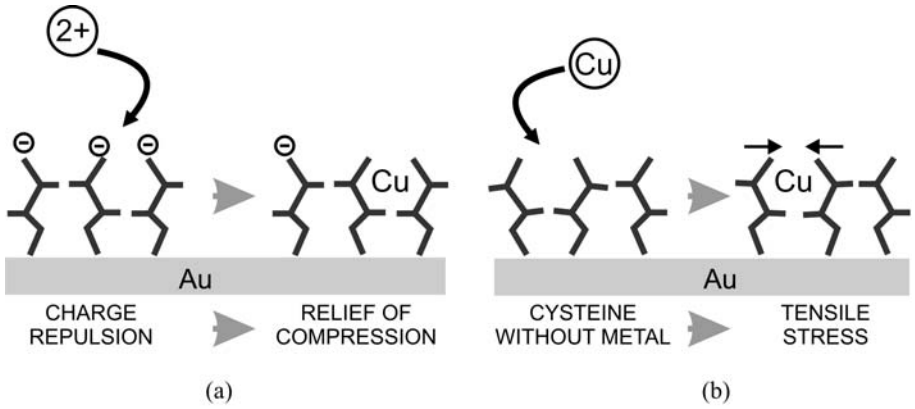

Figure 11.10: Two routes of generating a tensile differential stress: (a) The binding of the cation to the negatively charged carboxyl groups on the cysteine molecules reduces the negative charge of the layer, relieving compressive stress, which is observed as an increase in tensile stress. (b) Copper (II) ions coordinate to cysteine molecules in a 2:1 scheme, creating a physical link between two adjacent molecules as they strain to make the bond. Occurring across the surface this would manifest as a tensile stress.

A second source of observed tensile stress could be that formed within the layer due to binding, depicted in figure 11.10(b). Copper (II) ions are known to coordinate to cysteine in a 2:1 scheme [140, 170]. The cysteine molecules "reach" towards each other to create the bond due to the high affinity constant [169], which would be observed as a tensile stress on the cantilever surface. The observed cantilever deflection is most likely a combination of these two effects, although determining which one dominates is difficult without additional characterization.

The initial compressive stress seen in the cantilever response to 1 μM Cu^{2+} (figure 11.8) is far larger in magnitude and occurs for a longer time than the similar artifacts seen in the 10 μM solutions in Milli-Q or buffered electrolyte. All copper and EDTA solutions were made from the same buffered electrolyte (30 mM NH_4Ac and 30 mM KNO_3) stock solution, ruling out differences between measurement solutions. Mechanical vibrations, thermal effects, and sudden changes in flow can also be ruled out as well since the experiments were carefully controlled to avoid this. The initial compression closely resembles that seen in the 10 μM concentrations, both in figure 11.8 as well as figure 11.11 (discussed below). The only possible causes of

this anomalous response are forms of monolayer damage or surface contamination that would contribute to the cantilever response, which could have occurred unknowingly during drying or loading. Incomplete or damaging voltammetric cleaning of the reference cantilever could also contribute to the differential signal seen, although the reference response exhibits normal behavior.

A final note regarding cysteine-based copper sensing in buffered electrolyte is the final values attained by the cantilevers. Had only before and after measurements been performed they would have followed the same exposure procedure, *i.e.* 30 minutes exposure to a copper solution, then 30 minutes of rinsing. At the end of figure 11.8 we see each copper concentration reaches a different differential stress value; $\Delta\sigma = 0.7$ mN/m for 100 nM, $\Delta\sigma = -16.7$ mN/m for 1 μM, and $\Delta\sigma = -37.5$ mN/m for 10 μM. Thus, despite the behavior observed under real-time measurements, the final stress response does exhibit a trend of increasing compressive stress with increasing concentration.

11.2.3 Regeneration of Cysteine Layer

Chemical Regeneration - EDTA

The differential signal in figure 11.11 exhibits the same features as other cysteine-modified cantilever responses to 10 μM Cu^{2+}, complete with the initial compressive stress and the negative drift following exposure to copper. The 2 mM concentration of EDTA used was high enough to expect all copper to be removed within one or two minutes, but caused a large relative drift and thus exposure was kept to a minimum. It should immediately be noted that all three of the iterations of copper exposure are remarkably similar. Measured from the bottom of the initial compressive response to the "kink" or "elbow" that marks the end of the relatively linear binding region, the magnitude of the tensile stress response is $\Delta\sigma = 39.3, 34.7$, and 37.5 mN/m for the first, second, and third exposures to 10 μM Cu^{2+}. Each of the successive responses are comparable in magnitude, whether the surface is fresh, regenerated once, or regenerated twice. Following regeneration by EDTA, the flow of buffer is resumed resulting in the same stable, drift-free stress response seen when the experiment began. These two observations together indicate that the copper is completely removed from the cysteine-surface, and that all or most of the cysteine molecules remain bound to the gold. Regeneration by means of EDTA appears to be effective.

One feature of note in figure 11.11 is the initial compressive response, also seen previously in figures 11.6 and 11.8. The three stress responses seen in

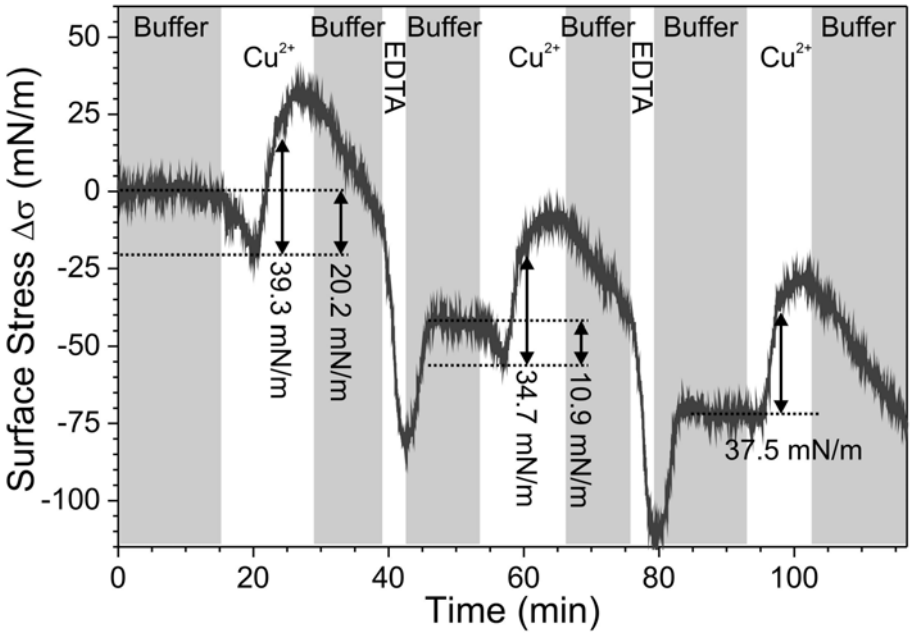

Figure 11.11: The differential stress response of a cysteine-modified cantilever during alternating exposure to 10 μM Cu^{2+} and EDTA. The buffer, 30 mM NH_4Ac and 30 mM KNO_3 (pH 6.8), is also the base solution, present during the entire experiment. The cycle proceeds as follows: stable baseline in buffered electrolyte, response to 10 μM Cu^{2+}, negative drift in buffer following copper exposure, copper ion removal in EDTA, stable baseline in buffered electrolyte restored. Notice the initial compressive stress before the tensile response due to the copper gets progressively smaller with each regeneration.

figure 11.11 are conducted on the same cantilever, using the same solutions, one after the other, yet there are three different initial compressive responses, with magnitudes of $\Delta\sigma = -20.2$, and -10.9 mN/m for the first and second copper exposure, with no discernable initial compression happening with the third exposure. While EDTA is known to bind with many transition metals very strongly, it is not expected to have any effect on the cysteine layer. Without knowing definitively what is causing this initial response it is impossible to understand the reasons behind this evolution. Following from the reason speculated in section 11.2.2 for the initial compression, it is possible that the cysteine layer is now "more active" and is capable of immediately coordinating with the copper ions. After the functionalization protocol the cysteine SAM may be weakly occupied by another species which must be displaced before the copper ions can bind, causing the initial compression observed. Such an explanation was given for a similar feature observed during the adsorption of alkanethiol chains [43]. This explanation would fit if the initial compressive response disappeared completely after the first regeneration instead of first being reduced by half.

Another possible explanation is that, with each successive exposure to Cu^{2+}, more copper ions become "embedded" in the layer. The ions that are responsible for the compressive stress remain in the layer after 3 cycles, such that the response is purely tensile by the third exposure.

Voltammetric Regeneration

Figure 11.12 plots the stress response of a cantilever that was electrochemically regenerated. No buffer was used for this experiment, only 50 mM KNO_3 as electrolyte. After acquiring a stable baseline copper (II) ions are injected at a concentration of 1 mM. There is an initial compressive stress response, similar to figures 11.6, 11.8, and 11.11, but much larger than previous reactions ($\Delta\sigma \sim 65$ mN/m), followed by the typical copper-binding curve seen previously for cysteine. Upon switching to a flow of KNO_3 the negative drift which accompanied the flow of the copper solution ceases, and the cantilever signal stabilizes. The nitrate flow was continued for 20 minutes to ensure that the only copper ions in the flow cell would be those specifically bound to the cysteine. A linear potential sweep was attempted, but the signal quickly returned to its stable value. Cyclic voltammetry was found to perform well in cleaning applications (section 11.2.1) and so was applied here. Holding the electrode surface at +0.5 V [25] or +0.3 V [170] in 0.1 M perchloric acid has been described as an effective means of removing copper ions from SAMs, but it was decided to avoid using perchloric acid in the flow cell.

The stress signal quickly stabilizes to the pre-copper-binding value following voltammetry. The system was left in a flow of KNO_3 for nearly 50 minutes to ensure a stable signal had truly been reached. Finally, 1 mM Cu^{2+} was injected a second time and a second stress response was observed. While the initial compressive response is only half as large as the first response (similar to observations during regeneration by EDTA), the magnitude of the second tensile response ($\Delta\sigma = 18.8$ mN/m) is very close to the first tensile response ($\Delta\sigma = 17.6$ mN/m). These results match remarkably well with the EDTA-induced regeneration. Additional tests yielded similar results, although the baseline did not always return to its value before copper injection (as in figure 11.11). Still, these results show promise for electrochemical regeneration of cysteine-modified cantilevers.

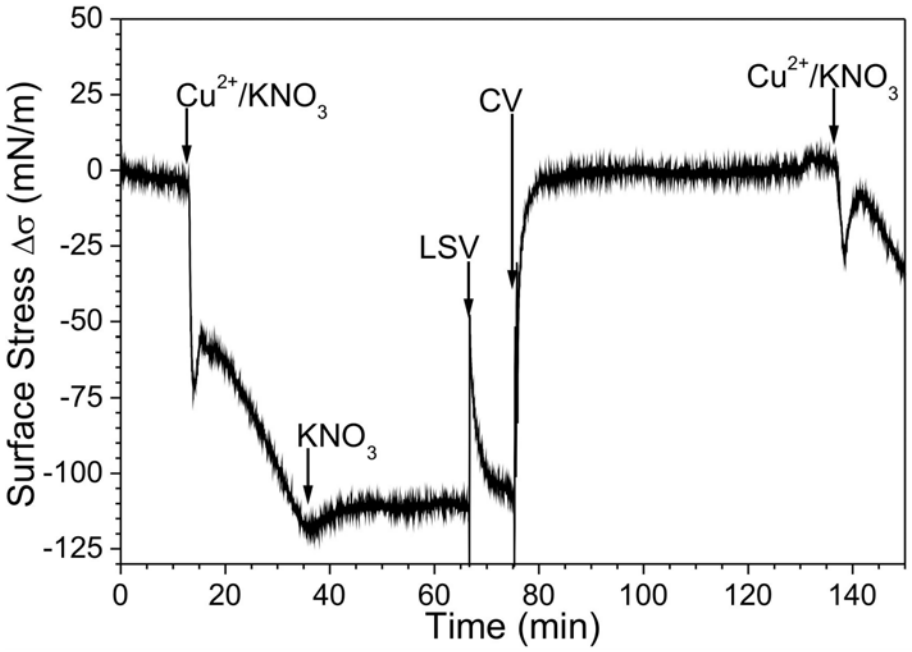

Figure 11.12: The surface stress of a cysteine-modified cantilever exposed to 1 mM Cu^{2+} (50 mM KNO_3 is the base electrolyte solution). After the cantilever stabilizes in a flow of 50 mM KNO_3 a linear sweep (LSV) is applied, from 0.6 V to -0.5 V. The cantilever signal stabilizes to its previous value as the LSV had little or no effect. The CV performed (0.5V to -0.4V, 0.1 V/s) causes the cantilever signal to stabilize at zero stress (the baseline value for this experiment). After some time 1 mM Cu^{2+} was injected again. The cysteine monolayer reacts again, but the magnitude of the response is lower than previously observed.

11.2.4 Cys-Gly-Gly-His-Modified Cantilevers

CGGH-Cu^{2+} Binding in Buffered Electrolyte

Figure 11.13 plots the differential stress response of CGGH to Cu^{2+}-ion concentrations of 10 μM, 1 μM, and 100 nM. Again, as seen in figure 11.8, here the 100 nM solution produces no appreciable stress response, especially when compared with the other two concentrations that exhibit tensile stresses in hundreds of mN/m. The 10 μM and 1 μM responses both exhibit the same shape, with the 10 μM signal simply occurring faster and being larger in magnitude. Unlike the cysteine responses there is no initial compressive stress before the tensile. However, like the cysteine response, there appears to be an fast specific binding region, followed by a slower increase in tensile stress. The 10 μM signal plateaus at a maximum value of $\Delta\sigma = 288$ mN/m, while the 1 μM signal continues to increase until the copper solution is switched for the buffered electrolyte.

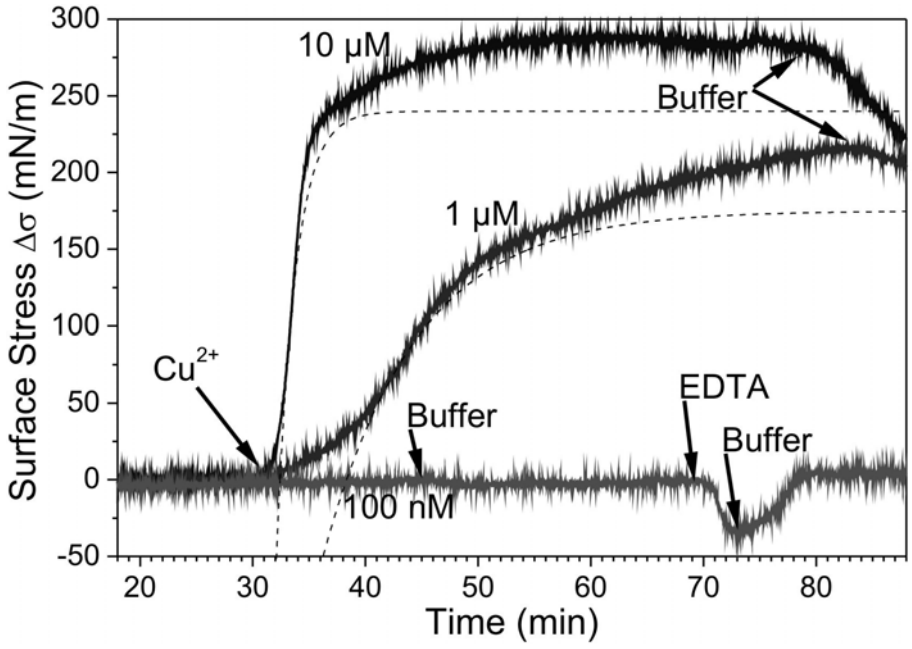

Figure 11.13: The differential stress signals observed for CGGH-modified cantilevers in response to Cu^{2+}-ion concentrations of 10 μM, 1 μM, and 100 nM. The dashed lines indicate the rough fitting of a Langmuir adsorption isotherm.

A simple Langmuir adsorption model was fit to the 10 μM and 1 μM responses according to equation 11.1, indicated by the dashed lines in figure 11.13. The affinity of the Gly-Gly-His complex for the copper (II) ion is believed to be high enough that desorption is negligible [176, 178, 181]. Observed rate constants were estimated from the rough fit to be $k_{obs} \approx 0.01$ s^{-1} for the 10 μM and $k_{obs} \approx 0.002$ s^{-1} for the 1 μM concentrations, giving an estimated adsorption constant of $\sim 9 \times 10^2$ $M^{-1}s^{-1}$. Available literature estimates similar adsorption rate constants to be between 0.1 and 2 $M^{-1}s^{-1}$ [222], but this is for a Cu-(GGHG) system in solution, whereas the system in this project is Cu-(CGGH) with the thiol on the cysteine residue bound to a gold surface. Such differences can account for orders of magnitude change in rate constants.

The functional and reference cantilever responses to a 10 μM Cu^{2+} solution are plotted in figure 11.14, with the differential signal plotted as well. Note that the magnitude of this response is far smaller than that of the 10 μM concentration in figure 11.13. The cantilevers in figure 11.14 were first exposed to 100 nM Cu^{2+} but exhibited no stress response. It appears that the functional layer was active on this cantilever, but the 100 nM concentration was unable to cause a stress. This may also be linked to the reason

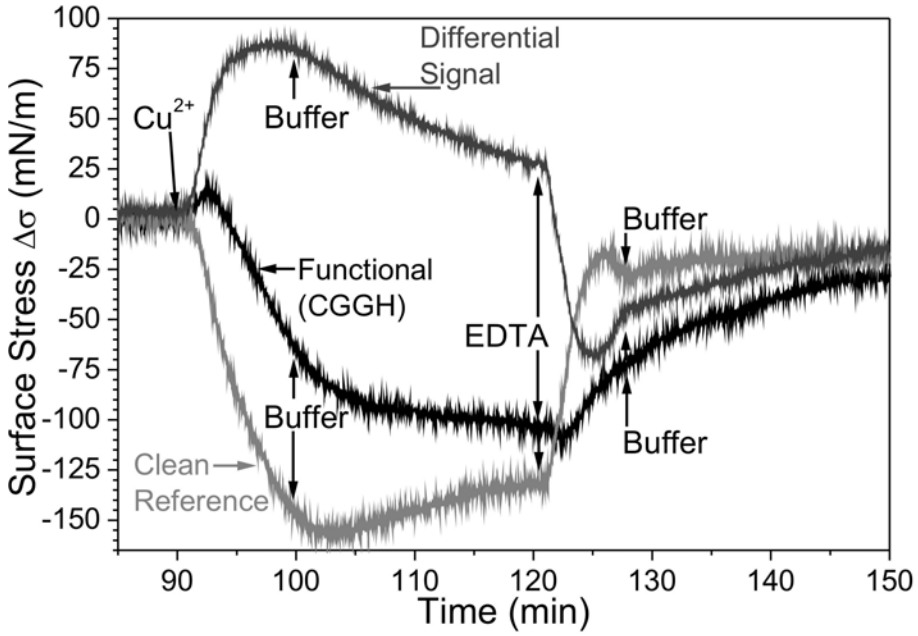

Figure 11.14: The surface stress signals of a CGGH-functionalized cantilever and a clean reference cantilever. The differential signal ([functional]-[reference]) is plotted as well. Note the initial tensile stress in the functionalized signal. This cantilever previously had 100 nM Cu^{2+} applied and exhibited no appreciable response.

why this 10 μM response is so much less than that seen in figure 11.13, *i.e.* this monolayer may have been damaged, incomplete, is simply less dense than others.

The 10 μM curve of the functional cantilever in figure 11.14 is qualitatively similar to that obtained by Xu *et al.* [25], which does not make use of a differential cantilever setup and uses GGH bound to a gold surface by MPA as the functional layer. Like the functional cantilever in figure 11.14, Xu *et al.* observed an initial tensile stress, attributed to a temporary 2:1 coordination scheme between Cu^{2+} and GGH, followed by a compressive stress caused by steric hindrance as the GGH coordinates 1:1 with the copper (figure 11.1(b)) that eventually plateaus. Similar features are observed in figure 11.14, indicating that the CGGH molecule is most likely coordinating to Cu^{2+} ions as intended[4]. Here too, as already confirmed by QCM in chapter 8, the copper ions can be removed by a 2 mM concentration of EDTA, seen in figure 11.14 as all signals return to their pre-Cu^{2+} values.

[4]Remember that this CGGH molecule was created for this purpose in chapter 8.

11.2.5 Reference Cantilever Response

The response of the reference cantilevers could come into question. It was shown that the clean reference experiences only a compressive stress upon encountering copper ions, most likely due to the associated effects of the non-specifically adsorbed ions and their solvation shells described in section 11.2.2. Figure 11.15 plots the responses of the voltammetrically-cleaned reference cantilevers to the three copper (II) ion concentrations. A compressive stress is observed which accumulates slower for lower concentrations. This effect is expected as the stress is due to the effects of solvated ions.

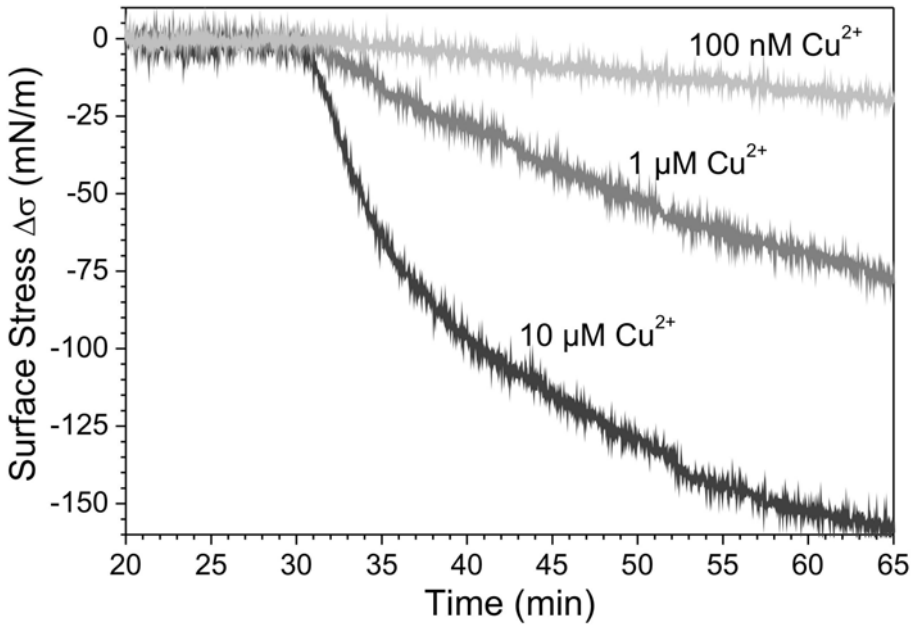

Figure 11.15: The stress response of the clean reference cantilevers to Cu^{2+} ion concentrations of 10 μM, 1 μM, and 100 nM, in 30 mM NH_4Ac / 30 mM KNO_3 (pH 6.8). The only effect observed is the compressive stress, which accumulates slower for lower concentrations, as expected.

11.3 Summary

The operation of the ECC platform for differential sensing of copper ions has been successfully demonstrated. A clean reference cantilever was generated by voltammetric cycling. The cleanliness of the cantilever was monitored during cleaning in real-time to determine the end point. The cleanliness of the reference cantilevers was also verified by observing the concentration-dependent response, which appeared to follow that of non-specific adsorp-

tion.

The reaction of a cysteine monolayer to Cu^{2+} ions was observed in Milli-Q water and an adsorption rate constant was determined to be 1.2×10^3 $M^{-1}s^{-1}$. The stress response of a cysteine layer to Cu^{2+} ions in buffered electrolyte was also investigated and compared to the observations in Milli-Q water. Both chemical and voltammetric techniques were found to be effective at regenerating the cysteine monolayer, which could then be used again to detect copper ions. The initial compressive response in the cysteine was found to generally be smaller for lower copper concentrations, and was observed to be smaller in responses after regeneration.

The CGGH molecule was also found to generate a response, and a rough estimate of the adsorption rate constant was determined ($\sim 9\times10^2$ $M^{-1}s^{-1}$). The raw response of the CGGH-functionalized cantilever was found to qualitatively agree with similar functionalization in literature, and the differential response for CGGH was found to be much larger than that observed for cysteine.

11.3.1 Outlook: Potential-Directed Assembly

The selective cleaning presented in this chapter is only the simplest case of the differential functionalization that could be done using this system. While using potential cycling to clean electrode surfaces is effective, selective deposition of functional monolayers would be much more useful. It has been shown that alkanethiol chains will selectively adsorb onto electrodes under a positive potential [159, 223–227], and will be desorbed from or will not adsorb to electrodes under a negative potential [84,157–159,217]. In fact Petrović *et al.* have shown that under the appropriate positive potential a significantly higher-quality monolayer of 1-dodecanethiol could be formed in 5 minutes than in 24 hours by conventional methods where no potential is applied [226].

Thus, in the ECC platform presented here, one could hold certain cantilevers at a positive potential while keeping the rest at a negative potential and introduce a functional thiol molecule. The thiol would quickly adsorb to the cantilevers under a negative potential with the rest of the array remaining unmodified. The modified cantilevers would then be chemically protected and could have all potential removed. Then this process could be repeated to functionalize every cantilever in the array, requiring only 5 minutes per functional layer. This differential functionalization method would remove the need for precise alignment (required in the techniques described in section 11.1.2), remove the need for additional deposition equipment (since modi-

fication is accomplished in the flow cell, using the inherent capabilities of the ECC chip), and result in quickly formed, high-quality functional layers. Further, since the electrode potential can be used to change the charge or redox state of the applied chemical layer [31, 32, 78, 79], it may be possible to perform layer-by-layer assembly of functional surfaces *in situ*, resulting in well-formed molecular layers in relatively short times. Efforts were made to investigate potential-directed assembly of alkanethiol monolayers, but practical issues surrounding electrochemistry in ethanol solutions did not permit further time to be spent exploring this avenue. However, given the capabilities of the ECC platform and the knowledge in the cited literature, this method of cantilever functionalization shows significant promise.

Chapter 12

An Investigation of Electromechanical Behavior

Microcantilevers are highly sensitive transducers of surface stress (chapter 2). Electrochemical methods allow control of the electrode potential while monitoring the current and charge (chapter 3), among other techniques. In conjunction with appropriate surface modifications, electrochemical-cantilever (ECC) measurements offer a means to mechanically investigate electrochemically-induced phenomena, *e.g.* monitoring potential-induced denaturing of DNA [81]. However, observing these events using such a highly coupled system requires the system itself be carefully characterized.

This chapter explores how an applied potential affects the motion of the cantilever. Step potentials were applied to the electrode in buffered electrolyte to actuate the cantilever. Surface stress during cyclic voltammetry was monitored in buffered electrolyte with and without a redox couple, and the effect of reduction and oxidation on surface stress were observed. This data was fit to a first order approximation of the Lippmann equation [69] to verify that the motion was caused by charge accumulation and dissipation. Finally, a cysteine-modified cantilever was voltammetrically cleaned, as in section 11.2.1, and the evolution of the current and surface stress signals was monitored. The work presented here demonstrates the full capabilities of the ECC platform for combined sensing.

12.1 Experimental Methods

12.1.1 Cantilever-Electrode Configuration

All measurements in this chapter were performed using the same electrode configuration. One cantilever was connected as a working electrode, while

an adjacent cantilever was connected as the reference/counter, thus creating an identical two-electrode system. This was done since a real reference electrode was not being incorporated, and analytical/quantitative electrochemistry would not be performed. The CHI 660C electrochemical workstation (figure 3.2(c)) was used to control potential and acquire current and charge data.

The working electrode cantilever was interrogated by the optical lever method using the NanoNose optical setup (section 10.3). Only one cantilever was monitored in these experiments since differential measurements were not required. Cantilevers were let to reach zero drift, first in a flow, and then in motionless electrolyte, before every measurement. All potential steps and sweeps were applied with the fluid at zero flow through the channel. All electrochemical data was recorded using the CHI 660C potentiostat software, while all cantilever deflection data was acquired using a LabView interface built by Søren Dohn. All data was combined in OriginPro 7.5 for processing and presentation.

12.1.2 Techniques

Potential Steps

Potential steps were applied to the clean gold cantilever-electrodes in an electrolyte consisting of 30 mM NH_4Ac and 30 mM KNO_3 (pH 6.8). The first experiment had potentials of $E = +0.4, +0.2, -0.2, -0.4$ and -0.6 V applied to the cantilever (vs. the Au reference cantilever electrode) for 30 s and then returned to open circuit potential, while monitoring cantilever deflection. The second experiment applied potential steps of 0.1 V (in both positive and negative directions) for 1 minute each, again, while monitoring deflection, as well as current through the cantilever surface.

Potential Sweeps

Potential sweeps were applied to the clean gold cantilever-electrodes in an electrolyte consisting of 50 mM H_2PO_4 and 50 mM KNO_3 (pH 6.2). Cyclic voltammetry was performed between potentials of $E = -0.5$ and $+0.5$ V, at a sweep rate of 0.05 V/s for 3 cycles. Voltammetry was performed in buffered electrolyte first without, and then with 1 mM $[Fe(CN)_6]^{3-/4-}$redox probe couple. The measurement setup (ECC chip/flow cell/NanoNose) were not moved, exchanged, opened, or realigned during this experiment, and between the CVs without and with the redox couple, so that runs could be directly compared.

Voltammetric Cleaning

Voltammetric cleaning was performed in the same manner as chapter 11. An ECC chip was functionalized with L-cysteine following cleaning, using the protocol described in section 11.1.1. Two cantilevers (one WE, one RE/CE) were connected to the potentiostat and cycled between potentials of $E = -1.2$ and $+1.2$ V at a rate of 0.1 V/s until the cyclic voltammagram ceased to change, indicating the charge transfer characteristics of the electrode surface were no longer improving. Cantilever deflection and current were monitored simultaneously to observe the change in surface stress.

12.2 Results

12.2.1 Response to Potential Steps

Potential steps were applied to cantilever electrodes for a duration of 30 s in buffered electrolyte, the results of which are plotted in figure 12.1. The first noteworthy feature in this plot is the direction of the surface stress with respect to the applied potential. Seen here in figure 12.1 and in other electrolytes lacking redox active species, the surface stress is compressive for a positive potential ($\Delta\sigma < 0$ for $E > 0$), and is tensile under a negative potential ($\Delta\sigma > 0$ for $E < 0$), similar to observations in literature [29, 34, 66, 86]. After 30 s the potential returns to open circuit, and the cantilevers slowly drift towards a stable stress value near zero.

Table 12.1: The surface stress caused by each step potential from figure 12.1.

Applied Potential (V)	Observed Stress (mN/m)
+0.4	-52
+0.2	-14
-0.2	+12
-0.4	+42
-0.6	+65

At higher potentials, $E = +0.4$ and -0.6 V, the stress signal exhibits a negative drift over the 30 s the potential is held. After the step function the three lower potentials appear to reach a stable stress level and remain constant. The rate of sweeping a potential is known to affect where the

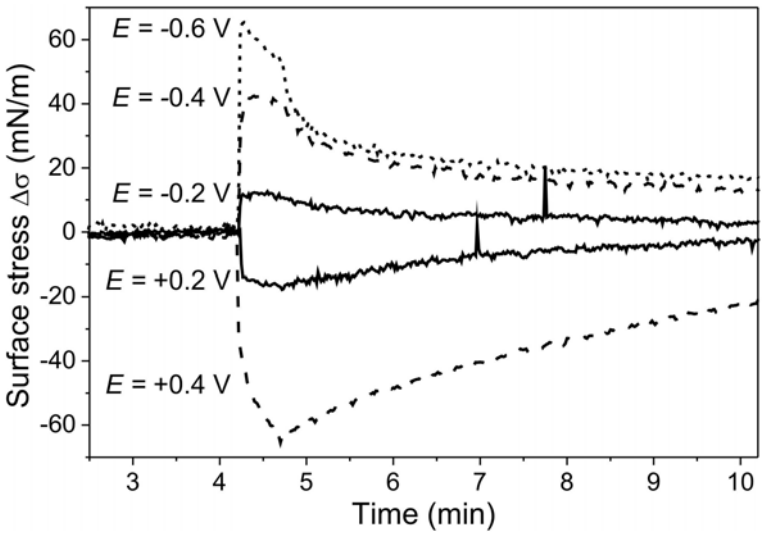

Figure 12.1: The indicated potentials where applied at $t = 4$ min 10 s and held constant for 30 s while recording cantilever deflection. Note that negative potentials cause a tensile stress, while positive potentials cause a compressive stress, and the significant negative drift at potentials of $E = -0.6$ V and $E = +0.4$ V. Surface stress values due to the potential step (ignoring drift) are tabulated in table 12.1. Electrolyte: 30 mM NH_4Ac and 30 mM KNO_3 (pH 6.8).

maximum stress develops, with respect to potential or time [57]. Similarly, potential steps larger in magnitude require a longer time to reach equilibrium than smaller steps. Even at the smaller positive potential, $E = +0.2$ V, a slight negative drift is noticeable.

A theoretical basis for this behavior is provided by Weigend *et al.* [87]. Surface atoms lack nearest neighbors, thus suffer from a reduced coordination number compared to atoms within the bulk. This causes charge redistribution to in-plane and interior bonds, resulting in a slight lateral and inward contraction, observed as a tensile surface stress [228]. In charged metal surfaces the excess electrons are located outside of the outermost layer of ions, creating a surface-excess electron density wave. This shifts the electrostatic center of gravity, causing the ions to relax to a new equilibrium position. Weigend found that the interaction between the ions and this density wave is attractive and relaxation is outward. This results in a negatively charged gold surface (*i.e.* with excess electrons) exhibiting a tensile stress relative to its charge-neutral state, with the reverse being true for a positively charged surface. This explains the stress-potential direction observed in figure 12.1.

Weigend also notes that counter charges outside the surface (*e.g.* ions in solution) typically cancel the electrostatic effect of the charged surface, thus

it is the relaxation previously described responsible for the stress [87]. However, a positively or negatively charged surface will attract anions or cations, respectively. The accumulation of such species in the process of creating an equilibrium at the interface creates a compressive stress, or rather a reduction of the tensile stress, by disrupting the surface charge density [88]. This compressive stress due to ion species was also observed in section 11.2.5. Thus, higher potentials will attract more ions, which will adsorb to the surface, causing a larger drift.

Figure 12.2 depicts an applied potential step series, with steps of 0.1 V. Again, with the measurements taken only in buffered electrolyte with no redox active species available there should be no charge transfer events. This is confirmed by the minuscule current read, and how it quickly drops to a value near zero. The electronic double layer is setup within seconds, and the non-Faradic current stops just as quickly. The surface stress follows the potential quite closely, again with negative potentials creating a tensile stress, and slight drifts are observed at held potentials. However, despite the drift, within this small potential range, surface stress appeared to be linear with potential at $\Delta\sigma/E \sim 75$ mNm^{-1}V^{-1}. Again, the reasons previously discussed for stress direction apply here.

12.2.2 Response to Cyclic Voltammetry

Figure 12.3 plots the surface stress and applied potential versus time in a buffered electrolyte, now 50 mM H_2PO_4 and 50 mM KNO_3 (pH 6.2). Once again, the opposite signs of surface stress and applied potential are apparent. The stress seems to follow the potential closely, with little or no lag at this scan rate (0.05 V/s). Due to the data acquisition electronics on the NanoNose, cantilever deflection data can only be acquired at one point per second, meaning faster scans incorporate fewer data points. It is for this reason that slower scans are preferred. While this figure is adequate for comparing shapes it is leaving out a major component of the voltammagram: the current.

Combined measurements are most easily interpreted when both surface stress and current are plotted versus the applied cyclic potential. Figure 12.4 plots the data from figure 12.3 in a stress-CV. Here the linear relationship between surface stress and potential is clearly visible, and the current signal confirms that there was no redox active species in the electrolyte. As expected from figures 12.1 and 12.2, in the absence of charge transfer events the surface stress is proportional to the applied potential. However, the stress per volt is different here, at $\Delta\sigma/E \sim 275$ mNm^{-1}V^{-1}, which can be attributed to a number of differences: pH, ionic concentration, ion species,

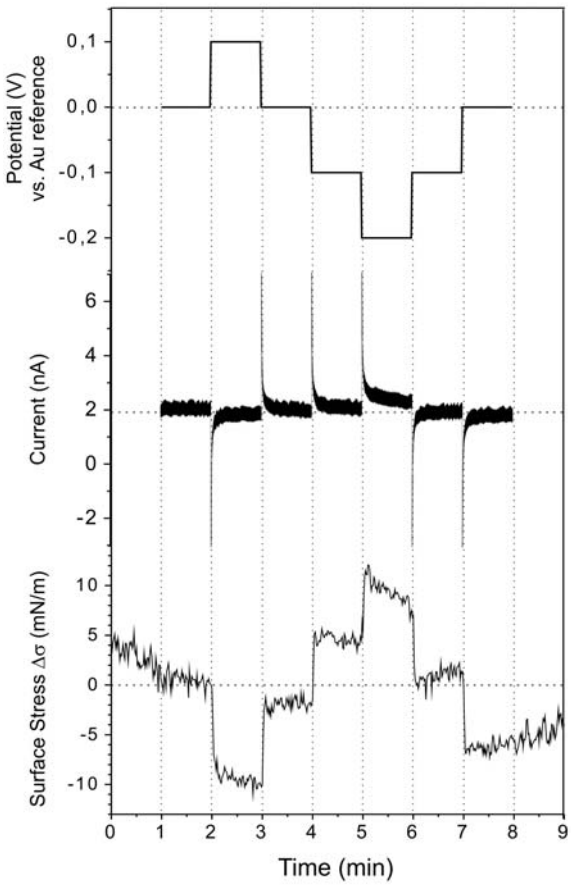

Figure 12.2: Plots of the applied potential (*top*), measured current (*middle*), and surface stress response (*bottom*). Starting at $t = 1$ min each indicated potential was held for 1 min, and changed in 0.1 V steps. Note that the current quickly becomes zero as this is the result of the double layer capacitance and non-Faradaic current. Drift notwithstanding, the steps in surface stress for each 0.1 V potential step are consistently 7-8 mN/m. Electrolyte: 30 mM NH_4Ac and 30 mM KNO_3 (pH 6.8).

scan rate. It is clear that, for proper comparison between experiments, strict control of all flow cell parameters must be kept.

All parameters under which the data plotted in figure 12.5 was taken were kept identical to those of figure 12.4, *i.e.* the buffer, pH, ionic concentration and species, scan range, scan rate, number of cycles, laser placement, and even PDMS gasket placement were kept constant. Thus the altered appearance of the stress-CV in figure 12.5 is solely due to the addition of 1 mM $[Fe(CN)_6]^{3-/4-}$. The addition of a redox active species means charge transfer events now occur, affecting the charge on the electrode surface, and thus

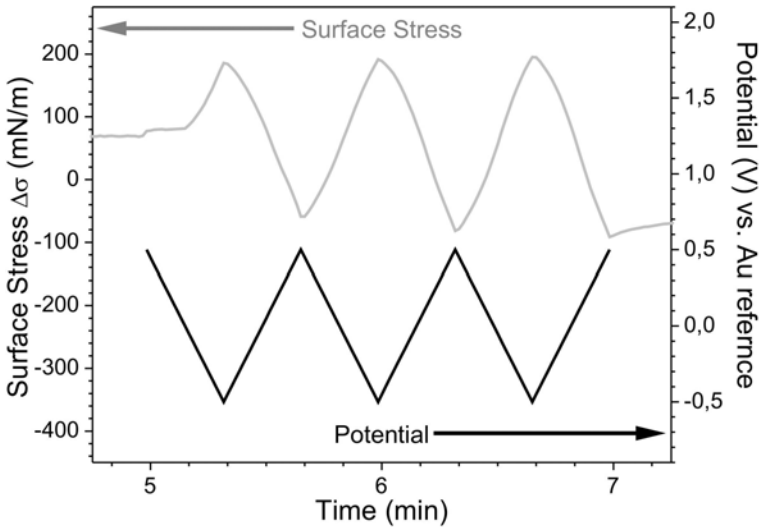

Figure 12.3: Plot of the applied potential (bottom signal, right axis) and resulting surface stress (top signal, left axis). As in figures 12.1 and 12.2, a positive potential causes a compressive (negative) stress, while a negative potential causes a tensile (positive) stress. As in figure 12.1, when the potential is released after 7 minutes, the surface stress stabilizes at a value close to where it began. Electrolyte: 50 mM H_2PO_4 and 50 mM KNO_3 (pH 6.2).

the stress. The stress signal is no longer linear with potential, but attains a maximum near $E = 0$ V, the equilibrium potential ($E_{1/2}$) in this system. Following the stress signal, as it cycles with potential it decreases (becomes less tensile) as it moves towards the negative potential limit. The stress continues to decrease after changing scan direction, and its rate of descent increases further at $E = +0.2$ V. While this stress-CV in $[Fe(CN)_6]^{3-/4-}$compares with those found in literature [29], the peaks in the stress signal do not directly correlate to any points on the voltammagram, which takes the standard shape of a reversible redox process.

It should be noted that buffered electrolyte is still present, meaning the stress signal in figure 12.5 is a superposition of the signals from both the electrolyte as well as the reduction and oxidation events.

While the data in figure 12.4 and 12.5 were not collected simultaneously, and thus do not constitute a true differential measurement, the stress signal in figure 12.4 can still be taken as a baseline and subtracted from the stress in figure 12.5. All parameters for the two experiments were kept identical, thus it is reasonable to use the data in figure 12.4 as a negative control. This yields figure 12.6, a stress-CV where the surface stress signal is due to the redox events in the solution, without the superimposed linear dependence

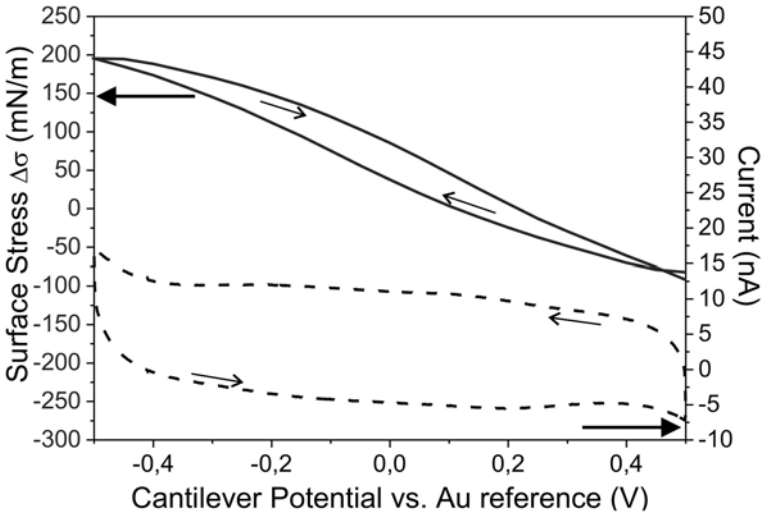

Figure 12.4: A plot of surface stress (solid line, left, axis) and current (dashed line, right axis) as a function of potential cycling, in buffered electrolyte: 50 mM H_2PO_4 and 50 mM KNO_3 (pH 6.2). The surface stress is linear with potential. It can be seen from both the stress and current signals that there are no reduction or oxidation events occurring. This is expected since the electrolyte contains no species which are electroactive in this potential range.

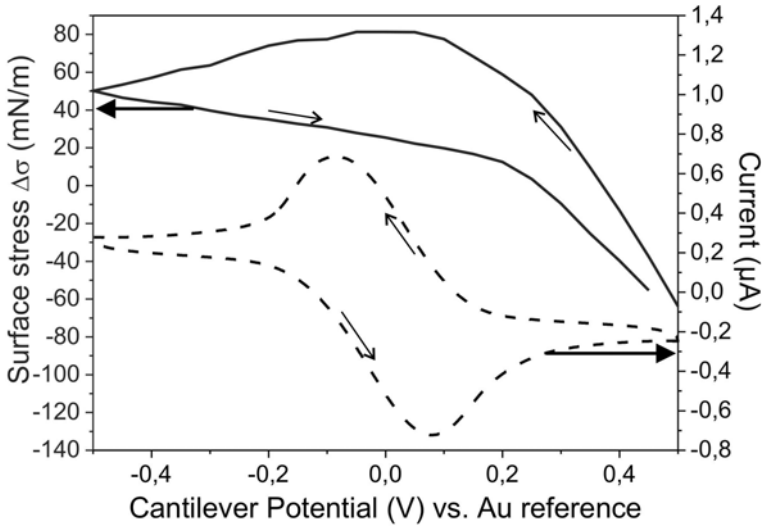

Figure 12.5: A plot of surface stress (solid line, left, axis) and current (dashed line, right axis) as a function of potential cycling, in buffered electrolyte with a redox couple: 1 mM $[Fe(CN)_6]^{3-/4-}$, 50 mM H_2PO_4 and 50 mM KNO_3 (pH 6.2). The current signal takes on the familiar shape of a reversible redox couple, while the surface stress reaches a maximum during the anodic (negative) sweep near $E = 0$ V, which is the $E_{1/2}$ in this setup.

on potential. The maximum on the anodic scan has moved to approximately $E = +0.2$ V, which is where the change in slope of the cathodic scan remains.

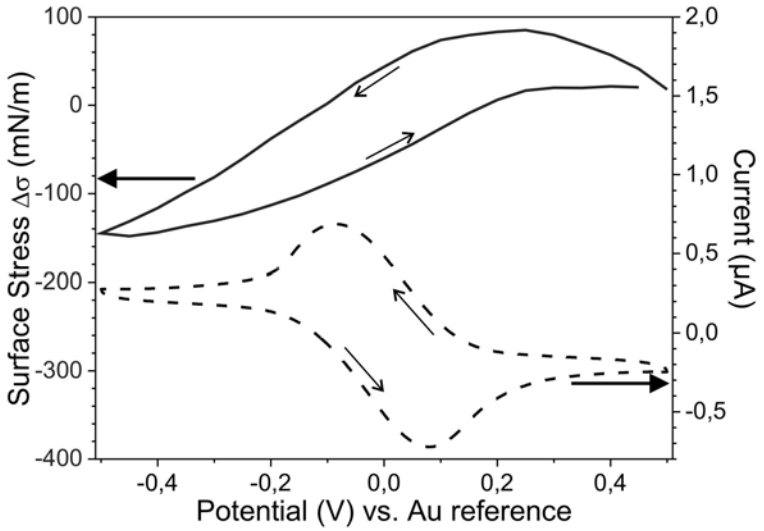

Figure 12.6: A differential surface stress signal is created by subtracting figure 12.4 from figure 12.5, to return only the stress due to the $[Fe(CN)_6]^{3-/4-}$reduction and oxidation events. The surface stress (solid line) and current (dashed line) are once again plotted against the cyclic applied potential. Once the signal from the buffered electrolyte alone has been subtracted the maximum on the anodic sweep moves to more positive potential at $E = +0.2$ V.

As described in chapter 4, the Shuttleworth equation [58] relates the surface stress, σ, to the surface tension, γ, as seen in equation 12.1:

$$\sigma = \gamma + \frac{d\gamma}{d\varepsilon} \tag{12.1}$$

where ε is the surface strain. Strictly speaking, in the case of solid electrodes the second term is needed to describe the surface energy due to elastic strain, unlike in the case of liquids where it is automatically zero. However, the second term of equation 12.1 is often noted to be much smaller than the first [26, 34, 66], and is thought to be smaller than the measurement noise in these systems. Thus, $\sigma = \gamma$ is a reasonable approximation. The Lippmann equation relates surface charge to stress and tension as follows:

$$\frac{d\gamma}{dE} = -q - (\gamma - \sigma)\frac{d\varepsilon}{dE} \tag{12.2}$$

with E being the electrode potential. It is generally agreed that the second term is negligible [29, 68, 69], again only contributing an error that is most likely below the detection limit in measurements. Thus the Lippmann equation is simplified to

$$-\frac{\partial\gamma}{\partial E} = q \tag{12.3}$$

Now, differentiating the simplified Shuttleworth equation with respect to applied potential, E, we obtain $\partial\gamma/\partial E = \partial\sigma/\partial E$. Substituting this into equation 12.3 we are left with

$$-\frac{\partial\sigma}{\partial E} = q \tag{12.4}$$

Equation 12.4, while a simple first-order approximation, presents an opportunity to test the data acquired in the above figures against theory. Figure 12.7 plots the charge of the electrode (q), acquired during voltammetry, with the negative first derivative of the surface stress with respect to the potential ($-\partial\sigma/\partial E$). Since the NanoNose only captures one data point per second and has visible signal noise at these stress levels, the quality of the derivative taken from this signal is correspondingly low. Still, it is possible to make out the basic shape of the $-\partial\sigma/\partial E$ curve and see that it resembles the charge signal, and that both signals have their maxima and minima at the same potentials. With the acquired data matching with a theoretical approximation the ECC platform is verified as a hybrid sensing platform.

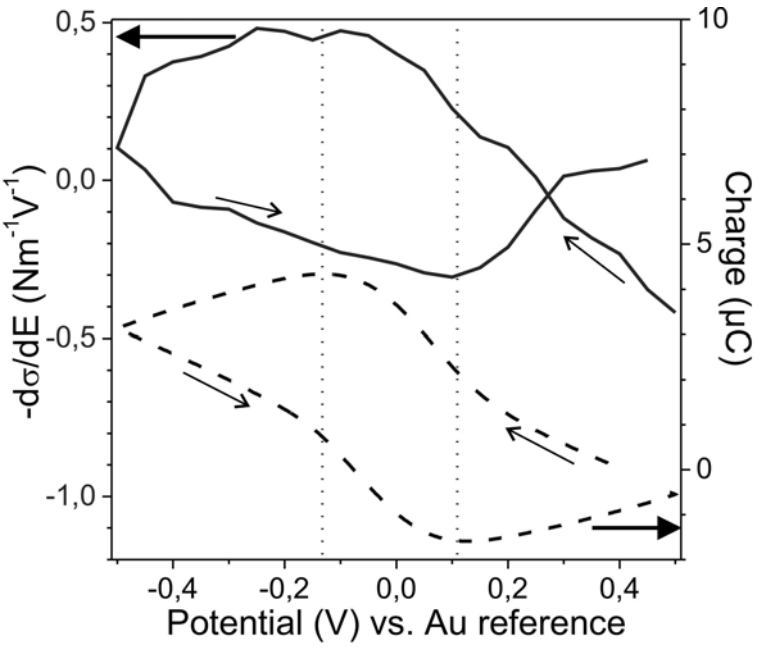

Figure 12.7: The negative first derivative ($-\partial\sigma/\partial E$) of the surface stress with respect to the potential is plotted (solid line) with the measured electrode charge (dashed line). The two plots resemble each other in shape, as expected from equation 12.4.

12.2.3 Combined Readout Monitoring of Voltammetric Cleaning

Finally, the ECC platform was used to explore the voltammetric cleaning application used in chapter 11. The potential applied to the cantilevers was cycled until the voltammagram ceased to change, indicating that the electrode surface was clean. As a first step in using this ECC platform to investigate potential-controlled phenomena, the effect of voltammetric cleaning on the evolution of surface stress was explored. Acquiring these measurements in real-time meant a progression would need to be plotted to observe the evolution of the signals. Figure 12.8 displays the raw surface stress and applied potential signals with respect to time. While this is not particularly useful for understanding the peaks that are generated, the evolution of the surface stress can be clearly seen.

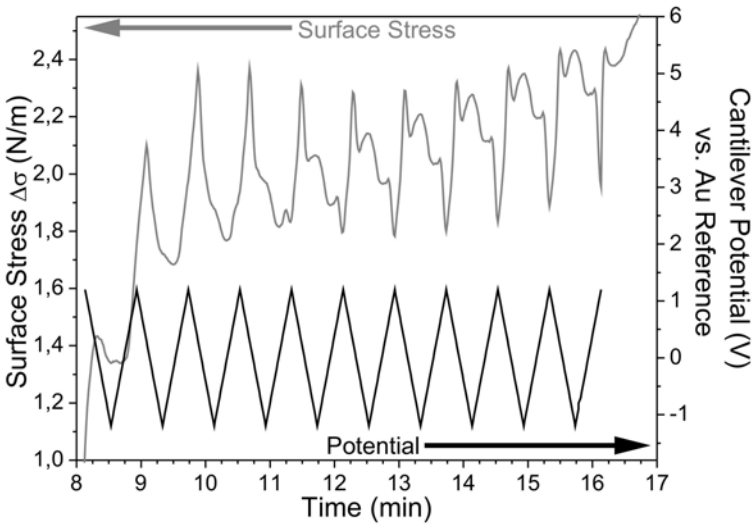

Figure 12.8: The surface stress (top signal, left axis) and applied potential (bottom signal, right axis) are plotted versus time for a cysteine-modified cantilever being voltammetrically cleaned, as described in section 11.2.1. Notice how the signal evolves over the course of the voltammetry, indicating that the charge transfer characteristics of the surface are being changed. Electrolyte: 1 mM $[Fe(CN)_6]^{3-/4-}$, 50 mM H_2PO_4 and 50 mM KNO_3 (pH 6.2).

Figure 12.9 and 12.10 plot the oxidation and reduction sweeps of the progression, respectively. Figure 12.9 shows the $[Fe(CN)_6]^{3-/4-}$peak in the oxidative voltammagram evolving towards zero (decreasing the ΔE), with a feature near $E = 1.1$ V being "smoothed out" over the course of the cycling. The oxidative stress curves develop from having a minimum near $E = 0$ V into the familiar shape observed in figure 12.5 of a clean gold surface.

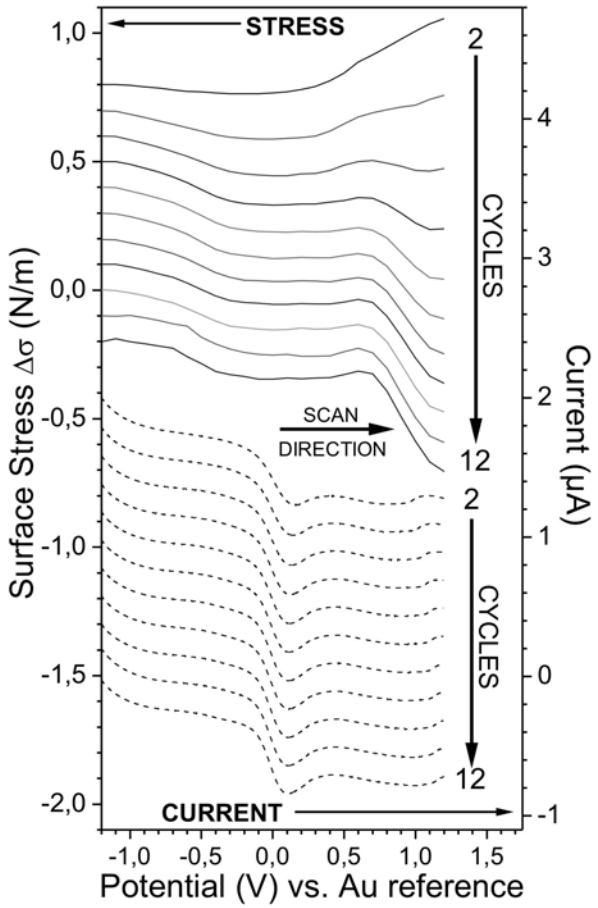

Figure 12.9: The progression of the oxidative (cathodic) sweeps, surface stress (solid line) and current (dashed line), are plotted versus cyclic potential. Features of note in the current signal include the oxidation peak shifting towards zero (narrowing the ΔE of the CV), and the flattening of the feature at $E = 1.1$ V. The tensile surface stress near the positive end of the potential axis decreases significantly and the signal takes on the familiar shape seen in figure 12.5. Electrolyte: 1 mM $[Fe(CN)_6]^{3-/4-}$, 50 mM H_2PO_4 and 50 mM KNO_3 (pH 6.2).

Similarly, the $[Fe(CN)_6]^{3-/4-}$reduction peak evolves toward $E = 0$ V[1] in figure 12.10, which shows the anodic sweeps of the cyclic voltammagrams. Further, an additional reduction peak develops at $E = +0.35$ V which cannot be attributed to a clean gold electrode in $[Fe(CN)_6]^{3-/4-}$, and thus must be an artifact of the cysteine monolayer. The reductive stress curve evolves from having merely an inflection point at $E = +0.3$ V to a more pronounced peak, similar to stress curves reported by Tian *et al.* [29]. The overall obser-

[1]As described in chapter 6, this decrease in ΔE indicates an improvement in electron transfer characteristics, which is indicative of a cleaner surface.

vation of figures 12.9 and 12.10 is that, in both the stress and current plots, the signals evolve smoothly over time as the number of cycles grows, and does not suddenly change.

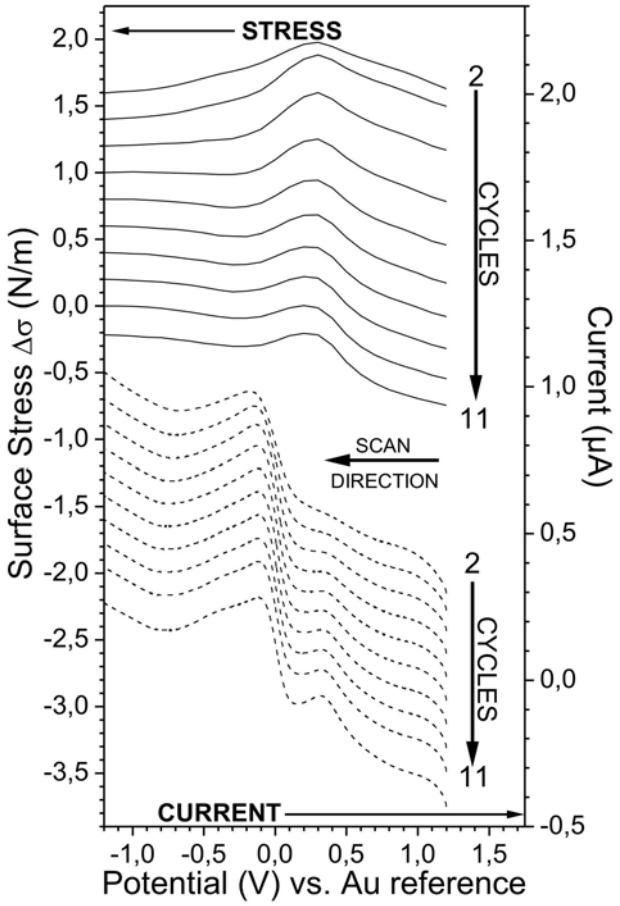

Figure 12.10: The progression of the reductive (anodic) sweeps, surface stress (solid line) and current (dashed line), are plotted versus the cyclic potential. Features of note in the current signal include the reduction peak shifting towards zero (narrowing the ΔE of the CV), and the appearance of a small peak at at $E = 0.3$ V. The surface stress evolves a more pronounced peak, which also shifts towards negative. Electrolyte: 1 mM $[Fe(CN)_6]^{3-/4-}$, 50 mM H_2PO_4 and 50 mM KNO_3 (pH 6.2).

To more clearly differentiate between the cysteine-modified cantilever before and after cleaning, figure 12.11 presents the first and last stress-voltammagrams taken in this series. The voltammagrams contain similar features to those previously acquired while cleaning cysteine-modified electrodes in chapter 11, including the new unidentified reduction peak. Again, this peak does not appear when using a clean gold electrode and thus must

be an artifact of the cysteine layer. Cantilever electrodes exhibiting this peak still behave in the expected manner as a clean cantilever, meaning this peak must not significantly interfere with the copper ion binding. Further investigation is required to determine the cause of this reduction peak.

In a system with so many components, determining the exact source of the stress curve shape is extremely difficult. It can be noted, however, that the final stress curve cycle much more closely resembles figure 12.5, as well as plots presented by Tian *et al.* [29], than does the stress curve from the first cycle. This, in addition to the CV, indicates that the surface of the cantilever has been permanently altered due to this potential cycling. Combined electrochemical-cantilever voltammetry is a powerful analytical tool for investigating this type of phenomena, but requires a high-level of understanding of both surface stress and electrochemical behaviors.

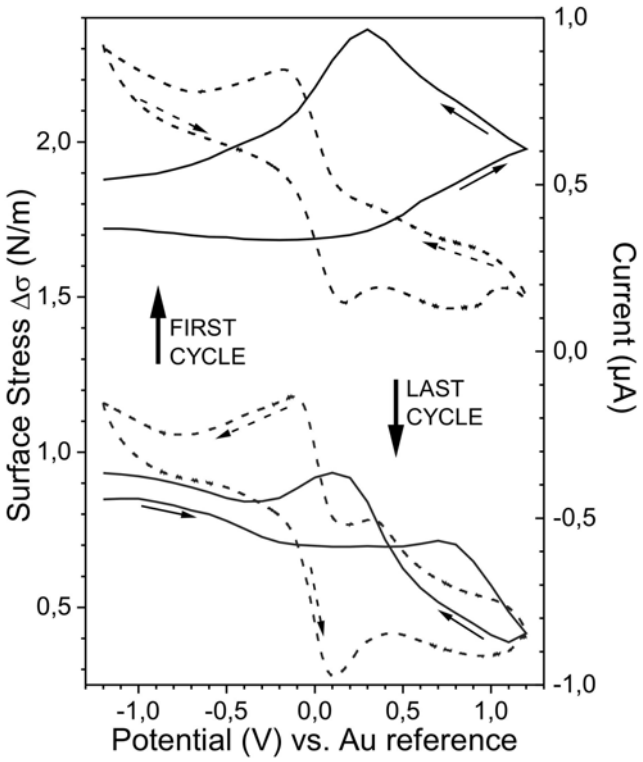

Figure 12.11: The surface stress (solid lines) and current (dashed lines) for the first and last cycle of the voltammetric cleaning are plotted versus the cycling potential. The features which were seen to evolve in figures 12.9 and 12.10 are more clearly visible here. Note that the shape of the "last cycle" is much closer to a clean CV in $[Fe(CN)_6]^{3-/4-}$than the "first cycle". Electrolyte: 1 mM $[Fe(CN)_6]^{3-/4-}$, 50 mM H_2PO_4 and 50 mM KNO_3 (pH 6.2).

12.3 Summary

12.3.1 Conclusion

This chapter presented an investigation of the electromechanical behavior of the ECC platform. The application of potential steps was yielded a linear dependence of surface stress on applied potential of ~ 75 mNm^{-1}V^{-1} within a range of -0.2 V $< E < +0.2$ V. The direction of the surface stress with respect to the sign of the applied potential was found to agree with observations reported in literature, as well as with currently accepted theory. Cyclic voltammetry was used to explore the effect of 1 mM $[Fe(CN)_6]^{3-/4-}$redox couple concentration on the stress-CV in buffered electrolyte. In the absence of redox events the surface stress responded linearly with applied potential, but a stress maximum and inflection points appeared upon introduction of redox active species. A plot of the negative first derivative of surface stress (with respect to potential) was found to have the same basic shape, as well as maximum and minimum value locations, as the cantilever charge. This agrees with a first-order approximation of the Lippmann equation. Finally, preliminary data was presented on real-time stress-voltammetry monitoring of the evolution of a cysteine-modified electrode surface during electrochemical cleaning. Several features in the plots were noted, but full identification of all features would require further investigation.

This chapter marks the final stage in the development of the ECC platform: full combined operation of and data acquisition with the hybrid platform, as well as understanding and verification of the basic principles and theory that govern its operation.

12.3.2 Outlook: Cantilever Voltammetry

Immediately following the presented investigation, several improvements to the system are obvious. First, the acquisition of data requires streamlining. Voltammetric and deflection data must be combined manually and start and finish points of the voltammagrams must be manually identified in the deflection graphs. A first attempt at remedying this would be to use the same LabView interface to acquire the cantilever potential along with the time and deflection. Second, a stable reference electrode is required to aid in identifying peaks. The current symmetric two-electrode setup served well in this chapter, but having a stable reference potential would allow partial identification of observed peaks. Third, a higher rate of data acquisition for the cantilever deflection is necessary to allow for faster scan rates, and to allow for averaging, thus reducing the effect of noise when taking the derivative of the surface stress.

The investigation of the electromechanical behavior, as well as the real-monitoring of the surface stress during voltammetric cleaning represent only a small percentage of what could be accomplished with such combined measurement techniques. Examining the real-time stress response of potential-directed events, such as the cleaning observed in this chapter, or the potential-induced denaturing of DNA performed by Bongrain *et al.* [81]. Also, since cantilever drift is due to the formation of an equilibrium between the composition of the electrical double layer and the intrinsic surface charge and stress, an applied potential could be used to quickly set the cantilever at its equilibrium instead of waiting an hour or more for stabilization.

Chapter 13

PROJECT SUMMARY

13.1 Conclusion

The goal of this project was to design, fabricate, and use a novel electrochemical-cantilever hybrid platform. Considering the work that has been presented within these pages, it is clear that this goal was achieved, and the combined measurement capabilities of the resulting platform have been verified.

A 1 mm^2 gold film electrode chip format, as well as a protocol to achieve a reliably clean gold surface was developed and used to screen functional layers for detecting Cu^{2+} ions. L-cysteine and Cys-Gly-Gly-His monolayers were screened for their ability to bind copper ions using voltammetry, impedance, and QCM methods. A number of Ph.D. students have since used the electrode design and cleaning protocol, as well as the custom CGGH peptide in their respective projects.

An optimized process was developed to microfabricate electrochemical-cantilever chips with integrated reference/counter electrodes, and multiple, individually-addressable cantilever working electrodes. The chips could be batch-fabricated and had a yield of nearly 100%. A polymer flow cell was designed, fabricated, and optimized to eliminate leaking and achieve reliable electrical contact and optical access. Together the ECC chip and flow cell provided an environment in which the surface stress of multiple electrodes could be monitored simultaneously during electrochemical measurements, with the ability to exchange fluid without disassembling the chamber. This chip format and flow cell has since been used by other Ph.D. students and assistant professors for combined electrochemical and cantilever measurements.

The cantilevers of the ECC platform were functionalized with cysteine and CGGH monolayers to sense Cu^{2+} ions. Cyclic voltammetry was used

to clean a reference cantilever for differential measurements, and rough estimates for adsorption rate constants were obtained. The electromechanical behavior of the platform was investigated using potential steps and sweeps, the direction of which was found to be consistent with theory. Combined cyclic voltammetry and stress measurements using an electrochemical probe, $[Fe(CN)_6]^{3-/4-}$, was fit to an approximation of Lippmann's equation, verifying the source of the surface stress in these experiments. Finally, surface stress was monitored during voltammetric cleaning of a cysteine-coated cantilever. The stress was observed to change with each cycle, reaching a cyclic voltammetry stress response characteristic of a clean gold cantilever electrode.

In conclusion, the work of this project yielded a verified cleaning protocol, a tested Cu^{2+}-sensitive molecule, and a fully-functional electrochemical cantilever platform, all of which have been used by others to further their own projects. A number of measurements were successfully performed with the ECC platform. However, it is quite clear that analyzing the data acquired from such complex measurements requires a high level of understanding of both surface stress and electrochemistry. Further characterization of the phenomena surrounding the operation of these devices is required if the electrochemical-cantilever is to become a useful analytical tool.

13.2 Outlook

Were work on metal ion detection and combined electrochemical-cantilever measurements to continue with this platform, there are a number of issues that require resolution, as well as improvements that increase reliability and usability of the system.

Functional Layers

Chapter 8 concluded with a successful demonstration of L-cysteine and CGGH being used to detect copper. While these layers responded to different concentrations of Cu^{2+}, the results presented only covered this one metal ion species. The attempt to design an As^{3+}-capturing peptide demonstrated how this methodology will not be so easily applied to other species. In the corresponding chapter crown ethers were cited to be highly specific receptors for metal ions. It is believed that this is a promising avenue to pursue regarding the specific detection of toxic heavy metal ions.

In chapter 11 a single cantilever was cleaned voltammetrically to remove its functional layer. This allowed the cantilever to be used as a reference

with respect to the funcationalized one, and differential measurements were obtained. However, applying a second chemical layer, one identical in composition but inert to the target species, would be a more accurate reference surface. As was suggested, potential-directed assembly could be employed to quickly ($\sim$ 5 min) and selectively functionalize each cantilever in the array with different active or inactive monolayers. This should be explored if more advanced differential measurements are to be performed.

Additionally, by applying potentials only to certain cantilevers, one could build multi-layered functional surfaces, and thus not be restricted to single monolayers. This would be useful when screening combinatorial arrays.

The ECC Platform

While the ECC platform functioned very well as a prototype, there are a number of obvious improvements to make.

First, the chip itself requires a modified fabrication process if true electrochemistry is to be performed. Specifically, an Ag/AgCl reference electrode should be integrated into the chip. A simple first attempt would be to use a shadow mask on released chips to cover one of the large area electrodes with Ag, then chlorinate it using either electrochemistry or a Cl-plasma.

Second, the exposed Cr adhesion layer poses a problem. While Au is inert and has a large potential window, Cr can be chemically attacked or oxidized much more easily. Thus, as was done in the 1 mm^2 electrode chips, protection of the edges of the electrode should be incorporated into a modified chip design.

Third, while the flow cell performed adequately, a number of improvements could be made to increase its robustness. The layered and clamped design should be kept, but the exterior should be made from machined aluminum. The interior should be made of Teflon, and a new gasket material, ideally one that will not take up water, should be found. The entire platform could be made extremely compact by reading out the cantilevers using vertical cavity surface emitting lasers (VCSELs) in the floor of the microchannel[1]. Such a system would require only an external potentiostat and would fit in the palm of your hand.

[1] A large amount of work with VCSEL-based cantilever interrogation has been done in the Nanoprobes group, in collaboration with DTU Photonics.

Measurements

The experiments performed within this thesis proved the capabilities of the system. However, a great deal more could be done. Exploring a larger parameter space would be immensely useful in further characterizing the operation of electrochemical-cantilevers. Effects of pH, electrolyte type and concentration, as well as the aforementioned potential-directed assembly are all areas that require further attention. Clearly, a deeper understanding of these factors is required before this powerful analysis technique can be used to its full capacity.

Bibliography

[1] W. H. Organization, "Guidelines for drinking-water quality - third edition," tech. rep., Geneva, 2008. ISBN 978 92 4 154761 1.

[2] A. Tessier, *Metal speciation and bioavailability in aquatic systems*. Chichester ;;New York: J. Wiley, 1995.

[3] R. Voegborlo, A. El-Methnani, and M. Abedin, "Mercury, cadmium and lead content of canned tuna fish," *Food Chemistry*, vol. 67, pp. 341–345, 1999.

[4] S. S. Vutukuru, "Acute effects of hexavalent chromium on survival, oxygen consumption, hematological parameters and some biochemical profiles of the indian major carp, labeo rohita," *International Journal of Environmental Research and Public Health*, vol. 2, no. 3, pp. 456–462, 2005.

[5] A. R. Oller, "Respiratory carcinogenicity assessment of soluble nickel compounds," *Environmental Health Perspectives*, vol. 110, no. Suppl. 5, pp. 841–844, 2002.

[6] M. A. Zoroddu, L. Schinocca, T. Kowalik-Jankowska, H. Kozlowski, K. Salnikow, and M. Costa, "Molecular mechanisms in nickel carcinogenesis: modeling Ni(II) binding site in histone h4," *Environmental Health Perspectives*, vol. 110 Suppl 5, pp. 719–723, Oct. 2002. PMID: 12426119.

[7] M. Hughes, "Arsenic toxicity and potential mechanisms of action," *Toxicology Letters*, vol. 133, no. 1, pp. 1–16, 2002.

[8] Y. Hu, L. Su, and E. T. Snow, "Arsenic toxicity is enzyme specific and its affects on ligation are not caused by the direct inhibition of DNA repair enzymes," *Mutation Research*, vol. 408, pp. 203–218, Sept. 1998. PMID: 9806419.

[9] R. Vindhini and M. Narayanan, "Bioaccumulation of heavy metals in organs of fresh water fish cyprinus carpio (Common carp)," *Int. J. Environ. Sci. Tech.*, vol. 5, no. 2, pp. 179–182, 2008.

[10] P. Apostoli, "Elements in environmental and occupational medicine," *Journal of Chromatography B*, vol. 778, pp. 63–97, 2002.

[11] M. Pesavento, G. Alberti, and R. Biesuz, "Analytical methods for determination of free metal ion concentration, labile species fraction and metal complexation capacity of environmental waters: A review," *Analytica Chimica Acta*, vol. 631, no. 2, pp. 129–141, 2009.

[12] G. Hanrahan, D. G. Patil, and J. Wang, "Electrochemical sensors for environmental monitoring: design, development and applications," *Journal of Environmental Monitoring*, vol. 6, no. 8, p. 657, 2004.

[13] W. Yang, J. J. Gooding, and D. B. Hibbert, "Redox voltammetry of sub-parts per billion levels of cu2+ at polyaspartate-modified gold electrodes," *The Analyst*, vol. 126, no. 9, pp. 1573–1577, 2001.

[14] G. Xu, Y. Yuan, S. Kim, and J. Lee, "Surface modification of gold by quercetin monolayer for the electrochemical determination of Copper(II)," *Electroanalysis*, vol. 20, no. 15, pp. 1690–1695, 2008.

[15] E. Chow, E. L. S. Wong, O. Pascoe, D. B. Hibbert, and J. J. Gooding, "Extending the dynamic range of electrochemical sensors using multiple modified electrodes," *Analytical and Bioanalytical Chemistry*, vol. 387, no. 4, pp. 1489–1498, 2007.

[16] B. Zeng, X. Ding, and F. Zhao, "Voltammetric response of glutathione and 3-Mercaptopropionic acid Self-Assembled monolayer modified gold electrodes to Cu(II)," *Electroanalysis*, vol. 14, no. 10, p. 651, 2002.

[17] A. Profumo, D. Merli, and M. Pesavento, "Self-assembled monolayer modified gold electrodes for traces Cu(II) determination," *Analytica Chimica Acta*, vol. 557, no. 1-2, pp. 45–51, 2006.

[18] H. P. Lang and C. Gerber, "Microcantilever sensors," in *Stm and Afm Studies On*, vol. 285 of *Topics in Current Chemistry*, pp. 1–27, Berlin: Springer-Verlag Berlin, 2008.

[19] H. P. Lang, M. Hegner, and C. Gerber, "Cantilever array sensors," *Materials Today*, pp. 30–36, Apr. 2005.

[20] J. Fritz, "Translating biomolecular recognition into nanomechanics," *Science*, vol. 288, no. 5464, pp. 316–318, 2000.

[21] J. Fritz, "Cantilever biosensors," *The Analyst*, vol. 133, no. 7, p. 855, 2008.

[22] H. Ji, T. Thundat, R. Dabestani, G. M. Brown, P. F. Britt, and P. V. Bonnesen, "Ultrasensitive detection of CrO42- using a microcantilever sensor," *Analytical Chemistry*, vol. 73, no. 7, pp. 1572–1576, 2001.

[23] S. Cherian, R. Gupta, B. Mullin, and T. Thundat, "Detection of heavy metal ions using protein-functionalized microcantilever sensors," *Biosensors and Bioelectronics*, vol. 19, no. 5, pp. 411–416, 2003.

[24] P. J. Chapman, Z. Long, P. G. Datskos, R. Archibald, and M. J. Sepaniak, "Differentially ligand-functionalized microcantilever arrays for metal ion identification and sensing," *Analytical Chemistry*, vol. 79, no. 18, pp. 7062–7068, 2007.

[25] Y. M. Xu, H. Q. Pan, S. H. Wu, and B. L. Zhang, "Interaction between tripeptide Gly-Gly-His and cu2+ probed by microcantilevers," *Chinese Journal of Analytical Chemistry*, vol. 37, no. 6, pp. 783–787, 2009.

[26] R. Raiteri and H. J. Butt, "MEASURING ELECTROCHEMICALLY INDUCED SURFACE STRESS WITH AN ATOMIC-FORCE MICROSCOPE," *Journal of Physical Chemistry*, vol. 99, no. 43, pp. 15728–15732, 1995.

[27] T. A. Brunt, E. D. Chabala, T. Rayment, S. J. Oshea, and M. E. Welland, "Measuring surface stress induced by electrode processes using a micromechanical sensor," *Journal of the Chemical Society-Faraday Transactions*, vol. 92, no. 20, pp. 3807–3812, 1996.

[28] W. Haiss, "Linear correlation between surface stress and surface charge in anion adsorption on au(111)," *Journal of Electroanalytical Chemistry*, vol. 452, no. 2, pp. 199–202, 1998.

[29] F. Tian, J. H. Pei, D. L. Hedden, G. M. Brown, and T. Thundat, "Observation of the surface stress induced in microcantilevers by electrochemical redox processes," *Ultramicroscopy*, vol. 100, no. 3-4, pp. 217–223, 2004.

[30] V. Tabard-Cossa, M. Godin, L. Y. Beaulieu, and P. Grutter, "A differential microcantilever-based system for measuring surface stress changes induced by electrochemical reactions," *Sensors and Actuators B-Chemical*, vol. 107, no. 1, pp. 233–241, 2005.

[31] M. Lahav, C. Durkan, R. Gabai, E. Katz, I. Willner, and M. E. Welland, "Redox activation of a Polyaniline-Coated cantilever: An Electro-Driven microdevice parts of this research are supported by the israel ministry of science and the israel science foundation. m.

lahav gratefully acknowledges the support of the clore israel foundation scholars programme.," *Angewandte Chemie International Edition*, vol. 40, no. 21, p. 4095, 2001.

[32] V. Tabard-Cossa, M. Godin, P. Grutter, I. Burgess, and R. B. Lennox, "Redox-induced surface stress of polypyrrole-based actuators," *Journal of Physical Chemistry B*, vol. 109, no. 37, pp. 17531–17537, 2005. J. Phys. Chem. B ISI Document Delivery No.: 964ZZ Times Cited: 16 Cited Reference Count: 34 AMER CHEMICAL SOC WASHINGTON.

[33] T. A. Brunt, T. Rayment, S. J. Oshea, and M. E. Welland, "Measuring the surface stresses in an electrochemically deposited metal monolayer: Pb on au(111)," *Langmuir*, vol. 12, no. 24, pp. 5942–5946, 1996.

[34] D. Lee, T. Thundat, and S. Jeon, "Electromechanical identification of molecules adsorbed on microcantilevers," *Sensors and Actuators B: Chemical*, vol. 124, no. 1, pp. 143–146, 2007.

[35] A. F. Bange, G. M. Brown, L. R. Senesac, and T. Thundat, "Stripping voltammetry of pb and cu using a microcantilever electrode," *Surface Science*, vol. 603, no. 21, pp. L125–L127, 2009.

[36] M. Alvarez and L. M. Lechuga, "Microcantilever-based platforms as biosensing tools," *Analyst*, vol. 135, no. 5, pp. 827–836, 2010.

[37] N. V. Lavrik, M. J. Sepaniak, and P. G. Datskos, "Cantilever transducers as a platform for chemical and biological sensors," *Review of Scientific Instruments*, vol. 75, no. 7, pp. 2229–2253, 2004.

[38] A. Boisen and T. Thundat, "Design & fabrication of cantilever array biosensors," *Materials Today*, vol. 12, no. 9, pp. 32–38, 2009.

[39] G. Hahner, "Normal spring constants of cantilever plates for different load distributions and static deflection with applications to atomic force microscopy," *Journal of Applied Physics*, vol. 104, no. 8, p. 084902, 2008.

[40] K. M. Goeders, J. S. Colton, and L. A. Bottomley, "Microcantilevers: sensing chemical interactions via mechanical motion," *Chemical Reviews*, vol. 108, no. 2, pp. 522–542, 2008.

[41] J. Fritz, M. K. Baller, H. P. Lang, T. Strunz, E. Meyer, H. J. Guntherodt, E. Delamarche, C. Gerber, and J. K. Gimzewski, "Stress at the solid-liquid interface of self-assembled monolayers on gold investigated with a nanomechanical sensor," *Langmuir*, vol. 16, no. 25, pp. 9694–9696, 2000.

[42] R. Desikan, S. Armel, H. M. M. III, and T. Thundat, "Effect of chain length on nanomechanics of alkanethiol self-assembly," *Nanotechnology*, vol. 18, no. 42, p. 424028, 2007.

[43] R. Berger, E. Delamarche, H. P. Lang, C. Gerber, J. K. Gimzewski, E. Meyer, and H. J. Guntherodt, "Surface stress in the self-assembly of alkanethiols on gold," *Science*, vol. 276, no. 5321, pp. 2021–2024, 1997.

[44] W. M. Shu, S. Laurenson, T. P. J. Knowles, P. K. Ferrigno, and A. A. Seshia, "Highly specific label-free protein detection from lysed cells using internally referenced microcantilever sensors," *Biosensors & Bioelectronics*, vol. 24, no. 2, pp. 233–237, 2008.

[45] M. Yue, J. C. Stachowiak, H. Lin, R. Datar, R. Cote, and A. Majumdar, "Label-Free protein recognition Two-Dimensional array using nanomechanical sensors," *Nano Letters*, vol. 8, no. 2, pp. 520–524, 2008.

[46] X. D. Yan, K. Hill, H. Y. Gao, and H. F. Ji, "Surface stress changes induced by the conformational change of proteins," *Langmuir*, vol. 22, no. 26, pp. 11241–11244, 2006.

[47] W. Shu, D. Liu, M. Watari, C. K. Riener, T. Strunz, M. E. Welland, S. Balasubramanian, and R. A. McKendry, "DNA molecular motor driven micromechanical cantilever arrays," *Journal of the American Chemical Society*, vol. 127, no. 48, pp. 17054–17060, 2005.

[48] R. McKendry, J. Zhang, Y. Arntz, T. Strunz, M. Hegner, H. P. Lang, M. K. Baller, U. Certa, E. Meyer, H. Gntherodt, and C. Gerber, "Multiple label-free biodetection and quantitative DNA-binding assays on a nanomechanical cantilever array," *Proceedings of the National Academy of Sciences*, vol. 99, no. 15, pp. 9783–9788, 2002.

[49] G. G. Stoney, "The tension of metallic films deposited by electrolysis," *Proceedings of the Royal Society of London A- Materials*, pp. 172–175, Jan. 1909.

[50] G. Meyer and N. M. Armer, "Novel optical approach to atomic force microscopy," *Applied Physics Letters*, vol. 53, no. 12, pp. 1045–1047, 1988.

[51] S. Alexander, L. Hellemans, O. Marti, J. Schneir, V. Elings, P. K. Hansma, M. Longmire, and J. Gurley, "An atomic-resolution atomic-force microscope implemented using an optical lever," *Journal of Applied Physics*, vol. 65, no. 1, p. 164, 1989.

[52] A. J. Bard, *Electrochemical Methods: Fundamentals and Applications*. Hoboken, NJ: John Wiley & Sons, Inc., 2nd ed., 2000.

[53] D. Sawyer, *Electrochemistry for chemists*. New York: Wiley, 2nd ed. ed., 1995.

[54] J. Bockris, *Modern electrochemistry : Electrodics*. New York: Plenum Press, 2000.

[55] T. R. Beck, "ELECTROCAPILLARY CURVES OF SOLID METALS MEASURED BY EXTENSOMETER INSTRUMENT," *Journal of Physical Chemistry*, vol. 73, no. 2, pp. 466–&, 1969.

[56] G. G. Lang, N. S. Sas, and S. Vesztergom, "Experimental determination of surface stress changes in electrochemical systems - possibilities and pitfalls," *Chem. Biochem. Eng. Q.*, vol. 23, no. 1, pp. 1–9, 2009.

[57] R. A. Fredlein, Damjanov.A, and J. O. Bockris, "DIFFERENTIAL SURFACE TENSION MEASUREMENTS AT THIN SOLID METAL ELECTRODES," *Surface Science*, vol. 25, no. 2, pp. 261–&, 1971.

[58] R. Shuttleworth, "The surface tension of solids," *Proceedings of the Physical Society. Section A*, vol. 63, no. 5, pp. 444–457, 1950.

[59] R. A. Fredlein and J. O. Bockris, "ELECTROCAPILLARY STUDY OF GOLD-PERCHLORIC ACID SOLUTION INTERFACE," *Surface Science*, vol. 46, no. 2, pp. 641–652, 1974.

[60] D. Kramer and J. Weissmuller, "A note on surface stress and surface tension and their interrelation via shuttleworths equation and the lippmann equation," *Surface Science*, vol. 601, no. 14, pp. 3042–3051, 2007.

[61] V. Marichev, "Comment on A note on surface stress and surface tension and their interrelation via shuttleworths equation and the lippmann equation by d. kramer and j. weissmuller [Surf. sci. 601 (2007) 3042]," *Surface Science*, 2008.

[62] D. Kramer and J. Weissmuller, "Reply to Comment on A note on surface stress and surface tension and their interrelation via shuttleworths equation and the lippmann equation by d. kramer and j. weissmller [Surf. sci. 601 (2007) 3042] by V.A. marichev," *Surface Science*, vol. 602, no. 5, pp. 1133–1134, 2008.

[63] V. A. Marichev, "Concept of reversible cleavage in surface tension of solids," *Protection of Metals and Physical Chemistry of Surfaces*, vol. 46, no. 1, pp. 21–26, 2010.

[64] V. Marichev, "Update on current state and problems in the surface tension of condensed matter," *Advances in Colloid and Interface Science*, vol. 157, no. 1-2, pp. 34–60, 2010.

[65] V. Tabard-Cossa, M. Godin, I. J. Burgess, T. Monga, R. B. Lennox, and P. Grutter, "Microcantilever-based sensors: Effect of morphology, adhesion, and cleanliness of the sensing surface on surface stress," *Analytical Chemistry*, vol. 79, no. 21, pp. 8136–8143, 2007.

[66] J. Yang and J. Zhou, *Potential-induced Surface Stress Change during the Electrochemical Reaction.* 2009 Ieee 8th International Conference on Asic, Vols 1 and 2, Proceedings, New York: Ieee, 2009.

[67] R. Raiteri, H. J. Butt, and M. Grattarola, "Changes in surface stress at the liquid/solid interface measured with a microcantilever," *Electrochimica Acta*, vol. 46, no. 2-3, pp. 157–163, 2000.

[68] J. Lipkowski, "Comments on the thermodynamics of solid electrodes," *Journal of Electroanalytical Chemistry*, vol. 452, no. 2, pp. 193–197, 1998.

[69] P. Couchman and C. Davidson, "The lippmann relation and surface thermodynamics," *Journal of Electroanalytical Chemistry*, vol. 85, no. 2, pp. 407–409, 1977.

[70] K. Ueno, "Study of adsorption of iodide ions on gold electrode by a Laser-Beam deflection method compared with a piezoelectric technique," *Journal of The Electrochemical Society*, vol. 146, no. 4, p. 1496, 1999.

[71] H. Ibach, C. E. Bach, M. Giesen, and A. Grossmann, "Potential-induced stress in the solid-liquid interface: Au(111) and au(100) in an HClO4 electrolyte," *Surface Science*, vol. 375, no. 1, pp. 107–119, 1997.

[72] G. Binnig and C. F. Quate, "Atomic force microscope," *Physical Review Letters*, vol. 56, no. 9, pp. 930–933, 1986.

[73] S. J. Oshea, M. E. Welland, T. A. Brunt, A. R. Ramadan, and T. Rayment, "Atomic force microscopy stress sensors for studies in liquids," *Journal of Vacuum Science & Technology B*, vol. 14, no. 2, pp. 1383–1385, 1996.

[74] W. Haiss and J. Sass, "Quantitative surface stress measurements on au(111) electrodes by scanning tunneling microscopy," *Langmuir*, vol. 12, no. 18, pp. 4311–4313, 1996.

[75] W. Haiss and J. Sass, "Adsorbate-induced surface stress at the solid|electrolyte interface measured with an STM," *Journal of Electroanalytical Chemistry*, vol. 386, no. 1-2, pp. 267–270, 1995.

[76] M. Seo and M. Yamazaki, "Changes in surface stress of gold electrode during underpotential deposition of pb," *Journal of The Electrochemical Society*, vol. 151, no. 8, p. E276, 2004.

[77] S. Ahmed, T. T. Ahmed, M. OGrady, S. Nakahara, and D. N. Buckley, "Investigation of stress and morphology in electrodeposited copper nanofilms by cantilever beam method and in situ electrochemical atomic force microscopy," *Journal of Applied Physics*, vol. 103, no. 7, p. 073506, 2008.

[78] F. Quist, V. Tabard-Cossa, and A. Badia, "Nanomechanical cantilever motion generated by a surface-conflned redox reaction," *Journal of Physical Chemistry B*, vol. 107, no. 39, pp. 10691–10695, 2003.

[79] L. L. Norman and A. Badia, "Redox actuation of a microcantilever driven by a Self-Assembled ferrocenylundecanethiolate monolayer: An investigation of the origin of the micromechanical motion and surface stress," *Journal of the American Chemical Society*, vol. 131, no. 6, pp. 2328–2337, 2009.

[80] R. Raiteri, M. Preuss, M. Grattarola, and H. J. Butt, "Preliminary results on the electrostatic double-layer force between two surfaces with high surface potentials," *Colloids and Surfaces a-Physicochemical and Engineering Aspects*, vol. 136, no. 1-2, pp. 191–197, 1998.

[81] A. Bongrain, H. Uetsuka, L. Rousseau, L. Valbin, S. Saada, C. Gesset, E. Scorsone, G. Lissorgues, and P. Bergonzo, "Measurement of DNA denaturation on B-NCD coated diamond micro-cantilevers," *physica status solidi (a)*, vol. 207, no. 9, pp. 2078–2083, 2010.

[82] M. Seo and Y. Serizawa, "Changes in surface stress of platinum electrode in acidic and alkaline sulfate or alkaline fluoride solutions," *Journal of The Electrochemical Society*, vol. 150, no. 10, p. E472, 2003.

[83] F. Amiot, F. Kanoufi, F. Hild, and J. P. Roger, "Charge redistribution in electrochemically actuated mechanical sensors," *Sensors and Actuators a-Physical*, vol. 152, no. 1, pp. 88–95, 2009.

[84] F. Amiot, F. Hild, F. Kanoufi, and J. P. Roger, "Identification of the electroelastic coupling from full multi-physical fields measured at the micrometre scale," *Journal of Physics D-Applied Physics*, vol. 40, no. 11, pp. 3314–3325, 2007.

[85] R. G. Maus, E. M. McDonald, and R. M. Wightman, "Imaging of nonuniform current density at microelectrodes by electrogenerated chemiluminescence," *Analytical Chemistry*, vol. 71, no. 21, pp. 4944–4950, 1999.

[86] D. Kramer, R. N. Viswanath, and J. Weissmller, "Surface-Stress induced macroscopic bending of nanoporous gold cantilevers," *Nano Letters*, vol. 4, no. 5, pp. 793–796, 2004.

[87] F. Weigend, F. Evers, and J. Weissmller, "Structural relaxation in charged metal surfaces and cluster ions," *Small*, vol. 2, no. 12, pp. 1497–1503, 2006.

[88] M. Godin, V. Tabard-Cossa, Y. Miyahara, T. Monga, P. J. Williams, L. Y. Beaulieu, R. B. Lennox, and P. Grutter, "Cantilever-based sensing: the origin of surface stress and optimization strategies," *Nanotechnology*, vol. 21, no. 7, p. 8, 2010.

[89] X. Xie, Z. Berner, J. Albers, and D. Stben, "Electrochemical behavior and analytical performance of an Iridium-Based ultramicroelectrode array (UMEA) sensor," *Microchimica Acta*, vol. 150, no. 2, pp. 137–145, 2005.

[90] J. Heinze, "Ultramicroelectrodes in electrochemistry," *Angewandte Chemie International Edition in English*, vol. 32, no. 9, pp. 1268–1288, 1993.

[91] W. L. Caudill, J. O. Howell, and R. M. Wightman, "Flow rate independent amperometric cell," *Analytical Chemistry*, vol. 54, no. 14, pp. 2532–2535, 1982.

[92] K. Cammann, U. Lemke, A. Rohen, J. Sander, H. Wilken, and B. Winter, "Chemical sensors and BiosensorsPrinciples and applications," *Angewandte Chemie International Edition in English*, vol. 30, no. 5, pp. 516–539, 1991.

[93] L. Xiao, W. Dietze, F. Nyasulu, and B. A. F. Mibeck, "Ultramicroband array electrode. 1. analysis of mercury in contaminated soils and flue gas exposed samples using a Gold-Plated iridium portable system by anodic stripping voltammetry," *Analytical Chemistry*, vol. 78, no. 14, pp. 5172–5178, 2006.

[94] S. Fletcher, "Random assemblies of microelectrodes (RAM electrodes) for electrochemical studies," *Electrochemistry Communications*, vol. 1, no. 10, pp. 502–512, 1999.

[95] J. Wang, J. Wang, W. K. Adeniyi, and S. P. Kounaves, "Adsorptive stripping analysis of trace nickel at Iridium-Based ultramicroelectrode arrays," *Electroanalysis*, vol. 12, no. 1, pp. 44–47, 2000.

[96] R. Feeney and S. P. Kounaves, "Microfabricated ultramicroelectrode arrays: Developments, advances, and applications in environmental analysis," *Electroanalysis*, vol. 12, no. 9, pp. 677–684, 2000.

[97] R. Feeney, J. Herdan, M. A. Nolan, S. H. Tan, V. V. Tarasov, and S. P. Kounaves, "Analytical characterization of microlithographically fabricated Iridium-Based ultramicroelectrode arrays," *Electroanalysis*, vol. 10, no. 2, pp. 89–93, 1998.

[98] A. Cohen, "Large-area interdigitated array microelectrodes for electrochemical sensing," *Sensors and Actuators B: Chemical*, vol. 62, no. 1, pp. 23–29, 2000.

[99] J. Pei, M. Tercier-Waeber, and J. Buffle, "Simultaneous determination and speciation of zinc, cadmium, lead, and copper in natural water with minimum handling and artifacts, by voltammetry on a Gel-Integrated microelectrode array," *Analytical Chemistry*, vol. 72, no. 1, pp. 161–171, 2000.

[100] A. R. Heiskanen, *Monitoring of cellular dynamics with focus on electrochemical detection techniques*. Ph.D., Lund University, Lund, Sweden, 2009.

[101] L. M. Fischer, M. Tenje, A. R. Heiskanen, N. Masuda, J. Castillo, A. Bentien, J. Emneus, M. H. Jakobsen, and A. Boisen, "Gold cleaning methods for electrochemical detection applications," *Microelectronic Engineering*, vol. 86, no. 4-6, pp. 1282–1285, 2009.

[102] J. Kang and P. A. Rowntree, "Gold film surface preparation for Self-Assembled monolayer studies," *Langmuir*, vol. 23, no. 2, pp. 509–516, 2007.

[103] N. S. McIntyre, "Uses of ultraviolet/ozone for hydrocarbon removal: Applications to surfaces of complex composition or geometry," *Journal of Vacuum Science & Technology A: Vacuum, Surfaces, and Films*, vol. 9, no. 3, p. 1355, 1991.

[104] C. G. Worley, "Removing sulfur from gold using ultraviolet/ozone cleaning," *Journal of Vacuum Science & Technology A: Vacuum, Surfaces, and Films*, vol. 13, no. 4, p. 2281, 1995.

[105] A. R. Heiskanen, C. F. Spegel, N. Kostesha, T. Ruzgas, and J. Emneus, "Monitoring of saccharomyces cerevisiae cell proliferation on Thiol-

Modified planar gold microelectrodes using impedance spectroscopy," *Langmuir*, vol. 24, no. 16, pp. 9066–9073, 2008.

[106] T. M. H. Lee and I. Hsing, "Sequence-Specific electrochemical detection of asymmetric PCR amplicons of traditional chinese medicinal plant DNA," *Analytical Chemistry*, vol. 74, no. 19, pp. 5057–5062, 2002.

[107] C. Spegel, A. Heiskanen, J. Acklid, A. Wolff, R. Taboryski, J. Emneus, and T. Ruzgas, "On-chip determination of dopamine exocytosis using mercaptopropionic acid modified microelectrodes," *Electroanalysis*, vol. 19, no. 2-3, pp. 263–271, 2007.

[108] M. F. M. Noh and I. E. Tothill, "Development and characterisation of disposable gold electrodes, and their use for lead(II) analysis," *Analytical and Bioanalytical Chemistry*, vol. 386, no. 7-8, pp. 2095–2106, 2006.

[109] T. A. Green, "Gold electrodeposition for microelectronic, optoelectronic and microsystem applications," *Gold Bulletin*, vol. 40, no. 2, pp. 105–114, 2007.

[110] K. Williams, K. Gupta, and M. Wasilik, "Etch rates for micromachining processing-part II," *Journal of Microelectromechanical Systems*, vol. 12, no. 6, pp. 761–778, 2003.

[111] P. T. Tang, *Fabrication of Microcomponents by electrochemical deposition*. Ph.D., Technical University of Denmark, Denmark, Mar. 1998.

[112] T. Ishida, S. Tsuneda, N. Nishida, M. Hara, H. Sasabe, and W. Knoll, "Surface-Conditioning effect of gold substrates on octadecanethiol Self-Assembled monolayer growth," *Langmuir*, vol. 13, no. 17, pp. 4638–4643, 1997.

[113] R. Shervedani and M. Bagherzadeh, "Hydroxamation of gold surface via in-situ layer-by-layer functionalization of cysteamine self-assembled monolayer: Preparation and electrochemical characterization," *Electrochimica Acta*, vol. 53, no. 22, pp. 6293–6303, 2008.

[114] L. G. Shaidarova, A. V. Gedmina, and G. K. Budnikov, "Voltammetry of a BenzoquinoneHydroquinone redox couple at electrodes modified with a polyvinylpyridine film doped with cobalt phthalocyanine," vol. 58, no. 2, pp. 171–175, 2003.

[115] H. Ron, S. Matlis, and I. Rubinstein, "Self-assembled monolayers on oxidized metals. 2. gold surface oxidative pretreatment, monolayer properties, and depression formation," *Langmuir*, vol. 14, no. 5, pp. 1116–1121, 1998.

[116] A. Ulman, "Formation and structure of Self-Assembled monolayers," *Chemical Reviews*, vol. 96, no. 4, pp. 1533–1554, 1996.

[117] J. Gooding, F. Mearns, W. Yang, and J. Liu, "Self-Assembled monolayers into the 21st century: Recent advances and applications," *Electroanalysis*, vol. 15, no. 2, pp. 81–96, 2003.

[118] A. J. Qavi, A. L. Washburn, J. Byeon, and R. C. Bailey, "Label-free technologies for quantitative multiparameter biological analysis," *Analytical and Bioanalytical Chemistry*, vol. 394, no. 1, pp. 121–135, 2009.

[119] S. M. Borisov and O. S. Wolfbeis, "Optical biosensors," *Chemical Reviews*, vol. 108, no. 2, pp. 423–461, 2008.

[120] J. C. Stachowiak, M. Yue, K. Castelino, A. Chakraborty, and A. Majumdar, "Chemomechanics of surface stresses induced by DNA hybridization," *Langmuir*, vol. 22, no. 1, pp. 263–268, 2006.

[121] K. M. Hansen, H. F. Ji, G. H. Wu, R. Datar, R. Cote, A. Majumdar, and T. Thundat, "Cantilever-based optical deflection assay for discrimination of DNA single-nucleotide mismatches," *Analytical Chemistry*, vol. 73, no. 7, pp. 1567–1571, 2001.

[122] M. Calleja, M. Nordstrom, M. Alvarez, J. Tamayo, L. Lechuga, and A. Boisen, "Highly sensitive polymer-based cantilever-sensors for DNA detection," *Ultramicroscopy*, vol. 105, no. 1-4, pp. 215–222, 2005.

[123] K. S. Hwang, S. M. Lee, S. K. Kim, J. H. Lee, and T. S. Kim, "Micro- and nanocantilever devices and systems for biomolecule detection," *Annual Review of Analytical Chemistry*, vol. 2, pp. 77–98, 2009.

[124] R. Marie, H. Jensenius, J. Thaysen, C. B. Christensen, and A. Boisen, "Adsorption kinetics and mechanical properties of thiol-modified DNA-oligos on gold investigated by microcantilever sensors," *Ultramicroscopy*, vol. 91, no. 1-4, pp. 29–36, 2002.

[125] A. Etorki, A. Roberthillman, K. Ryder, and A. Glidle, "Quartz crystal microbalance determination of trace metal ions in solution," *Journal of Electroanalytical Chemistry*, vol. 599, no. 2, pp. 275–287, 2007.

[126] P. Dutta, P. J. Chapman, P. G. Datskos, and M. J. Sepaniak, "Characterization of Ligand-Functionalized microcantilevers for metal ion sensing," *Analytical Chemistry*, vol. 77, no. 20, pp. 6601–6608, 2005.

[127] L. A. Pinnaduwage, V. I. Boiadjiev, G. M. Brown, T. Thundat, and S. W. Petersen, "Detection of hexavalent chromium in ground water using a single microcantilever sensor," *Sensor Letters*, vol. 2, no. 1, pp. 25–30, 2004.

[128] G. R. Stafford and U. Bertocci, "In situ stress and nanogravimetric measurements during underpotential deposition of pd on (111)-Textured au," *The Journal of Physical Chemistry C*, vol. 113, no. 1, pp. 261–268, 2009.

[129] S. Zhang, C. M. Cardona, and L. Echegoyen, "Ion recognition properties of self-assembled monolayers (SAMs)," *Chemical Communications*, no. 43, pp. 4461–4473, 2006.

[130] G. S. Xuan and S. Kim, "Formation of some cysteine-containing peptide monolayers on au electrodes and their applications for metal ion sensing and electrocatalytic reactions," *Bulletin of the Korean Chemical Society*, vol. 29, no. 7, pp. 1301–1302, 2008.

[131] A. M. Johnson and J. A. Holcombe, "Poly(L-cysteine) as an electrochemically modifiable ligand for trace metal chelation," *Analytical Chemistry*, vol. 77, no. 1, pp. 30–35, 2005.

[132] A. Singh, S. Mehtab, and A. Jain, "Selective electrochemical sensor for copper (II) ion based on chelating ionophores," *Analytica Chimica Acta*, vol. 575, no. 1, pp. 25–31, 2006.

[133] Z. Wang, M. J. Cook, A. Nygrd, and D. A. Russell, "Metal-Ion chelation and sensing using a Self-Assembled molecular photoswitch," *Langmuir*, vol. 19, no. 9, pp. 3779–3784, 2003.

[134] W. Wang, S. Zhang, P. Chinwangso, R. C. Advincula, and T. R. Lee, "Electric potential stability and ionic permeability of SAMs on gold derived from bidentate and tridentate chelating alkanethiols," *The Journal of Physical Chemistry C*, vol. 113, no. 9, pp. 3717–3725, 2009.

[135] M. Heitzmann, C. Bucher, J. Moutet, E. Pereira, B. Rivas, G. Royal, and E. Saintaman, "Complexation of poly(pyrrole-EDTA like) film modified electrodes: Application to metal cations electroanalysis," *Electrochimica Acta*, vol. 52, no. 9, pp. 3082–3087, 2007.

[136] M. A. Rahman, M. Won, and Y. Shim, "Characterization of an EDTA bonded conducting polymer modified electrode: its application for the simultaneous determination of heavy metal ions," *Analytical Chemistry*, vol. 75, no. 5, pp. 1123–1129, 2003.

[137] N. Guimard, N. Gomez, and C. Schmidt, "Conducting polymers in biomedical engineering," *Progress in Polymer Science*, vol. 32, no. 8-9, pp. 876–921, 2007.

[138] J. Wang, V. B. Nascimento, J. Lu, D. S. Park, and L. Angnes, "Disposable nickel screen-printed sensor based on dimethylglyoxime-

containing carbon ink," *Electroanalysis*, vol. 8, no. 7, pp. 635–638, 1996.

[139] J. Scaggs, D. D. Russell, S. P. Duttagupta, and M. W. Hill, "A mercury selective electrode," *MRS Proceedings*, vol. 665, pp. 101–107, 2002.

[140] E. Chow and J. J. Gooding, "Peptide modified electrodes as electrochemical metal ion sensors," *Electroanalysis*, vol. 18, no. 15, pp. 1437–1448, 2006.

[141] D. Harris, *Quantitative chemical analysis*. New York: W.H. Freeman and Co., 6th ed. ed., 2003.

[142] T. Komura, "Interfacial charge-transfer resistance at ionizable thiol monolayer-modified gold electrodes as studied by impedance spectroscopy," *Electrochimica Acta*, vol. 49, no. 4, pp. 597–606, 2004.

[143] R. P. Janek, W. R. Fawcett, and A. Ulman, "Impedance spectroscopy of self-assembled monolayers on au(111): Sodium ferrocyanide charge transfer at modified electrodes," *Langmuir*, vol. 14, no. 11, pp. 3011–3018, 1998.

[144] W. Sanders, R. Vargas, and M. R. Anderson, "Characterization of carboxylic Acid-Terminated Self-Assembled monolayers by electrochemical impedance spectroscopy and scanning electrochemical microscopy," *Langmuir*, vol. 24, no. 12, pp. 6133–6139, 2008.

[145] R. Schweiss, "Impedance spectroscopy studies of interfacial acidbase reactions of self-assembled monolayers," *Journal of Electroanalytical Chemistry*, vol. 540, pp. 145–151, 2003.

[146] P. Diao, "Fractional coverage of defects in self-assembled thiol monolayers on gold," *Journal of Electroanalytical Chemistry*, vol. 480, no. 1-2, pp. 59–63, 2000.

[147] C. Miller, P. Cuendet, and M. Graetzel, "Adsorbed .omega.-hydroxy thiol monolayers on gold electrodes: evidence for electron tunneling to redox species in solution," *The Journal of Physical Chemistry*, vol. 95, no. 2, pp. 877–886, 1991.

[148] J. Xu, H. Li, and Y. Zhang, "Relationship between electronic tunneling coefficient and electrode potential investigated by using self-assembled alkanethiol monolayers on gold electrodes," *The Journal of Physical Chemistry*, vol. 97, no. 44, pp. 11497–11500, 1993.

[149] E. Sabatani and I. Rubinstein, "Organized self-assembling monolayers on electrodes. 2. monolayer-based ultramicroelectrodes for the study of very rapid electrode kinetics," *The Journal of Physical Chemistry*, vol. 91, no. 27, pp. 6663–6669, 1987.

[150] P. Diao, M. Guo, and R. T. Tong, "Characterization of defects in the formation process of self-assembled thiol monolayers by electrochemical impedance spectroscopy," *Journal of Electroanalytical Chemistry*, vol. 495, no. 2, pp. 98–105, 2001.

[151] V. A. Pedrosa, T. Paixao, R. S. Freire, and M. Bertotti, "Studies on the electrochemical behavior of a cystine self-assembled monolayer modified electrode using ferrocyanide as a probe," *Journal of Electroanalytical Chemistry*, vol. 602, no. 2, pp. 149–155, 2007.

[152] D. Garciaraya, R. Madueno, J. Sevilla, M. Blazquez, and T. Pineda, "Electrochemical characterization of a 1,8-octanedithiol self-assembled monolayer (ODT-SAM) on a au(111) single crystal electrode," *Electrochimica Acta*, vol. 53, no. 27, pp. 8026–8033, 2008.

[153] C. K. Wang, S. Jiang, and S. H. Pun, "Localized cell uptake of His-Tagged polyplexes immobilized on NTA Self-Assembled monolayers," *Langmuir*, vol. 26, no. 19, pp. 15445–15452, 2010.

[154] D. F. Kelly, P. D. Abeyrathne, D. Dukovski, and T. Walz, "The affinity grid: A pre-fabricated EM grid for monolayer purification," *Journal of Molecular Biology*, vol. 382, no. 2, pp. 423–433, 2008.

[155] B. Nastasijevic, N. Becker, S. Wurster, and L. Jamesmaheriii, "Sequence-specific binding of DNA and RNA to immobilized nickel ions," *Biochemical and Biophysical Research Communications*, vol. 366, no. 2, pp. 420–425, 2008.

[156] H. Dong, X. Xu, M. Deng, X. Yu, H. Zhao, H. Song, and Y. Geng, "Expression and bioactivity of recombinant segments of human perforin," *Biochemistry and Cell Biology*, vol. 85, no. 2, pp. 203–208, 2007.

[157] S. ichiro Imabayashi, D. Hobara, T. Kakiuchi, and W. Knoll, "Selective replacement of adsorbed alkanethiols in Phase-Separated binary Self-Assembled monolayers by electrochemical partial desorption," *Langmuir*, vol. 13, no. 17, pp. 4502–4504, 1997.

[158] C. A. Widrig, C. Chung, and M. D. Porter, "The electrochemical desorption of n-alkanethiol monolayers from polycrystalline au and ag electrodes," *Journal of Electroanalytical Chemistry*, vol. 310, no. 1-2, pp. 335–359, 1991.

[159] T. Sumi and K. Uosaki, "Electrochemical oxidative formation and reductive desorption of a Self-Assembled monolayer of decanethiol on a au(111) surface in KOH ethanol solution," *The Journal of Physical Chemistry B*, vol. 108, no. 20, pp. 6422–6428, 2004.

[160] G. Wu, R. H. Datar, K. M. Hansen, T. Thundat, R. J. Cote, and A. Majumdar, "Bioassay of prostate-specific antigen (PSA) using microcantilevers," *Nature Biotechnology*, vol. 19, 2001.

[161] G. Wu, H. F. Ji, K. Hansen, T. Thundat, R. Datar, R. Cote, M. F. Hagan, A. K. Chakraborty, and A. Majumdar, "Origin of nanomechanical cantilever motion generated from biomolecular interactions," *Proceedings of the National Academy of Sciences*, vol. 98, no. 4, pp. 1560–1564, 2001.

[162] F. Huber, M. Hegner, C. Gerber, H. Guntherodt, and H. Lang, "Label free analysis of transcription factors using microcantilever arrays," *Biosensors and Bioelectronics*, vol. 21, no. 8, pp. 1599–1605, 2006.

[163] M. F. Hagan, A. Majumdar, and A. K. Chakraborty, "Nanomechanical forces generated by surface grafted DNA," *The Journal of Physical Chemistry B*, vol. 106, no. 39, pp. 10163–10173, 2002.

[164] A. R. Paniagua, M. D. Vazquez, M. L. Tascon, and P. S. Batanero, "Determination of chromium(VI) and chromium(III) by using a diphenylcarbazide-modified carbon paste electrode," *Electroanalysis*, vol. 5, no. 2, pp. 155–163, 1993.

[165] R. Blankespoor, B. Limoges, B. Schllhorn, J. Syssa-Magal, and D. Yazidi, "Dense monolayers of Metal-Chelating ligands covalently attached to carbon electrodes electrochemically and their useful application in affinity binding of Histidine-Tagged proteins," *Langmuir*, vol. 21, no. 8, pp. 3362–3375, 2005.

[166] M. Nishizawa, T. Sunagawa, and H. Yoneyama, "Underpotential deposition of copper on gold electrodes through Self-Assembled monolayers of propanethiol," *Langmuir*, vol. 13, no. 20, pp. 5215–5217, 1997.

[167] H. Shen, J. E. Mark, C. J. Seliskar, H. B. Mark, and W. R. Heineman, "Stripping voltammetry of copper and lead using gold electrodes modified with self-assembled monolayers," *Journal of Solid State Electrochemistry*, vol. 1, no. 3, pp. 241–247, 1997.

[168] K. Uvdal, P. Bodo, and B. Liedberg, "l-cysteine adsorbed on gold and copper: An x-ray photoelectron spectroscopy study," *Journal of Colloid and Interface Science*, vol. 149, no. 1, pp. 162–173, 1992.

[169] A. C. Liu, D. C. Chen, C. C. Lin, H. H. Chou, and C. H. Chen, "Application of cysteine monolayers for electrochemical determination of sub-ppb copper(II)," *Analytical Chemistry*, vol. 71, no. 8, pp. 1549–1552, 1999.

[170] W. Yang, J. J. Gooding, and D. Hibbert, "Characterisation of gold electrodes modified with self-assembled monolayers of l-cysteine for the adsorptive stripping analysis of copper," *Journal of Electroanalytical Chemistry*, vol. 516, no. 1-2, pp. 10–16, 2001.

[171] S. de Silva, R. M. de Silva, and K. N. de Silva, "Molecular mechanics (MM), molecular dynamics (MD) and semi-empirical study of co2+, cu2+, ni2+ and cd2+ binding to n-terminal of human serum albumin (HSA)," *Journal of Molecular Structure: THEOCHEM*, vol. 711, no. 1-3, pp. 73–81, 2004.

[172] J. Dong, C. Liu, J. Zhang, Z. Xin, G. Yang, B. Gao, C. quan Mao, N. Liu, F. Wang, N. Shao, M. Fan, and Y. Xue, "Selection of novel nickel-binding peptides from flagella displayed secondary peptide library," *Chemical Biology <html_ent glyph="@amp;" ascii="&"/> Drug Design*, vol. 68, no. 2, pp. 107–112, 2006.

[173] A. Kolozsi, I. Vosekalna, T. Martinek, E. Larsen, and B. Gyurcsik, "Copper(ii) and zinc(ii) ion binding properties of a MAP type branched ligand with histidines as surface functionalities," *Dalton Transactions*, no. 29, p. 5647, 2009.

[174] P. Rousselot-Pailley, O. Snque, C. Lebrun, S. Crouzy, D. Boturyn, P. Dumy, M. Ferrand, and P. Delangle, "Model peptides based on the binding loop of the copper metallochaperone atx1: selectivity of the consensus sequence MxCxxC for metal ions Hg(II), Cu(I), Cd(II), Pb(II), and Zn(II)," *Inorganic Chemistry*, vol. 45, no. 14, pp. 5510–5520, 2006.

[175] S. Lau, T. P. Kruck, and B. Sarkar, "A peptide molecule mimicking the Copper(II) transport site of human serum albumin: A COMPARATIVE STUDY BETWEEN THE SYNTHETIC SITE AND ALBUMIN," *Journal of Biological Chemistry*, vol. 249, pp. 5878–5884, 1974.

[176] T. P. Kruck, S. Lau, and B. Sarkar, "Molecular design to mimic the copper(II) transport site of human albumin: studies of equilibria between copper(II) and glycylglycyl-<small>L</small>-histidine-N-methyl amide and comparison with human albumin," *Canadian Journal of Chemistry*, vol. 54, no. 8, pp. 1300–1308, 1976.

[177] W. R. Yang, E. Chow, G. D. Willett, D. B. Hibbert, and J. J. Gooding, "Exploring the use of the tripeptide Gly-Gly-His as a selective recognition element for the fabrication of electrochemical copper sensors," *Analyst*, vol. 128, no. 6, pp. 712–718, 2003.

[178] E. Chow, E. L. S. Wong, T. Bocking, Q. T. Nguyen, D. B. Hibbert, and J. J. Gooding, "Analytical performance and characterization of MPA-Gly-Gly-His modified sensors," *Sensors and Actuators B-Chemical*, vol. 111, pp. 540–548, 2005. Sens. Actuator B-Chem. ISI Document Delivery No.: 977RM Times Cited: 23 Cited Reference Count: 34 18th Eurosensors Conference SEP 12-15, 2004 Rome, ITALY ELSEVIER SCIENCE SA LAUSANNE Sp. Iss. SI.

[179] G. Liu, Q. Nguyen, E. Chow, T. Bcking, D. Hibbert, and J. Gooding, "Study of factors affecting the performance of voltammetric copper sensors based on Gly-Gly-His modified glassy carbon and gold electrodes," *Electroanalysis*, vol. 18, no. 12, pp. 1141–1151, 2006.

[180] E. Chow, D. B. Hibbert, and J. J. Gooding, "Voltammetric detection of cadmium ions at glutathione-modified gold electrodes," *Analyst*, vol. 130, no. 6, pp. 831–837, 2005.

[181] K. Koch, M. M. O. Pena, and D. J. Thiele, "Copper-binding motifs in catalysis, transport, detoxification and signaling," *Chemistry & Biology*, vol. 4, no. 8, pp. 549–560, 1997.

[182] M. Rodahl and B. Kasemo, "A simple setup to simultaneously measure the resonant frequency and the absolute dissipation factor of a quartz crystal microbalance," *Review of Scientific Instruments*, vol. 67, no. 9, p. 3238, 1996.

[183] F. Hook, M. Rodahl, P. Brzezinski, and B. Kasemo, "Energy dissipation kinetics for protein and antibody-antigen adsorption under shear oscillation on a quartz crystal microbalance," *Langmuir*, vol. 14, no. 4, pp. 729–734, 1998.

[184] G. Zhang and C. Wu, "Quartz crystal microbalance studies on conformational change of polymer chains at interface," *Macromolecular Rapid Communications*, vol. 30, no. 4-5, pp. 328–335, 2009.

[185] A. Torrado, G. K. Walkup, and B. Imperiali, "Exploiting polypeptide motifs for the design of selective Cu(II) ion chemosensors," *Journal of the American Chemical Society*, vol. 120, no. 3, pp. 609–610, 1998.

[186] H. Won, "Nickel-Binding properties of the C-Terminal tail peptide of bacillus pasteurii UreE," *Journal of Biochemistry*, vol. 136, no. 5, pp. 635–641, 2004.

[187] S. Ray, J. Asthana, J. M. Tanski, M. M. Shaikh, D. Panda, and P. Ghosh, "Design of nickel chelates of tetradentate n-heterocyclic carbenes with subdued cytotoxicity," *Journal of Organometallic Chemistry*, vol. 694, no. 15, pp. 2328–2335, 2009.

[188] D. Menzel, "Arsenic binding proteins from human lymphoblastoid cells," *Toxicology Letters*, vol. 105, no. 2, pp. 89–101, 1999.

[189] K. T. Kitchin and K. Wallace, "Arsenite binding to synthetic peptides based on the zn finger region and the estrogen binding region of the human estrogen receptor-," *Toxicology and Applied Pharmacology*, vol. 206, no. 1, pp. 66–72, 2005.

[190] K. T. Kitchin and K. Wallace, "The role of protein binding of trivalent arsenicals in arsenic carcinogenesis and toxicity," *Journal of Inorganic Biochemistry*, vol. 102, no. 3, pp. 532–539, 2008.

[191] X. Zhang, F. Yang, J. Shim, K. Kirk, D. Anderson, and X. Chen, "Identification of arsenic-binding proteins in human breast cancer cells," *Cancer Letters*, vol. 255, no. 1, pp. 95–106, 2007.

[192] M. Delnomdedieu, M. M. Basti, M. Styblo, J. D. Otvos, and D. J. Thomas, "Complexation of arsenic species in rabbit erythrocytes," *Chemical Research in Toxicology*, vol. 7, pp. 621–627, Oct. 1994. PMID: 7841340.

[193] Y. X. Liu and W. Z. Wei, "Jointly modified single-walled carbon nanotubes on low resistance monolayer modified electrode for arsenic(III) detection," *Journal of Electroanalytical Chemistry*, vol. 624, no. 1-2, pp. 299–304, 2008.

[194] H. Ji, R. Dabestani, G. M. Brown, and P. F. Britt, "A novel self-assembled monolayer (SAM) coated microcantilever for low level caesium detection," *Chemical Communications*, no. 6, pp. 457–458, 2000.

[195] Y. M. Xu, B. L. Zhang, S. H. Wu, and Y. Xia, "The adsorption of dopamine on gold and its interactions with iron(III) ions studied by microcantilevers," *Analytica Chimica Acta*, vol. 649, no. 1, pp. 117–122, 2009. Anal. Chim. Acta ISI Document Delivery No.: 486AZ Times Cited: 0 Cited Reference Count: 44 Xu, Yingming Zhang, Bailin Wu, Sanhua Xia, Yong National Natural Science Foundation of China [20675077, 20735001]; Program of Knowledge Innovation, Chinese Academy of Sciences [2007AA061501]; [KJCX2-YW-H11] This paper was supported by the National Natural Science Foundation of China (Nos. 20675077 and 20735001), the Project KJCX2-YW-H11, Program of Knowledge Innovation, Chinese Academy of Sciences and 863 Project (2007AA061501). ELSEVIER SCIENCE BV AMSTERDAM.

[196] A. Bietsch, J. Zhang, M. Hegner, H. P. Lang, and C. Gerber, "Rapid functionalization of cantilever array sensors by inkjet printing," *Nanotechnology*, vol. 15, no. 8, pp. 873–880, 2004.

[197] C. Liu, Y. Liu, M. Sokuler, D. Fell, S. Keller, A. Boisen, H. Butt, G. K. Auernhammer, and E. Bonaccurso, "Diffusion of water into SU-8 microcantilevers," *Physical Chemistry Chemical Physics*, vol. 12, no. 35, p. 10577, 2010.

[198] M. Tenje, S. Keller, S. Dohn, Z. J. Davis, and A. Boisen, "Drift study of SU8 cantilevers in liquid and gaseous environments," *Ultramicroscopy*, vol. 110, no. 6, pp. 596–598, 2010.

[199] Z. Lee, C. Ophus, L. M. Fischer, N. Nelson-Fitzpatrick, K. L. Westra, S. Evoy, V. Radmilovic, U. Dahmen, and D. Mitlin, "Metallic NEMS components fabricated from nanocomposite AlMo films," *Nanotechnology*, vol. 17, no. 12, pp. 3063–3070, 2006.

[200] E. J. Luber, B. C. Olsen, C. Ophus, V. Radmilovic, and D. Mitlin, "All-metal AFM probes fabricated from microstructurally tailored CuHf thin films," *Nanotechnology*, vol. 20, no. 34, p. 345703, 2009.

[201] E. Luber, R. Mohammadi, C. Ophus, Z. Lee, N. Nelson-Fitzpatrick, K. Westra, S. Evoy, U. Dahmen, V. Radmilovic, and D. Mitlin, "Tailoring the microstructure and surface morphology of metal thin films for nano-electro-mechanical systems applications," *Nanotechnology*, vol. 19, no. 12, p. 125705, 2008.

[202] N. Nelson-Fitzpatrick, C. Ophus, E. Luber, L. Gervais, Z. Lee, V. Radmilovic, D. Mitlin, and S. Evoy, "Synthesis and characterization of AuTa nanocomposites for nanomechanical cantilever devices," *Nanotechnology*, vol. 18, no. 35, p. 355303, 2007.

[203] C. Ophus, N. N. Fitzpatrick, Z. Lee, E. Luber, C. Harrower, K. Westra, U. Dahmen, V. Radmilovic, S. Evoy, and D. Mitlin, "Resonance properties and microstructure of ultracompliant metallic nanoelectromechanical systems resonators synthesized from al32at.%mo amorphous-nanocrystalline metallic composites," *Applied Physics Letters*, vol. 92, no. 12, p. 123108, 2008.

[204] P. Pal, K. Sato, and S. Chandra, "Fabrication techniques of convex corners in a (100)-silicon wafer using bulk micromachining: a review," *Journal of Micromechanics and Microengineering*, vol. 17, no. 10, pp. R111–R133, 2007.

[205] N. Noeth, *Microfluidic sensors based on perforated cantilevers.* Doctoral, Technical University of Denmark, Denmark, 2010.

[206] M. Grnefeld, *Fabrication of a test device for a fluid cell.* Masters, Technical University of Denmark, 2008.

[207] T. Fujii, "PDMS-based microfluidic devices for biomedical applications," *Microelectronic Engineering*, vol. 61-62, no. 1-3, pp. 907–914, 2002.

[208] R. Pantoja, "Silicon chip-based patch-clamp electrodes integrated with PDMS microfluidics," *Biosensors and Bioelectronics*, vol. 20, no. 3, pp. 509–517, 2004.

[209] S. Senturia, *Microsystem design*. Boston: Kluwer Academic Publishers, 2001.

[210] S. Campbell, *The science and engineering of microelectronic fabrication*. New York: Oxford University Press, 2nd ed. ed., 2001.

[211] J. Teva, Z. J. Davis, and O. Hansen, "Electroless porous silicon formation applied to fabrication of boronsilicaglass cantilevers," *Journal of Micromechanics and Microengineering*, vol. 20, no. 1, p. 015034, 2010.

[212] Y. Berdichevsky, J. Khandurina, A. Guttman, and Y. H. Lo, "UV/ozone modification of poly(dimethylsiloxane) microfluidic channels," *Sensors and Actuators B-Chemical*, vol. 97, no. 2-3, pp. 402–408, 2004.

[213] T. Rokob and G. Lang, "Remarks on the electrochemical application of optical methods for the determination of stress in electrodes," *Electrochimica Acta*, vol. 51, no. 1, pp. 93–97, 2005.

[214] H. Lang, "An artificial nose based on a micromechanical cantilever array," *Analytica Chimica Acta*, vol. 393, no. 1-3, pp. 59–65, 1999.

[215] F. Battiston, "A chemical sensor based on a microfabricated cantilever array with simultaneous resonance-frequency and bending readout," *Sensors and Actuators B: Chemical*, vol. 77, no. 1-2, pp. 122–131, 2001.

[216] M. Baller, H. P. Lang, J. Fritz, C. Gerber, J. K. Gimzewski, U. Drechsler, H. Rothuizen, M. Despont, P. Vettiger, F. Battiston, J. P. Ramseyer, P. Fornaro, E. Meyer, and H. Gntherodt, "A cantilever array-based artificial nose," *Ultramicroscopy*, vol. 82, no. 1-4, pp. 1–9, 2000.

[217] D. E. Weisshaar, B. D. Lamp, and M. D. Porter, "Thermodynamically controlled electrochemical formation of thiolate monolayers at gold: characterization and comparison to self-assembled analogs," *Journal of the American Chemical Society*, vol. 114, no. 14, pp. 5860–5862, 1992.

[218] M. Watari, J. Galbraith, H. Lang, M. Sousa, M. Hegner, C. Gerber, M. A. Horton, and R. A. McKendry, "Investigating the molecular mechanisms of In-Plane mechanochemistry on cantilever arrays,"

Journal of the American Chemical Society, vol. 129, no. 3, pp. 601–609, 2007.

[219] T. Miyatani and M. Fujihira, "Calibration of surface stress measurements with atomic force microscopy," *Journal of Applied Physics*, vol. 81, no. 11, p. 7099, 1997.

[220] R. Berger, E. Delamarche, H. Lang, C. Gerber, J. Gimzewski, E. Meyer, and H. Güntherodt, "Surface stress in the self-assembly of alkanethiols on gold probed .by a force microscopy technique," *Applied Physics A: Materials Science & Processing*, vol. 66, no. 7, pp. S55–S59, 1998.

[221] H. Ibach, "Adsorbate-induced surface stress," *Journal of Vacuum Science & Technology A: Vacuum, Surfaces, and Films*, vol. 12, no. 4, p. 2240, 1994.

[222] A. Hanaki and A. Odani, "Transport of Cu(II) from an albumin mimic peptide, GlyGlyHisGly, to histidine and penicillamine," *Journal of Inorganic Biochemistry*, vol. 101, no. 10, pp. 1428–1437, 2007.

[223] J. Wang, M. Jiang, A. M. Kawde, and R. Polsky, "Electrochemically induced deposition of Thiol-Based monolayers onto closely spaced microelectrodes," *Langmuir*, vol. 16, no. 25, pp. 9687–9689, 2000.

[224] S. Dondapati, J. Montornes, P. Sanchez, J. Sanchez, C. O'Sullivan, and I. Katakis, "Site-Directed immobilization of proteins through electrochemical deprotection on electroactive Self-Assembled monolayers," *Electroanalysis*, vol. 18, no. 19-20, pp. 1879–1884, 2006.

[225] P. Diao, Q. Hou, M. Guo, M. Xiang, and Q. Zhang, "Effect of substrate potentials on the structural disorders of alkanethiol monolayers prepared by electrochemically directed assembly," *Journal of Electroanalytical Chemistry*, vol. 597, no. 2, pp. 103–110, 2006.

[226] Z. Petrovic, M. Metikoshukovic, and R. Babic, "Potential-assisted assembly of 1-dodecanethiol on polycrystalline gold," *Journal of Electroanalytical Chemistry*, vol. 623, no. 1, pp. 54–60, 2008.

[227] A. J. Downard, "Electrochemically assisted covalent modification of carbon electrodes," *Electroanalysis*, vol. 12, no. 14, pp. 1085–1096, 2000.

[228] H. Ibach, "The role of surface stress in reconstruction, epitaxial growth and stabilization of mesoscopic structures," *Surface Science Reports*, vol. 29, no. 5-6, pp. 195–263, 1997.

Appendices

Appendix A

Gold Film Microelectrodes: Detailed Process Flow

This is the detailed process flow for the 1^{st} gen. electrode chips used in chapter 5, and the 2^{nd} gen. electrode chips used in chapters 6, and 7. It should be noted that the 2^{nd} gen. chips have also been used by Ph.D. students Xueling Quan and Shoko Yamada for their projects. Step numbers correspond to the steps of the process flow.

Start
Silicon (100) wafer
100-mm-diameter
500-μm-thick
Doping is irrelevant

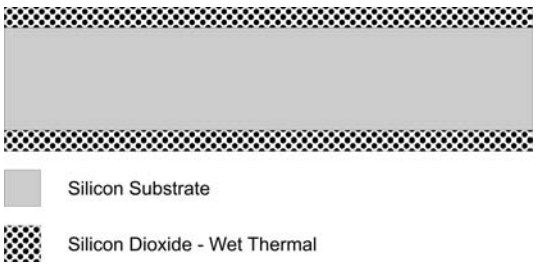

Step 1
Wet thermal oxidation
1.5 hours @ 1050 degC
500 nm SiO_2

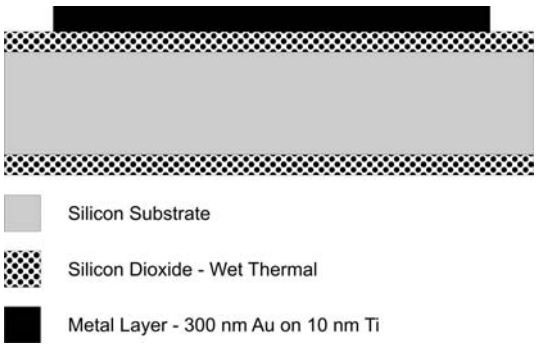

Step 2-10
HDMS, resist, mask exposure
Metallization:
10 nm Ti adhesion layer
300 nm Au electrode layer
Patterned by lift-off in acetone

Step 11
Deposition of PECVD
Silicon Nitride
Approx. 1 μm thick

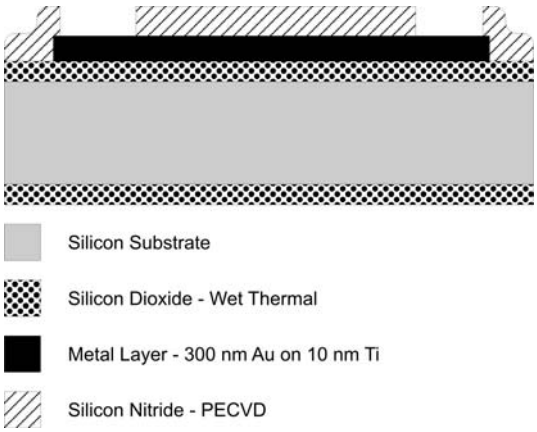

Step 12-19
HMDS, resist, exposure
Reactive Ion Etching (RIE)
Resist removal

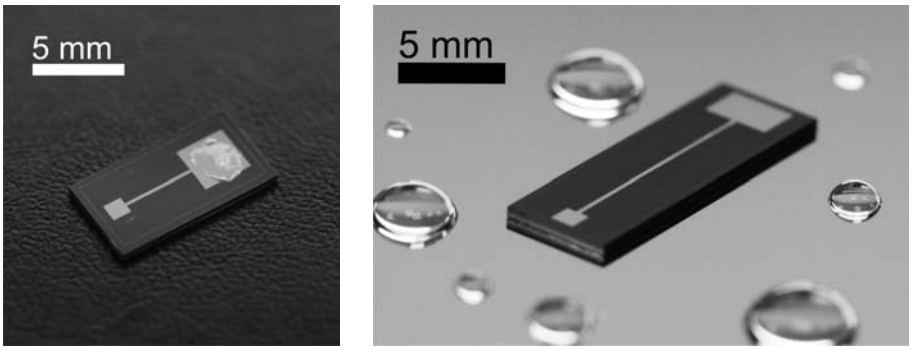

(a) (b)

Figure A.1: Finished chips: (a) 1^{st} gen., and (b) 2^{nd} gen.

Step	Process	Equipment	Recipe / Parameters	Comments
1	*WetThermal Oxidation*	Oxide/Aneal Furnace	Wet Oxidation / 1.5 hours / 1050°C	Use standard Si (100) wafers, doping is unimportant
2	*HMDS*	HMDS Oven	Reciple 4 / normal	
3	*Spin-coating photoresist*	Track 1	PR2_2 / AZ5214e 2.2 µm	
4	*1st Mask Exposure*	KS Aligner	Soft contact / Exp. Time: 6.5s	Mask: **METAL LAYER**. First exposure, first mask.
5	*Reversal Bake*	Track 1	REV_120S / 120C for 120s	Reversal bake for negative tone on AZ resist.
6	*Flood Exposure*	KS Aligner	Lamp Test for 35s	Flood exposure for first mask.
7	*Photoresist Development*	Developer 1 or 2	Dev. Time: 60s - 90s	Make sure developer is reasonably fresh. Bubble rinse and spin dry.
8	*Metal Deposition*	Wordentec	10nm Cr / 300nm Au	Standard evaporation powers
9	*Lift Off*	Lift Off Bath	20-30 minutes, possible sonication	Use sonication only if necessary, as it has been known to cause grain reorganization.
10	*Photoresist Removal*	Plasma Asher 1 or 2	~1mTorr; O2=420l/min; N2=50l/min	Clean for 10-20 minutes.
11	*Nitride Deposition*	PECVD 3	LFSiN / 20 minutes / ~1 µm	Nearly 1 µm of nitride is required to cover the wire, to prevent cracks and flaking
12	*HMDS*	HMDS Oven	Reciple 4 / normal	
13	*Spin-coating photoresist*	Track 1	PR2_2	On "frontside" of wafer.
14	*2nd Mask Exposure*	KS Aligner	Soft contact / Exp. Time: 6.5s	Mask: **ELECTRODE DEFINITION**. First exposure, second mask.
15	*Reversal Bake*	Track 1	REV_120S / 120C for 120s	Reversal bake for negative tone on AZ resist.
16	*Flood Exposure*	KS Aligner	Lamp Test for 35s	Flood exposure for second mask.
17	*Photoresist Development*	Developer 1 or 2	Dev. Time: 60s - 90s	Make sure developer is reasonably fresh. Bubble rinse and spin dry.
18	*Nitride Etching*	RIE1	OH_POLYA / 40nm/min	Selectivity is 1:1 for SiN:Si. Etch time of 18 minutes for 500mn SiN. Recipe same as BGE-NITR.
19	*Photoresist Removal*	Plasma Asher 1 or 2	~1mTorr; O2=420l/min; N2=50l/min	Clean for 10-20 minutes.

Appendix B

ECC Chips: Detailed Process Flow

This is the detailed process flow for the electrochemical-cantilever (ECC) chips designed in chapter 9, and used in chapters 11 and 12. These chips have also been fabricated and used for combined electrochemical-cantilever measurements by Ph.D. student Xueling Quan and Assistant Professor Maria Tenje. Described below is the ECCv2.1n fabrication process flow, which is the final optimized fabrication process developed in this project. All chips used for measurements in chapters 11 and 12 were created using this process. Step numbers correspond to the steps of the process flow.

(a) (b) (c)

Figure B.1: Masks used in the ECC chip fabrication process: (a) 1^{st} mask: CANTILEVERS (front side), (b) 2^{nd} mask: BODY CHIP (back side), and (c) 3^{rd} mask: ELECTRODES (front side).

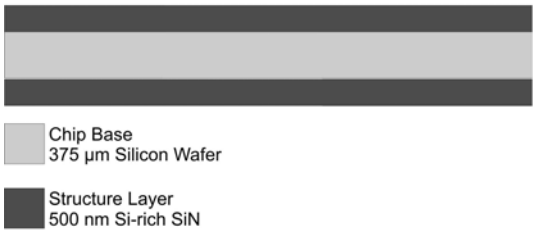

Step 1
LPCVD Deposition
Si-rich Silicon Nitride
375-μm-thick (100) wafer
Doping is irrelevant

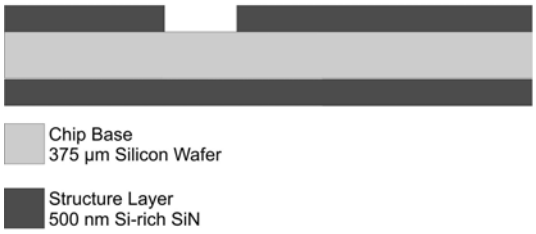

Step 2-9
HMDS, resist
1^{st} exposure: CANTILEVERS mask
RIE silicon nitride etch

Step 10-17
HDMS, resist
2^{nd} exposure: BODY CHIP mask
RIE silicon nitride etch

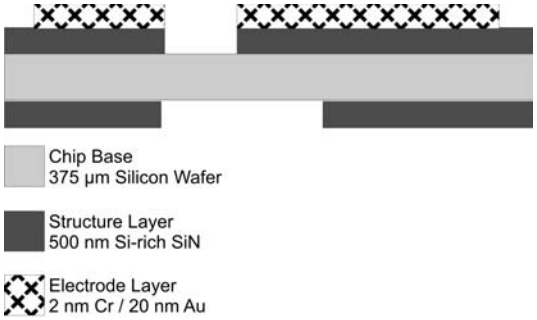

Step 18-25
HMDS, resist
3^{rd} exposure: ELECTRODES mask
Metallization:
2 nm Cr / 20 nm Au
Lift-off in acetone

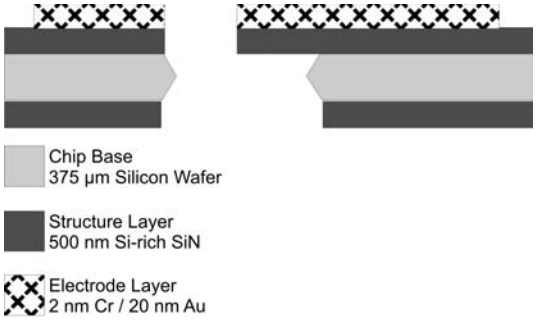

Step 26
KOH release
Water and ethanol rinse
Oven dry

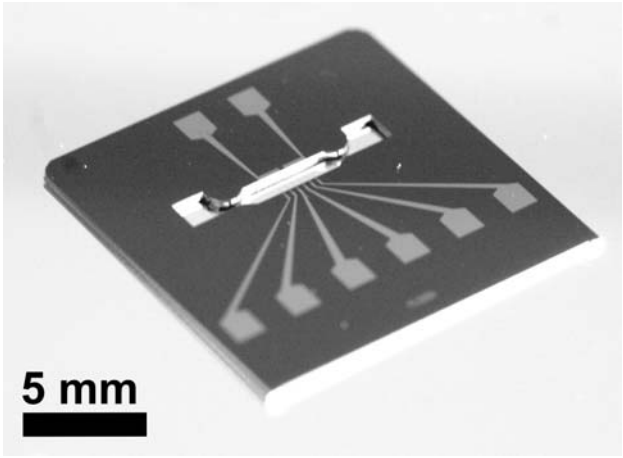

(a)

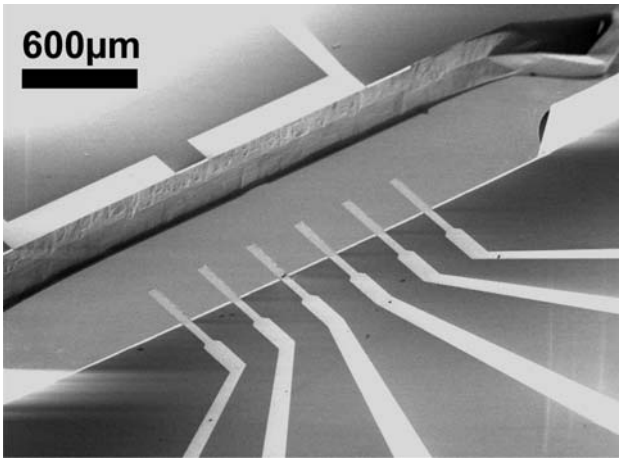

(b)

Figure B.2: The finished electrochemical-cantilever chip: (a) a photo of the whole chip, and (b) a SEM image of the channel and cantilevers.

Step	Process	Equipment	Recipe / Parameters	Comments
1	*Silicon Nitride Deposition*	SiN LPCVD Furnace	LOWSTR / ~280nm/hour	Single depositions can occur for no longer than 60 minutes. Do multiple deps for thicker films.
2	*HMDS*	HMDS Oven	Reciple 4 / normal	
3	*Spin-coating photoresist*	Track 1	PR2_2	On "backside" of wafer.
4	*1st Mask Exposure*	KS Aligner	Soft contact / Exp. Time: 6.5s	Mask: **CANTILEVERS (frontside)**. First exposure, first mask.
5	*Reversal Bake*	Track 1	REV_120S / 120C for 120s	Reversal bake for negative tone on AZ resist.
6	*Flood Exposure*	KS Aligner	Lamp Test for 35s	Flood exposure for first mask.
7	*Photoresist Development*	Developer 1 or 2	Dev. Time: 60s - 90s	Make sure developer is reasonably fresh. Bubble rinse and spin dry.
8	*Nitride Etching*	RIE1	ASN-NITR / 40nm/min	Selectivity is 1:1 for SiN:Si. Etch time of 18 minutes for 500mn SiN. Recipe same as BGE-NITR.
9	*Photoresist Removal*	Plasma Asher 1 or 2	~1mTorr; O2=420l/min; N2=50l/min	Clean for 20-30 minutes. 10 minute acetone soak prior to ashing reduces plasma time.
10	*HMDS*	HMDS Oven	Reciple 4 / normal	
11	*Spin-coating photoresist*	Track 1	PR2_2	On "frontside" of wafer.
12	*2nd Mask Exposure*	KS Aligner	Soft contact / Exp. Time: 6.5s	Mask: **BODY CHIP (backside)**. First exposure, second mask.
13	*Reversal Bake*	Track 1	REV_120S / 120C for 120s	Reversal bake for negative tone on AZ resist.
14	*Flood Exposure*	KS Aligner	Lamp Test for 35s	Flood exposure for second mask.
15	*Photoresist Development*	Developer 1 or 2	Dev. Time: 60s - 90s	Make sure developer is reasonably fresh. Bubble rinse and spin dry.
16	*Nitride Etching*	RIE1	ASN-NITR / 40nm/min	Selectivity is 1:1 for SiN:Si. Etch time of 18 minutes for 500mn SiN. Recipe same as BGE-NITR.
17	*Photoresist Removal*	Plasma Asher 1 or 2	~1mTorr; O2=420l/min; N2=50l/min	Clean for 20-30 minutes. 10 minute acetone soak prior to ashing reduces plasma time.
18	*HMDS*	HMDS Oven	Reciple 4 / normal	
19	*Spin-coating photoresist*	Track 1	PR2_2	On "frontside" of wafer.
20	*3rd Mask Exposure*	KS Aligner	Soft contact / Exp. Time: 6.5s	Mask: **ELECTRODES (frontside)**. First exposure, third mask.
21	*Reversal Bake*	Track 1	REV_120S / 120C for 120s	Reversal bake for negative tone on AZ resist.
22	*Flood Exposure*	KS Aligner	Lamp Test for 35s	Flood exposure for third mask.
23	*Photoresist Development*	Developer 1 or 2	Dev. Time: 60s - 90s	Make sure developer is reasonably fresh. Bubble rinse and spin dry.
24	*Metal Deposition*	Wordentec	2nm Cr / 23nm Au	Use extremely low deposition rates. Soak powers: 2.5% & 5% for Cr, 25% & 45% for Au
25	*Lift Off*	Lift Off Bath	20-30 minutes, possible sonication	Use sonication only if necessary, as it has been known to cause grain reorganization.
26	*KOH Release*	KOH Fumehood	Saturated KOH / 80C / 3.5h	Use mild stirring. Rinse in 4 baths of still, clean DI water. Replace water with ethanol and oven dry.

Appendix C

Flow Cell: Engineering Drawings

This appendix contains the dimensions for the flow cell components. PMMA and PDMS components were fabricated using a CO_2 laser marking system: 48-5S Duo Lase carbon dioxide laser, SYNRAD Inc., USA, with a FH/Fenix 200 mm writing head. The pyrex optical window was cut to dimension using a Disco wafer dicing saw. All dimensions in the drawings below are in millimeters (mm).

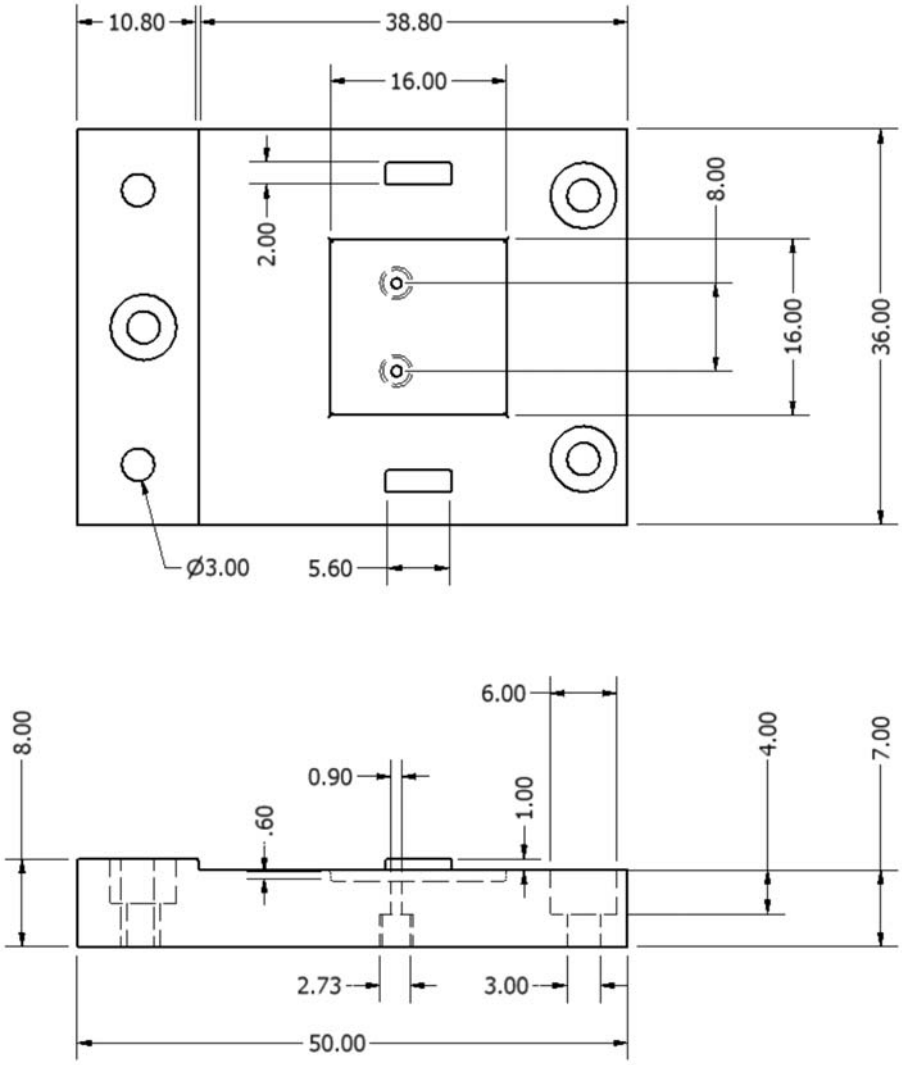

Figure C.1: Engineering drawing with dimensions for the PMMA bottom plate.

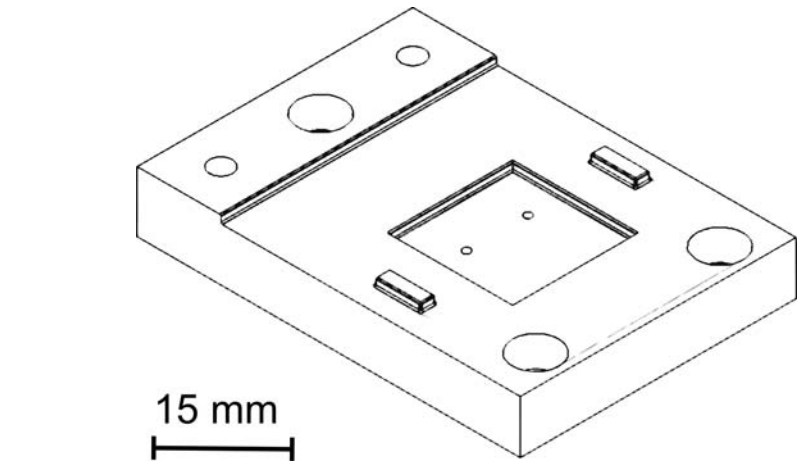

(a)

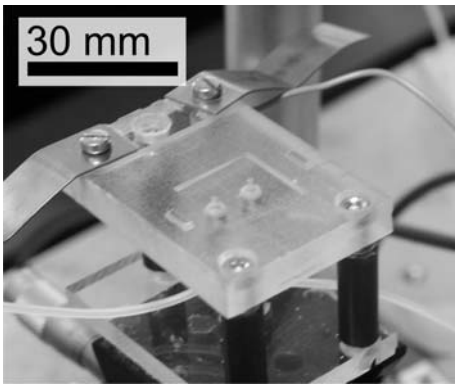

(b)

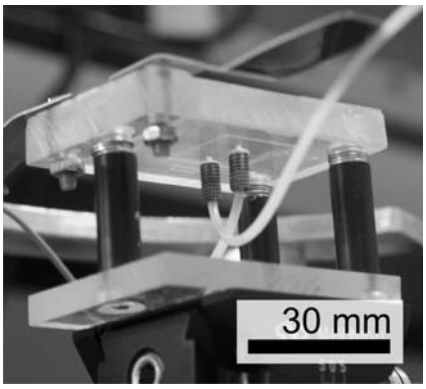

(c)

Figure C.2: (a) An isometric drawing of the PMMA bottom plate. Photographs of the finished PMMA bottom plate from the (a) top, and (b) bottom, where the fluidic tubing can be seen.

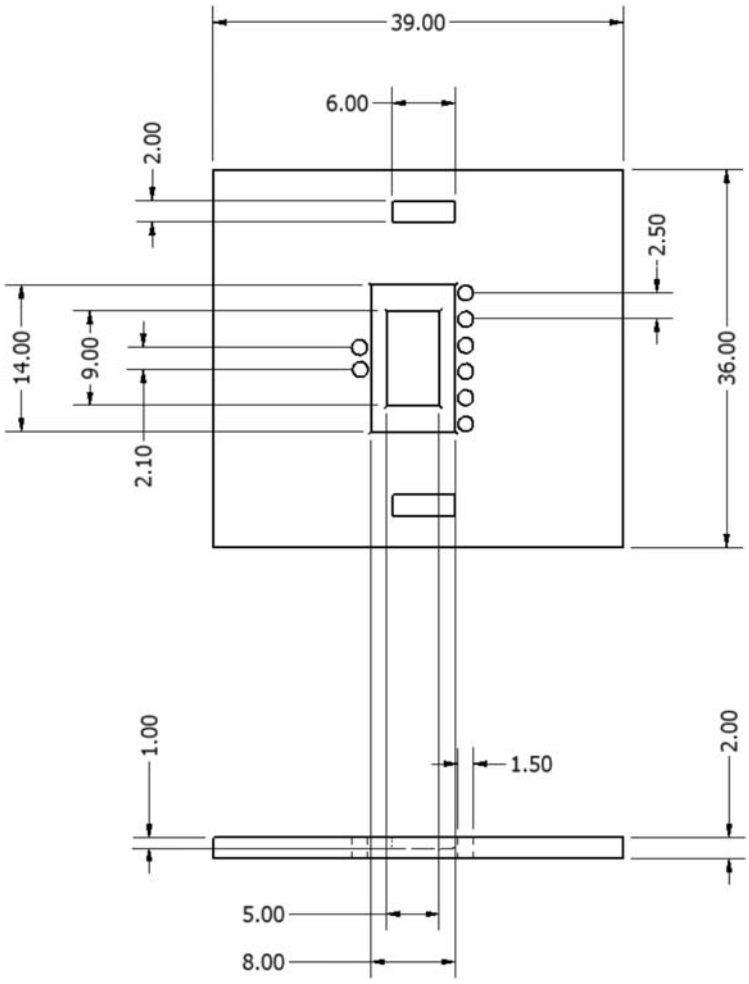

Figure C.3: Engineering drawing with dimensions for the PMMA top plate.

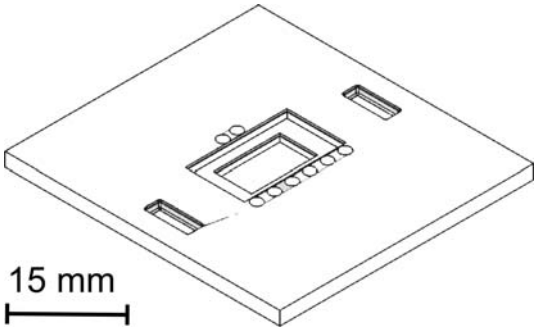

(a)

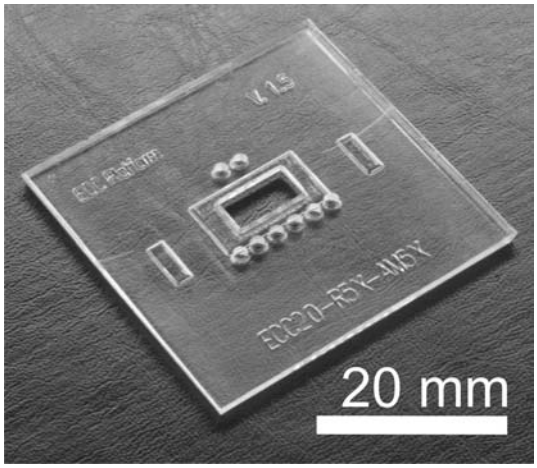

(b)

Figure C.4: ((a) An isometric drawing of the PMMA top plate. (b) A photograph of the finished PMMA top plate.

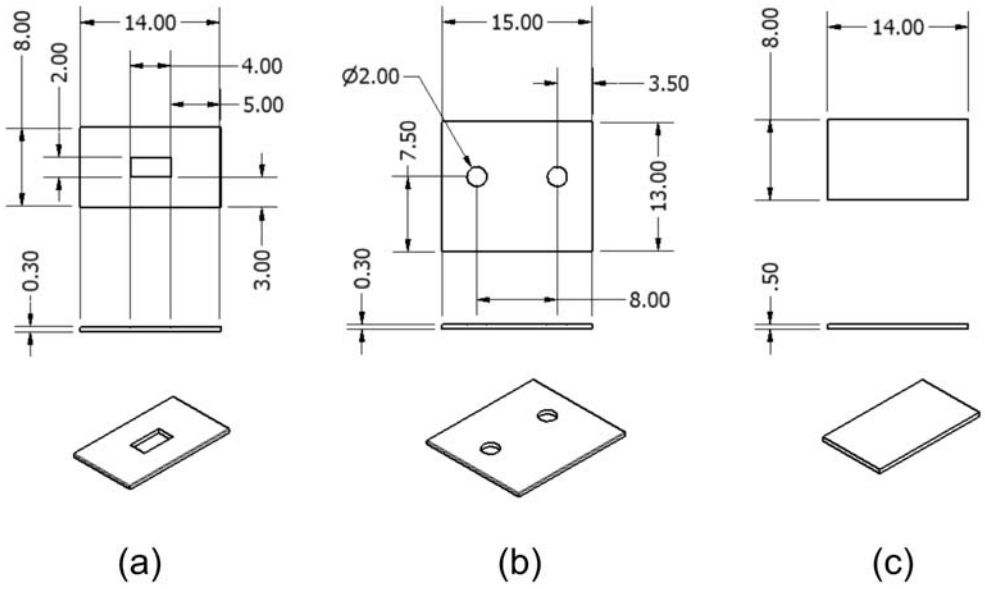

Figure C.5: Engineering drawings with dimensions for (a) the PDMS top gasket, (b) the PDMS bottom gasket, and (c) the pyrex window.

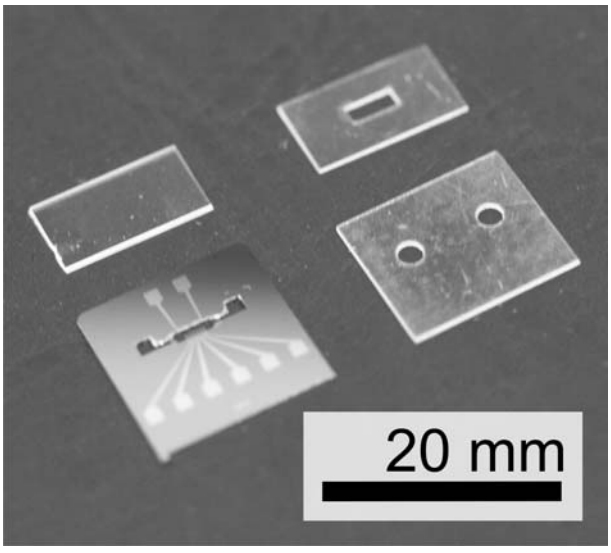

Figure C.6: A photograph of the PDMS top and bottom gasket, the pyrex window, and the ECC chip.

Appendix D

List of Publications

D.1 Refereed Contributions

D.1.1 Journal Articles

1. L.M. Fischer, C. Pedersen, K. Elkjær, S. Dohn, A. Boisen, M. Tenje, "Development of a microfabricated electrochemical-cantilever hybrid platform," *Sensors and Actuators B: Chemical*, Submitted: 12 November 2010.

2. Xueling Quan, Lee M. Fischer, Anja Boisen, Maria Tenje, "Development of nanoporous gold electrodes for electrochemical applications," *Microelectronic Engineering*, Submitted: 14 September 2010.

3. C. Ophus, E.J. Luber, M. Edelen, Z. Lee, L.M. Fischer, S. Evoy, D. Lewis, U. Dahmen, V. Radmilovic, D. Mitlin, "Nanocrystalline-amorphous transitions in Al-Mo thin films: Bulk and surface evolution," *Acta Materialia*, vol. 57, pp. 4296-4303, 2009.

4. L.M. Fischer, M. Tenje, A.R. Heiskanen, N. Masuda, J. Castillo, A. Bentien, J. Emnéus, M.H. Jakobsen, A. Boisen, "Gold cleaning methods for electrochemical detection applications," *Microelectronic Engineering*, vol. 86, pp. 1282-1285, 2009.

5. L.M. Fischer, V.A. Wright, C. Guthy, N. Yang, M.T. McDermott, J.M. Buriak, S. Evoy, "Specific detection of proteins using nanomechanical resonators," *Sensors and Actuators B: Chemical*, vol. 134, pp. 613-617, 2008.

D.1.2 Patents

1. "FABRICATION AND USE OF SUBMICRON WIDE SUSPENDED STRUCTURES," Stephane Evoy, Lee M. Fischer, Csaba Guthy, U.S. Patent Publication No. US 2010/0083762 A1, Granted 8 April 2010.

D.2 Conference Contributions

D.2.1 Proceedings

1. L.M. Fischer, S. Dohn, A. Boisen, M. Tenje, "An electrochemical-cantilever platform for hybrid sensing applications," *Proceedings of the IEEE: The 24th International Conference on Micro Electro Mechanical Systems (IEEE MEMS 2011)*, Paper No. 0338, Cancún, Mexico, 24-27 January 2011.

2. L.M. Fischer, A. Nielsen, S. Dohn, M. Tenje, A. Boisen, "An electrochemical-cantilever hybrid sensor for metal ions," *Proceedings of the IEEE: The 9th Annual Conference on Sensors (IEEE Sensors 2010)*, Paper No. 1693, Waikaloa, HI, USA, 1-4 November 2010.

D.2.2 Oral Presentations

1. Lee MacKenzie Fischer, Allan Svejstrup Nielsen, Søren Dohn, Maria Tenje, Anja Boisen, "An electrochemical-cantilever hybrid sensor for metal ions," *The 9th Annual IEEE Conference on Sensors (IEEE Sensors 2010)*, Lecture No. A3L-C1, Waikaloa, HI, USA, 1-4 November 2010.

2. Maria Tenje, Lee M. Fischer, Xueling Quan, Anja Boisen, "Introducing electrochemical readout to mechanical sensors," *Dansk Elektrokemisk Forening: Conference on Electrochemical Science and Technology*, Lyngby, Denmark, 30 September - 1 October, 2010.

3. C. Guthy, L.M. Fischer, V.A. Wright, A. Singh, J.M. Buriak, S. Evoy, "Nanomechanical resonators for specific detection of proteins," *AVS 55th International Symposium & Exhibition*, Lecture No. MN-Tu4, Boston, MA, 19-24 October, 2008.

4. C. Guthy, L.M Fischer, V.A. Wright , A. Singh, J.M. Buriak, S. Evoy, "Nanomechanical Resonators for Specific Detection of Proteins," *Canadian NanoForum*, Oral Presentation, Edmonton, Canada, 28-29 May 2008.

5. C. Guthy, L.M Fischer, V.A. Wright , A. Singh, J.M. Buriak, S. Evoy, "Specific Detection of Proteins using Nanomechanical Resonators," *5th Annual Conference on Foundations of Nanoscience (FNANO)*, Snowbird, USA, 22-25 April 2008.

D.2.3 Posters

1. L.M. Fischer, S. Dohn, A. Boisen, M. Tenje, "An electrochemical-cantilever platform for hybrid sensing applications," *The 24th Interna-*

tional Conference on Micro Electro Mechanical Systems (IEEE MEMS 2011), Poster No. 0338, Cancún, Mexico, 24-27 January 2011.

2. Xueling Quan, Erol Zekovic, Lee M. Fischer, Anja Boisen, Maria Tenje, "Characterization of nanoporous gold electrodes by electrochemical methods," *Dansk Elektrokemisk Forening: Conference on Electrochemical Science and Technology*, Lyngby, Denmark, 30 September - 1 October, 2010.

3. Xueling Quan, Lee M. Fischer, Anja Boisen, Maria Tenje, "Development of nanoporous gold electrodes for electrochemical applications," *MNE2010: 36th International Conference on Micro and Nano Engineering*, Poster No. P-MEMS-74, Genoa, Italy, 20-22 September 2010.

4. Lee MacKenzie Fischer, Christoffer Pedersen, Karl Elkjær, Søren Dohn, Maria Tenje, Anja Boisen, "An electrochemical-cantilever hybrid platform," *MNE2010: 36th International Conference on Micro and Nano Engineering*, Poster No. P-MEMS-8, Genoa, Italy, 20-22 September 2010.

5. Lee M. Fischer, Maria Tenje, Jaime Castillo, Anders Bentien, Jenny Emnéus, Mogens Havsteen Jakobsen, Anja Boisen, " Gold cleaning methods for electrochemical detection applications," *MNE08: 34th International Conference on Micro and Nano Engineering* Poster No. MEMS2-P11, Athens, Greece, 16-18 September 2008.

6. L.M. Fischer, M. Tenje, J. Castillo, A. Bentien, J. Emnéus, M.H. Jakobsen, A. Boisen, "Characterization of NTA-thiol monolayers on Au electrodes for application in a cantilever-based heavy metal ion sensor," *The 5^{th} International Workshop on Nanomechanical Cantilever Sensors*, Mainz, Germany, 19-21 May 2008.